The Dissertation Committee for Christopher Joseph Certifies that this is the approved version of the following dissertation:

Old Dog, New Tricks: Repurposing Iron-Carbide-Carbonyl Clusters as Precursors for Structural Modeling of the Nitrogenase Cofactor

Committee:

Michael J. Rose, Supervisor

Simon M. Humphrey

Richard A. Jones

Eric V. Anslyn

Delia J. Milliron

Old Dog, New Tricks: Repurposing Iron-Carbide-Carbonyl Clusters as Precursors for Structural Modeling of the Nitrogenase Cofactor

by

Christopher Joseph

Dissertation

Presented to the Faculty of the Graduate School of

The University of Texas at Austin

in Partial Fulfillment

of the Requirements

for the Degree of

Doctor of Philosophy

The University of Texas at Austin

May 2020

Dedication

To my mother,
who instilled within me the collection of practical knowledge that has served in every aspect of my life,
as well as the infallible and time-saving philosophy that if you are going to do something, you might as well do it right the first time.

To my brother,
who I can always count on to lend an ear without judgement or a helping hand without condition. Moreover, you consistently inspire me with your independent spirit, giving me the fortitude that has allowed me to carve out my own path thus far.

To my father,
For all the times we watched *Nature*, or *Nova*, or even your favorite *Animals are Beautiful People* together; For all the unsolicited interruptions with physics and math problems, each of which would initially seem like a chore but inevitably would morph into an undeniably engaging lesson; For all the memories in which we watched thunderstorms together, dissected computers together, or discussed politics or culture or philosophy together; For every incredible and subtle moment in which you managed to make the world around me seem unfathomable yet invigorating: Thank you.

Finally, to the family dogs, past and present,
Woof! Woof, woof!

Acknowledgements

First, I would like to gratefully acknowledge Dr. Subramaniam Kuppuswamy for providing the initial synthetic foundation upon which the work presented in this dissertation is built. Secondly, I wish to thank Dr. Vincent Lynch for patiently fielding every crystallographic question I could throw at him, regardless of whether I was asking the question for the first or the fiftieth time.

I am especially grateful to my cohort, Dr. Spencer Kerns and Dr. Patrick Shupp, for their recurring and invaluable input, our entertaining conversations, and an all-around enjoyable six years. I would also like to convey my thanks to the Rose Group members for letting me bounce an unending torrent of good and bad ideas off them.

Finally, I am most grateful to Prof. Mike Rose for taking a clueless first-year who was, admittedly, a bit full of himself and helping him grow into a competent scientist. The lessons I have learned under your mentorship and guidance have become the foothold I will need to continue towards a successful scientific journey. Because of you, I enthusiastically look forward to what my future has in store.

Abstract

Old Dog, New Tricks: Repurposing Iron-Carbide-Carbonyl Clusters as Precursors for Structural Modeling of the Nitrogenase Cofactor

Christopher Joseph, Ph.D.

The University of Texas at Austin, 2020

Supervisor: Michael J. Rose

Nitrogenases are the only known biological enzyme capable of catalyzing the transformation of dinitrogen (N_2) into ammonia (NH_3). The active site of nitrogenase is comprised of a double-cuboidal iron-sulfur cluster featuring an interstitial carbide as the shared vertex, three 'belt' sulfides bridging the cuboidal components, and either a homocitrate-bearing heterometal (Mo, V) or an Fe at one of the distal capping metal sites. Out of the three nitrogenases, the Mo-dependent variant demonstrates the highest activity for N_2 conversion. The active-site cofactor of Mo-dependent nitrogenase (FeMoco) was first isolated in 1977; however, after decades of kinetic, structural, and spectroscopic research, many questions surrounding the mechanism of substrate reduction and the electronic structure of reaction intermediates remain unanswered. In this regard, the synthetic modelling community has contributed significantly towards directing mechanistic discussions with N_2-reducing functional model compounds. Furthermore, structural model compounds have played a pivotal role in deciphering the structural and electronic properties of FeMoco, including the identification of the central carbide and

assignment of metal-site valence and spin states. Despite this remarkable progress, a synthetic model featuring a paramagnetic iron cluster with sulfides, interstitial carbide, and heterometal Mo has yet to be reported.

The work relayed in this dissertation outlines our efforts towards pursuing this synthetic goal. As such, we utilize a family of carbonyl-supported iron clusters — first reported in the 1960s — featuring iron-coordinated inorganic carbide. However, the highly symmetric packing structures have made heterometal-containing carbidocarbonyl iron clusters difficult to unambiguously characterize by X-ray crystallography. Moreover, the strongly π-acidic ligation sphere enforces low metal-valance states and overall diamagnetism, and ligand substitution of COs is difficult to control. Here, we demonstrate a strategy to disrupt the symmetry in molybdenum-containing heteroclusters to unambiguously characterize the Mo site in XRD. Additionally, CO→S ligand substitution is achieved with the utilization of electrophilic sulfur sources, leading to progressively higher oxidation state Fe sites. These synthetic approaches for heterometal incorporation and oxidative sulfur insertion will serve as fundamental stepping-stones towards future endeavors in utilizing and functionalizing carbidocarbonyl iron clusters as synthetic precursors and ultimately, in biomimetically modeling the nitrogenase active site cluster.

Table of Contents

List of Tables

List of Figures

List of Schemes

Chapter 1: Structural and Electronic Considerations for Synthetic Modeling of the Mo-dependent Nitrogenase Cofactor

1.1 Ecological and Industrial Fixation of Molecular Dinitrogen

The importance of biological and agricultural access to utilizable nitrogen is not easily overstated: All living organisms require nitrogen to grow. As nitrogen is an essential component for the synthesis of nucleic acids and proteins, the biological requirements for access to this element are enormous. On average, for every 100 carbon atoms incorporated into cells, between 2 and 20 atoms of nitrogen are present.[1] Ecologically usable nitrogen is most commonly present in the forms of nitrates (NO_3^-) in aerobic environments or ammonia (NH_3) in anaerobic conditions, and access to these compounds often serves as the limiting factor for the organism growth and ecological productivity. Nonetheless, nitrogen is overwhelmingly abundant on Earth — which carries over 10^{20} moles of nitrogen atoms. However, nearly half of this nitrogen remains fixed as molecular dinitrogen (N_2) and is unusable to most forms of life (**Figure 1.1**).

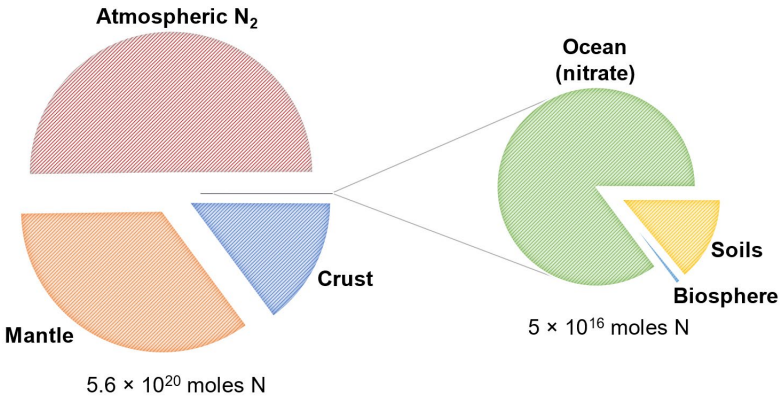

Figure 1.1 Nitrogen reservoirs on earth. Nearly half of earth's nitrogen atoms are chemically fixed as atmospheric dinitrogen. Data sourced from ref. 1.

Despite its high natural abundance in the atmosphere, molecular N_2 is not well-utilized by most organisms. The thermodynamic strength of the N≡N triple bond renders the gas essentially inert for many biological systems. Enthalpically, the conversion of $N_2 \rightarrow 2\ NH_3$ is a net exothermic (–21 kcal/mol) reaction, and the N≡N bond dissociation energy of 224 kcal/mol is comparable to that of the acetylene HC≡CH triple bond (230 kcal/mol), though the latter enjoys a wider range of room-temperature activation reactions.[2,3] Thus, the chemical inertness of N_2 is attributed to a kinetic barrier rather than a strictly thermodynamic one. This is confirmed by the relatively high dissociation energy of 98 kcal/mol required for cleavage of the first N≡N bond, which is nearly half the total dissociation enthalpy (**Figure 1.2**). Furthermore, the conversion of dinitrogen to the diazene intermediate is itself endothermic ($N_2 \rightarrow N_2H_2$, ΔH = +51 kcal/mol). Conversely, cleavage of the first HC≡CH bond both is lower (53 kcal/mol) in activation barrier and results in an overall exothermic (–42 kcal/mol) conversion towards ethylene (C_2H_4). Notably, the 53 kcal/mol barrier energy is less than a quarter of the total energy stored in the HC≡CH triple bond (230 kcal/mol). As such, the initiation of reduction for N_2 is a considerably more difficult chemical endeavor than for HC≡CH, despite the fact that acetylene has the thermodynamically stronger triple bond. Two additional observations consistent with the high kinetic barrier of N_2 are (1) the large HOMO-LUMO gap (10.82 eV in N_2 vs. 8.47 eV in acetylene) which hinders 1 e^- or 2 e^- reduction and (2) the poor proton affinity exhibited by N_2 (118 kcal/mol) is lower than those of HC≡CH (153 kcal/mol), CO (142 kcal/mol), and even CH_4 (130 kcal/mol), which makes protonation of N_2 considerably unfavorable, even in the presence of strong acid.[3,4]

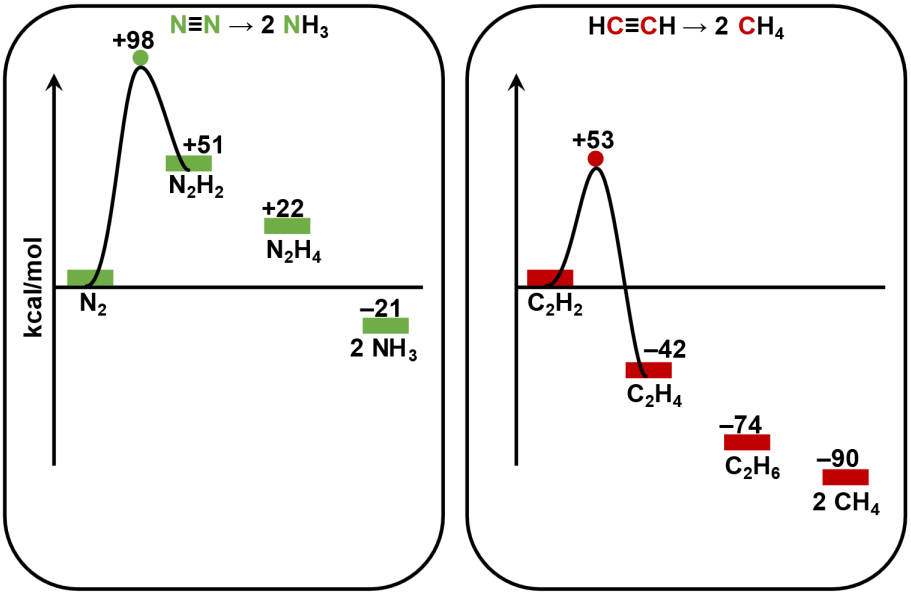

Figure 1.2 Reaction coordinate diagrams for the uncatalyzed reduction reactions $N_2 \rightarrow 2\ NH_3$ (*left*) and $HC{\equiv}CH \rightarrow 2\ CH_4$ (*right*). Data sourced from ref. 3.

Commercial utilization of fixed nitrogen is primarily dominant in the agricultural sector, where ammonium and nitrates are used as fertilizer (**Figure 1.3**).[5,6] With the development in the 1950s of a commercial-scale process for $N_2 \rightarrow 2\ NH_3$ conversion (the Haber-Bosch process), ammonia became the principal source of nitrogen in fertilizer. This industrial synthesis is performed by passing a mixture of N_2 and H_2 gases under high pressure (3000 psi) over a heated (400 °C) Fe/Ru catalytic bed (**Scheme 1.1**).[7] However, a single pass of this process yields only a conversion efficiency of ~15% — though an overall 97% conversion may be achieved by recycling the unconverted gases.[8] Consequently, this energy- and capital-intensive process ranks as the second-most energy-consumptive industrial process in the world (following cement production) and is responsible for ~1–2% of global energy usage yearly. Furthermore, the H_2 utilized for the Haber-Bosch process is almost entirely derived from fossil fuels, resulting in an overall $CH_4 \rightarrow CO_2$ conversion.

Thus, the carbon-less conversion of N_2 and H_2 into NH_3 is indeed associated with a carbon footprint.

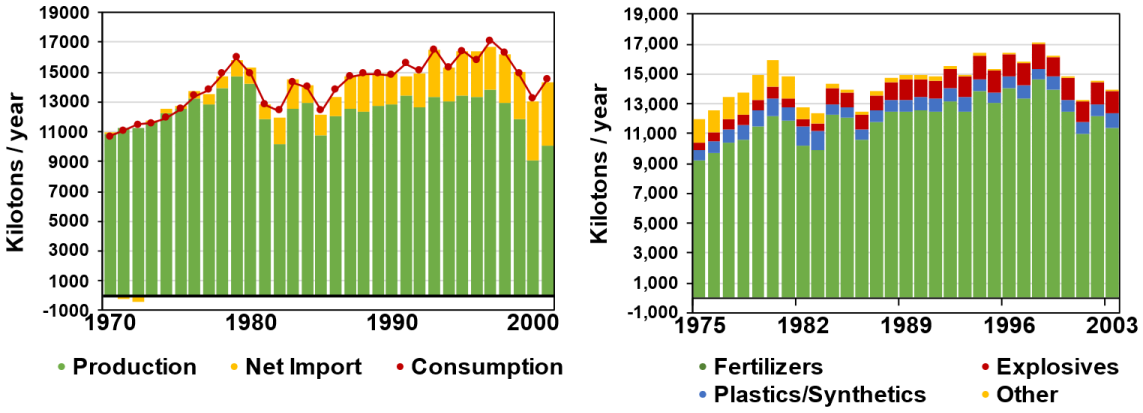

Figure 1.3 Ammonia production, consumption, and trade in the United States (*left*). Ammonia end use in the United States (*right*). Data sourced from refs. 5,6.

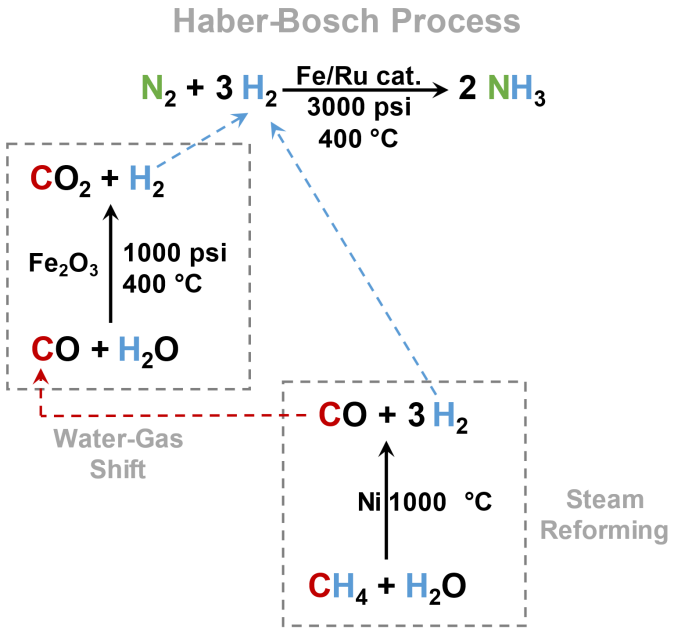

Scheme 1.1 Schematic representations of the industrial Haber-Bosch Process, as well as industrial sources of H_2 gas derived from methane.[9]

On the other hand, biological catalytic systems do not have access to the extreme conditions as those seen in the industrial setting and are instead confined to ambient temperatures and pressures. The nitrogenases — a class of enzymes which catalyze ammonia synthesis from dinitrogen — are the only biological systems known to catalyze $N_2 \rightarrow 2\ NH_3$ conversion. In contrast to the H_2-consuming Haber-Bosch process, dinitrogen reduction by the nitrogenase (N_2ase) is achieved using 8 H^+ and 8 e^-, liberating 1 obligatory equiv of H_2 (**Figure 1.4**).[10] Three variants of nitrogenase are known: Mo-dependent, V-dependent, and Fe-type; the Mo-dependent nitrogenase, however, exhibits the highest rate of catalytic activity.[11] Crystal structure data of the enzyme, first reported in 1992, reveals a homodimeric enzyme, in which each monomer consists of two components: (1) dinitrogenase (MoFe protein in Mo-dependent nitrogenase), in which the catalytic active site is contained, and (2) dinitrogenase reductase (Fe protein), an electron-transfer protein.[12,13] Despite this initial crystal structure data, a complete structural and electronic portrait of the resting-state active site was not elucidated for over two decades. Additionally, the catalytic mechanism of the active site still remains unknown despite the accumulation of structural and functional information. This chapter will summarize the known structural and electronic details of the N_2ase active site — with heavy emphasis on the Mo-dependent N_2ase cofactor (FeMoco). Additionally, the collective of synthetic, spectroscopic, and reactivity studies conducted by the biomimetic modeling community and have demonstrated a profound impact upon the mechanistic debate surrounding N_2ase. Therefore, a number of highly impactful model constructs are discussed, highlighting both the synthetic achievements and shortcomings of current N_2ase model compounds. Finally, the overarching objectives are outlined for the work presented in this dissertation.

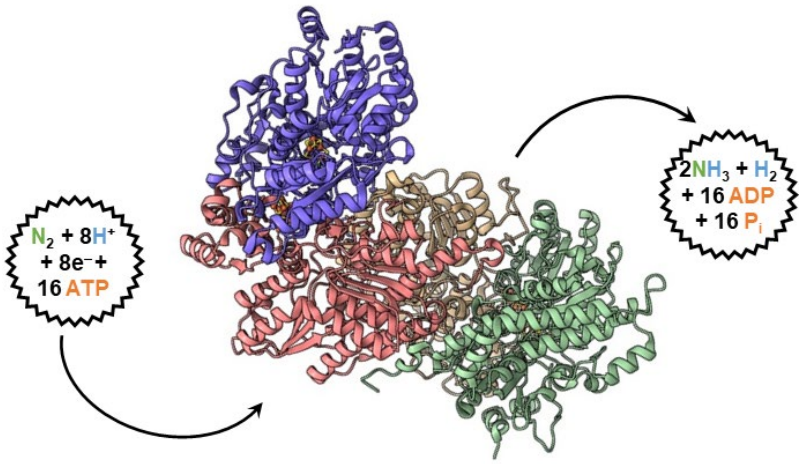

Figure 1.4 Biological catalysis of dinitrogen to ammonia proceeds by utilization of 8 H^+, 8 e^-, and 16 ATP. An obligatory H_2 molecule is liberated for each N_2 molecule that undergoes reduction. Structural data sourced from ref 14 and visualized using *ChimeraX*.[15]

1.2 Structural Elucidation of the Nitrogenase Active Site

The iron-molybdenum cofactor (FeMoco) was first isolated from the MoFe protein in 1977 by Shah and Brill and was photospectrometrically assigned an Fe:Mo:S ratio of 8:1:6.[16,17] However, the first crystal structure (**Figure 1.5**, *left*) — reported in 1992 by Rees *et al.* and determined with 2.9 Å resolution — revealed an active site initially described as a 2-component active site comprised of two clusters: a 4Fe:4S cluster and 1Mo:3Fe:2S cluster bridged by three non-protein ligands (designated as two sulfides and one unresolved site).[12,13] The cofactor is tethered to the protein by two ligands coordinated to the two distal metal sites: a cysteine residue ($Cys^{\alpha 275}$) located at the distal iron site and a histidine residue ($His^{\alpha 442}$) ligated to molybdenum. The molybdenum site is additionally coordinated by two oxygens from a bidentate homocitrate (HC) ligand. However, the six proximal Fe sites in this proposed structure appear to be supported by non-planar trigonal coordination sphere, which is uncharacteristic for biological iron in a resting state enzyme. A decade following

the 1992 report, a higher resolution structure (1.16 Å resolution) of FeMoco by Einsle, Rees *et al.* revealed the presence of a central, interstitial hexacoordinate light (2*p*) atom residing in the tetrahedral hole of the six proximal Fe sites.[18,19] Einsle and Rees initially postulated the site to be a nitride based on electron density integration studies; however, they suggested that carbon and oxygen could not be unambiguously discounted.

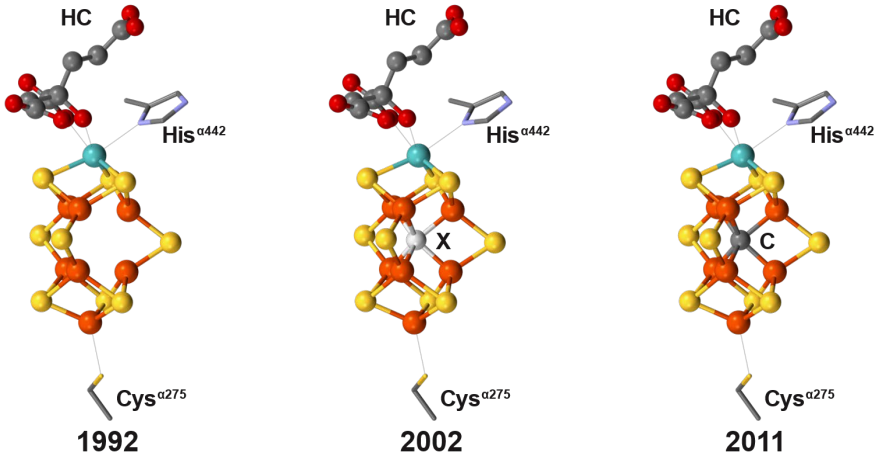

Figure 1.5 Progression of structure refinement for the iron-molybdenum cofactor (FeMoco) from structural X-ray diffraction (XRD) data and spectroscopic pulse EPR and X-ray emission (XES) data. Structural data visualized using *Mercury*.[20]

In 2011, two independent research efforts concurrently ascertained the identity of the central atom to be a carbide, rather than a nitride. Rees, Einsle *et al.* confirmed the carbide experimentally utilizing two separate experiments: (1) improved structural resolution (1.0 Å) for electron density integration analysis and (2) comparative pulsed EPR (ESEEM) on isotopically labeled (^{13}C or ^{15}N) MoFe protein (resting state S = ³⁄₂), in which significant hyperfine coupling was observed in the ^{13}C-labeled (I = ½) protein.[21] These monumental findings were printed onto a single page in the mid-November 2011 issue of *Science*. In the very same issue, a publication of equal magnitude by DeBeer *et al.* utilized a combination of valence-to-core X-ray emission spectroscopy (V2C-XES) and

computationally calculated spectra for cofactors bearing various interstitial atoms (C^{4-}, N^{3-}, and O^{2-}) to determine the identity of the interstitial atom.[22] The capability of V2C-XES to distinguish between light atoms within a multimetallic cluster was demonstrated in a preceding study by DeBeer *et al.* comparing synthetic and computational model compounds bearing various interstitial atoms to differentiate between Fe_6 hexacoordinate C, N, and O sites.[23] These results of these studies identified the interstitial atom in FeMoco as a carbide. Thus, the concurrent findings by the Einsle and DeBeer research groups unambiguously established the presence of an interstitial carbide in the N_2ase cofactor.

In the years following confirmation of the identity of the carbide in FeMoco, Ribbe and Hu proceeded to investigate the biogenesis pathway of carbide formation in the M-cluster. Using isotope-labeling experiments and CW and pulse EPR, the origin of the carbide was determined to be a methyl group from S-adenosylmethionine (SAM) during protein assembly by NifB.[24–26] Following initial transfer from SAM onto a sulfide in the $(Fe_4S_4)_2$ K-cluster (**Figure 1.6**), the CH_3 group undergoes H-atom abstraction by an additional equiv of SAM, followed by continued, iterative deprotonation/dehydrogenation to for the L-cluster. Subsequent maturation by the NifEN assembly protein leads to substitution of a distal Fe site with Mo(HC) to achieve the final M-cluster. The complete portrait of M-cluster biogenesis is an extensive and ongoing body of research. While the collection of is not discussed here any further, interested readers may refer to the works of Ribbe and Hu.[27–29]

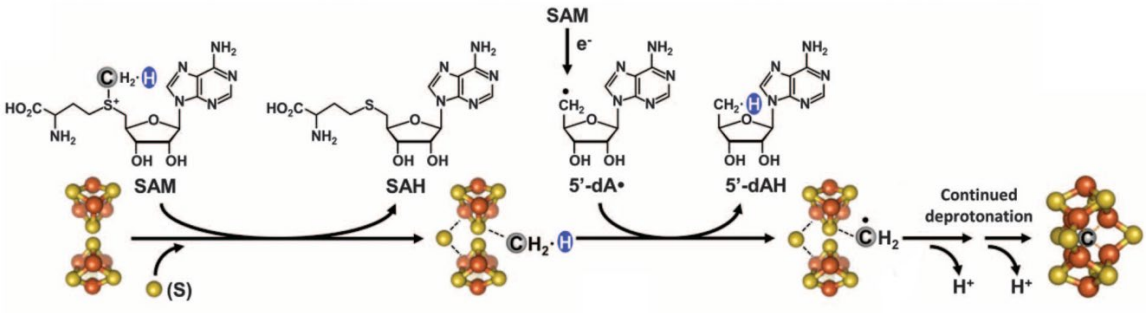

Figure 1.6 Biogenesis pathway for insertion and formation of the carbide and the 9th sulfide during protein assembly by NifB. Proposed by Ribbe and Hu. Image adapted from Wiig; Hu; Lee; Ribbe. *Science* **2012**, 337, 1672. Reprinted with permission from AAAS.

In many respects, FeMoco is structurally similar to other synthetic and biological iron sulfur clusters. The average Fe–Fe distance of 2.63 ± 0.04 Å places individual iron sites within range to induce bonding interaction between metal centers. Similarly, the average Fe–Mo distance of 2.684 ± 0.008 Å is typical for reported synthetic heterometal-iron-sulfur clusters.[30] Fe–S contacts exhibit an average distance of 2.25 ± 0.03 Å. Finally, the Fe–C bond is not a known motif in iron-sulfur clusters outside of the nitrogenases. Moreover, synthetic clusters in the Cambridge Structural Database do feature Fe-coordinated N and O sites, but examples with carbon are lacking. Nonetheless, the average Fe–C distance of 2.00 ± 0.02 Å observed in FeMoco fall within the range of distances displayed in compounds with N (Fe–N range: 1.871–1.977 Å) or O (Fe–O range: 2.052–2.190 Å) incorporated donor atoms.

Of additional structural note is the identity of the heterometal atom. The active site of Mo-dependent nitrogenase — also referred to as the iron molybdenum cofactor (FeMoco) or the M-cluster — displays the greatest catalytic activity among the various nitrogenases for ammonia synthesis and, consequently, is the subject of most nitrogenase-related research.[11] In environments where available Mo is scarce, paralogous vanadium-

and iron-nitrogenases are expressed. The active site of each in the resting state is *mostly* structurally analogous to FeMoco, with the key distinction being that the Mo site is occupied by V (FeVco or V-cluster) or Fe (L-cluster).[31] The precise role of the heterometal in substrate reduction is still unknown. Interestingly, FeVco does display greater CO-reducing activity over FeMoco with conversion towards partially unsaturated hydrocarbon products with various carbon chain lengths (C2 to C7).[32] Additionally, published crystallographic data of FeVco typically presents a structure in which one of the 3 belt sulfides (see **Figure 1.6**) has been substituted with an bridging carbonate (CO_3^{2-}).[33,34] Furthermore, the all-Fe nitrogenase homologue — which exhibits the lowest rate of N_2 conversion — is capable of complete reduction of C1 substrates (CO, CN^-) to methane (CH_4).[35,36]

1.3 Electronic and Mechanistic Insights

1.3.1 Electronic Structures of Metal Sites in FeMoco and FeVco

Soon after Shah and Brill reported a method for reproducibly isolating the MoFe protein in 1977, Münck *et al.* found that an electron spin assignment of S = ½ observed in EPR that was attributable to FeMoco as concluded by Mössbauer data.[37] While this spin assignment for the overall cluster was confirmed by ENDOR, XAS, and additional Mössbauer spectroscopic data, the oxidation states of individual Fe sites remained unresolved for decades.[38,39] Following the completed structural elucidation of the active site, single crystal EPR data demonstrated that the main g_z axis oriented along the C_{3v} axis of the cluster, as expected on the basis of structural symmetry. However, this study also found the EPR data was consistent with rhombic distribution of spin, and that the resultant g_y aligned towards the Fe3–Fe7 edge (**Figure 1.7**).[40] Additional spatially-resolved

refinement of the data suggested sites Fe1, Fe3, and Fe7 were reduced (ferrous Fe^{2+}) relative to Fe2, Fe4, Fe5, and Fe6 (ferric, Fe^{3+}).[41]

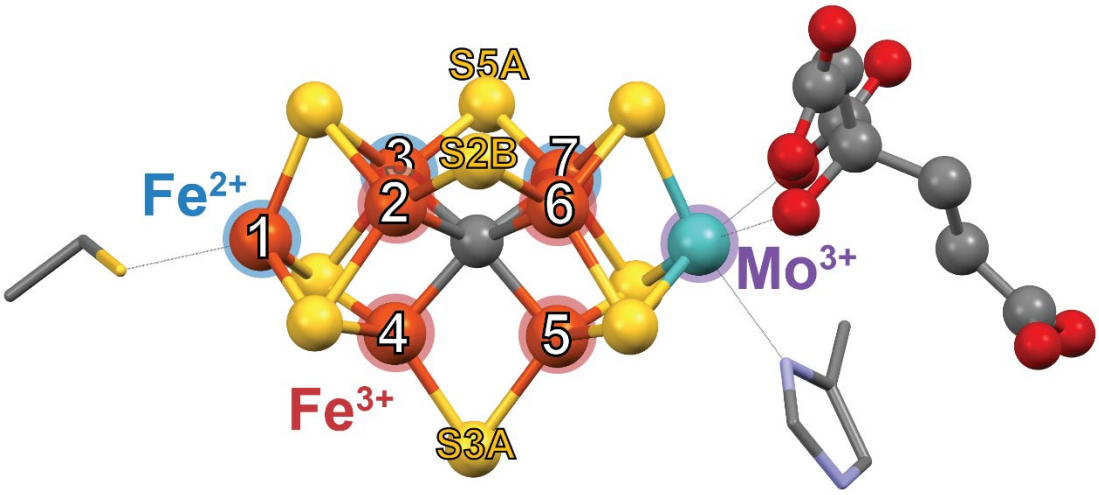

Figure 1.7 Fe and Mo oxidation states, Fe site literature numbering scheme, and labeled belt sulfides. Fe1, Fe3, and Fe7 are formally designated as ferrous (Fe^{2+}, highlighted blue); Fe2, Fe4, Fe5, and Fe6 are formally designated as ferric (Fe^{3+}, highlight red); the molybdenum site has been determined as Mo^{3+}. The belt sulfides in FeMoco are labelled S2B, S3A, and S5A in literature, as shown. Structure visualized using *Mercury*.[20]

Initial spectroscopic studies (XAS, ENDOR) of the Mo site in FeMoco assigned the heterometal an oxidation state of Mo^{4+}, though the authors noted that the assignment was not definitive.[42,43] However, high-resolution Mo K-edge XAS data reported in 2014 — along with spectroscopic comparisons to Mo-containing model compounds — demonstrated the true oxidation state of molybdenum to be Mo^{3+}.[44] Additionally, computational data suggests that the Mo^{3+} oxidation state is maintained in FeMoco throughout a variety of cluster redox states. The electronic structure of vanadium in FeVco was a topic of interest in the field due to the observed kinetic and functional differences displayed between the Mo and V homologues in N_2 vs CO reduction. Experimental

evidence suggests a V^{3+} ion, providing one fewer *d* electron at the heterometal site in FeVco (d^2 vs d^3 in Mo^{3+}). Despite this, the overall electron spin of the FeVco cluster remains the same, suggesting that a ferric iron site in FeMoco is ferrous in FeVco (**Figure 1.8**).[45] This assignment has additionally been supported by computational data along with comparison with spectroscopic data for synthetic heterometal FeS clusters, and this difference in spin states likely account for the significantly different reactivities observed between the clusters.

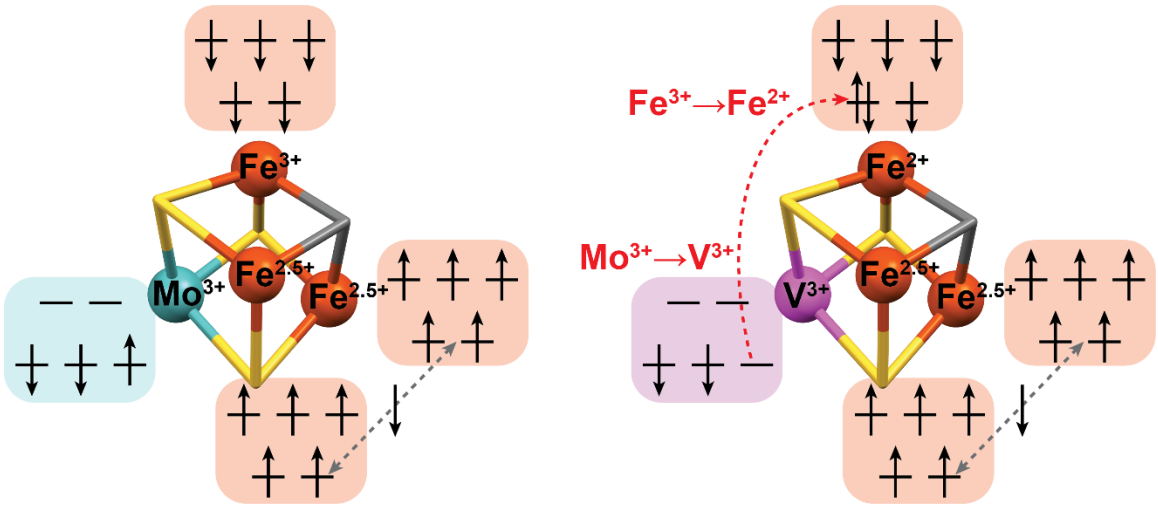

Figure 1.8 Proposed spin coupling diagrams for the FeMoco and FeVco clusters. M = Mo (*left*), V (*right*). DFT calculations predict a trivalent heterometal site in both cases. Consequently, an Fe site in FeVco exists in a reduced state compared to its FeMoco counterpart. Proposed by DeBeer *et al.*[45] Structures visualized using *Mercury*.[20]

1.3.2 Proposed Mechanistic Schemes for Dinitrogen Reduction

Initial insight into the nitrogenase mechanism was primarily founded upon extensive kinetic studies conducted throughout the 1970s to 1980s. Lowe and Thorneley famously proposed a rudimentary kinetic scheme (**Scheme 1.2**) whereby the resting-state N_2ase cofactor (designated E_0) undergoes four iterative protonation/reduction events (E_1–

E_4), at which point the stage is set for substrate binding. Concurrent with the liberation of one equiv H_2, N_2 binds and proceeds to be reduced to two NH_3 as the cofactor continues to undergo subsequent protonation & reduction. Liberation of the second equiv NH_3 returns the cofactor to it resting state, E_0.[10] Notably, H_2 gas can be liberated at the E_2 through E_4, prior to N_2 binding, necessitating additional protonation/reduction events to reach the E_4 state. Recently, Siegbahn proposed — with computational evidence — that the central carbide is protonated prior to the start of the catalytic cycle.[46,47] In this mechanistic scheme, the resting state cluster undergoes four protonation/reduction events (each intermediate designated A_0–A_4), protonating the central carbide to form an Fe-bound methylide and displaced to a peripheral position on the cluster. The fourth proton resides on a sulfur site, and four electrons maintain the overall charge of the cluster. The final A_4 step, then, is equivalent to E_0 in the LT kinetic scheme and catalytic turnover can begin. However, it should be noted that a protonated carbon in FeMoco has not been experimentally observed. Notably, a published crystal structure by Einsle *et al.* depicting, ostensibly, a FeVco intermediate during substrate turnover (possibly representing E_6 or E_7) depicts the carbide residing at the same interstitial position (and presumably unprotonated) as that observed in the resting state FeVco.[34] An alternative explanation for the role of the carbide grounded on observations of synthetic model compounds and spectroscopic data proposes a stabilizing role for the interstitial carbide, such that it modulates covalency to preserve the structural integrity of the overall cluster.[45,48–50]

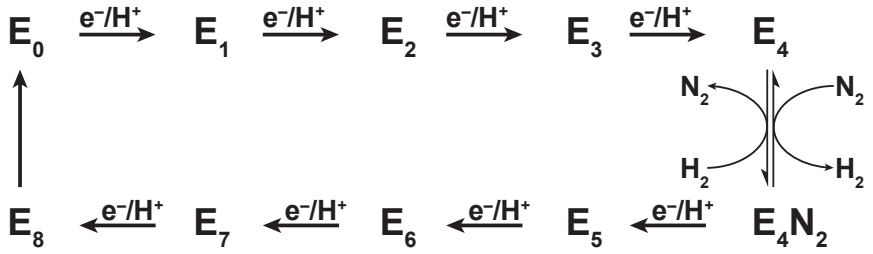

Scheme 1.2 Simplified Lowe-Thorneley kinetic scheme.[10]

The precise geometric and electronic structural details of the E_1–E_4 intermediates are still mostly unknown. However, very recent spectroscopic and computational information about the E_1 state has begun to emerge. Spectroscopic data (Mössbauer, XAS) from the DeBeer group suggest that the E_1 step involves reduction of an Fe site in conjunction with protonation of a belt-sulfide.[51,52] Comparative energy calculations indicate that the belt sulfides are more basic than the other sulfides. Additionally, sites S2B and S5A appear more favorable towards protonation than S3A. A nearby histidine residue (His195) positioned above the cluster face encompassing S2B and S5A has been implicated as a possible proton donor. On the other hand, the mechanistic model proposed by Siegbahn indicates the formation of a hydride, thereby resulting in oxidation of the metal sites rather than reduction.[47]

The question of where on the cluster substrate binding occurs was a topic of considerable debate during the last two decades. The differences in N_2-reducing activity between the M-cluster, V-cluster, and L-cluster nominated the heterometal (i.e. Mo in FeMoco) as a likely site for substrate binding. This conclusion gained additional support with the publication in 2003 of Schrock's synthetic, Mo-centered complex as the first report of a synthetic and functional N_2-reducing catalyst with a N_2ase-relavent metal center.[53] A decade later (2013), however, Peters published a synthetic Fe complex bearing a 2*p* donor atom (B) in its ligation sphere and capable of catalytic N_2 conversion.[48]

Experimental and computational evidence with FeMoco and FeVco began to implicate iron as likely N_2-binding site. Inhibition of FeMoco with carbon monoxide (CO) and crystallization of the resulting MoFe protein revealed a structure in which the S2B belt sulfide — which bridges Fe2 and Fe6 — has been substituted with a bridging CO.[54] Additionally, treatment of FeMoco with KSeCN demonstrated similar lability of the belt sulfides: 1 equiv KSeCN under argon atmosphere resulted in substitution of S2B with Se.[55] Subsequent catalytic turnover with N_2 produced structures in which the Se migrated to the 5A or 3A positions. Crystallization and XRD of vanadium-dependent N_2ase during turnover presented a FeVco structure in which the S2B position was occupied by a small bridging ligand (presumably N or NH_x, though O or OH_x cannot be discounted).[34] Finally, the computational work surrounding the Mo site suggests that one of the oxygen donors dissociates from Mo during the E_2–E_4 steps, leaving an possible open coordination site. However, energy calculations suggest that activation of N_2 at this site results in significantly high increase in energy, and that binding at Fe2 and Fe6 is much more thermodynamically favorable (though still endothermic).[56] The conclusion drawn from these reports, then, is that a single or multi-centered iron site is the likely candidate for N_2 binding.

Finally, the proposed mechanisms of N_2 reduction proceed *via* one of three avenues: (1) the distal N is hydrogenated first and liberated as NH_3, leaving behind a N^{3-} nitride; (2) each N site undergoes hydrogenation in an alternating sequence, and liberation of NH_3 occurs in the last two steps; or (3) a hybrid mechanism that compromises between the distal and alternating pathways. The distal pathway generally describes N_2 reduction performed upon Mo and W complexes and exclusively presumes that N_2 binds in an end-on binding mode. In this context, it is sometimes referred to as the "Chatt cycle."[57] FeMoco is typically associated with the alternating mechanism, based on computational data as well as

experimental observation that diazene (HN=NH) is an intermediate in the reduction pathway.[58,59] However, Peters has also proposed a hybrid mechanism based on observed N_2-reduction pathways observed in synthetic model compounds.[60]

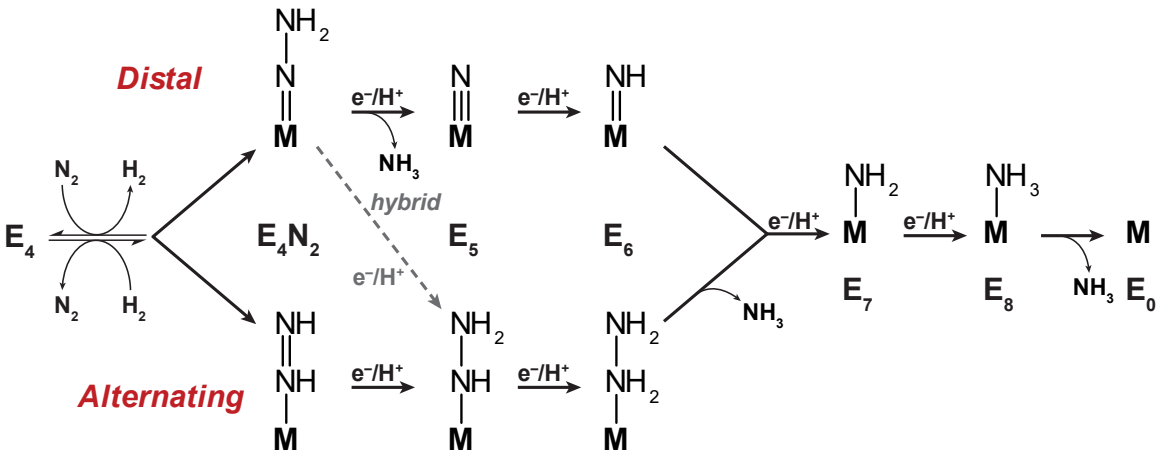

Scheme 1.3 Distal and Alternating mechanistic pathways for N_2 reduction. Note that the depicted single-centered, end-on binding mode is not necessary for all pathways.[59]

1.4 Synthetic Compounds for the Functional and Structural Modelling of FeMoco

As referenced throughout the previous section, studies utilizing synthetic model compounds have contributed greatly to the early mechanistic and electronic discussions surrounding nitrogenase in lieu of the highly sophisticated spectroscopic and computational techniques that have only recently become available for studying the complicated active site. The Schrock catalyst, a Mo complex featuring a sterically protected substrate-binding site (see **Scheme 1.4**), initially invigorated the debate to determine the binding site of FeMoco.[53] Nishibayashi has reported pincer-based

monomeric and dimeric Mo complexes which catalytically reduce N_2.[61,62] A pincer motif was later used by the same group to develop a catalytically active Fe-centered complex as well.[63] The Peters research group has published a series of Fe complexes featuring a tripodal ligand set with various axial donor atoms. The Si-ligated complex was first shown to bind N_2, followed by reports of B- and C-ligated complexes that could catalytically perform the reduction.[48,64,65] Spectroscopic and mechanistic studies with these compounds have demonstrated the axial atom modulates covalency with the Fe center throughout catalysis to support the various oxidation states and substrate coordination modes. Results from these studies were used to hypothesize a stabilizing role for the central carbide in FeMoco, performing similar modulations throughout turnover. The proposed hybrid distal-alternating mechanism determined for Peters' compounds was similarly extended to FeMoco as a possible mechanistic pathway.[60] Moreover, the tripodal donor set was later adapted to include a structurally relevant S donor as a bridging thiolate.[66] Synthetic work pursued by the Holland group has demonstrated activation of dinitrogen by multimetallic cooperation between two or four iron sites, representing a possible model for the binding mode of N_2 in FeMoco.[67,68] Additional synthetic work with an iron-carbenyl-thiolate complex utilize a tridentate ligand set and is capable of N_2 activation.[69]

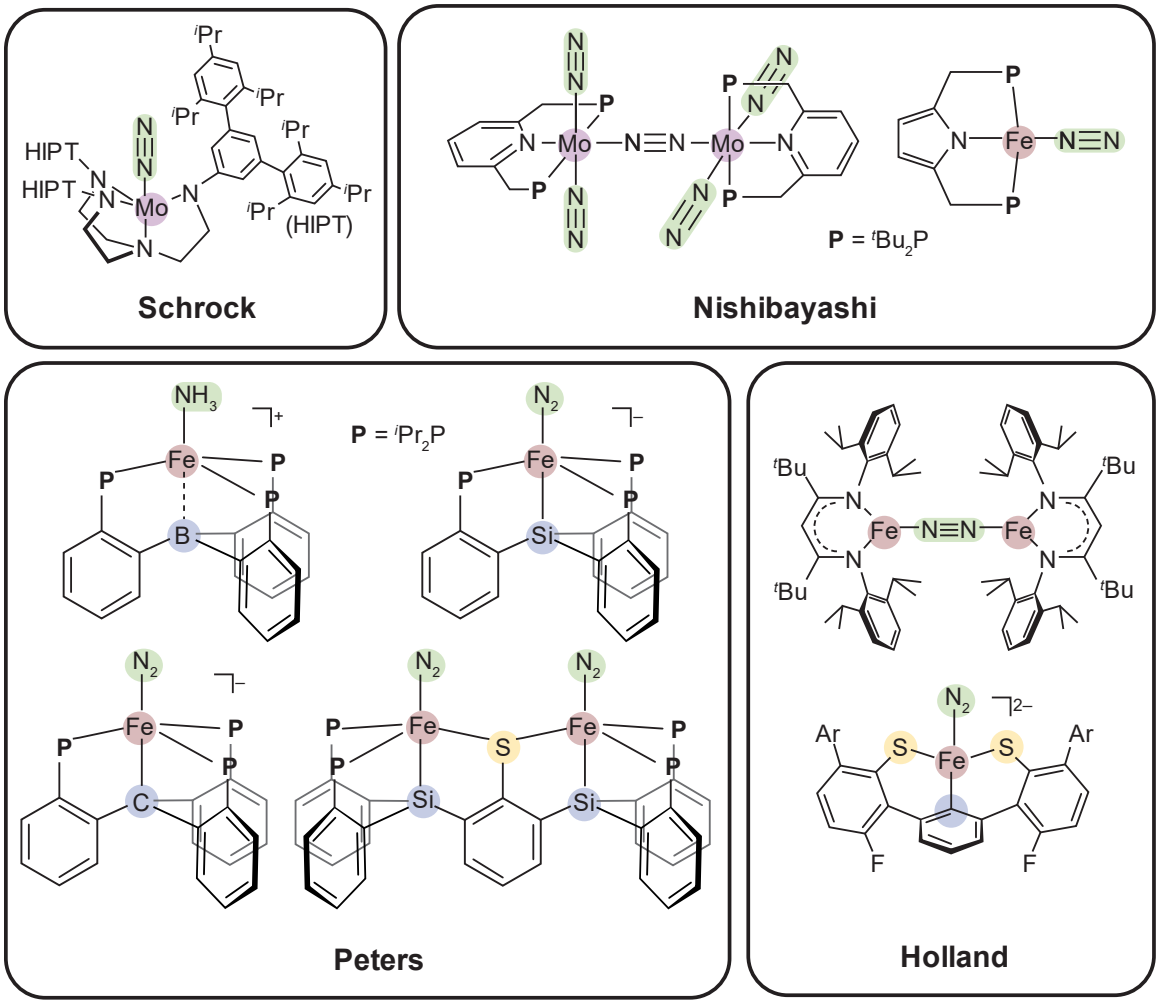

Scheme 1.4 Selected functional synthetic compounds for N_2 activation and/or reduction from the Schrock, Nishibayashi, Peters, and Holland research groups.

Functional synthetic model compounds capable of catalytically reducing or activating dinitrogen in various modes were particularly impactful towards early mechanistic discussions surrounding nitrogenase. In recent years, structural models have also been extensively utilized as synthetic references in studies probing for structural and electron information about FeMoco and FeVco. The carbonyl-supported hexa-iron cluster $[Fe_6(\mu_6\text{-}C)(CO)_{16}]^{2-}$ — which contains an interstitial, 6-coordinate carbide and is featured

prominently throughout this dissertation — was utilized along with its nitride congener $[Fe_6(\mu_6\text{-}N)(CO)_{16}]^-$ as a means calibrating X-ray emission spectra to distinguish between 2*p* atoms in multimetallic frameworks, thereby setting the stage for identification of the interstitial carbide in FeMoco.[23] Synthetic iron sulfur clusters developed by the Holm group and featuring heterometallic Mo^{3+} and V^{3+} sites assisted in the assignment of spin states at individual metal sites in the resting-state M- and V- clusters.[45,70,71] Outstanding work by the Agapie group has demonstrated electronic and catalytic modulation of iron clusters sites performed by substitution of various interstitial light atoms.[72,73] Synthetic structural modelling work from the Tatsumi group has presented a highly-relevant dicuboidal, vanadium-containing FeS cluster and an astonishingly remarkable cluster featuring belt-thiolates and an interstitial oxide.[74,75] Finally, Rauchfuss has recently published the first known multi-iron cluster to feature an intestinal carbide and inorganic sulfide.[76]

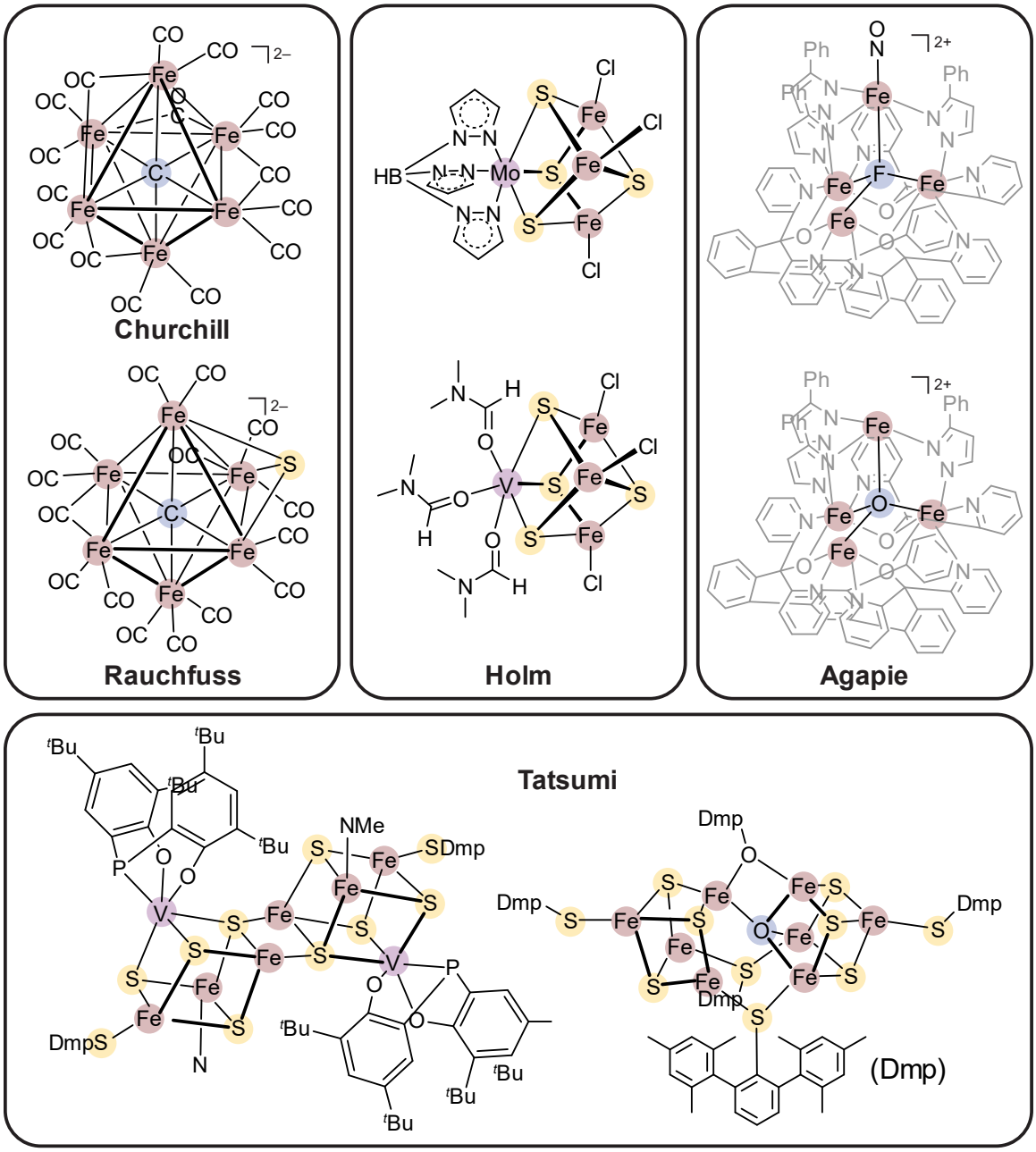

Scheme 1.5 Selected synthetic structural models for the nitrogenase active site, including works published by the Holm, Agapie, Tatsumi, and Rauchfuss.

1.5 Overarching Objectives for this Work

Undoubtedly, the field of structural modelling in the context of nitrogenase has been invaluable in advancing our structural, electronic, and mechanistic understanding of the nitrogenase active site. However, much synthetic work remains unaccomplished: As of this writing, the synthetic "Holy Grail" for FeMoco modeling of achieving a paramagnetic iron cluster with sulfides, interstitial carbide, and heterometal Mo continues to be sought after. Additionally, synthetic modelling work applied to the FeMoco biogenesis — such as the intermediate steps involved in carbide formation — are scarce, if not absent completely. Through the work outlined in the following chapters, we wish to expand upon the compendium of structural models in progression towards incorporation of important structural and electronic attributes of FeMoco (**Scheme 1.6**) into synthetic clusters.

To this end, we utilize a family of carbonyl-supported iron clusters featuring interstitial carbides — the first of which was reported by Braye *et al.* in 1962.[77] The hexa-iron cluster $(NEt_4)_2[Fe_6(\mu_6\text{-}C)(CO)_{16}]$ reported by Churchill et al. (see **Scheme 1.5**)[78,79] serves as a synthetic starting point towards highly FeMoco-relevant structural models, demonstrating flexibility between multiple redox states and versatility for heterometal substitution and sulfide incorporation. First, detailed synthetic procedures for the optimized generation of the various carbidocarbonyl iron clusters is related in Chapter 2. In Chapter 3, the synthetic pathway towards molybdenum incorporation into the cluster is described, along with a preliminary foray into nitrogenase-relevant catalysis. Finally, Chapter 4 explores a strategy for ligand CO→S substitution via utilization of electrophilic sulfur.

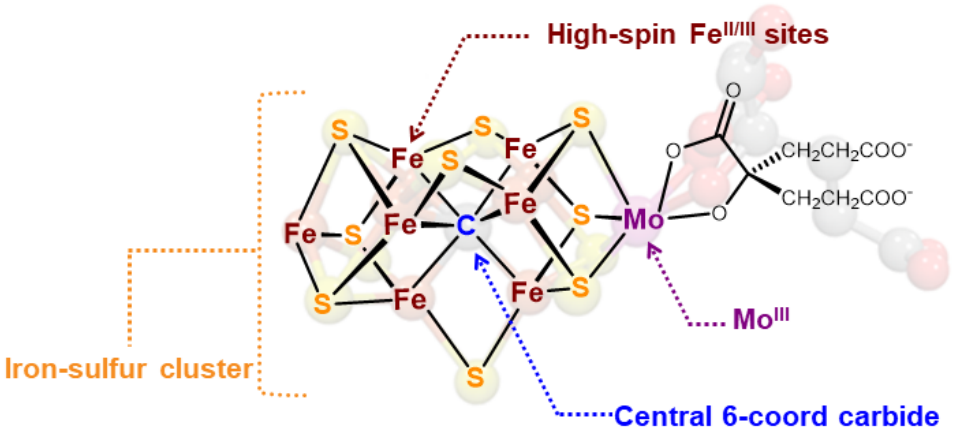

Scheme 1.6 Target structural and electronic attributes of interest in FeMoco for biomimetic modelling.

Chapter 2: Systematic, Optimized Syntheses of Iron Carbidocarbonyl Clusters*

2.1 INTRODUCTION

Small-molecule transition-metal clusters containing interstitial light (2*p*) atoms have provided a fascinating curiosity in inorganic chemistry for many decades. Since the discovery of the first such cluster — a carbonyl-supported square pyramid cluster encapsulating a basal interstitial carbide — by Braye *et al.* in 1962,[77] research into cluster chemistry has contributed to the understanding of bonding in multi-nuclear compounds and has presented opportunities to model heterogenous catalysis while also providing molecular, multi-metallic systems that may be modulated *via* ligand substitution. Diamagnetic 4*d* and 5*d* transition-metal clusters have demonstrated utility in alkene and carbonyl hydrogenation,[80–82] while iron-carbonyl clusters have been studied as avenues for catalytic hydrofomylation,[83–85] Fisher-Tropsch and CO reduction chemistry,[86–89] and amide hydrogenation.[90] More recently, iron clusters containing interstitial nitrides[91–93] and oxides[94,95] have been explored for their electrocatalytic capabilities in hydrogen evolution reactivity (HER) and CO_2 reduction.

The initial generation of iron pentacarbonyl was reported in late 1891.[96] However, it would not be for another nearly four decades before the first iron-carbonyl clusters — $Fe_2(CO)_9$ in 1927 and $Fe_3(CO)_{12}$ in 1932 — were reported.[97,98] In 1962, the first-reported iron-carbonyl-carbide cluster, $[Fe_5(\mu_5\text{-}C)(CO)_{15}]$, was generated as a minor product (0.5% yield) in a reaction of $Fe_3(CO)_{12}$ with methylphenylacetylene. Nearly a decade later,

---

* Portions of this chapter were published in:
Kuppuswamy, S.; Wofford, J. D.; Joseph, C.; Xie, Z.; Ali, A. K.; Lynch, V. M.; Lindahl, P. A.; Rose, M. J. *Inorg. Chem.* **2017**, *56* (10), 5998–6012.

Churchill *et al.* reported the synthesis and characterization of the first known anionic carbidocarbonyl cluster $(NMe_4)_2[Fe_6(\mu_6\text{-}C)(CO)_{16}]$ by reaction of the reduced manganate $Na[Mn(CO)_5]$ and $Fe(CO)_5$.[78,79] This dianionic cluster would go on to serve as the building block for the systematic syntheses of lower-nuclearity Fe_5 and Fe_4 clusters. Over the next two decades, pioneering work by Paolo Chini in synthetic techniques for deliberate and systematic synthesis of platinum-carbonyl clusters[99] introduced the techniques that would provide similar methodologies to be utilized in synthetic iron-carbonyl cluster chemistry by Tachikawa and Muetterties for five-iron clusters[100,101] and Bradley for four-iron clusters.[102–105] This chapter will discuss the utilization of $FeCl_3$ as an inner-sphere electron oxidizing agent under varying reaction conditions to achieve the selective removal of one or two Fe sites and generate Fe_5 and Fe_4 carbidocarbonyl clusters (**Scheme 2.1**). Additionally, the use of ferrocenium as an outer-sphere oxidizing agent upon $[Fe_6]^{2-}$ induces a 2 e^- oxidation while maintaining the 6-iron count of the cluster core to afford the previously unreported neutral cluster $[Fe_6(\mu_6\text{-}C)(CO)_{18}]$, which we recently reported as a synthetic "missing link" to this family of carbidocarbonyl iron clusters.[106] Finally, the electron counting rules prescribed by Polyhedral Skeletal Electron Pair Theory (PSEPT) are shown to rationalize cluster core geometries of known structures and predict those of unidentified cluster compounds.

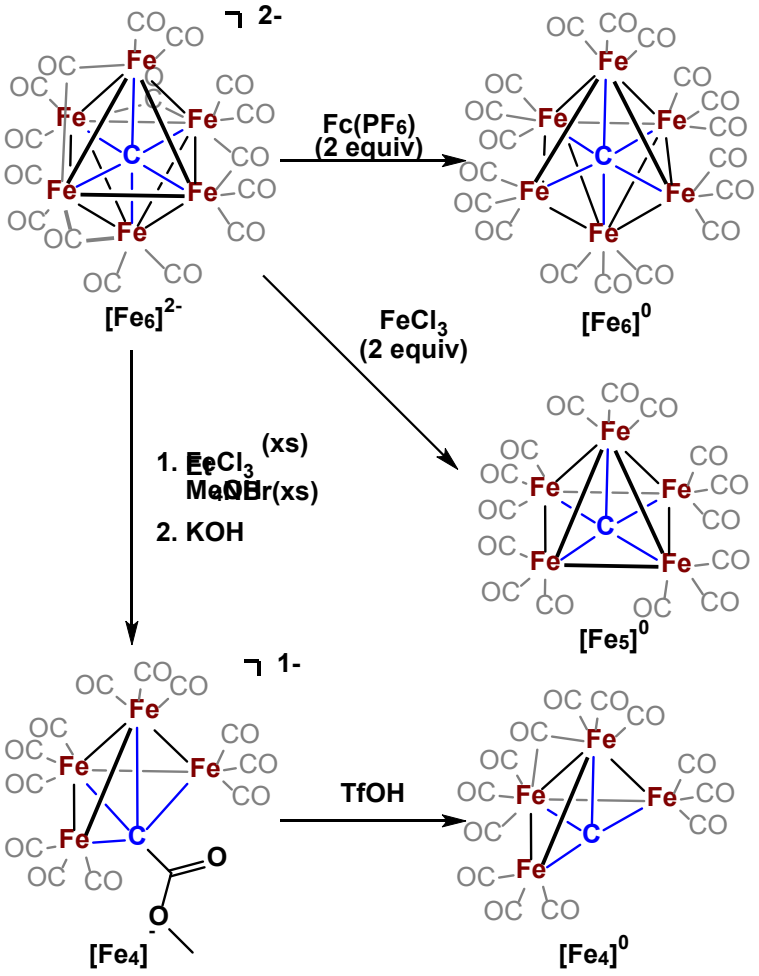

Scheme 2.1 Synthetic cluster-core transformations starting from $[Fe_6(\mu_6\text{-}C)(CO)_{16}]^{2-}$ to obtain the neutral Fe_6, Fe_5, and Fe_4 species.

2.2 Detailed Experimental Procedures

2.2.1 Solvents and Reagents

Diglyme and methylcyclohexane was purchased from Sigma Aldrich and used as received. Methanol was purchased from Fisher Scientific, dried by distillation over molecular sieves, and sparged with nitrogen for 30 min prior to use. All other solvents were purchased as HPLC grade from EMD, Fisher, Macron or J.T. Baker, and dried through an alumina column system (Pure Process Technology). Deuterated solvents were purchased

from Cambridge Isotopes and used as received. Naphthalene (Fisher Scientific), sodium (Fisher Scientific), $Fe(CO)_5$ (Strem), NEt_4Cl (TCI), $FeCl_3•H_2O$ (Fisher Scientific), NEt_4Br (Acros Organics), anhydrous $FeCl_3$ (Strem), trifluoromethanesulfonic acid (TfOH, Acros Organics), ferrocenium hexafluorophosphate ($Fc(PF_6)$, Sigma Aldrich), and BioBeads S-X12 Support (BioRad) were used as received.

Caution: Metal carbonyls are extremely toxic. It is advised that these compounds are handled in well-ventilated fume hoods under an inert gas atmosphere.

2.2.2 Synthetic Procedures

$Na_2[Fe(CO)_4]•2THF$ In an argon-atmosphere glovebox, sodium metal (1.7 g, 74 mmol) was added into a 500-mL Schlenk flask with 100 mL of THF, and magnetic stir bar. The flask was then capped with a rubber septum, pumped out of the glovebox, and affixed to a Schlenk line under N_2 atmosphere. The contents were frozen (without stirring) at –195 °C by submersion of flask into liquid nitrogen, and solid naphthalene (9.5 g, 74 mmol) was added through the mouth onto the frozen supernatant. The headspace of the flask was cycled 3 times with vacuum and nitrogen, and the contents of the flask were thawed and stirred for 3 h. The resulting is a dark-green solution was cooled to 0 °C using a water-ice bath, and a neat aliquot of $Fe(CO)_5$ (5 mL, 37 mmol) was added dropwise via syringe and needle. The solution was allowed to stir overnight, resulting in a dark-orange solution. The THF solvent was removed under reduced pressure and the flask transferred into the glovebox. The dark-orange semi-solid was re-dissolved in a minimal amount of THF (~100 mL) and precipitated by addition of pentane (~150 mL). The solid was isolated via vacuum filtration and stored at –20 °C until further use. Yield: 17.1 g (65%) of light

red-orange solid. Selected IR peaks (**Figure 2.1**), solid, ν(CO): 1992(m), 1857(s), 1692(s) cm^{-1}.

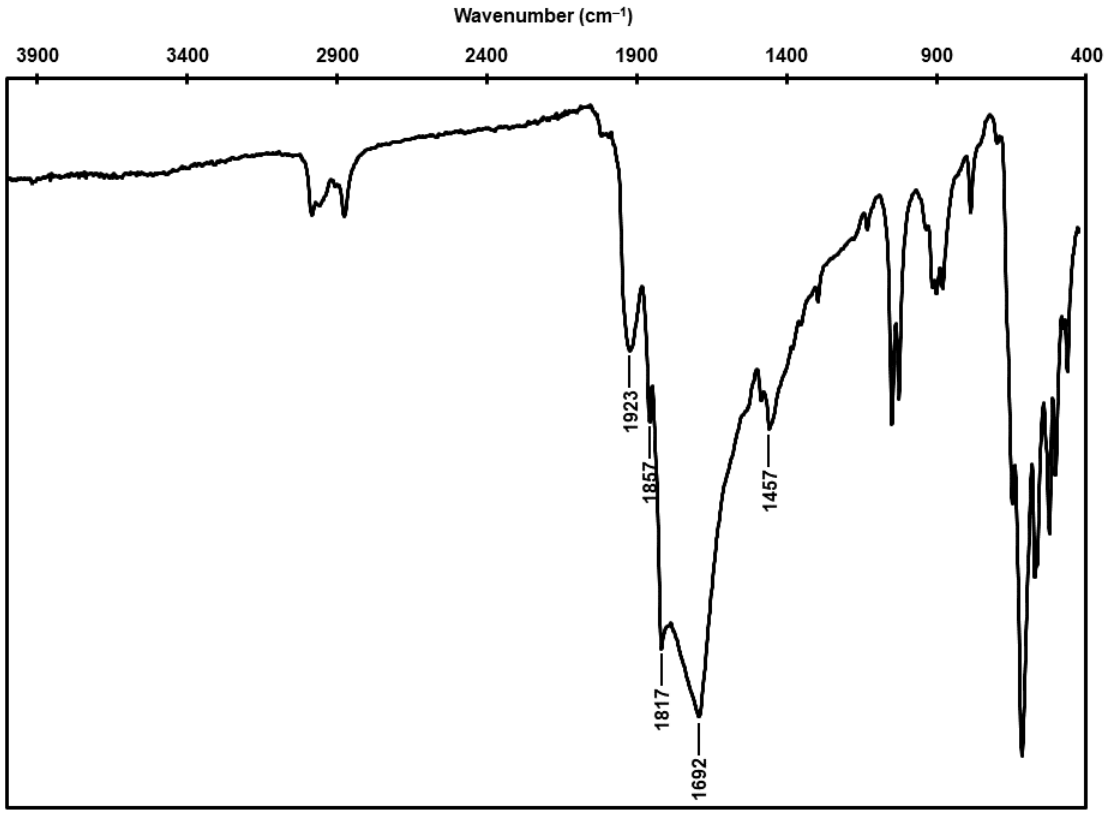

Figure 2.1 IR spectrum of $Na_2[Fe(CO)_4]$•2THF in the solid state.

$(NEt_4)_2[Fe_6(\mu_6\text{-}C)(CO)_{16}]$ In an argon-atmosphere glovebox, a 250-mL Schlenk flask was charged with $Na_2[Fe(CO)_4]$•2THF (2.6 g, 7.3 mmol), 25 mL diglyme, and a magnetic stir bar. The flask was then capped with a rubber septum, pumped out of the glovebox, and affixed to a Schlenk line under N_2 atmosphere. A neat aliquot of $Fe(CO)_5$ (5 mL, 37 mmol) was added dropwise via syringe and needle. The flask was then equipped with an air-free reflux condenser, and its contents heated and stirred at 160 °C for 6 h. The resulting dark-violet oil was washed with 3×50 mL hexanes and then extracted into 400 mL degassed water. The aqueous solution was poured into a large, air-free coarse fritted filter

tube and allowed to gravity filter through a 2 cm-thick pad of Celite into a 500-mL Schlenk flask charged with NEt_4Cl (3.0 g, 18 mmol) and a magnetic stir bar (**Figure 2.2**), leaving behind a fine, black powder. The aqueous mixture stirred for 3 h, and the resulting dark violet precipitate was collected by vacuum filtration through a 2 cm-thick pad of Celite over a coarse fritted filter. The product/Celite mixture was washed several times with Et_2O and allowed to dry one the vacuum filter before being extracted into 400 mL THF and filtered into a 500-mL Schlenk flask. The THF solvent was removed *in vacuo*, and the violet, crystalline solid was brought into a glovebox, where it dissolved in THF and layered with pentane by vapor diffusion to afford 3.87 g (51% yield) of dark violet crystalline product. Selected IR peaks (**Figure 2.3**), solid, ν(CO): 2032(w), 1917(s), 1755(s) cm^{-1}. $^{13}C\{^1H\}$ NMR (100.5 MHz, THF-d_8): interstitial carbide peak at δ 484.7 ppm.

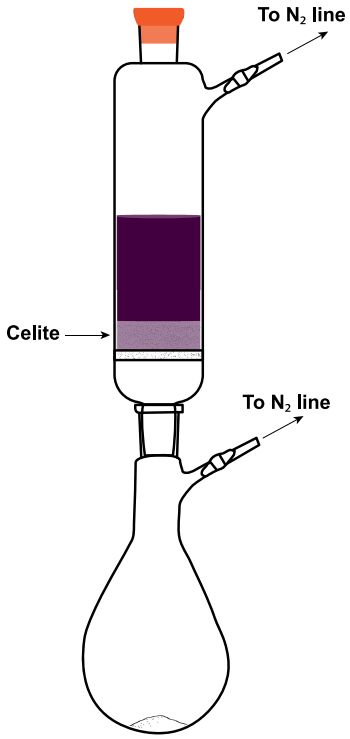

Figure 2.2 Apparatus set-up for filtration of aqueous $Na_2[Fe_6(\mu_6\text{-}C)(CO)_{16}]$ into solid NEt_4Cl.

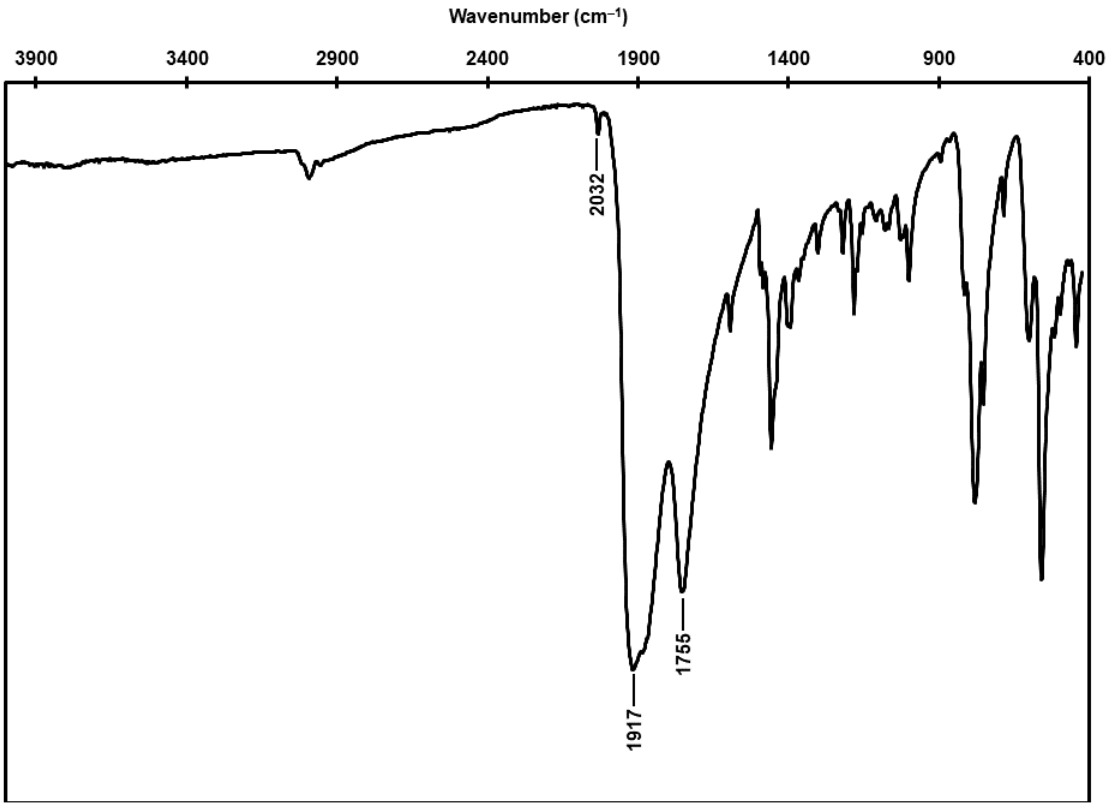

Figure 2.3 IR spectrum of $(NEt_4)_2[Fe_6(\mu_6\text{-}C)(CO)_{16}]$ in the solid state.

$[Fe_5(\mu_5\text{-}C)(CO)_{15}]$ directly from $Na_2[Fe(CO)_4]$•2THF. In a reaction setup similar to that described for the synthesis of $(NEt_4)_2[Fe_6(\mu_6\text{-}C)(CO)_{16}]$, $Na_2[Fe(CO)_4]$•2THF (2.6 g, 7.3 mmol) and $Fe(CO)_5$ (5 mL, 37 mmol) were stirred in 25 mL diglyme at 160 °C for 6 h. The resulting dark-violet oil was washed with 3×50 mL hexanes, extracted into 400 mL degassed water, and the aqueous solution passed through a 2 cm-thick pad of Celite into an empty 500-mL Schlenk flask with a magnetic stir bar. The flask was cooled to 0 °C in a water-ice bath and equipped with a 125-mL dropping addition funnel capped with a rubber septum. A solution of $FeCl_3$•$6H_2O$ (3.37 g, 12.5 mmol) in 75 mL degassed water

was added to the dropping addition funnel and allowed to add dropwise into the violet solution under rapid stirring over the course of 10-15 min. The solution was then stirred for 1 h at 0 °C and an additional 30 min at room temperature, resulting in the formation of a black precipitate. The precipitate was collected by vacuum filtration through a 1 cm-thick pad of Celite over a coarse fritted filter, washed with 3×50 mL degassed water, and delivered into a 250-mL Schlenk flask. Residual water was dried overnight *in vacuo*, and the flask was brought into an N_2-atmosphere glovebox. The product/Celite mixture was washed with 4×50 mL pentane, extracted into 400 mL toluene, and passed through a medium-pore-size fritted filter. The toluene was removed *in vacuo* to afford 1.34 g (26% yield) of black solid powder. Selected IR peaks, solid (**Figure 2.4**), ν(CO): 2099(w), 1948(s) cm^{-1}. $^{13}C\{^1H\}$ NMR (150.8 MHz, benzene-d_6): interstitial carbide peak at δ 485.3 ppm.

$[Fe_5(\mu_5\text{-}C)(CO)_{15}]$ synthesized from $(NEt_4)_2[Fe_6(\mu_6\text{-}C)(CO)_{16}]$. In an N_2-atmosphere glovebox, a 500-mL Schlenk flask with a magnetic stir bar was charged with a suspension of $(NEt_4)_2[Fe_6(\mu_6\text{-}C)(CO)_{16}]$ (2.35 g, 2.23 mmol) in 200 mL toluene. The flask was then capped with a rubber septum, pumped out of the glovebox, and affixed to a Schlenk line under N_2 atmosphere. A 150 mL degassed, aqueous solution of $FeCl_3 \bullet 6H_2O$ (1.22 g, 4.51 mmol) was added into the rapidly stirring toluene suspension and stirred for 20 h at room temperature, resulting in a biphasic suspension with a pale-yellow aqueous phase, a black toluene phase, and unreacted solid $(NEt_4)_2[Fe_6(\mu_6\text{-}C)(CO)_{16}]$. The toluene phase was collected and washed with 3×100 mL degassed water, filtered through a medium-pore-size fritted filter into a 500-mL Schlenk flask, and the solvent removed under reduced pressure. The flask was brought into a glovebox and the black solid was collected, yielding 332.5 mg (21% yield) of product.

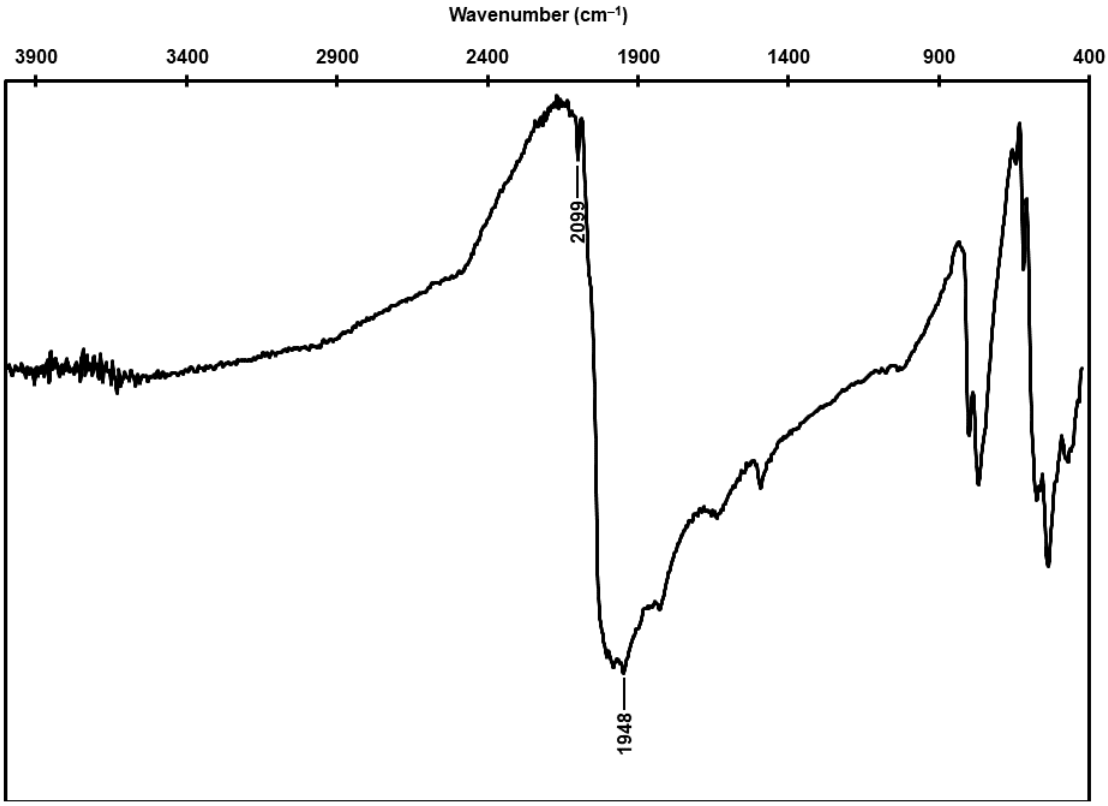

Figure 2.4 IR spectrum of $[Fe_5(\mu_5\text{-}C)(CO)_{15}]$ in the solid state.

$(NEt_4)[Fe_4(\mu_4\text{-}C(COOMe))(CO)_{12}]$ On a Schlenk line under N_2 atmosphere, a 500-mL Schlenk flask was charged with 150 mL of a violet, degassed, methanolic solution of $(Et_4N)_2[Fe_6(\mu_6\text{-}C)(CO)_{16}]$ (2.00 g, 1.89 mmol) and Et_4NBr (2.10 g, 10.4 mmol). Solid anhydrous $FeCl_3$ (2.15 g, 13.3 mmol) was added into the methanolic solution, and the solution stirred for 30 min. Solid KOH (0.11 g, 2.0 mmol) was stirred into solution for 5 min, and the solvent removed *in vacuo*. The resulting dark solid was extracted into 300 mL DCM and the extraction solutions washed with degassed water, filtered into a 500-mL Schlenk flask, and the DCM removed under reduced pressure. The flask was then brought into an N_2-atmosphere glovebox, and the contents were dissolved in THF and layered with pentane by vapor diffusion to afford 656 mg (46 % yield) of dark amber

crystalline product. Selected IR peaks (**Figure 2.5**), solid, ν(CO): 2067(w), 1899(s), 1748 cm^{-1}.

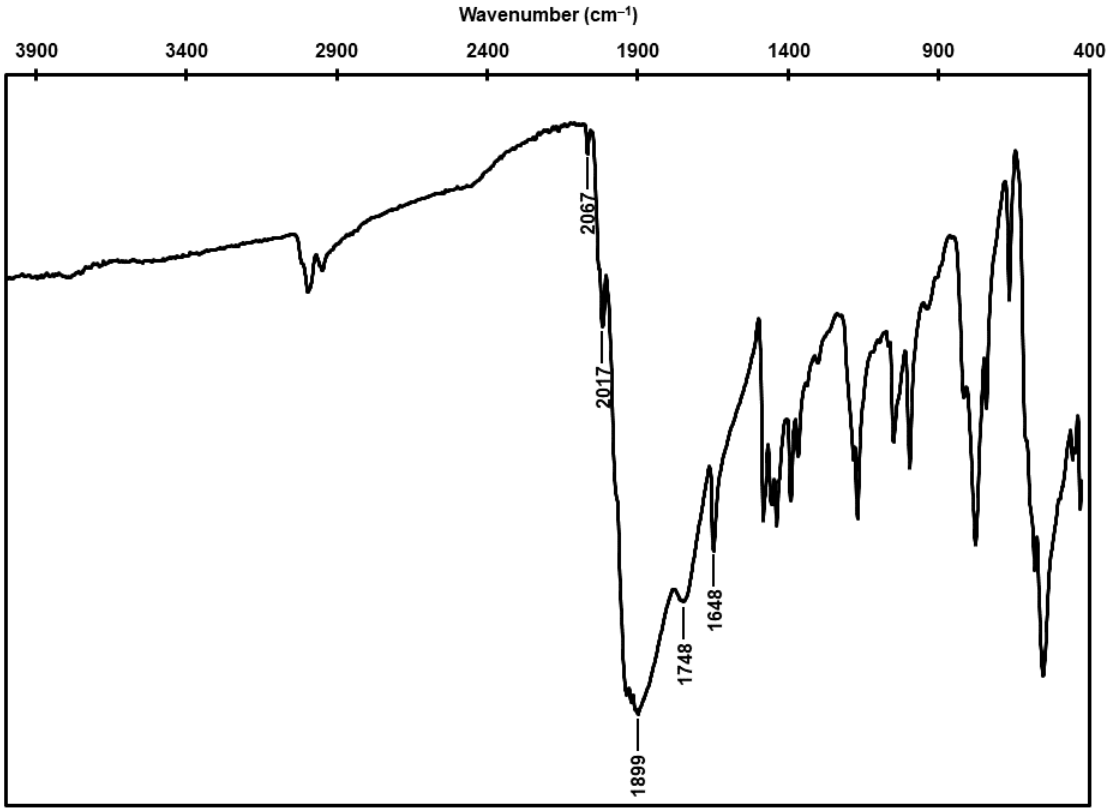

Figure 2.5 IR spectrum of $(NEt_4)[Fe_4(\mu_4\text{-}C(COOMe))(CO)_{12}]$ in the solid state.

$[Fe_4(\mu_4\text{-}C)(CO)_{13}]$ On a Schlenk line under N_2 atmosphere, a 250-mL Schlenk flask was charged with $(Et_4N)[Fe_4(\mu_4\text{-}C(COOMe))(CO)_{12}]$ (755.0 mg, 0.9924 mmol) and 45 mL methylcyclohexane. An aliquot of neat TfOH (0.80 mL, 9.0 mmol) was added dropwise into the suspension, and the solution stirred for 5 min. A 40-mL volume of degassed water was added; and the solution stirred an additional 20 min, resulting in a biphasic mixture comprised of a colorless aqueous phase and black organic phase. The organic phase was collected and washed with 3×20 mL degassed water, filtered through a medium-pore-size

fritted filter into a 100-mL Schlenk flask, and the solvent removed under reduced pressure. The flask was brought into an N_2-atmosphere glovebox and the black solid was collected, affording 261.0 mg (44% yield) of product. Selected IR peaks (**Figure 2.6**), solid, ν(CO): 2101(w), 1974(s), 1873(s) cm^{-1}.

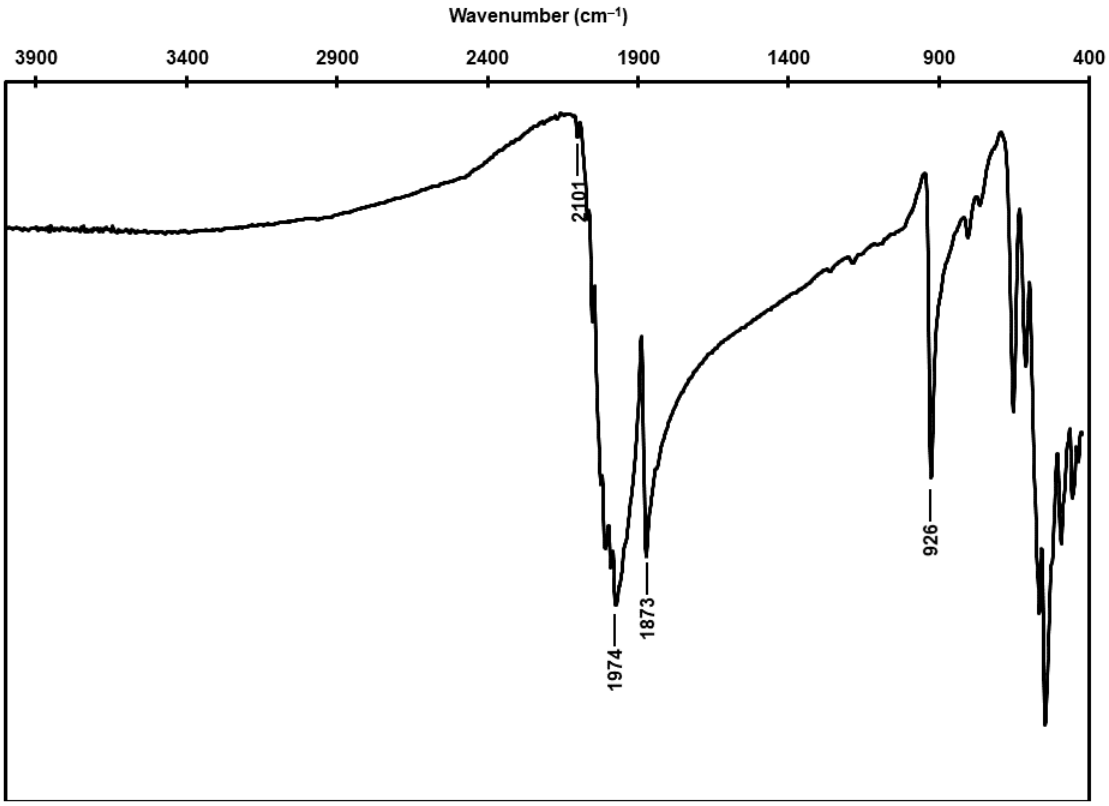

Figure 2.6 IR spectrum of $[Fe_4(\mu_4\text{-}C)(CO)_{13}]$ in the solid state.

$[Fe_6(\mu_6\text{-}C)(CO)_{18}]$ On a Schlenk line under N_2 atmosphere, a solution of $(NEt_4)_2[Fe_6(\mu_6\text{-}C)(CO)_{16}]$ (505.2 mg, 0.4785 mmol) in THF (15 mL) in a 100-mL Schlenk tube equipped with a Kontes valve was frozen at −78 °C. Solid ferrocenium hexafluorophosphate (310.0 mg, 0.9366 mmol) was added onto the frozen solution, and the tube was allowed to warm to room temperature under CO atmosphere while its contents

stirred overnight. The tube was then brought into an argon-atmosphere glovebox, the insoluble materials were removed by filtration, and all volatiles (THF and ferrocene) were removed *in vacuo*. Residual ferrocene was removed by pentane washes (until colorless), and the pentane-insoluble solid was extracted into toluene and passed through a pipette column packed with BioBeads (3−4 cm height). The toluene was then removed *in vacuo*, affording 217.4 mg (53% yield) of dark red solid. Selected IR peaks, solid (**Figure 2.7**), ν(CO): 2099(w), 1958(s) cm^{-1}.

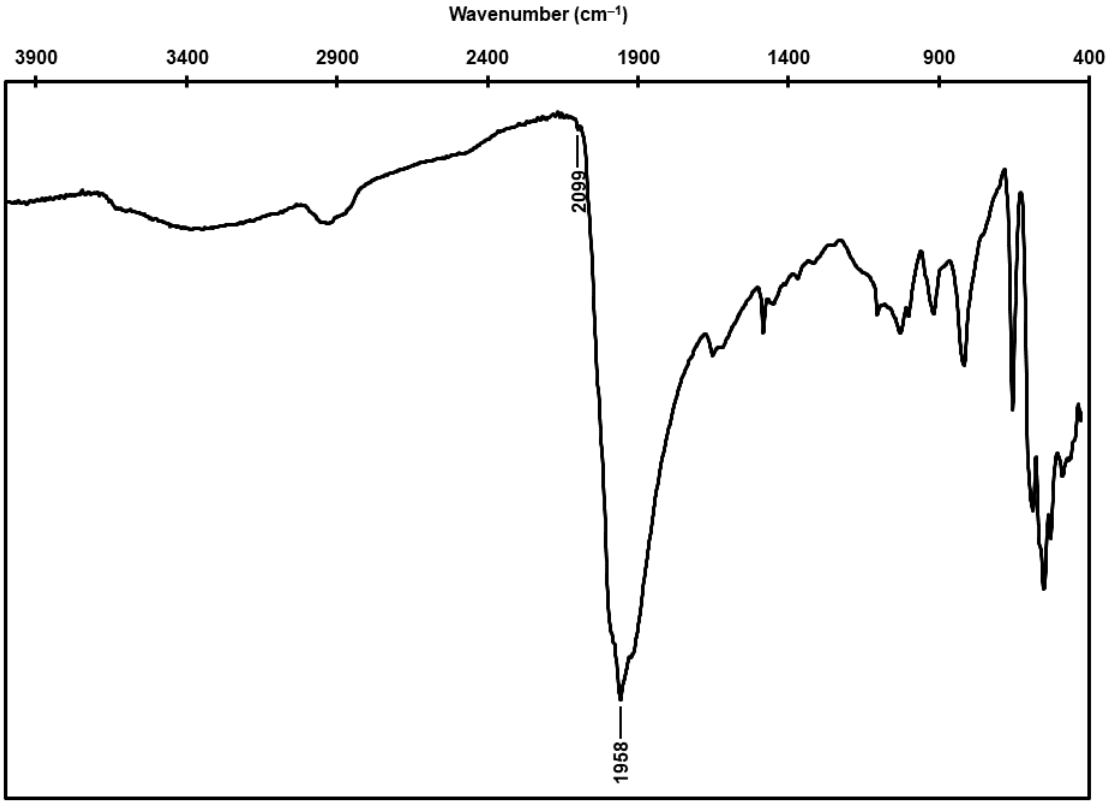

Figure 2.7 IR spectrum of $[Fe_6(\mu_6\text{-}C)(CO)_{18}]$ in the solid state.

2.3 Discussion of Carbidocarbonyl Iron Cluster Syntheses

With the overarching goal of achieving clean, direct synthesis of the starting hexa-iron cluster, the reduced iron-carbonyl $Na_2[Fe(CO)_4]$ — colloquially referred to as Collman's reagent — was used as the reductant instead of $Na[Mn(CO)_5]$ as reported by Churchill. From here, $[Fe_6(\mu_6\text{-}C)(CO)_{16}]^{2-}$ is treated with $FeCl_3$ under various reaction conditions to selectively remove either one or two iron sites *via* and generate the penta- or tetra-iron clusters. Additionally, treatment with Fc^+ preserves a hexa-iron core and affords a neutral cluster.

2.3.1 Carbide formation in $[Fe_6(\mu_6\text{-}C)(CO)_{16}]^{2-}$ synthesis

Prior to the synthesis of the $[Fe_6(\mu_6\text{-}C)(CO)_{16}]^{2-}$ dianionic cluster, sodium tetracarbonylferrate $Na_2[Fe(CO)_4]$ is synthesized by the reduction of $Fe(CO)_5$ by sodium naphthalide and isolated as a THF-solvated species.[107] The isolated $Na_2[Fe(CO)_4]$•2THF was then reacted in diglyme with 5 equiv $Fe(CO)_5$ at 160 °C for 6 h to give a violet oil of $Na_2[Fe_6(\mu_6\text{-}C)(CO)_{16}]$. The absence of an obvious carbon donor — such as a carbon halide carbocation donor or radically-initialed carbon atom donor[108,109] — suggests that the origin of the carbide in $[Fe_6]^{2-}$ likely traces back to a CO ligand. A tentative mechanism for carbide formation is illustrated in **Scheme 2.2**. The synthesis of the non-carbide cluster $[Fe_4(CO)_{13}]^{2-}$ from reflux of reduced iron carbonyls in THF was first demonstrated by van Buskirk *et al.*[110] Treatment of this cluster under acidic conditions at room temperature leads to the loss of a water molecule and the isolation of an Fe_4-carbide cluster.[89,111] Under heated conditions, a CO ligand undergoes Lewis acid-induced reduction by a nearby CO group, which leaves as a CO_2 molecule.[112] Refluxing the $[Fe_4]^{2-}$ cluster spontaneously leads to the formation of the $[Fe_6]^{2-}$, presumably by utilization of sacrificial $[Fe_4]^{2-}$ as an iron-carbonyl

source.[110] In the reaction conditions described above for $[Fe_6]^{2-}$ synthesis, the presence of 5 stoichiometric equiv of $Fe(CO)_5$ to $Na_2[Fe(CO)_4]$ mitigates the need for a sacrificial $[Fe_4]^{2-}$ equiv. Additionally, the coordination sphere of these clusters is highly fluxional in solution. Treatment with ^{13}C-labeled CO gas demonstrates facile substitution of CO ligands, while the carbide remains inert to ^{13}C-enrichment.[110] Consequently, ^{13}C-enrichment of the carbide would be easily achieved by treatment of the starting iron carbonyls or Fe_4-non-carbide cluster with ^{13}CO prior to $[Fe_6]^{2-}$ synthesis. This mechanism of carbide formation *via* CO oxidation is distinctly different from that in FeMoco, whereby the carbide originates via H-atom abstraction and subsequent deprotonation of an organic methyl group.[24] However, the spontaneous carbide formation and subsequent assembly of the octahedral $[Fe_6]^{2-}$ are indicative of the thermodynamic stability of the 6-coordinate carbide.

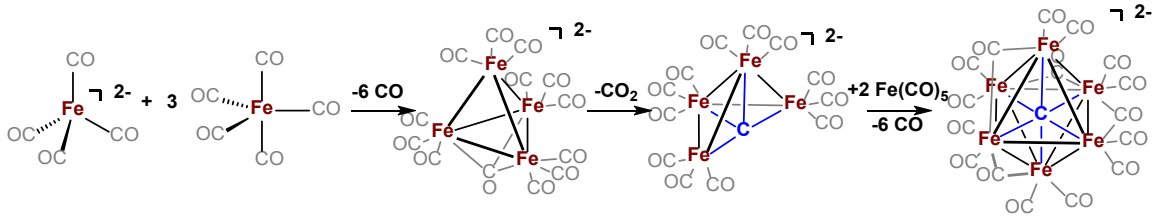

Scheme 2.2 Tentative mechanistic formation of carbide from CO ligand.

2.3.2 Practical considerations in cluster syntheses

Despite the stoichiometric reaction conditions given for the synthesis of $[Fe_6(\mu_6\text{-}C)(CO)_{16}]^{2-}$, an insoluble and ferromagnetically-active black solid biproduct does form during the heated reaction in diglyme. This solid is also observed when pure samples of the various iron clusters are subject to heated conditions (typically >90 °C). Before

proceeding with cation exchange in $[Fe_6]^{2-}$ synthesis (or $FeCl_3$ addition in $[Fe_5]^0$ synthesis), this solid must be removed from *via* gravity filtration. This fine powder easily clogs fritted glass; and the use of a thick pad of Celite packed by vacuum filtration of an aqueous Celite suspension is suggested (the use of vacuum during the filtration of the aqueous $Na_2[Fe_6(\mu_6\text{-}C)(CO)_{16}]$ extract is advised against). Isolation of the sodium salt as a solid is hindered by the coordinating presence of diglyme, necessitating cation exchange with NMe_4Cl, NEt_4Cl, or PPh_4Cl and subsequent crystallization by THF/Et_2O or THF/pentane vapor diffusion.[106] The synthesis of $[Fe_5(\mu_5\text{-}C)(CO)_{15}]$ from $Na_2Fe(CO)_4$, which proceeds through $Na_2[Fe_6(\mu_6\text{-}C)(CO)_{16}]$ as an intermediate, is achieved by treatment of the sodium salt of the Fe_6 dianion with $FeCl_3$. $[Fe_5(\mu_5\text{-}C)(CO)_{15}]$ may also be achieved from $(NEt_4)_2[Fe_6(\mu_6\text{-}C)(CO)_{16}]$ by suspension in a biphasic toluene/water mixture with dissolved $FeCl_3$. Both syntheses result in the generation of $Fe_3(CO)_{12}$ as a side product, which must be removed by washing with pentane. $[Fe_5(\mu_5\text{-}C)(CO)_{15}]$ yields can be improved by passing the pentane washes through a silica column with degassed hexanes as the eluent: The green $Fe_3(CO)_{12}$ band elutes first, followed by a black band of $[Fe_5(\mu_5\text{-}C)(CO)_{15}]$. The presence of $Fe_3(CO)_{12}$ is indicative of non-stoichiometric conversion of $[Fe_6(\mu_6\text{-}C)(CO)_{16}]^{2-}$ $\rightarrow[Fe_5(\mu_5\text{-}C)(CO)_{15}]$ — in which 1 equiv of an $\{Fe(CO)\}^{2-}$ unit is displaced — and consequently explains the generally poor yields in these reactions as sacrificial $[Fe_6]^{2-}$ starting material is consumed in $[Fe_6(\mu_6\text{-}C)(CO)_{16}]^{2-}\rightarrow Fe_3(CO)_{12}$ conversion.

Synthesis of the capped-carbide cluster $(NEt_4)[Fe_4(\mu_4\text{-}C(COOMe))(CO)_{12}]$ is achieved by treatment of $(NEt_4)_2[Fe_6(\mu_6\text{-}C)(CO)_{16}]$ with excess $FeCl_3$ in methanol and in the presence of bromide ion, which has been demonstrated as necessary in this synthesis to facilitate the oxidative removal of the second Fe site.[113] Additionally, while this reaction proceeds via the $[Fe_4(\mu_4\text{-}C)(CO)_{13}]$ as an intermediate, the neutral cluster is converted to the monoanion *via* methoxide ligation to facilitate purification from unconverted Fe_5

cluster. Once isolated, the Fe_4^- cluster is easily converted to its neutral congener by protonation with triflic acid and the loss of methanol. Finally, treatment of $(NEt_4)_2[Fe_6(\mu_6\text{-}C)(CO)_{16}]$ with $FcPF_6$ under inert (argon) atmosphere leads to a mixture of neutral carbonyl clusters: $Fe_2(CO)_9$ (yellow), $Fe_3(CO)_{12}$ (green), the carbide-cluster $[Fe_5(\mu_5\text{-}C)(CO)_{15}]$, and the target $[Fe_6(\mu_6\text{-}C)(CO)_{18}]$ cluster. However, the same reaction under CO atmosphere cleanly affords the red solid of $[Fe_6(\mu_6\text{-}C)(CO)_{18}]$ in good yield. To ensure purity, the compound is purified through cross-linked polystyrene beads (BioBeads).

The carbidocarbonyl iron cluster compounds described here have been previously characterized by X-ray diffraction, with the exception of $[Fe_6(\mu_6\text{-}C)(CO)_{18}]$ (see below for discussion regarding proposed structure). However, IR spectroscopy can be reliably utilized for routine characterization, and characteristic IR peaks are summarized in **Table 2.1**. The ν_{CO} values are categorized into three types: (1) $\nu_{highest}$ corresponds to the most blue-shifted peak. This peak typically presents as a very weak transition and has been attributed to a highly symmetric, dipole-forbidden vibrational mode; (2) ν_{max} denotes the feature having the most prominent peak intensity and can generally be used to describe the terminal CO stretching frequency; and finally, (3) $\nu_{bridging}$ denotes the peak associated with bridging CO ligands, if present. Additionally, literature references for the for the published crystal structures of these compounds are given.

	IR ν_{CO} (cm^{-1})			Xtal
	$\nu_{highest}$	ν_{max}	$\nu_{bridging}$	
$(NEt_4)_2[Fe_6(\mu_6\text{-}C)(CO)_{16}]$	2032	1917	1755	Refs. [79,106]
$[Fe_6(\mu_6\text{-}C)(CO)_{18}]$	2099	1958		
$[Fe_5(\mu_5\text{-}C)(CO)_{15}]$	2099	1948		Refs. [77,106]
$(NEt_4)[Fe_4(\mu_4\text{-}C(COOMe))(CO)_{12}]$	2067	1899		Ref. [104]
$[Fe_4(\mu_4\text{-}C)(CO)_{13}]$	2101	1974	1873	Ref. [114]

Table 2.1 Characteristic ν_{CO} IR values and literature references for crystal structures of clusters. The ν_{CO} values are categorized into three types: (1) $\nu_{highest}$ corresponds to the most blue-shifted peak, (2) ν_{max} denotes the peak having the most prominent intensity, and $\nu_{bridging}$ denotes the peak associated with bridging CO.

2.4 Structural Adherence to Electron Counting Rules

Against the backdrop of prolific synthetic developments in cluster chemistry during the 1960s to 1980s, a set of straightforward electron-counting rules were eloquently formulated in 1971 by Kenneth Wade to describe the geometries of cluster compounds based on the number of discrete "skeletal electron pairs" determined in the molecule.[115] These rules work well to rationalize geometries of sphere-like, electron deficient clusters — clusters in which skeletal electrons are delocalized — and were extended by D. M. P. Mingos, who recognized that cluster electron count can be rationalized without *a priori* knowledge of the CO binding modes (terminal vs. bridging).[116,117] These rules — collectively referred to as Wade-Mingos rules and described by Polyhedral Skeletal Electron Pair Theory (PSEPT) — provide simple, monomial expressions to predict expected cluster structures. Particularly useful for describing the iron clusters discussed in these chapters are the $14n + 2$, $14n + 4$, and $14n + 6$ rules, which correspond to *closo*, *nido*, and *arachno* clusters, respectively (**Scheme 2.3**).[118] Known collectively as the debor

principle, these rules can be used in conjunction with covalent electron-counting rules to provide a systematic rationalization for observed geometric arrangements of the cluster core and CO coordination number in the ligation sphere. Considering $[Fe_6]^{2-}$ in a covalent electron-counting rationale, the carbide (4 e^-), six iron centers (48 e^-), 16 CO ligands (32 e^-), and two extra electrons (dianionic, 2 e^-) afford an 86 e^- cluster. This predicts a *closo*-M_6 structure: (14 × 6) + 2 = 86 e^-. Similarly, electron counts for the Fe_5 and Fe_4 clusters are determined to be 74 e^- and 62 e^-, respectively (the {C(O)OMe} ligand is considered a 1 e^- donor).

Additionally, the predictive power of these rules was demonstrated in the structural determination of $[Fe_6]^0$, for which elucidation by X-ray crystallography proved untenable. Elemental analysis of the compound indicated at formula of $[Fe_6(C)(CO)_{18}]$ and IR indicated the presence of only terminally-ligated carbonyl groups. Thus, DFT computations were used to predict the structure of an octahedral $[Fe_6(\mu_6\text{-}C)(CO)_{18}]$ cluster. In principle, this formulation could include six $\{Fe(CO)_3\}$ units capping the central carbide (only terminal COs). However, this general structure proved unstable: using severely restricted gradient perturbation parameters prevented the DFT system from converging. Additionally, rationalizing $[Fe_6]^0$ as a *closo*-$[Fe_6(\mu_6\text{-}C)(CO)_{18}]$ was unproductive: this cluster is an 88 e^- formulation, while the *closo*-$[Fe_6]$ electron-counting predicts only 86 e^-. An alternate explanation would be a formulation with one less CO ligand, as *closo*-$[Fe_6(\mu_6\text{-}C)(CO)_{17}]$ (86 e^-). However, this would require the presence of a single bridging CO ligand, and no experimental or computational evidence for a truly bridging (i.e., not "semibridging") CO ligand was observed. Continuing with the $[Fe_6(C)(CO)_{18}]$ formulation, a DFT-optimized structure determined by imposing looser constraints on geometry optimization revealed a very different core structure for $[Fe_6]^0$ versus that for $[Fe_6]^{2-}$. One face of the cluster was opened by breaking an equatorial Fe−Fe bond and the

remaining equatorial Fe–Fe bonds shortened slightly, resulting in a *nido*-pentagonal bipyramid (PBP) structure — i.e. a PBP with one Fe missing.[106] This cluster is, of course, also formulated as an 88 e^- cluster and also conforms to the *nido* cluster electron-counting rule for a six-metal cluster with an "open" metal site (14n + 4 = 88 e^-). Indeed, the cluster electron counting rules should provide a framework for predicting the isolability of higher nuclearity iron carbide clusters. For example, the pentanuclear PBP cluster *closo*-$[Fe_7(\mu_7\text{-C})(CO)_{21}]$ or the related dianion *closo*-$[Fe_7(\mu_7\text{-C})(CO)_{20}]^{2-}$ may be isolable clusters with 100 e^- count. Computational details related to this study may be found in reference [106].

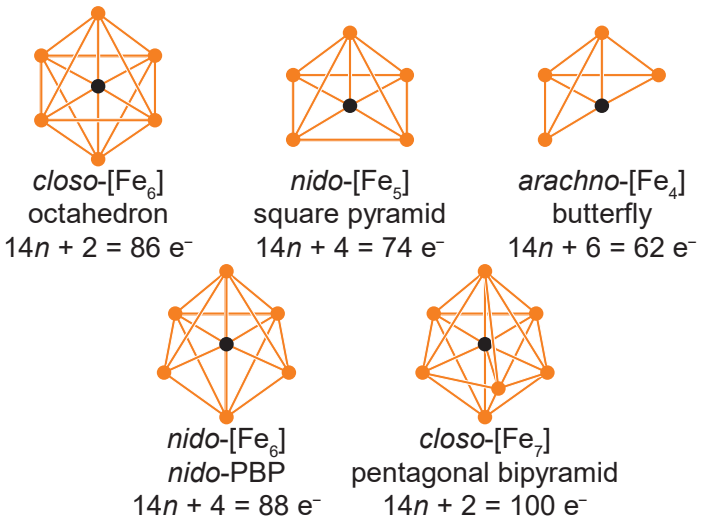

Scheme 2.3 General formulation and electron-counting for the iron–carbidocarbonyl clusters discussed in this chapter as well as a predicted *closo*-Fe_7 cluster.

2.5 CONCLUSIONS

In conclusion, we have reformulated a series of synthetic pathways by which neutral Fe_6, Fe_5, and Fe_4 clusters can be efficiently and purely generated. This is achieved by the treatment of $[Fe_6]^{2-}$ with $FeCl_3$ as an inner-sphere electron oxidizing agent under varying reaction conditions to achieve the selective removal of one or two Fe sites and generate Fe_5 and Fe_4 carbidocarbonyl clusters or alternatively, the use of ferrocenium as an outer-sphere oxidizing agent to induce a 2 e^- oxidation while preserving the 6-iron count of the cluster core. In the latter case, the initially *closo*-Fe_6 core — upon oxidation — opens asymmetrically to exhibit a *nido*-PBP structural configuration. This geometry is predicted by the electron-counting rules prescribed by PSEPT, to which all the iron carbidocarbonyl clusters described here consistently adhere. The various cluster identities can be reliably confirmed by IR spectroscopy, as each cluster displays unique features in the carbonyl stretching frequency range. The carbide containing iron clusters described here will serve as important building blocks for the heterometal substitution and sulfide incorporation reactions discussed in the following chapters.

Chapter 3: Multi-step Iterative Heterometal (Mo) Substitution into the Carbidocarbonyl Iron Octahedron†

3.1 INTRODUCTION

While the precise role of the molybdenum site in Mo-dependent nitrogenase remains under debate, experimental evidence comparing kinetic rates of N_2-reduction between the M-cluster (FeMoco), V-cluster (FeVco), and L-cluster (all-Fe cofactor) demonstrate increased activity by the heterometallic cofactors, with FeMoco displaying the highest activity.[11] Therefore, the capability to incorporate heterometals into synthetic nitrogenase analogues is valuable to elucidate the structure-function relationships between the various nitrogenases. Several contributions by Coucouvanis have provided synthetic examples of Mo-containing iron-sulfur heteroclusters: including cuboidal,[119–121] double-cuboidal,[122–124] and basket clusters[125–127] (as well as a V-containing example[128]) — many of which bear biologically-relevant bidentate ligands with sp^3 O-donors or monodentate sp^2 N-donors, analogous to homocitrate and histidine, respectively (**Scheme 3.1**). Additionally, a myriad of contributions have been provided by both Holm[129,130] and Tatsumi[74,131] representing cuboidal or double-cuboidal Mo-containing and V-containing clusters. Notably, all reports of double-cuboidal synthetic clusters are symmetric such that the heteroatom is present in each component cube. This is distinctly different from the structure of FeMoco and FeVco, both of which feature asymmetric cofactors containing only one heteroatom in total.

† Portions of this chapter were published in:
Joseph, C.; Kuppuswamy, S.; Lynch, V. M.; Rose, M. J. *Inorg. Chem.* **2018**, *57*, 20−23.

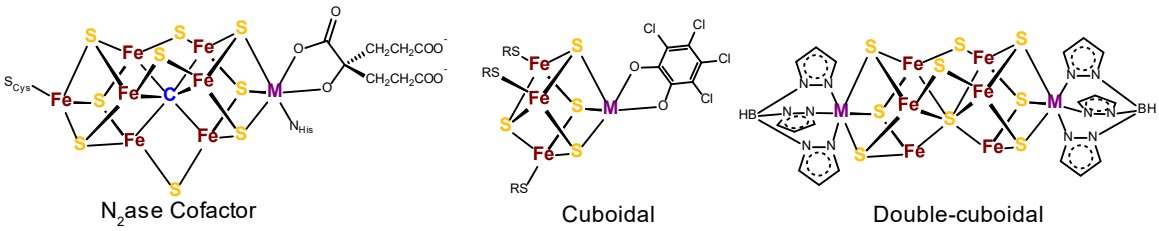

Scheme 3.1 Structure of the Mo- and V-dependent nitrogenase cofactors (M = Mo, V) and representative examples of cuboidal and double-cuboidal synthetic iron-sulfur clusters reported by Coucouvanis, Holm, and Tatsumi.

While vanadium and molybdenum heteroclusters are plentiful in the FeS cluster literature, heterometal substitution in the iron-carbide clusters is generally confined to late-transition metals (**Scheme 3.2**). Within this subset of carbidocarbonyl iron clusters, Lewis acidic Cu- and Au-bearing Group 11 transition metal donors are most prolific, in which the heterometal-bearing moiety acts as an electrophile towards anionic Fe_4 and Fe_5 clusters which bind at the most nucleophilic site (*i.e.* the carbide-coordinating position).[30,132–134] Similar reactions with the octahedral $[Fe_6(\mu_6\text{-C})(CO)_{16}]^{2-}$ cluster or bidendate Au ligands also demonstrate chemical transformations such that Au occupies edge-bridging Fe–Fe sites.[135–137] Heterometal substitution with Group 9 metals Co and Rh has only been observed by CO-supported incorporation, though these works report disorder and ambiguous atom identities at transition metal sites.[138–140] The Group 10 metals, however, appear to traverse the line between necessitating π-electron-withdrawing CO supports and acting upon the clusters as Lewis acids. Heteroclusters incorporating Ni and Pt present with the largest variety of ligands, ranging from such π-accepting ligands as CO and MeCN to σ-donating phosphines and cyclopentadienyls.[141,142] A systematic approach for CO-supported-heterometal incorporation into Fe_5 clusters was previously reported by Tachikawa and Muetterties — including one that incorporates Mo. However, evidence for

the successful achievement in of heterometals is incomplete, relying primarily on IR spectroscopic data or unreported crystallographic data; and the full structure of the Fe_5Mo cluster in particular is not available in the CSD.[100,101] Our own attempts to replicate the reported Fe_5Mo procedure yielded ambiguous results (discussed below).

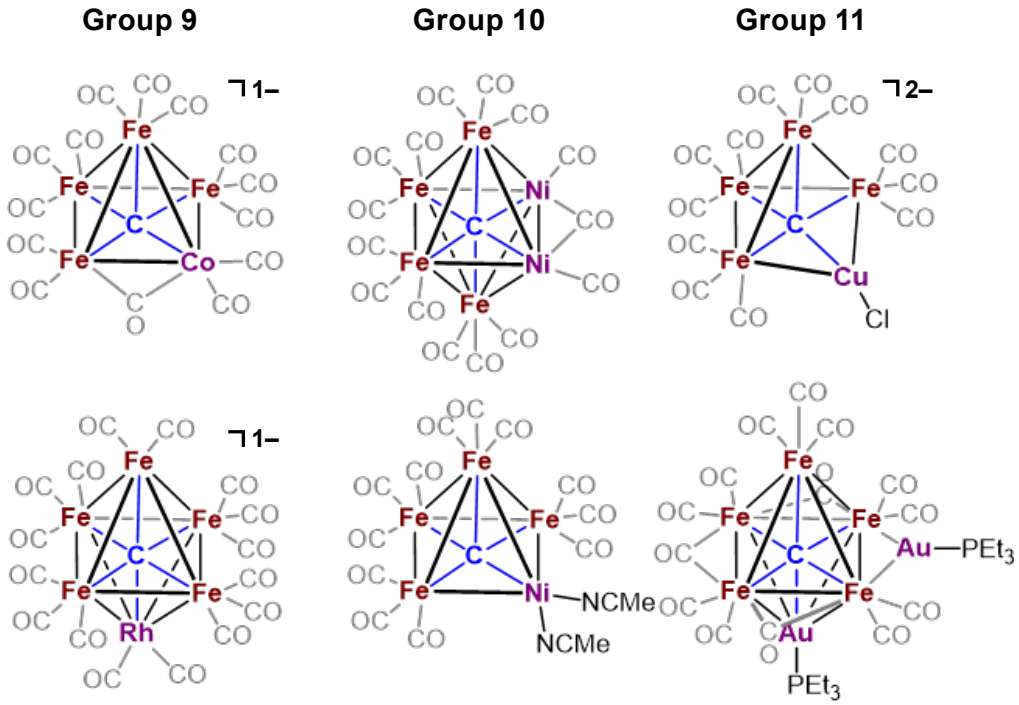

Scheme 3.2 Representative examples of carbidocarbonyl heterometallic clusters from the Crystal Structural Database.

In this chapter, a strategy for achieving iterative Fe→Mo substitutions upon the Fe_6 octahedron is demonstrated to be successful for the reliable synthesis and crystallographic characterization of the dianionic $[Fe_5Mo]^{2-}$ and $[Fe_4Mo_2]^{2-}$ clusters (**Scheme 3.3**). The neutral Fe_5 and Fe_4 clusters discussed in the previous chapter serve as synthetic starting points for the series, undergoing reduction by 2 equiv of KC_8 and subsequent addition of either one or two $\{Mo(CO)_3\}$ units. The utilization of the $\{Mo(CO)_3\}$ moiety is informed

by the PSEPT electron-counting rules (M_6 = 86 e^-), and as such each member of the series is more accurately described as an {Fe}→{Mo(CO)} substitution. Additionally, the Fe_5Mo cluster is demonstrated to perform selective reductions with diphenylacetylene (DPA) as an E≡E model substrate, while reactivity with N_2 and related dinitrogen-fixation substrates (HN=NH, $H_2N–NH_2$) proved generally unfruitful with all three clusters.

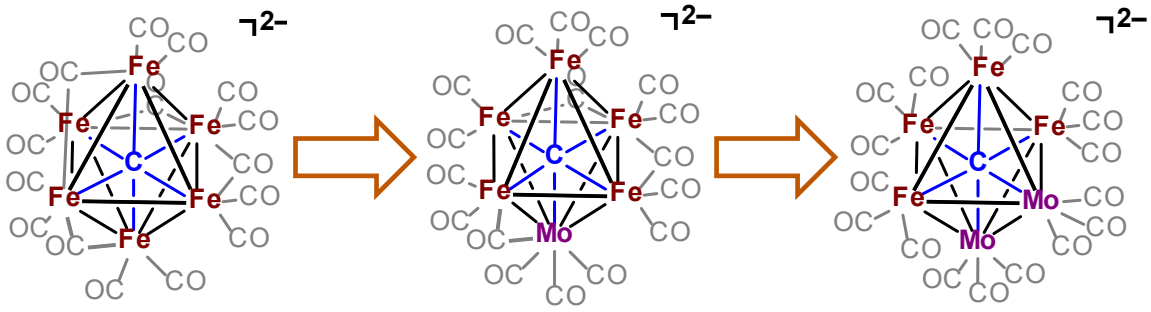

Scheme 3.3 Thematic illustration of the series of dianionic, octahedral clusters discussed in this chapter exhibiting iterative multi-step Fe→Mo substitutions.

3.2 Syntheses and Characterization of Heterometal Clusters

Syntheses of the Fe_5Mo and Fe_4Mo_2 dianionic clusters were achieved from the Fe_5 and Fe_4 neutral clusters, respectively. First, the all-iron dianion is generated by 2 e^- reduction of the respective neutral cluster, and subsequent introduction of a $\{Mo(CO)_3\}$ source into the reaction mixture to afford the heterometal cluster. The all-iron dianion can be isolated and crystallographically characterized prior to addition of the Mo source. The original report of Fe_5Mo conducted the reduction of $[Fe_5C(CO)_{15}]$ by equimolar amounts of $Na_2[Fe(CO)_4]$.[100] However, the $[Fe_5C(CO)_{14}]^{2-}$ product is susceptible to secondary reactions (Fe insertion into cluster) under these conditions, compelling us to utilize

potassium graphite (KC_8) as an alternative reducing agent. Secondly, $Mo(CO)_3$(chpt) was utilized as a $\{Mo(CO)_3\}$ source in lieu of $Mo(CO)_3(THF)_3$ employed by Tachikawa *et al.* because of its facile isolation and storage and similar reactivity to the THF-solvated reagent. The choice of a tricarbonyl Mo-source (vs. a di- or tertracarbonyl) is informed by the electron-counting rules, which predict $[Fe_5MoC(CO)_{17}]^{2-}$ to be a stable *closo* cluster. This rationale can similarly be extended to the previously unreported Fe_4Mo_2 dianionic cluster, in which $[Fe_4Mo_2C(CO)_{18}]^{2-}$ is predicted to be the stable *closo* cluster, and $[Fe_4C(CO)_{12}]^{2-}$ is generated as the intermediate dianion from $[Fe_4C(CO)_{13}]$ (**Scheme 3.4**). The syntheses of KC_8 and $Mo(CO)_3$(chpt) have been previously reported,[143,144] and adapted experimental procedures are given in Section 3.5.

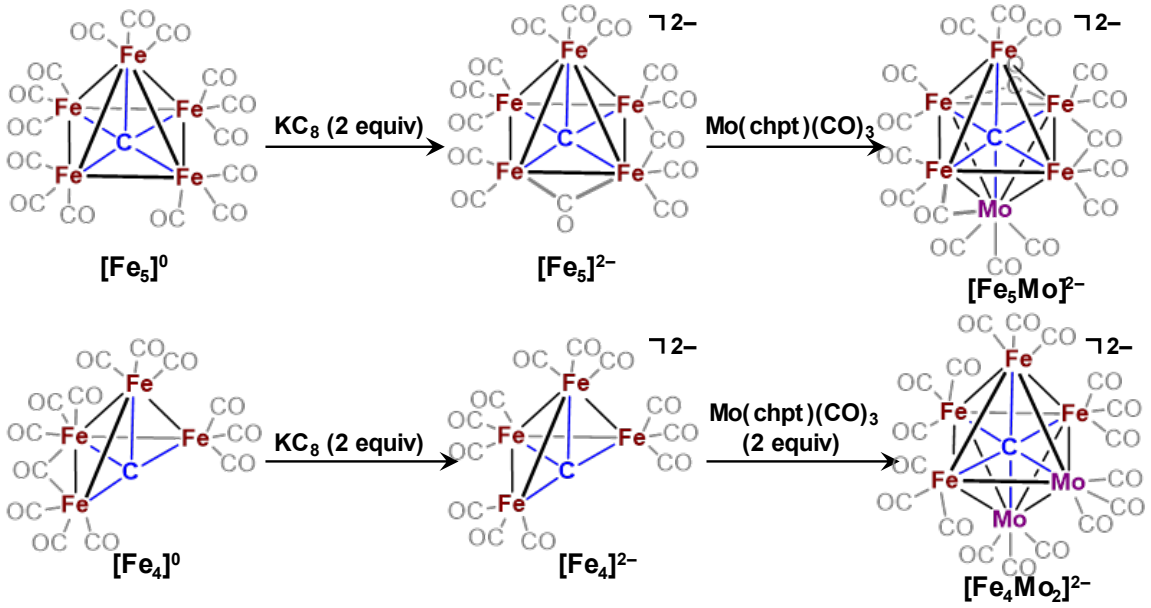

Scheme 3.4 Reduction of neutral clusters and subsequent Mo insertion to afford octahedral heterometal clusters.

3.2.1 Disruption of crystallographic symmetry in Fe_5Mo salts

Initial attempts to replicate the previously reported reaction conditions for $[Fe_5Mo]^{2-}$ necessitated the isolation of the NEt_4^+ salt of $[Fe_5]^{2-}$ by cation exchange of the K^+ salt with excess NEt_4Cl in THF as previously isolated and characterized by our lab.[106] Treatment of this cluster with $Mo(CO)_3$(chpt) and subsequent crystallization and XRD data collection produced a structure in the cubic space group $Fm\bar{3}m$, wherein the high-symmetry gives rise to ambiguous metal atom identities ($^4/_5$ Fe + $^1/_5$ Mo) (**Figure 3.1**). Additionally, the crystallographically determined model of the cation does not chemically represent NEt_4. As such, the crystal structure implies a formula of $[Fe_5Mo(\mu_6\text{-}C)(\mu_2\text{-}CO)_{12}]^{2-}$ and contains an inversion center at the carbide — as well as rotation axes and reflection planes that encompass the carbide — such that all CO ligands are crystallographically equivalent. However, the 76 e^- count indicated by this molecular formula is a vast departure from the 86 e^- count expected for a *closo*-M_6 cluster, which would predict a ligand count of 17 carbonyls. Additionally, the observed high-frequency CO stretches at ν = 2037 cm^{-1} and ν = 1929 cm^{-1} in the IR spectrum are inconsistent with a cluster featuring only bridging carbonyls. Furthermore, the structure of the $[Fe_5Mo]$ cluster can be inferred from its reported gold-coordinated derivatives, which feature 17 carbonyl ligands.[145]

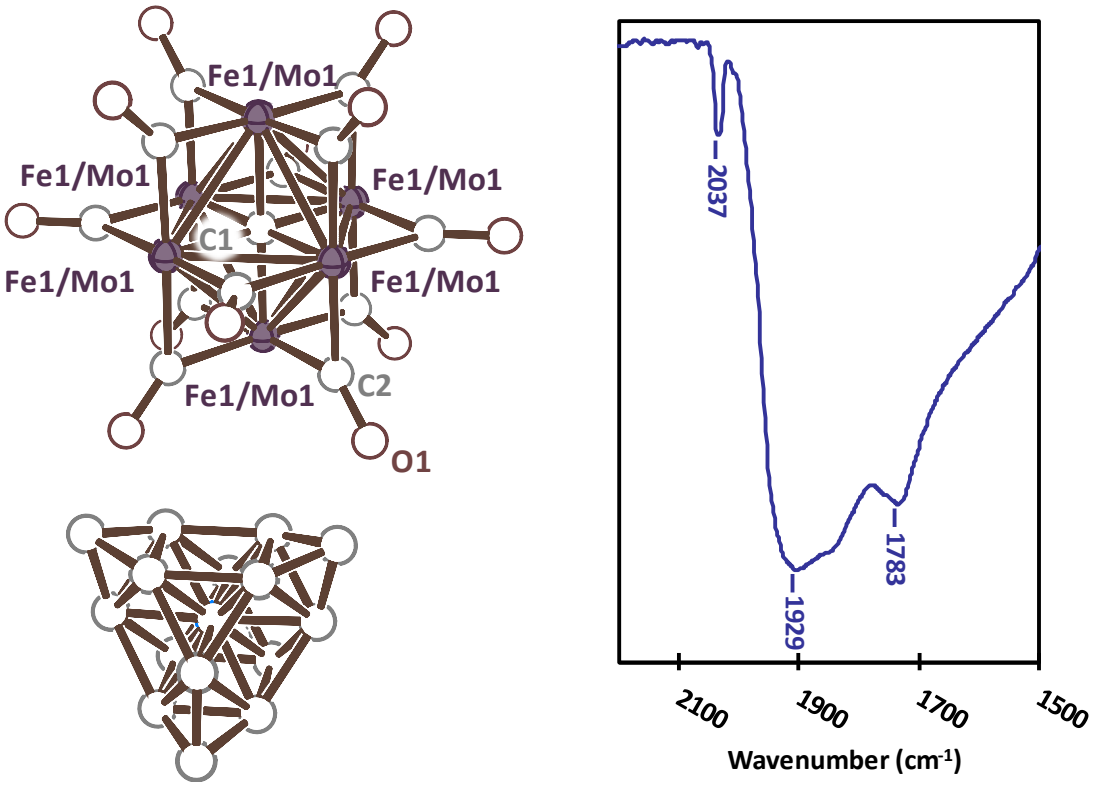

Figure 3.1 Crystal structure solution determined by single crystal XRD of $(NEt_4)_2[Fe_5Mo(\mu_6\text{-}C)(\mu_2\text{-}CO)_{12}]$ (*left*) and IR spectrum of the crystalline solid (*right*). The inversion symmetry in the crystal structure at the central carbide results in ambiguous metal identities and a highly disordered NEt_4^+.

To shed light on the observed inconsistencies in the data for "$(NEt_4)_2[Fe_5MoC(CO)_{12}]$," we sought cluster species with alternative cations by which a lower-symmetry crystal structure could be obtained. However, NMe_4^+, PPh_4^+, and PPN^+ salts produced similarly symmetric results as the NEt_4^+ salt. We subsequently found that by inducing an interaction between the cluster and its counterion, a crystal structure with unambiguous metal ion identities was obtained. This was achieved by omitting the cation exchange step and utilizing potassium salts in which the K^+ is ligated by a benzo-18-crown-6 ether to facilitate crystallization. First, a black oil of $[K(\text{benzo-18-crown-6})]_2[Fe_5(\mu_5\text{-}C)(CO)_{14}]$ (**1**) was obtained by addition of solid benzo-18-crown-6 ether into

THF reaction mixture of $K_2[Fe_5(\mu_5\text{-}C)(CO)_{14}]$ and subsequent removal of solvent *in vacuo*. Single crystals of **1** were grown as black plates by extraction of the oil into fluorobenzene (FPh) and slow vapor diffusion of Et_2O at –20 °C. The most optimal crystallization conditions determined were to use capped 2-dram vials, having each cap punctured with a single hole by a stainless-steel cocktail pick. The crystalline material is itself not soluble in FPh; however, the extraction of the oil into FPh is facilitated by presence of residual THF. The XRD data of these crystals exhibited co-crystallization with an impurity, making it difficult to obtain a crystal structure suitable for publication.

However, recrystallization of these crystals by DCE/Et_2O (DCE = 1,2-dichloroethane) vapor diffusion yielded exemplary data, exhibiting a *nido*-$[Fe_5(\mu_5\text{-}C)]$ core motif with an open coordination site (or, more accurately, an 'open dative site') at the basal position of the carbide (**Figure 3.2**). The equatorial Fe–C bond distances of 1.859(3), 1.857(3), 1.860(3), and 1.887(3) [$Fe–C_{avg}$ = 1.87±0.01 Å] lie in a somewhat broad range due to the asymmetry of the two bridging CO ligands on one side of the cluster. A similar arrangement is found in the reported NEt_4 salt, where $Fe–C_{avg}$ = 1.89±0.05 Å. In contrast, the Fe–C distance to the apical Fe site is relatively elongated at 1.994(3) Å. Consequently, the carbide resides 0.174 Å below the least-squares plane derived from the positions of the equatorial Fe sites. The four equatorial Fe–Fe distances in **1** are also somewhat varied (2.63±0.07 Å), while the Fe–Fe distances to the apical iron lie in a much narrower range (2.60±0.02 Å). The average Fe–Fe values for the K-crown and NEt_4 clusters are virtually identical in this regard [2.63±0.06 Å; 2.60±0.02 Å, respectively, for NEt_4 salt]. Despite the close contacts between the crowned potassium ions in **1** to O3 and O12 [K···O(C) = 2.745(3), 2.650(2) Å], the structure remains analogous to the structure obtained using the exclusively outer sphere NEt_4 cation. Lastly, the IR spectrum of **1** (**Figure 3.11**) exhibits several features bracketed between the highest energy (terminal) ν_{CO} = 2030 cm^{-1} and the

lowest energy (bridging) ν_{CO} = 1751 cm^{-1}, and a resonance in the ^{13}C NMR spectrum (THF-d_8) at 478.8 ppm (μ_5-C).

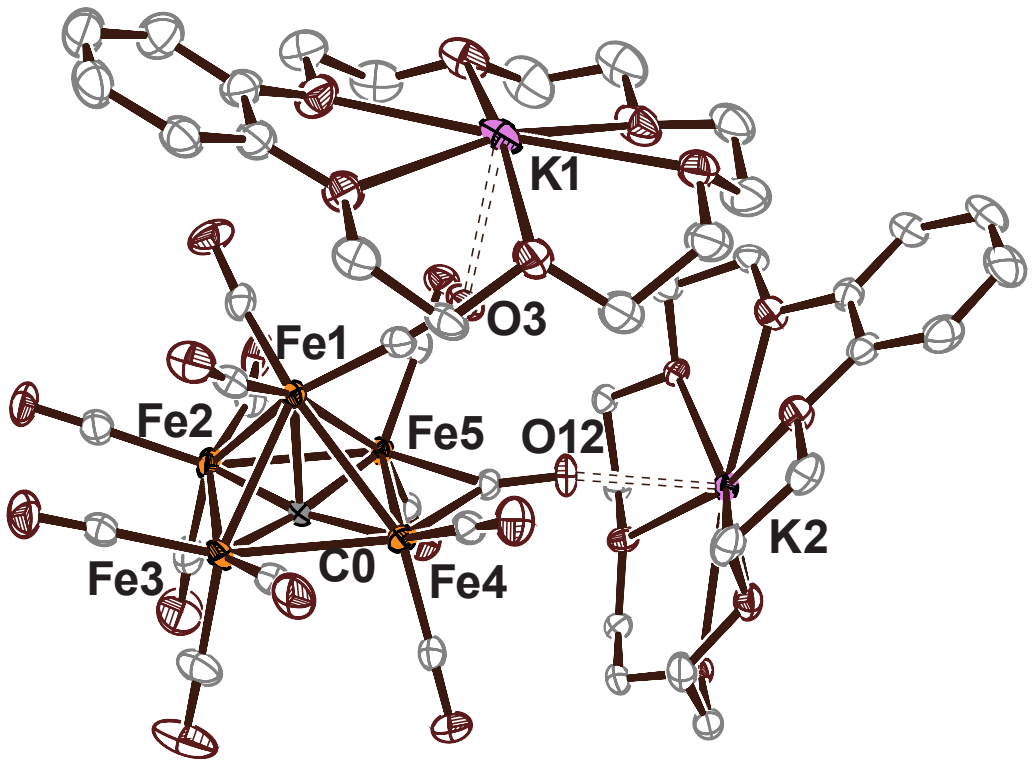

Figure 3.2 Thermal ellipsoid plot (50% probability) of $[K(benzo\text{-}18\text{-}crown\text{-}6)]_2[Fe_5(\mu_5\text{-}C)(CO)_{14}]$ (**1**). Orange = Fe; Gray = C; Maroon = O; Pink = K. Hydrogen atoms and one DCE solvent molecule have been removed for clarity.

Following the successful characterization of **1**, we reasoned that the open carbide dative site could be capped with a heterometal to afford the corresponding Fe_5M carbide structure. We thus attempted metalation of the carbide with chromium, molybdenum, and tungsten carbonyls. Reactions of $[M(CO)_3(L)]$ [where L = chpt (cycloheptatriene) or $(THF)_3$] with M = Cr and Mo in THF afforded adducts postulated as $[Fe_5M(\mu_6\text{-}C)(CO)_{17}]^{2-}$ (**Scheme 3.5**), as judged by their IR spectra (blue-shifted features ≈ 1940 and 1785 cm^{-1}). However, whereas the Mo adduct proved stable under crystallization conditions, the

{Cr(CO)$_3$} unit spontaneously dissociated over time, even at low temperatures (−20 °C) during crystallization. Treatment of **1** with [W(CO)$_3$(THF)$_3$] did not install the {W(CO)$_3$} unit to the carbide site under any tested condition, possibly because of the poor orbital overlap between the diffuse W 5*d* set and the contracted C 2*p* set. On the basis of the stability of the [Fe$_5$Mo]$^{2-}$ cluster, structural characterization was forthcoming (FPh/Et$_2$O vapor diffusion), affording black plates of [K(benzo-18-crown-6)]$_2$[Fe$_5$Mo(μ_6-C)(μ_2-CO)$_3$(CO)$_{14}$] (**2**; **Figure 3.3**). The structure exhibits a "capped" μ_6-carbide motif, incorporating the {Mo(CO)$_3$} unit at a distance of 2.113(6) Å from the carbide. Regarding the *trans* effect of the capping {Mo(CO)$_3$} unit, the apical Fe ion is substantially compressed toward the carbide at Fe−carbide = 1.937(6) Å versus the five-iron cluster [1.994(3) Å]. Conversely, the carbide resides closer to the least-squares plane derived from the equatorial irons (0.099 Å). The equatorial Fe−carbide distances remain largely unchanged. The Mo site exhibits three terminal CO ligands [Mo−C(O) = 1.972(7), 1.961(7), and 1.961(8) Å] and one bridging CO ligand [Mo−C(O) = 2.344(6) Å] with Fe5.

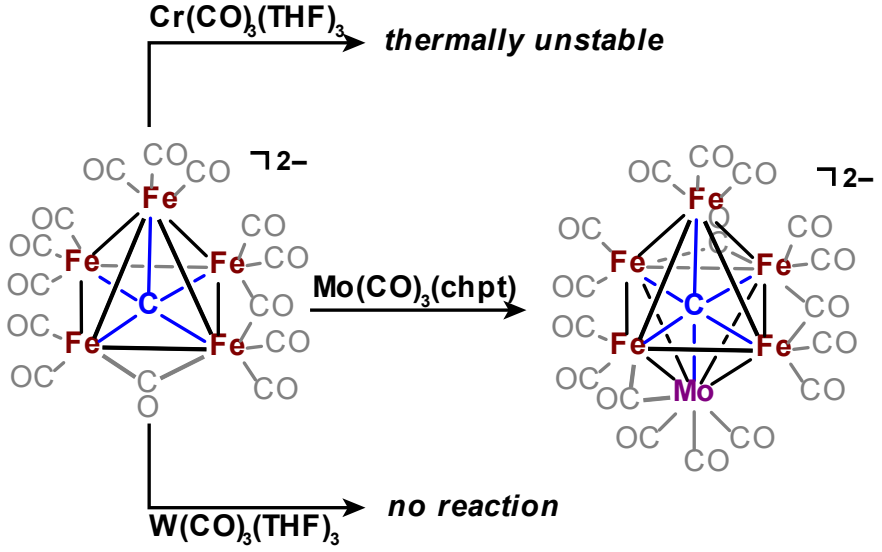

Scheme 3.5 Reactions of [Fe$_5$]$^{2-}$ (**1**) with various Group 6 {M(CO)$_3$} reagents.

Overall, the Mo center participates in nine bonding interactions (including one bridging CO), whereas the highest coordination-number Fe site (Fe3; also coordination number = 9) exhibits two bridging CO ligands. Thus, while polyhedral skeletal electron pair theory (PSEPT) accurately predicts the total number of CO ligands, simple inspection of the metal oxidation states [Mo^0 versus Fe^I] indicates the location of the "extra" CO on the Mo site. Incubation of **2** under a CO atmosphere results in no change in the IR spectrum or enhanced features in the ^{13}C NMR, indicating no further CO binding and the validity of the PSEPT rules in this case. The bond metrics of the terminal and bridging CO ligands on the Fe sites remain largely unchanged [avg $Fe{-}C(O)_{term}$ = 1.778 ± 0.017; $Fe{-}C(O)_{bridg}$ = 1.968 ± 0.141 Å]. Lastly, the crowned K ions exhibit close contacts with two terminal CO ligands [K···O = 2.831(5) and 2.916(8) Å], similar to the K···O contacts found in **1**.

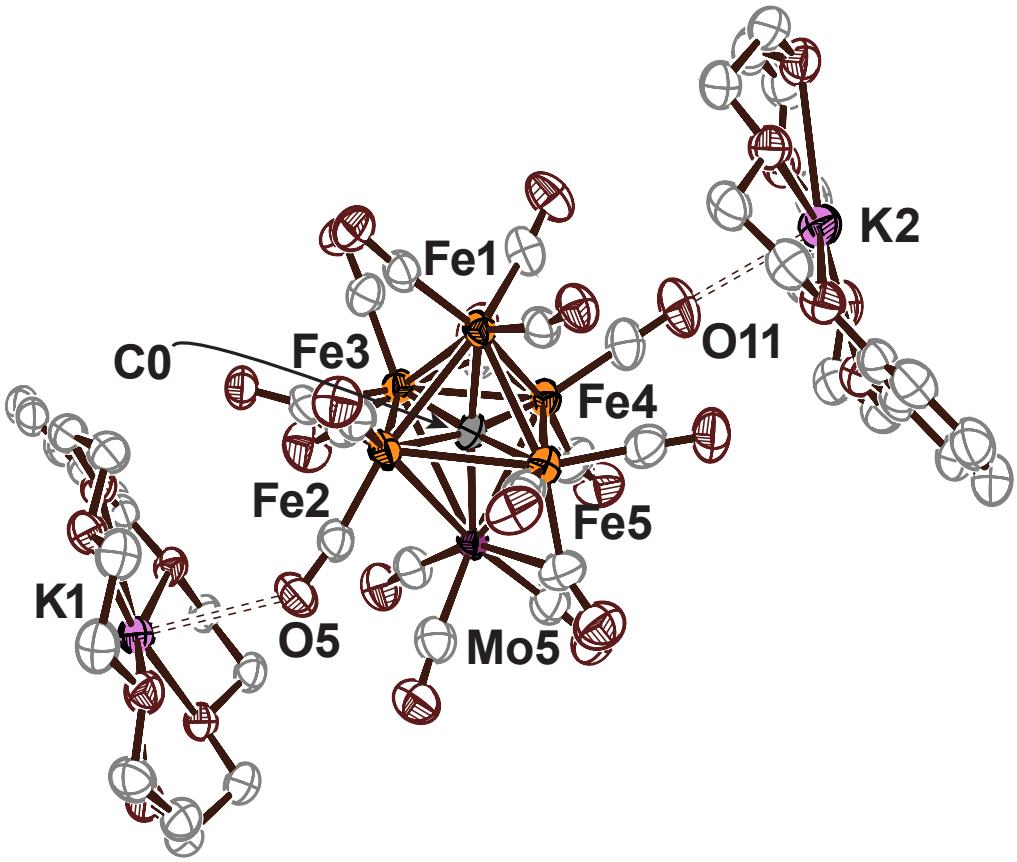

Figure 3.3 Thermal ellipsoid plot (50% probability) of [K(benzo-18-crown-6)]$_2$[Fe$_5$Mo(μ_6-C)(μ_2-CO)$_3$(CO)$_{14}$] (**2**). Orange = Fe; Purple = Mo; Gray = C; Maroon = O; Pink = K. Hydrogen atoms and two FPh solvent molecules have been removed for clarity.

3.2.2 Synthesis and Characterization of $[Fe_4]^{2-}$ and $[Fe_4Mo_2]^{2-}$ Clusters

Synthesis of the dianionic [Fe$_4$(μ_4-C)(CO)$_{12}$]$^{2-}$ was accomplished using reaction conditions similar to those employed for the dianionic pentairon cluster. Treatment of the neutral tetrairon [Fe$_4$(μ_4-C)(CO)$_{13}$] cluster in THF with 2 equiv of KC_8 as reductant followed by addition of 2 equiv of benzo-18-crown-6 yielded the desired dianionic species, [K(benzo-18-crown-6)]$_2$[Fe$_4$(μ_4-C)(CO)$_{12}$] (**3**). Removal of THF *in vacuo* leaves a dark

brown oil which was extracted into FPh, and the cluster was crystallized by slow vapor diffusion of Et_2O into this solution at –20 °C using similar conditions to those described for **1**. Crystal structure data for **3** (**Figure 3.4**) revealed an asymmetric unit comprised of two chemically equivalent but crystallographically distinct tetrairon carbide cluster dianion sites (denoted "site A" and "site B") and three crystallographically distinct $[K(benzo\text{-}18\text{-}crown\text{-}6)]^+$ cation sites. Examination of the site occupancies for each unit are consistent with a dianionic cluster, such that the cluster atoms modeled at site A are half-occupied (s.o.f. = 0.5) and the cluster atoms modeled at site B as well as all three K-crown units are fully occupied (s.o.f. = 1), resulting in an asymmetric unit comprised (empirically) of 1.5 $[Fe_4(\mu_4\text{-}C)(CO)_{12}]^{2-}$ units and three $[K(benzo\text{-}18\text{-}crown\text{-}6)]^+$, where the site A carbide is located near an inversion center. The Fe–C bond distances at both sites exhibit a significantly broad range with an average distance of 1.9 ± 0.1 Å, though it remains within typical range for carbidocarbonyl iron clusters. Similarly, the Fe–Fe bond distances (avg. 2.62 ± 0.04 Å) are unremarkable and conform to expected values. The K···O(C) contacts [2.723(7), 2.60(3), 2.915(6), 3.136(7), 2.944(8) Å] are also comparable to those of the Fe_5 dianion, though the presence of multiple contacts at K3 results in a broad range of distance values. Finally, the IR spectrum of **3** (**Figure 3.15**) is consistent with the crystal structure, exhibiting peaks in only the terminal CO range between ν_{CO} = 2026 cm^{-1} and ν_{CO} = 1930 cm^{-1}. The carbide resonance in the ^{13}C NMR spectrum (MeCN-d_3) appears at 478.6 ppm.

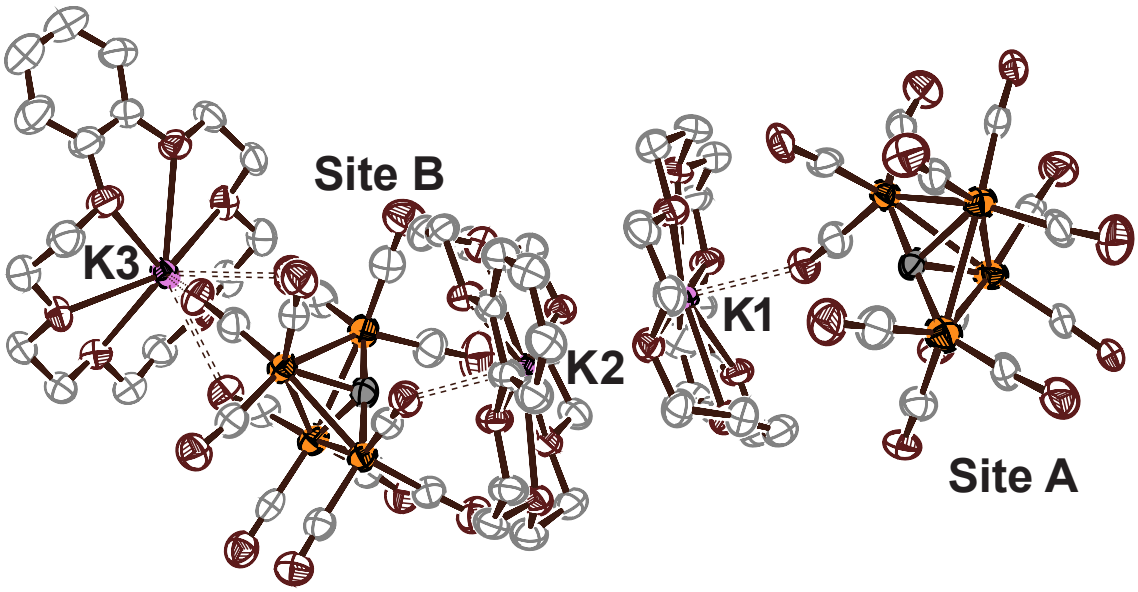

Figure 3.4 Thermal ellipsoid plot (50% probability) of $[K(benzo\text{-}18\text{-}crown\text{-}6)]_2[Fe_4(\mu_4\text{-}C)(CO)_{12}]$ (**3**). Orange = Fe; Gray = C; Maroon = O; Pink = K. Hydrogen atoms and two FPh solvent molecules have been removed for clarity.

Stoichiometric addition of $Mo(CO)_3(chpt)$ to **3** led to a mixture of Fe_4 and Fe_4Mo clusters that co-crystallized and were difficult to separate. While crystal structure data supported the formation of an Fe_4Mo cluster with Mo occupying a basal site (a partial structure is depicted in **Figure 3.5**), the intrinsic impurity of the crystal hampered unambiguous structural determination. However, a pure crystalline sample of $[K(benzo\text{-}18c6)]_2[Fe_4Mo_2(\mu_6\text{-}C)(CO)_{16}(\mu_2\text{-}CO)_2]$ (**4**) was isolated by reaction of **3** with excess $Mo(CO)_3(chpt)$ and mild heating (80 °C) to ensure complete reaction. The crystal structure thus obtained of **4** (**Figure 3.6**) reveals that the Fe_4 'butterfly' motif remains unchanged, imposing *cis*-Mo coordination upon the carbide. This is to be expected as there is no CCDC structure for tetrairon-heterometal carbide or nitride cluster that does not preserve the Fe_4 butterfly (a unique counterexample is presented in Chapter 4). The asymmetric unit of the structure is modeled such that the site occupancy of the cluster dianion is half-occupied

relative to the K-crown unit. Upon insertion of the two molybdenum atoms, the average Fe–Fe and Fe–$C_{carbide}$ contacts become elongated to 2.65 ± 0.07 Å and 1.92 ± 0.02 Å, respectively. Finally, the crowned K cations exhibit close contacts with carbonyl oxygen atoms (avg 2.82 ± 0.1 Å) similar to those in the previously discussed structures.

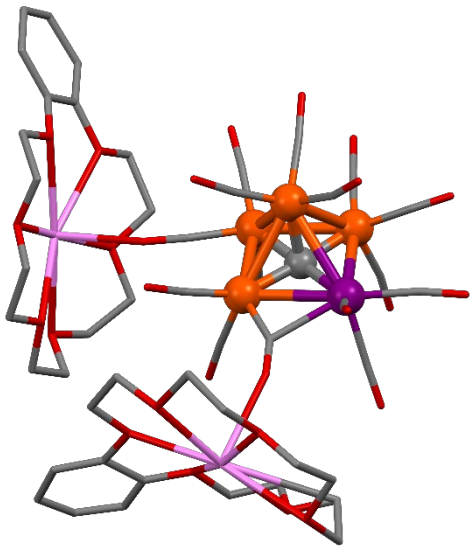

Figure 3.5 Preliminary X-ray structure of $[K(benzo\text{-}18c6)]_2[Fe_4Mo(\mu_5\text{-}C)(CO)_{15}]$. Orange = Fe; Purple = Mo; Gray = C; Red = O; Pink = K.

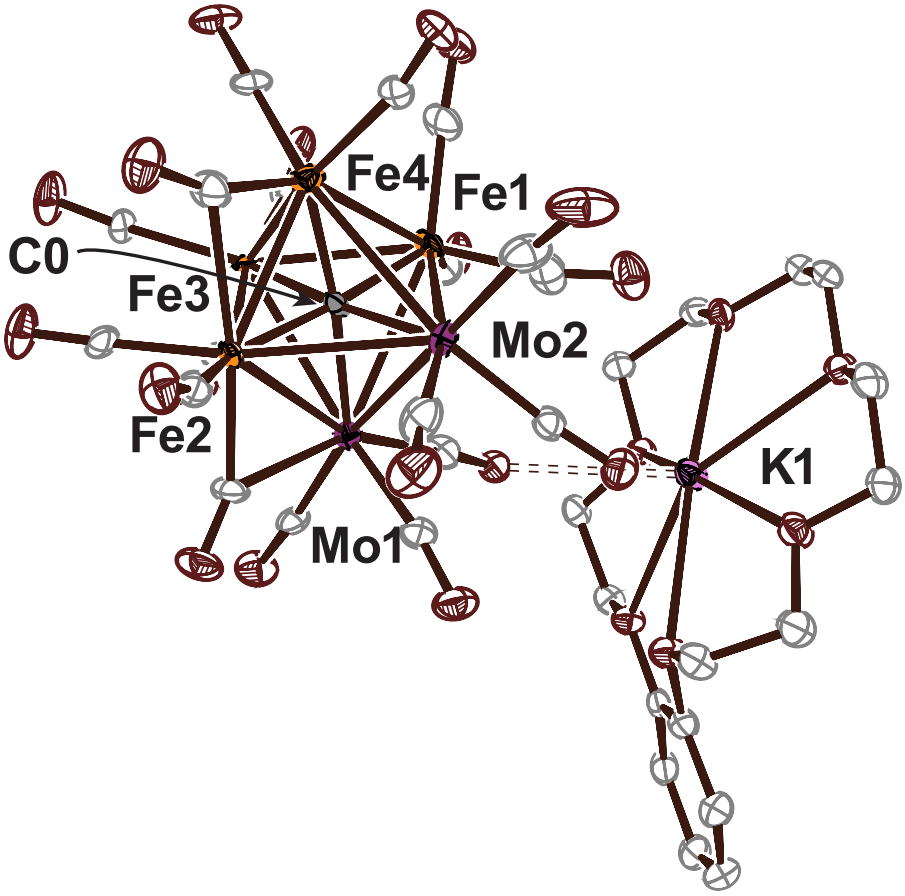

Figure 3.6 Thermal ellipsoid plot (50% probability) of $[K(benzo\text{-}18c6)]_2[Fe_4Mo_2(\mu_6\text{-}C)(CO)_{16}(\mu_2\text{-}CO)_2]$ (**4**). Orange = Fe; Purple = Mo; Gray = C; Maroon = O; Pink = K. Hydrogen atoms have been removed for clarity.

3.2.3 Crystallographic Comparisons with FeMoco

While the presence of direct Mo–C bonds in **2** and **4** does not encompass any biomimetic relevance, it is interesting to draw comparisons between the synthetic compounds and biological system. **Table 3.1** delineates the average bond distances described in the previous sections as well as distances of interest from FeMoco isolated from *Clostridium pasteurianum*.[14] The Fe–C bond distances are slightly shorter than those

found in FeMoco (~1.9 Å vs. 2.00 ± 0.02 Å). Surprisingly, the Fe–Fe distances are quite comparable, and all lie within 0.03 Å of distances found in FeMoco (2.63 ± 0.04 Å). On the other hand, while the Mo···Fe distances (2.684 ± 0.008 Å) are only slightly elongated relative to Fe····Fe, they are considerably short relative to the analogous distances in **2** and **4** by ~0.2 Å.

Bond	Fe_5 (1)	Fe_5Mo (2)	Bond	Fe_4 (3)	Fe_4Mo_2 (4)	Bond	FeMoco
Fe_{ax}–C	1.994(3)	1.937(6)	Fe–C	1.9±0.1	1.91±0.02	Fe–C	2.00±0.02
Fe_{eq}–C	1.87±0.01	1.892±0.009					
C–Fe_{eq} plane	0.174	0.099					
Mo–C		2.113(6)	Mo–C		2.117±0.006		
Fe_{ax}–Fe_{eq}	2.60±0.02	2.635±0.005	Fe–Fe	2.62±0.04	2.65±0.07	Fe···Fe	2.63±0.04
Fe_{eq}–Fe_{eq}	2.63±0.07	2.7±0.1	Mo–Mo		3.077(3)		
Mo–Fe		2.9±0.1	Mo–Fe		2.89±0.05	Mo···Fe	2.684±0.008
K···O	2.70±0.07	2.87±0.06	K···O	2.8±0.1	2.82		

Table 3.1 Selected average bond distances exhibited by clusters **1**–**4** and FeMoco.

3.3 Reactivity with N_2-Model Substrates

Despite the structural differences in clusters **2** and **4** from the nitrogenase cofactor, we sought to investigate the possible use of these synthetic clusters in catalytic N_2 reduction reactions. This exploration was initially informed by preliminary reports by Nishibayashi *et al.* demonstrating catalytic silylation of dinitrogen by the mononuclear iron complexes $Fe(CO)_5$ and $Fe(Cp)_2$.[146] Our own attempts to replicate similar reactivity using the clusters showed poor turnover numbers rarely above 1; these results are summarized in **Table 3.2**. As such, we pursued model substrates that were more easily activated (diphenylacetylene,

diazene, and hydrazine) to determine the substrate activation capabilities of the various clusters.

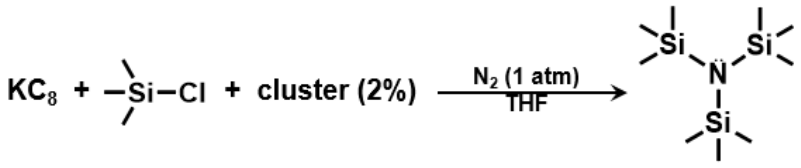

cluster	Equiv. $N(TMS)_3$ per cluster
$(NEt_4)_2$**[Fe_6]**	**0.84**
$(NEt_4)_2$**[Fe_5Mo]**	**1.07**
[$Fe(CO)_5$]	**0.65**
[$Mo(CO)_6$]	**0.08**
$[K(b18c6)]_2$**[Fe_5Mo]**	**0.35**
$[K(b18c6)]_2$**[Fe_5]**	**0.48**

Table 3.2 Dinitrogen silylation reaction conditions with various mononuclear and multinuclear catalysts and results delineated in equiv of $N(TMS)_3$ product as an indication of turnover number.

3.3.1 Catalytic Reduction of Diphenylacetylene by $[Fe_5Mo]^{2-}$

To probe the redox activity of **1** and **2**, we performed cyclic voltammetry (CV) to determine the accessibility of the reduced congeners of **1** and **2**. A cathodic sweep of **1** in THF (**Figure 3.7**) did not exhibit any reduction events. The return anodic sweep, however, did reveal two oxidation events assigned to the conversion of the dianionic cluster to the known neutral species. Alternately, the CV for the Mo-containing cluster **2** (**Figure 3.8**) revealed a set of reversible features with a reduction event at −2.00 versus Fc. The accessibility of these redox events to common chemical reductants, such as KC_8 and sodium perylenide (Na_2Per), led us to explore reactions of the reduced cluster with model substrates that provide insight into selective reductions of triply-bonded functional groups.

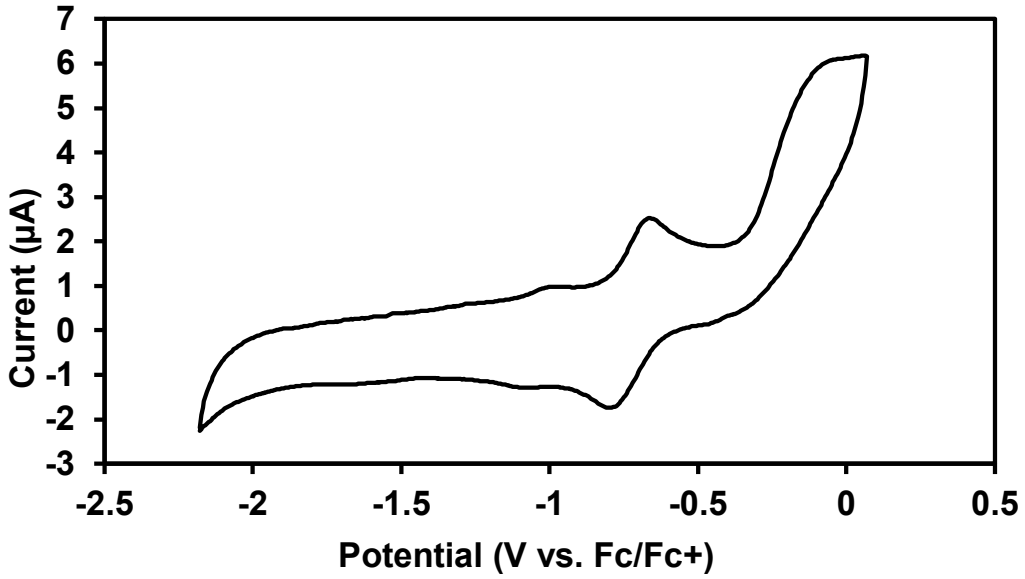

Figure 3.7 Cyclic voltammogram (vs Fc/Fc^+) of THF solution of 0.2 mM of **1** in MeCN containing 2 mM $LiClO_4$. *Experiment setup:* Glassy carbon working electrode, platinum wire counter electrode, silver wire quasi-reference electrode; scan rate: 50 mV/s.

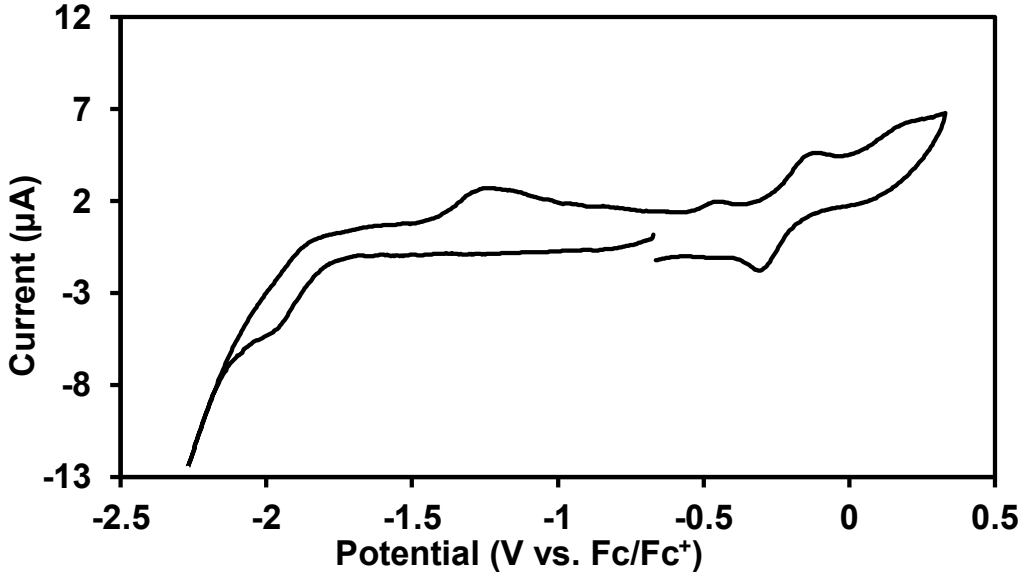

Figure 3.8 Cyclic voltammogram (vs Fc/Fc^+) of THF solution of 0.2 mM of **2** in MeCN containing 2 mM $LiClO_4$. *Experiment setup:* Glassy carbon working electrode, platinum wire counter electrode, silver wire reference electrode; scan rate: 50 mV/s.

On the basis of these findings and literature precedent demonstrating the activation of alkynes by iron carbonyls,[147] we pursued reactions of the model substrate DPA with each cluster under reducing conditions in the presence of varying proton sources. Selected results are delineated in **Table 3.3**. Previous studies explored the reduction of DPA using palladium-catalyzed or electrochemical means to obtain *cis*-alkene.[148–150] In contrast, there is just a single report of a single-molecule catalyst (intriguingly, an $[Fe_4S_4](SR)_4]^{2-}$ cluster) for DPA reduction.[151] A general, unbalanced formula for the reaction performed here is given in **Scheme 3.6**.

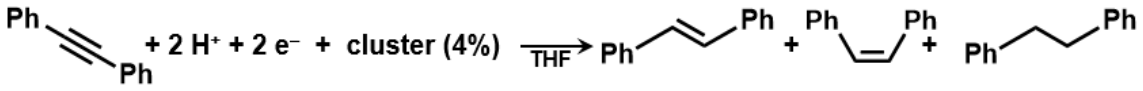

Scheme 3.6 Generalized reaction conditions for DPA reduction and expected products (stoichiometrically unbalanced).

First, control reactions with no cluster (KC_8, LutH·OTf) revealed a poorly selective 0.25 ratio of the intermediately reduced product (diphenylethylene) to the fully reduced alkane product (diphenylethane) with 21.8% DPA conversion. None of the desired *cis*-alkene was observed in the control reaction. In contrast, the presence of catalytic **2** (KC_8, LutH·OTf) provided better selectivity for alkene/alkane conversion (1.58 ratio), indicating over a 6-fold improvement in the selectivity, despite a diminished 14.1% overall conversion. Within the possible alkene products (*trans* and *cis*), cluster **2** did provide some, albeit minimal, *cis* product (*cis*/*trans* = 0.22). A secondary control reaction replaced cluster **2** as a catalyst with its individual metal center components. When 5 equiv of $Fe(CO)_5$ was used in conjugation with 1 equiv of $Mo(CO)_6$, moderate selectivity was maintained. However, substrate conversion decreased dramatically (3.6%). A screening of different

proton sources revealed poor activity with phenols and more consistently beneficial results using nitrogen-based acids. Additionally, it was found that bulkier, lower pK_a proton sources yielded higher substrate conversion and *cis* selectivity. A sterically encumbered anilinium triflate (2,4,6-trimethylanilinium triflate) provided the highest overall conversion (25.4%), moderate alkene/alkane selectivity (0.36), and a higher *cis*/*trans* ratio (0.30) than other conditions. By comparison, the Fe-only cluster **1** provided a low overall conversion (9.7%) and only an intermediate alkene/alkane selectivity (0.60). The less beneficial results from **1** are most likely due to its inaccessible redox activity by KC_8 and the decreased stability of the [Fe_5] core versus the [Fe_5Mo] core under catalytic conditions.

catalyst	reductant	H^+ source	pK_a	Temp.	conversion %	C=C/C-C	*cis*/*trans*
none	KC_8	[LutH]OTf	6.60	r.t.	21.8	0.25	0.00
Fe_5	KC_8	[LutH]OTf	6.60	r.t.	9.7	0.60	0.34
Fe_5Mo	KC_8	[LutH]OTf	6.60	r.t.	14.1	1.58	0.22
5 Fe + Mo	KC_8	[LutH]OTf	6.60	r.t.	3.6	0.62	0.82
Fe_5Mo	KC_8	2,6-^{t}Bu$_2$,4-MeOPhOH	13.04	r.t.	0.6	0.99	0.00
Fe_5Mo	KC_8	[Et_3NH]OTf	10.75	r.t.	2.0	0.83	0.02
Fe_5Mo	KC_8	[$PhNH_3$]OTf	4.60	r.t.	13.8	0.09	0.11
Fe_5Mo	KC_8	[$MesNH_3$]OTf	4.37	r.t.	25.4	0.36	0.30
Fe_5Mo	Na_2(Per)	[$MesNH_3$]OTf	4.37	r.t.	17.9	3.01	0.56
none	Na_2(Per)	[$MesNH_3$]OTf	4.37	r.t.	12.1	2.22	0.01
5 Fe + Mo	Na_2(Per)	[$MesNH_3$]OTf	4.37	r.t.	15.9	4.61	0.63
Fe_5Mo	Na_2(Per)	[$MesNH_3$]OTf	4.37	–20 °C	28.8*	1.66	0.03
Fe_5Mo	Na_2(Per)	[$MesNH_3$]OTf	4.37	60 °C	3.7	6.55	1.15*
Fe_5Mo	Na_2(Per)	[2,4,6-^{t}Bu$_3$PhNH$_3$]OTf	3.30	r.t.	15.9	16.0*	0.65
none	Na_2(Per)	[2,4,6-^{t}Bu$_3$PhNH$_3$]OTf	3.30	r.t.	0.8	C=C only	0.00
Fe_5Mo	Na_2(Per)	[2,4,6-^{t}Bu$_3$PhNH$_3$]OTf	3.30	60 °C	14.9	10.8	0.57

Table 3.3 Conversions in the reduction of diphenylacetylene (DPA) to *cis*/*trans*-diphenylethylene (DPE) and diphenylethane (DPEthane). LutH = 2,6-Lutidinium; $MesNH_3$ = 2,4,6-trimethylanilinium; Na_2(Per) = sodium perylenide; 5 Fe + Mo = 5 $Fe(CO)_5$ + $Mo(CO)_6$; **Fe_5** = Cluster **1**; **Fe_5Mo** = Cluster **2**. The asterisks denote the best result for each column.

To further optimize the conversion and selectivity of the reaction, a weaker reducing agent (sodium perylenide, generated *in situ*) was used. While substrate conversion dropped modestly (from 25% to 18%), the selectivity of *cis*-alkene increased significantly (alkene/alkane = 3.01; *cis*/*trans* = 0.56). Interestingly, temperature was found to be inversely correlated with substrate conversion while being directly correlated with selectivity toward *cis*-alkene. Performing the reaction at 60 °C exhibited the highest selectivity (alkene/alkane = 6.55; *cis*/*trans* = 1.15), although it suffered from poor substrate conversion (3.7%). Finally, 2,4,6-tri-tert-butylanilinium triflate was used as an even bulkier proton source, which dramatically increased the alkene/alkane selectivity (16.0) while the overall conversion and *cis* selectivity remained moderate. The corresponding control reaction (no catalyst) provided only 0.8% overall conversion, and no *cis* product was detected.

To establish the integrity of the cluster throughout the catalytic process, we determined several spectroscopic properties of the *in situ* cluster product. After catalysis with **2**, the IR spectrum of the reaction mixture exhibited a distinct ν_{CO} feature at 1963 cm^{-1} (**Figure 3.9**); this is distinct from the starting IR of **2**, at 1943 cm^{-1} (**Figure 3.15**). To provide context for this observation and to gain insight into the mechanism of substrate reaction, stoichiometric reactions of **2** with reductants and substrates were performed (**Figure 3.10**). Treatment of cluster **2** with 1 equiv of Na_2(Per) resulted in a blue shift to 1958 cm^{-1}. Subsequent addition of 1 equiv of DPA resulted in no significant change (ν_{CO} at 1959 cm^{-1}), indicating no direct interaction of reduced **2** with DPA. In contrast, treatment of reduced **2** with 1 equiv of [$MesNH_3$]OTf resulted in a slightly shifted ν_{CO} at 1962 cm^{-1} (closer to the crude mixture value of 1963 cm^{-1}), indicating direct reaction of reduced **2** with the proton source. Also, while the ^{1}H NMR spectrum of this anilinium-treated solution did not exhibit a hydride resonance, treatment of the solution with a stronger acid (TfOH)

did afford a distinct hydride resonance at −26 ppm (**Figure 3.11**), attributed to the formation of a bridging hydride species (IR: ν_{CO} = 1962 cm^{-1}). This feature is analogous to protonation of the corresponding $[Fe_6]^{4-}$ species, which also affords a bridging hydride (−21 ppm).[136] Overall, it can be postulated that the cluster core structure is maintained throughout catalysis and that the primary mechanism of substrate reduction proceeds through a cluster−hydride intermediate that acts upon the DPA substrate.

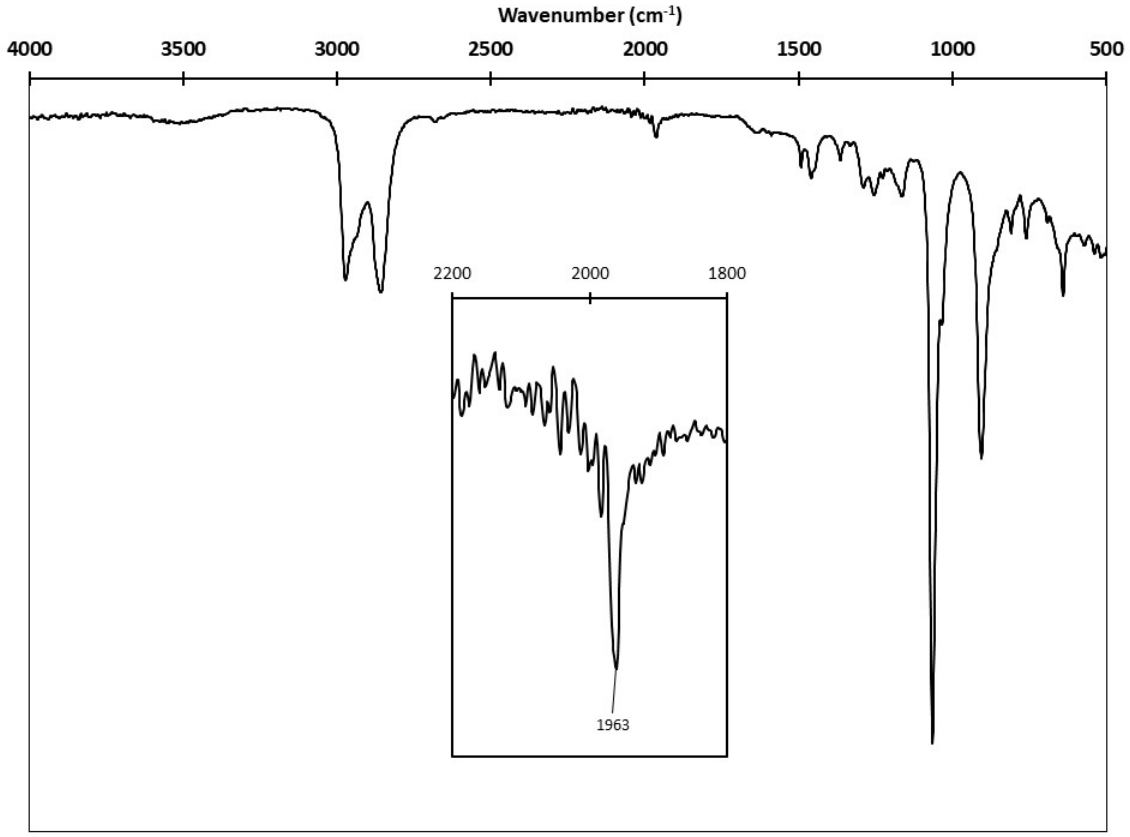

Figure 3.9 IR spectrum collected after DPA reduction reaction with cluster **2**, Na_2(Per), and [$MesNH_3$]OTf. The reaction mixture was drop-casted by pipette onto the IR stage prior to collection. Inset: enlarged view of CO region.

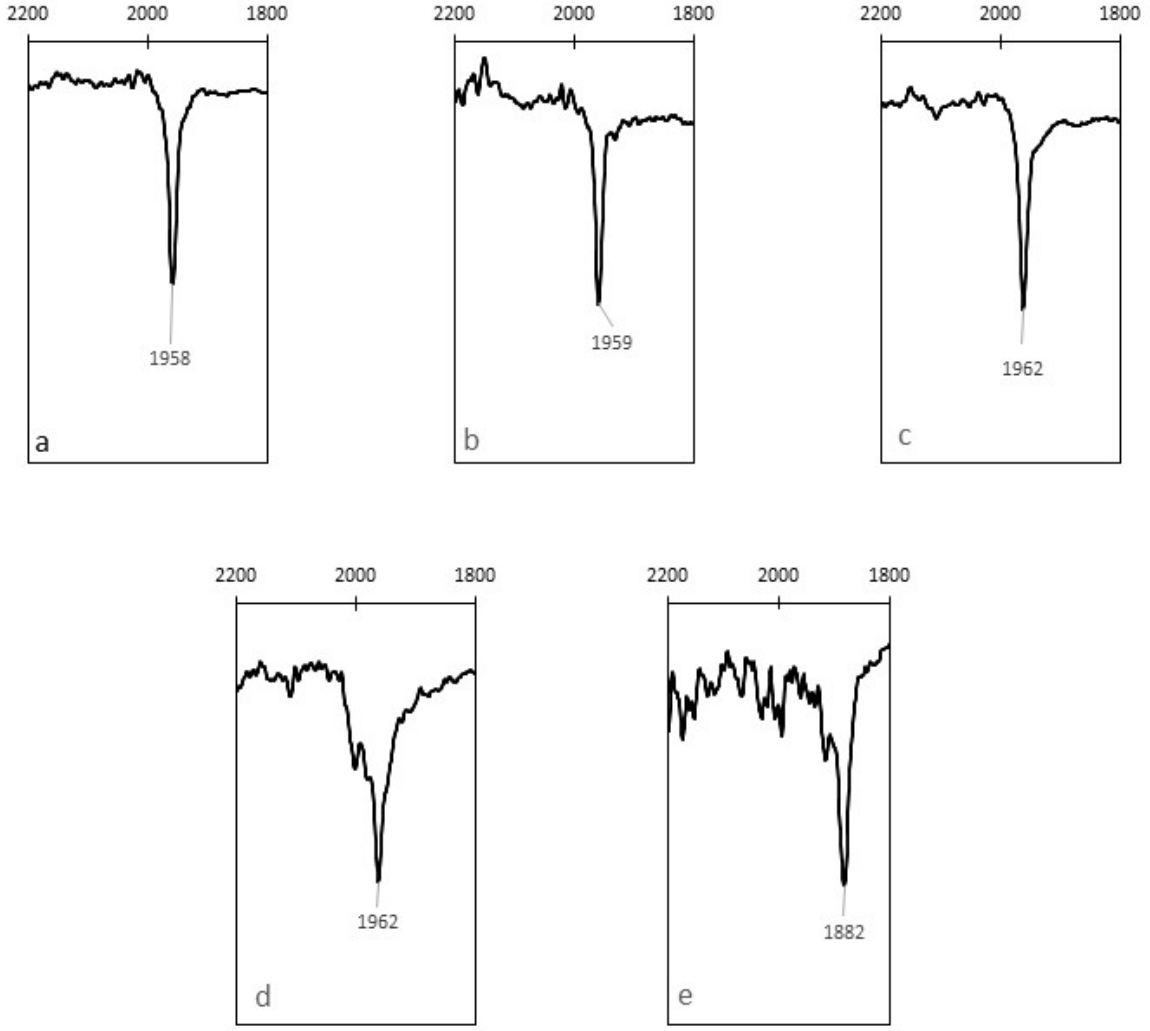

Figure 3.10 IR **(**CO region) of various solutions drop-casted by pipette onto IR stage: (a) A solution of Na_2(Per) in THF (0.0218 M, 0.76 mL, 0.017 mmol) was added dropwise into a THF solution of cluster **2** (26.0 mg, 0.0166 mmol) and stirred for 6 h. (b) The solution was then divided into two equal portions. To the first portion, a THF solution of diphenylacetylene (8.42 mM, 1.0 mL, 0.0083 mmol) was added and the solution stirred 1 h. (c) To the second portion, a THF solution of [$MesNH_3$]OTf (8.42 mM, 1.0 mL, 0.0083 mmol) was added and the solution stirred 1 h. (d) Treating a solution prepared in the same manner as solution (a) with a slight excess of TfOH (~1.3 eq) resulted in spectrum (d). (e) A solution of Na_2(Per) in THF (0.0218 M, 0.76 mL, 0.017 mmol) was added dropwise into a THF solution of $Fe(CO)_5$ (21.0 mg, 0.107 mmol) and stirred for 6 h.

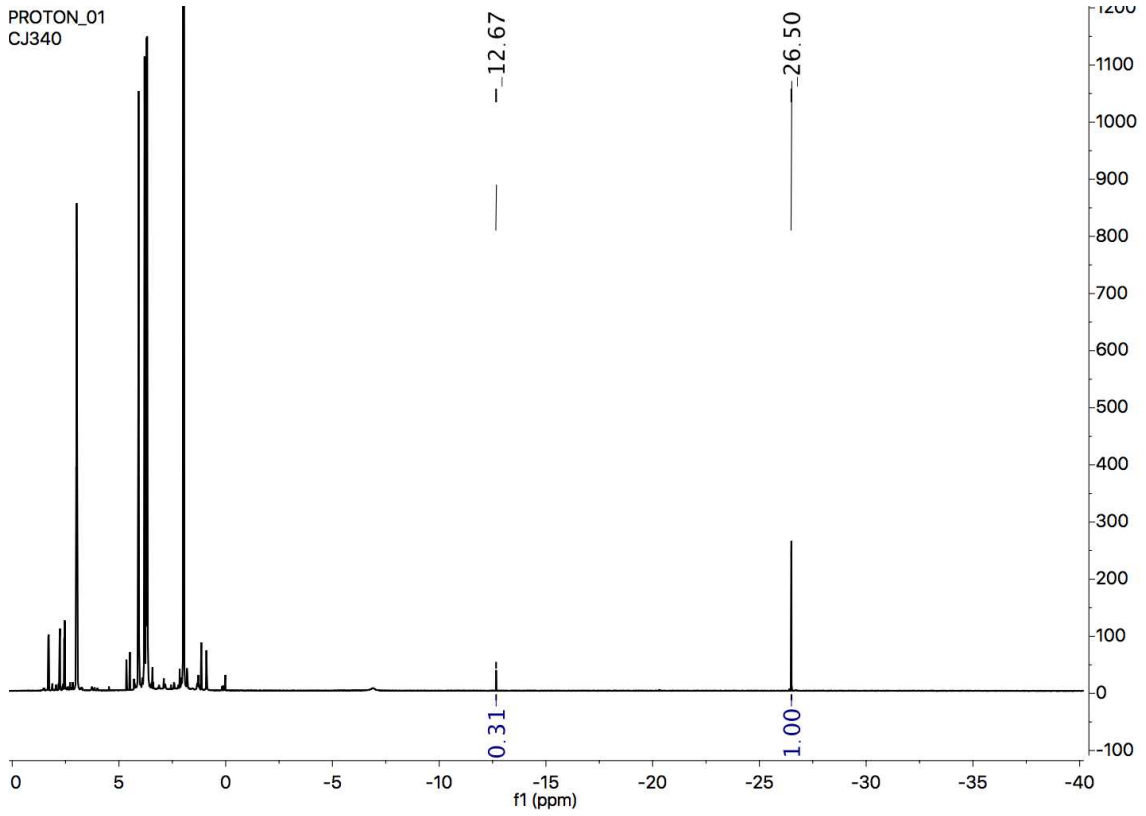

Figure 3.11 ^{1}H NMR spectrum resulting from the treatment of cluster **2** with 1 equiv of Na_2(Per) followed by addition of slight excess of TfOH. Solution (d) from **Figure 3.10** was pumped down and the resulting material dissolved in MeCN-*d*$_3$ to obtain this spectrum.

3.3.2 Dinitrogen-Relevant-Substrate Activation Efforts with Fe_4Mo_2

In an effort to study biologically relevant catalytic activity with the Fe_4Mo_2 cluster, reactivity studies were explored with hydrazine ($H_2N–NH_2$) and diazene (HN=NH) substrates. This was predicated on the generalized observation that enzymes decrease the

kinetic barrier of catalyzed reactions in *both* the forward and reverse directions. Thus, we were interested in probing for substrate binding to the cluster and subsequent oxidation or reduction in the presence of an oxidizing (Fc^+) or reducing agent (KC_8). Treatment of **4** with either 1 equiv or an excess of hydrazine exhibited no change to the IR spectral features of **4**. The N–N stretching frequency of hydrazine (free N_2H_4 at ν_{N-N} = 1602 cm^{-1}) also remains unchanged. Continuing on to diazene activation, we sought to generate the gaseous substrate *in situ* to bubble through a solution of cluster **4** in DCE. A method for this experiment was developed based on a previously reported procedure by Seefeldt *et al.* (**Scheme 3.7**), whereby azodicarbonamide (adca) undergoes hydrolysis to afford diazene dicarboxylate (dadc). Addition of aqueous dadc solution into phosphate buffer (pH 6–8) immediately effervesces diazene (N_2H_2) and CO_2. However, treatment of **4** with diazene in the presence or absence of either $Fc(PF_6)$ or KC_8 exhibited no significant shifts in the IR spectrum.

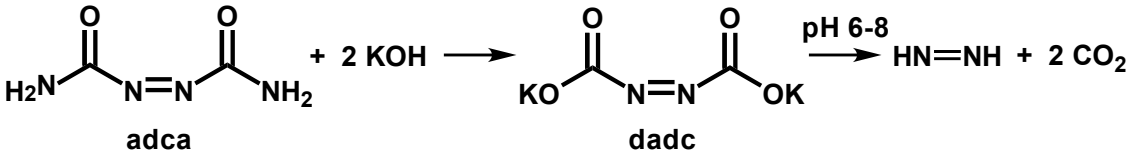

Scheme 3.7 Schematic pathway of *in situ* diazene generation from azodicarbonamide.

3.4 CONCLUSIONS

In summary, we have structurally characterized two K-crown supported, carbide-based heterometalloclusters (**2** and **4**) which exhibit molybdenum-carbide motifs and five or four iron-carbide bonds. The accessible reduction potential of **2** allows for activation

with sodium perylinide and protonation to afford the corresponding cluster−hydride species; this provides enhanced selectivity in the reduction of DPA to the *cis*-alkene product. However, activation efforts of dinitrogen and related substrates (diazene and hydrazine) were unsuccessful. Regarding structural metrics, the Mo···Fe distances found in **2** and **4** (2.77−3.05 Å) are slightly longer than those found in the FeMoco cluster (~2.7 Å), thus providing an interesting comparison to the carbide−sulfide supported FeMoco cluster in nitrogenase. However, more synthetic work is needed to address the substitution of terminal and bridging CO units to biologically relevant, sulfur-based supports (sulfides, thiolates, and thioethers).

3.5 Experimental Procedures

3.5.1 Solvents and Reagents

Fluorobenzene (Oakwood Chemical), *n*-octane (Sigma Aldrich), and 1,2-dichloroethane (Fisher Scientific) were dried by distillation over molecular sieves and underwent three freeze-pump-thaw cycles prior to use. All other solvents were purchased from EMD, Fisher, Macron or J.T. Baker, and dried through an alumina column system (Pure Process Technology). Deuterated solvents (THF-d_8 and MeCN-d_3) were purchased from Cambridge Isotopes and used as received. [$Fe_5(\mu_5\text{-}C)(CO)_{15}$] and [$Fe_4(\mu_4\text{-}C)(CO)_{13}$] were prepared as described in Chapter 2. Potassium metal (Alfa Aesar), graphite (Acros Organics) molybdenum hexacarbonyl ($Mo(CO)_6$, Acros Organics), cycloheptatriene (Matrix Scientific), benzo-18-crown-6 (Acros Organics), diphenylacetylene (Acros Organics) and azodicarbonamide (Anslyn Group) were used as received.

3.5.2 Synthetic Procedures

Potassium graphite (KC_8) In an argon-atmosphere glovebox, graphite powder (2.4190 g, 201.4 mmol) and potassium chunks (0.9843 g, 25.18 mmol) were added into a 100-mL air-tight pressure vessel (*without* magnetic stir bar) such that the potassium chunks sat atop the graphite powder. The pressure vessel was pumped out and heated over sand bath to 200 °C overnight. The vessel was brought back into the glovebox and the contents pulverized and mixed using a sturdy, stainless steel spatula. The vessel was again pumped out, heated over sand bath, and the process repeated until all the potassium was consumed and only a homogenous bronze powder remained. The powder was stored in the pressure vessel until further use.

[K(benzo-18-crown-6)]$_2$[Fe$_5$(μ_5-C)(CO)$_{12}$(μ_2-CO)$_2$] (1) Under an argon box atmosphere, a vial charged with a solution of [Fe$_5$(μ_5-C)(CO)$_{15}$] (238.2 mg, 0.3348 mmol) in THF (10 mL) was brought down to –20 °C. To this solution, solid KC_8 (94.0 mg, 0.695 mmol) was added, and the solution stirred for 8 h at room temperature. The resulting solution was passed through a pipette filter packed with Celite (1–2 cm height) to remove graphite, and solid benzo-18-crown-6 (209.2 mg, 0.6697 mmol) was stirred into the filtrate. The solvent was removed *in vacuo*, and the resulting dark-brown oil was washed with pentane then Et_2O. The oil was then extracted into fluorobenzene and slowly layered with Et_2O at –20 °C by vapor diffusion through pierced caps to afford black crystals. Crystals suitable for XRD are grown by vapor diffusion of Et_2O into a 1,2-DCE solution of compound. Yield: 315.8 mg (68%). Selected IR peaks (**Figure 3.12**), solid, ν(CO): 2030(w), 1926(s), 1884(s), 1751(m) cm^{-1}. $^{13}C\{^1H\}$ NMR (100.5 MHz, THF-d_8): interstitial carbide peak at δ 478.8 ppm. Anal. Calcd. for $C_{47}H_{48}O_{26}Fe_5K_2$: C, 40.72; H, 3.49. Found: C, 40.75; H, 3.51.

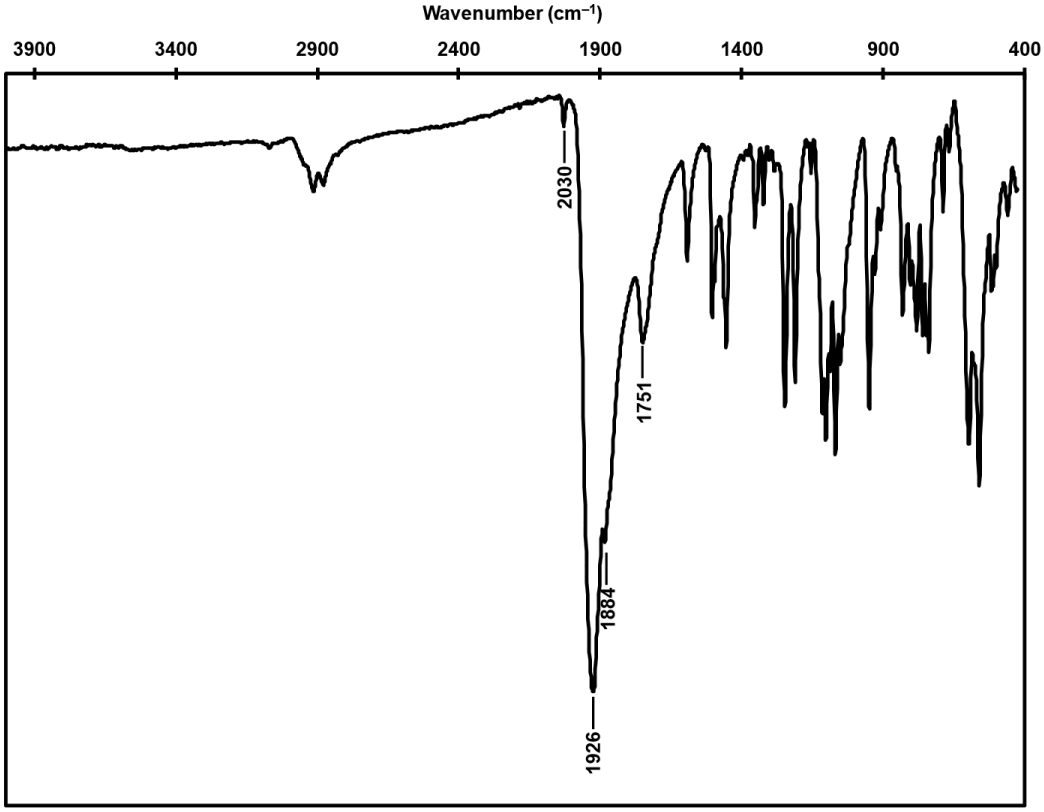

Figure 3.12 IR spectrum of $[K(benzo\text{-}18\text{-}crown\text{-}6)]_2[Fe_5(\mu_5\text{-}C)(CO)_{12}(\mu_2\text{-}CO)_2]$ (**1**) in the solid state.

$Mo(CO)_3(chpt)_3$ In an argon-atmosphere glovebox, a 100-mL Schlenk flask was charged with $Mo(CO)_6$ (2.5 g, 9.43 mmol) and cycloheptatriene (1.7 g, 19.21 mmol) suspended in 10 mL *n*-octane. The flask was then capped with a rubber septum, pumped out of the glovebox, affixed to a Schlenk line under N_2 atmosphere, and equipped with a reflux condenser and gas adapter. The solution was vigorously stirred, slowly heated to 150 °C, and allowed to react for 4 h. *Note*: $Mo(CO)_6$ sublimes at increased temperatures. In order to avoid loss of starting reagent, compressed air was passed across the neck of the Schlenk flask (**Figure 3.13**), and any deposited $Mo(CO)_6$ was knocked back into solution every hour using a stainless steel spatula. After 4 h, the air stream was removed, and

$Mo(CO)_6$ was allowed to deposit into the reflux condenser. The reaction flask was cooled, and the contents were transferred into a small Soxhlet extractor and extracted into 25 mL of pentane. The volatiles (pentane and *n*-octane) were removed *in vacuo*, affording 489.1 mg (19% yield) of bright red crystalline solid. Selected IR peaks (**Figure 3.14**), solid, ν(CO): 1963(m), 1890(s,sh), 1841(s) cm^{-1}.

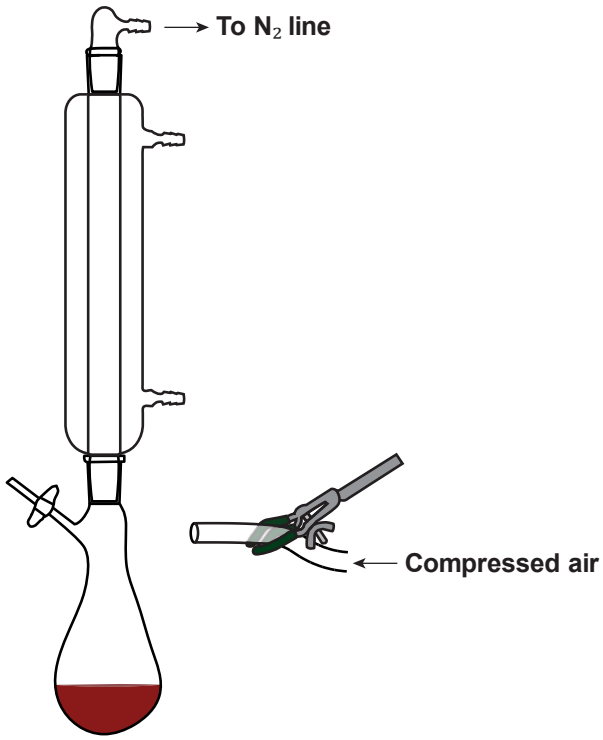

Figure 3.13 Apparatus set-up for synthesis of $Mo(CO)_3(chpt)_3$.

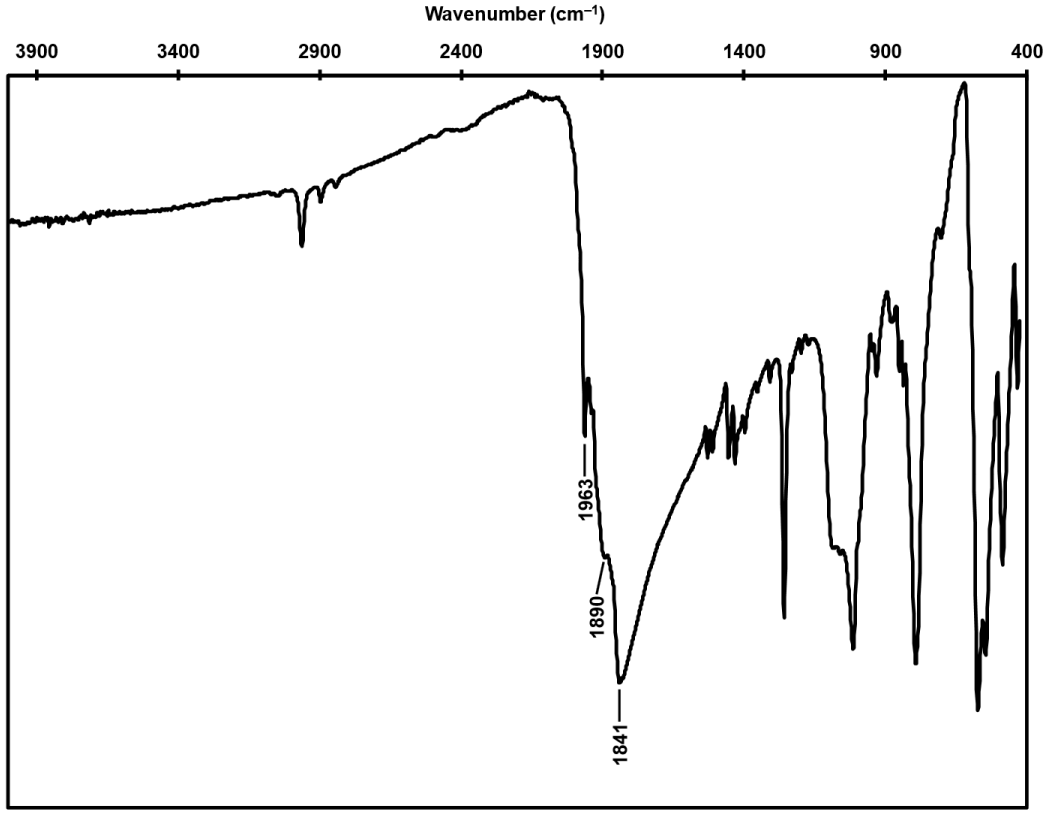

Figure 3.14 IR spectrum of $Mo(CO)_3(chpt)_3$ in the solid state.

[K(benzo-18-crown-6)]$_2$[Fe$_5$Mo(μ_6-C)(CO)$_{14}$(μ_2-CO)$_3$] (2) Under an argon box atmosphere, a vial containing a solution of [Fe$_5$(μ_5-C)(CO)$_{15}$] (99.6 mg, 0.140 mmol) in THF (7 mL) was brought down to –20 °C. To this solution, solid KC_8 (41.5 mg, 0.307 mmol) was added and the solution stirred for 8 h at room temperature. Solid $Mo(chpt)(CO)_3$ (39.7 mg, 0.146 mmol) and benzo-18-crown-6 (95.3 mg, 0.305 mmol) were added into the reaction solution, and the solution was stirred overnight. The solution was then passed through a Celite pipette filter (1–2 cm) and dried under reduced pressure. The resulting dark-brown oil was washed with pentane and Et_2O and subsequently brought under vacuum to afford a black solid. Yield: 173.1 mg (79%). X-ray quality crystals were grown by slow vapor diffusion of Et_2O into a fluorobenzene solution of the product through

pierced caps at –20 °C. Selected IR peaks (**Figure 3.15**), solid, ν(CO): 2035(w), 1943(s), 1866(s), 1788(m) cm^{-1}. Anal. Calcd. for $C_{62}H_{58}O_{29}Fe_5Mo_{0.78}K_2$: C, 42.86; H, 3.36. Found: C, 41.10; H, 3.39.

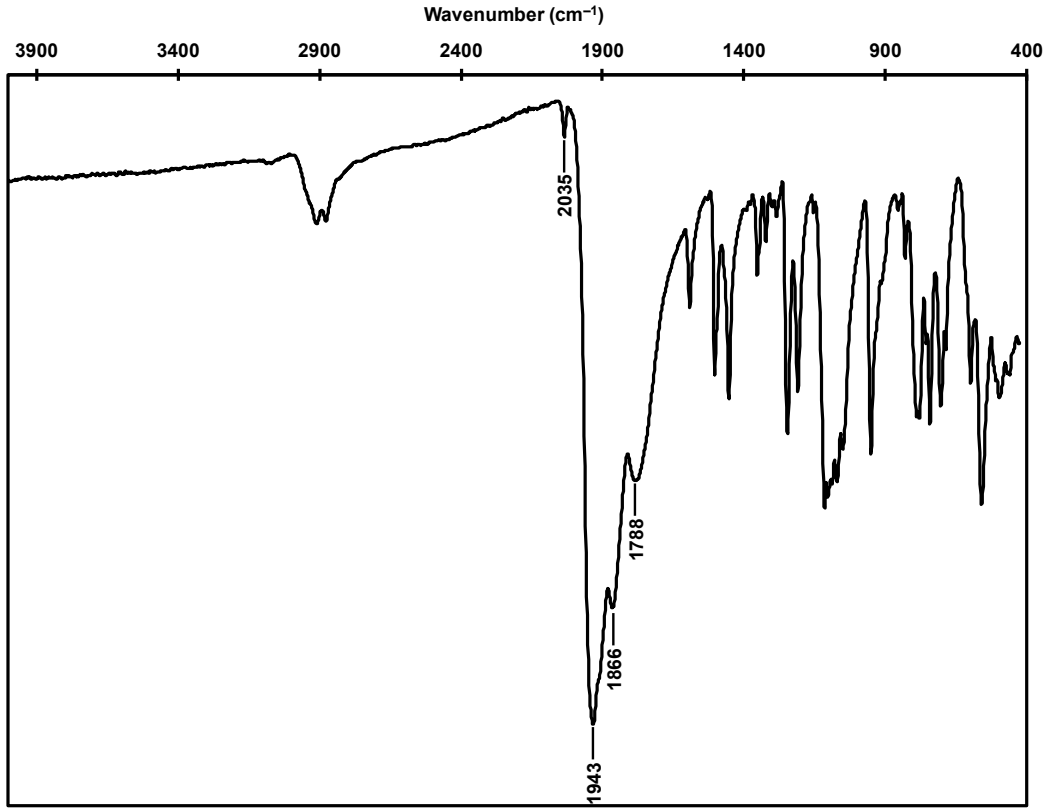

Figure 3.15 IR spectrum of $[K(benzo\text{-}18\text{-}crown\text{-}6)]_2[Fe_5Mo(\mu_6\text{-}C)(CO)_{14}(\mu_2\text{-}CO)_3]$ (**2**) in the solid state.

$[K(benzo\text{-}18\text{-}crown\text{-}6)]_2[Fe_4(\mu_4\text{-}C)(CO)_{12}]$ (3) In a glovebox under an argon atmosphere, a vial containing a solution of $[Fe_4(\mu_4\text{-}C)(CO)_{13}]$ (98.0 mg, 0.164 mmol) in THF (10 mL) was cooled to –20 °C. To this solution, solid KC_8 (46.6 mg, 0.367 mmol) was added, and the solution was stirred for 8 h at room temperature. A portion of solid benzo-18-crown-6 (120.1 mg, 0.3845 mmol) was added into the reaction, and the solution was stirred for 1 h. The solution was filtered through Celite, and the filtrate was evaporated

to afford dark-brown oil. After washing with Et_2O, the product was extracted into FPh and then dried under reduced pressure to afford a black semi-solid. X-ray quality crystals were grown by vapor diffusion of Et_2O into a fluorobenzene solution of the product through pierced caps at –20 °C. Yield: 129.7 mg (62%). Selected IR peaks (**Figure 3.16**), solid, ν(CO): 2026(w), 1962(m,sh), 1930(s), 1907 cm–1. $^{13}C\{^1H\}$ NMR (125.8 MHz, MeCN-d_3): interstitial carbide at δ 478.6 ppm. Anal. calcd. for $C_{45}H_{48}O_{24}Fe_4K_2$: C, 42.41; H, 3.80. Found: C, 39.88; H, 4.21.

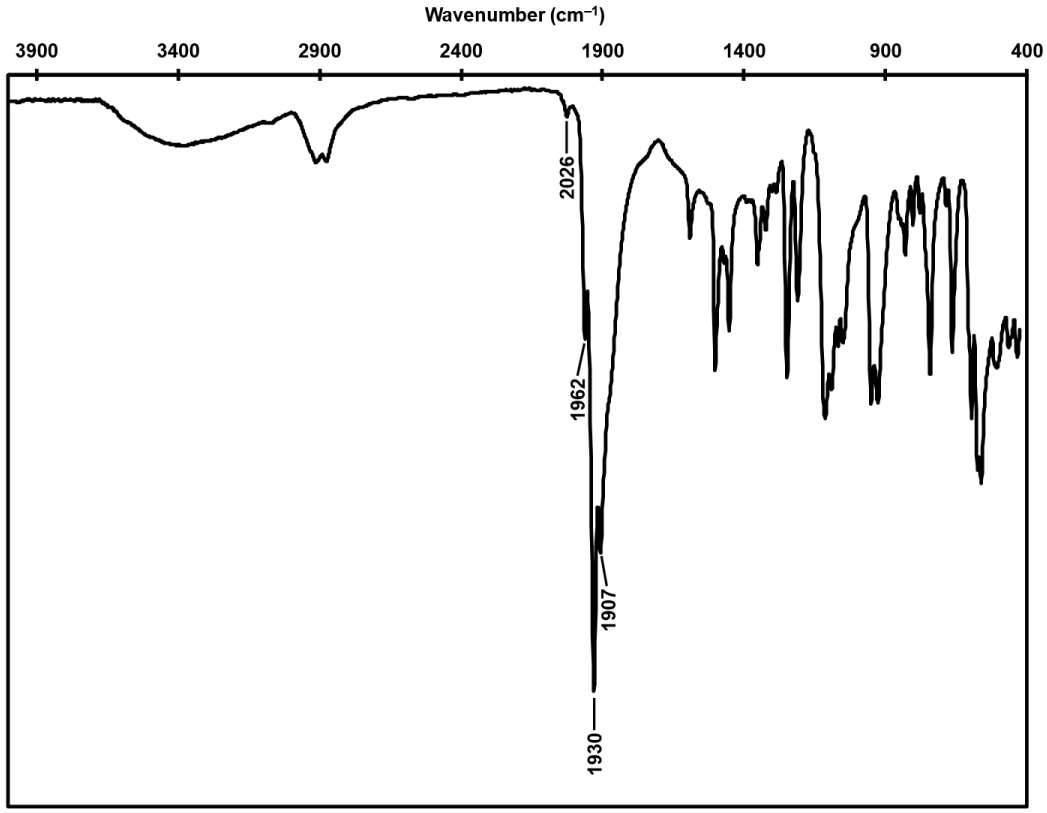

Figure 3.16 IR spectrum of $[K(benzo\text{-}18\text{-}crown\text{-}6)]_2[Fe_4(\mu_4\text{-}C)(CO)_{12}]$ (**3**) in the solid state.

$[K(benzo\text{-}18\text{-}crown\text{-}6)]_2[Fe_4Mo_2(\mu_6\text{-}C)(CO)_{16}(\mu_2\text{-}CO)_2]$ (4) Under an argon box atmosphere, solid $Mo(chpt)(CO)_3$ (111.3 mg, 0.4090 mmol) was added into a pressure tube

charged with [K(benzo-18-crown-6)]$_2$[Fe$_4$(μ_4-C)(CO)$_{12}$] (101.1 mg, 0.0793 mmol) in 1,2-dichloroethane (5 mL) and the solution was stirred for 8 h at 80 °C. The solution was then passed through a Celite filter and dried under reduced pressure. The resulting dark-brown oil was washed with pentane and Et2O and subsequently recrystallized by vapor diffusion of pentane into a DCE solution of the product. X-ray quality crystals were grown by vapor diffusion of Et$_2$O into a 1:1 DCE/FPh solution of the product at –20 °C. Yield: 83.0 mg (64%). Selected IR peaks (**Figure 3.17**), solid, ν(CO): 2038(w), 1937(s, sh), 1923(s), 1828(s) cm^{-1}. ^{13}C{^{1}H} NMR (125.8 MHz, MeCN-d_3): interstitial carbide at δ 473.4 ppm. Anal. calcd. for $C_{51}H_{48}O_{30}Fe_4Mo_2K_2$: C, 37.48; H, 2.96. Found: C, 36.20; H, 3.48.

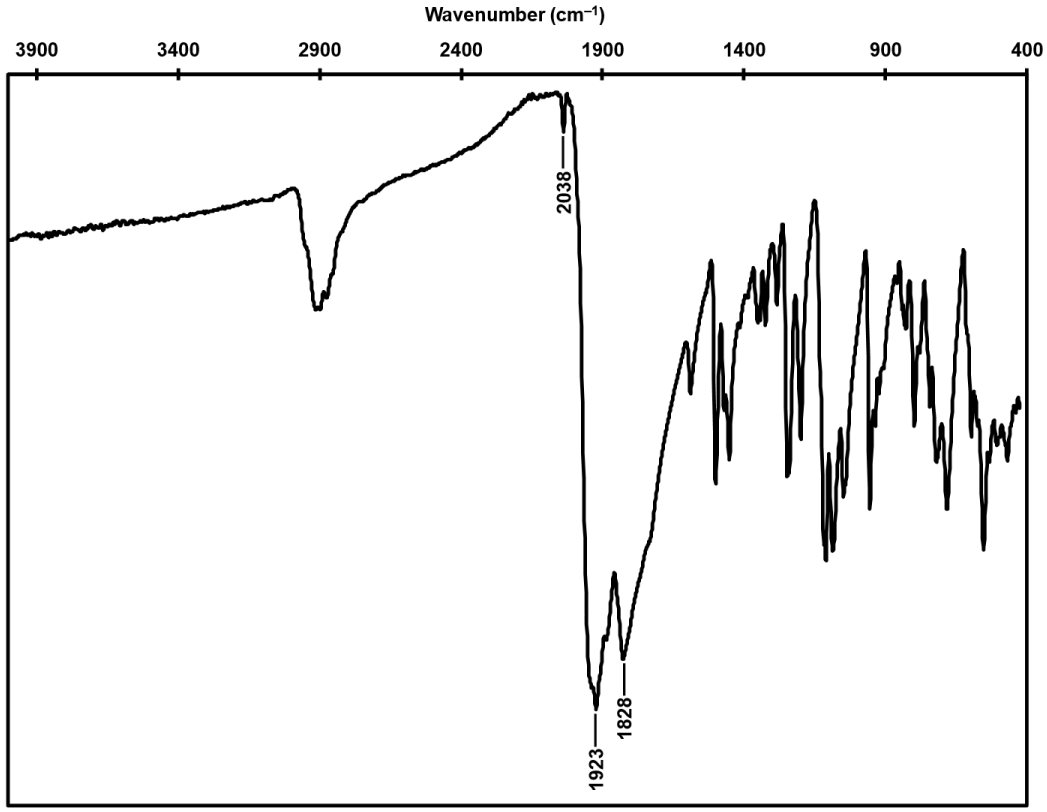

Figure 3.17 IR spectrum of [K(benzo-18-crown-6)]$_2$[Fe$_4$Mo$_2$(μ_6-C)(CO)$_{16}$(μ_2-CO)$_2$] (**4**) in the solid state.

Diphenylacetylene Reduction. KC_8 reactions. Under an argon box atmosphere, the catalytic cluster (0.016 mmol), KC_8 (30 equiv.), diphenylacetylene (15 equiv), and the proton source (30 equiv) were dissolved into 7 mL of THF. The resulting mixture was allowed to stir for 20 h, centrifuged for 10 min, and the supernatant filtered through a pipette packed with Celite to remove graphite. The filtrate was subjected to GCMS to determine relative ratios of DPA to *cis*-DPE, *trans*-DPE, and DPEthane as described below.

GCMS analysis was conducted on a Trace 2000 Series GC instrument equipped an Agilent J&W DB-WAXetr capillary column (30 m × 0.25 mm) coupled with a Finnigan Trace MS instrument using EI ionization method. A 1.0 μL aliquot of the diluted sample was injected into the GC at an initial temperature of 40 °C, which was held for 1.00 min and ramped up by 15 °C/min until a final temperature of 240 °C was reached and held for 3.00 min. Retention times of DPEthane, *cis*-DPE, DPA, and *trans*-DPE were 12.25, 12.45, 14.24, and 14.78 min, respectively.

Diphenylacetylene Reduction. Na_2(Per) reactions. Under an argon box atmosphere, sodium (11.5 mg, 0.500 mmol) was stirred into a 5 mL THF solution of perylene (63.1 mg, 0.251 mmol) at –20 °C and allowed to stir for 4 hours at room temperature. The resulting dark purple solution was added into a concentrated THF solution of the catalytic cluster (0.016 mmol), diphenylacetylene (15 equiv), and the proton source (30 equiv). The resulting mixture was allowed to stir for 20 h and the resulting solution subjected to GCMS as described in the above KC_8 procedure.

***In situ* Generation of Diazene.** On a ventilated fume hood open to air, a solid portion of azodicarbonamide (adca, 400 mg, 3.45 mmol) was added into an aqueous KOH solution (8 g, 16 mL, 9 M) and stirred for 10 min, resulting in a bright yellow solution. Ethanol (100 mL) was added directly into the aqueous solution, and the diazene

dicarboxylate (dadc) precipitated out as a yellow solid. The solid was collected *via* vacuum filtration, washed with 1:1 EtOH:Et_2O, and dried for 5 minutes on the filter. The experimental apparatus depicted in **Figure 3.18** was set up using (1) a degassed 80 mM phosphate buffer (0.3599 g Na_2HPO_4, 0.4259 g NaH_2PO_4, 30 mL water) in a 100-mL 3-neck round bottom flask equipped with a rubber septum, a gas adapter with stopcock, and an open gas adapter; and (2) a solution of the cluster under evaluation in a 25-mL Schlenk flask equipped with a gas bubbler connected to the 3-neck flask by a short length of vacuum tubing. The dadc was dissolved into aqueous KOH solution (30 mg in 5 mL), drawn into a syringe, and delivered *dropwise* into the phosphate buffer, resulting in immediate effervescence. The gaseous diazene/carbon dioxide mixture was directed through the cluster solution and into the Schlenk line.

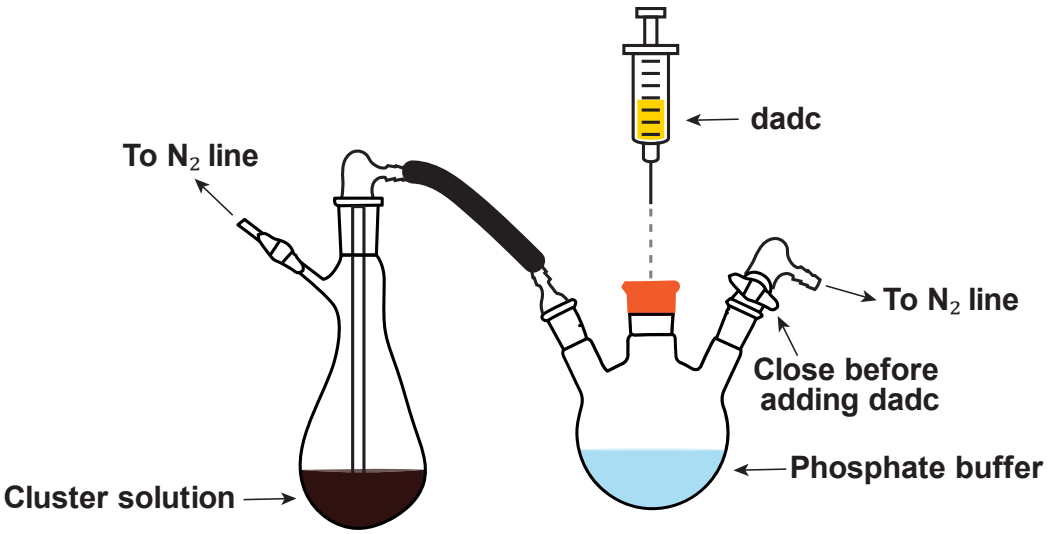

Figure 3.18 Apparatus set-up for *in situ* generation of diazene.

Chapter 4: Ligand Substitution by Electrophilic Sulfur as a Synthetic Pathway Towards Inorganic Carbide- and Sulfide-Containing Iron Clusters

4.1 Introduction

Over the past two decades, the structural complexity of the iron-sulfide-carbide cluster found in the various nitrogenases has inspired many avenues of biomimetic modeling research. However, the chemical synthesis of a synthetic cluster exhibiting concomitant assembly of ferrous/ferric sites, sulfides, and an interstitial and purely inorganic carbide has to date remained elusive. Nonetheless, an array of synthetic models intended to emulate the ligation sphere of the cluster iron sites have been developed. Peters has reported an elegant series of iron complexes bearing ligands featuring chelating phosphines either anchored by an organic carbanion,[65] or bridged by an organic thiolate.[66] Relatedly, Holland has reported structures derived from sulfur-containing thiolate[69,152] and sulfide ligands.[153,154] An incredibly thorough and long-standing research program by Tatsumi has yielded highly complex iron-sulfur structures embodying multiple nuclearities,[74,155,156] including structures bearing an interstitial sulfide as found in the nitrogenase P-cluster[157,158] and another containing an interstitial oxide.[75] In a similar vein, the Holm group reported an iron-sulfur cluster that incorporates a silyl-nitride into the cluster core.[159] Two reports from our group demonstrated a series of interconversions between Fe_2S_2 and Fe_3S clusters in preliminary work[109,160] for modeling carbon atom insertion as seen in FeMoco biogenesis,[24,25] although ultimately carbide insertion proved unsuccessful.

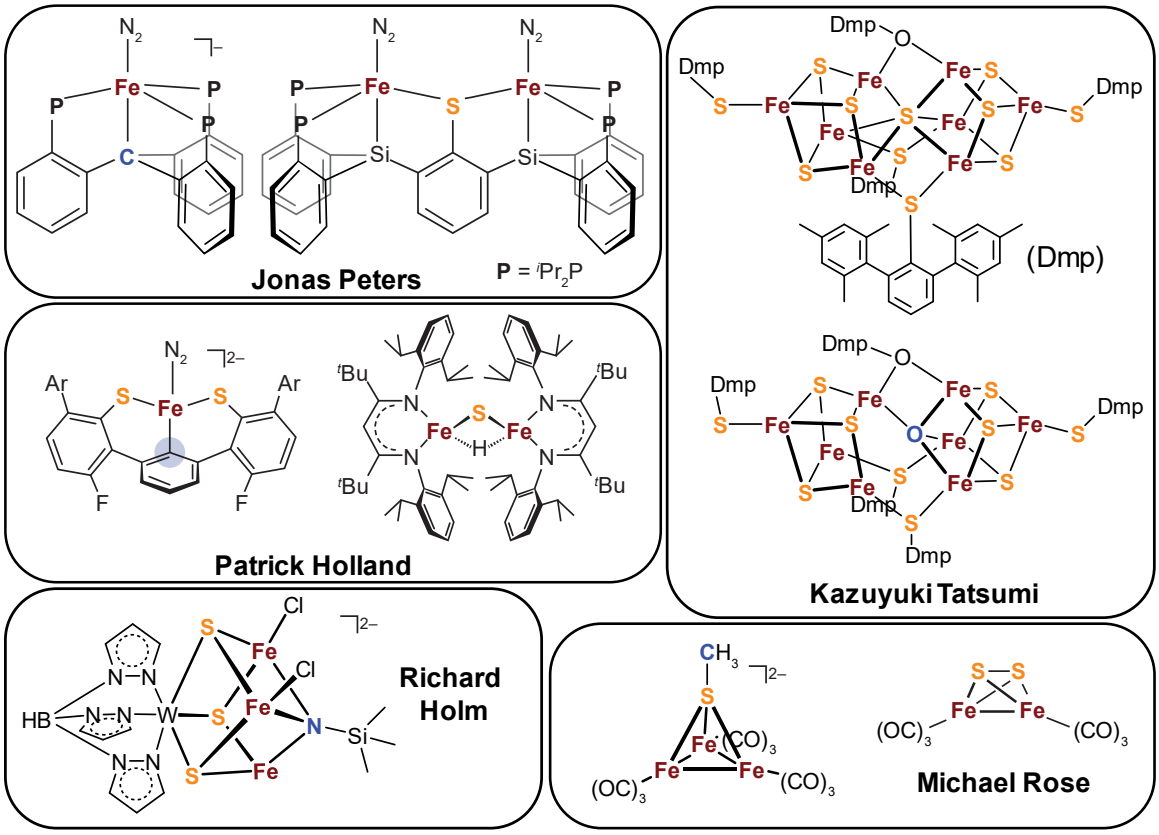

Scheme 4.1 Representative synthetic model compounds from literature incorporating iron centers, sulfides or sulfur-bearing ligands, and light 2*p* atom donor.

Despite this remarkable progress in understanding the synthetic, structural and functional aspects of iron, sulfur and carbon motifs, the synthetic challenge of incorporating both the biomimetic interstitial carbide and inorganic sulfide has proven difficult. A recent report by Rauchfuss provided the first example of a synthetic cluster incorporating both these motifs in a multi-iron construct *via* a multi-step synthetic pathway utilizing $[Fe_6(\mu_6\text{-}C)(CO)_{16}]^{2-}$ as a precursor.[76] And while past literature regarding these clusters has reported limited transformations upon the cluster core (see Chapter 3); this family of iron clusters has proven difficult to control during ligand substitution. Direct substitution of CO has only been achieved with phosphines or ligands with electropositive

donor atoms like NO, SO_2, and various gold phosphines.[30,135,161,162] In fact, the sulfide in the Rauchfuss structure arises from a three-step removal of oxides from the SO_2-ligated structure first reported by Shriver (**Scheme 4.2**).[162] Relatedly, iron clusters with an interstitial nitride appear to demonstrate a similar recalcitrance towards controlled substitution. A notable recent addition to this field is the ligation of isocyanide groups to a nitride cluster as reported by Figueroa.[163]

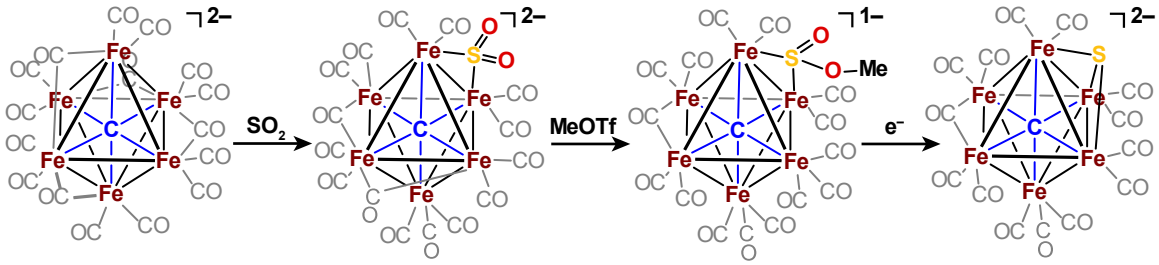

Scheme 4.2 Multi-step synthetic pathway reported by Rauchfuss *et al.* to generate the iron-sulfido-carbide cluster: $[Fe_6(\mu_6\text{-}C)(\mu_3\text{-}S)(CO)_{14}]^{2-}$.

The work presented in this chapter relates the first report of direct CO→sulfide substitution upon an iron-carbide-carbonyl cluster, namely the hexanuclear $(NEt_4)_2[Fe_6(\mu_6\text{-}C)(CO)_{16}]$ described in Chapter 2. Treatment of this cluster (and its relatives) with electropositive (S_2Cl_2) or neutral (S_8) sulfur reagents leads to cluster oxidation, CO loss, and binding of inorganic sulfide motifs. Overall, these reactions provide synthetic routes to afford two pairs of thematically similar sulfide- and carbide-containing structures: (*i*) one pair of charged, dianionic clusters featuring a bridging μ_4-S in which the all-Fe coordination environment encompassing the carbide is preserved and (*ii*) another pair of neutral clusters, each featuring multiple sulfur sites, a 'dangler' (and potentially ferrous) iron site, and a remarkable and biomimetically relevant $\{CS\}^{4-}$ motif. The electronic structures of these compounds are explored computationally by DFT methods and

spectroscopically by X-ray photoelectron spectroscopy, revealing Fe sites that are of generally higher oxidation states (relative to carbonyl-only clusters) and may even indicate the presence of a ferrous dangler Fe site in the multi-sulfide cluster.

4.2 Initial Ligand Substitution Attempts

While transformations conducted upon the multinuclear core (*i.e.* oxidative removal of Fe site, heterometal incorporation) were relatively facile, the carbidocarbonyl clusters demonstrated either no reaction or undesirable conversions and decompositions in the presence of conventional inorganic ligands. Our initial foray into ligand substitution reactions began with utilization of a bidentate, anthracene-scaffolded bis-phenylthiolate ligand set (**Scheme 4.3**). The choice of the anthracene scaffold was motivated by the observation that the 5.1 Å distance between the 1 and 8 positions on the anthracene backbone closely correlated with the 5.0 Å S•••S distance between distal sulfide sites in FeMoco. However, treatment of $[Fe_6]^{2-}$ with disodium 1,8-bis(phenylthiolato) anthracene does not induce any color change in the reaction mixture. In 2015, Figueroa *et al.* reported on isocyanide analogues of iron carbonyls, noting that isocyanides — similar to carbonyls — act as excellent π-acceptors, but additionally exhibit stronger σ-donating ability relative to carbon monoxide, increasing the reactivity of their host metal towards substrates including N_2.[164] Following this line of research, $[Fe_6]^{2-}$ was treated with 2,6-dimethylphenyl isocyanide, resulting in a reaction solution dominated by a dark green color — indicative of decomposition to $Fe_3(CO)_{12}$ — and an unknown white, feathery precipitate.

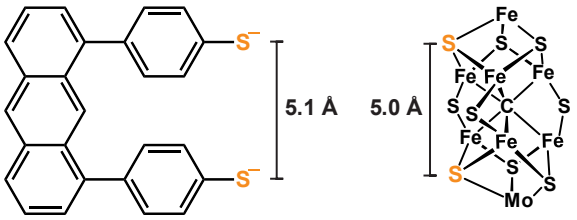

Scheme 4.3 S•••S distances between the 1 and 8 positions on an anthracene scaffold (*left*) and the distal sulfides in FeMoco (*right*).

Another effort to incorporate sulfur into carbidocarbonyl iron cluster was in the direct reaction of $[Fe_5]^0$ with ½ equiv of elemental sulfur (S_8) in toluene, which was monitored at variable temperatures by chromatographic separation. Following addition of S_8 into a toluene solution containing $[Fe_5]^0$ at room temperature and 3 h of stirring, an aliquot of the reaction mixture was passed through a pipette packed with silica gel and eluted with hexanes, revealing a single, red-brown band (consistent with no conversion of the five-iron cluster). Performing the same reaction at 60 °C results in the formation of a small amount of an insoluble and ferromagnetic black powder (presumably metallic iron) that does not elute and the unconverted $[Fe_5]^0$ band. Increasing the temperature to 90 °C significantly decomposes $[Fe_5]^0$ into the same black powder, and reaction at 120 °C results in total decomposition. Alternatively, a literature report found that elements from the pnictogen series could be reacted with $[Fe_5]^0$ in the presence of H_2SO_4 at 100 °C for 30 min to generate a tri-iron methylidene cluster with the formula $Fe_3(\mu_3\text{-}CH)E(CO)_9$ (E = As, Sb, Bi).[165] Elemental arsenic and bismuth were found to work for this reaction; interestingly, the Sb cluster could only be achieved with $SbCl_5$. Our efforts to replicate these conditions with elemental sulfur produced a dark red-orange solution, which was passed through silica column with hexanes and the isolated red solution was allowed to sit at –20 °C for several days, affording crystals of the non-carbide-containing cluster

$Fe_3S_2(CO)_9$. Similarly, using selenium powder under the same conditions gave crystals of $Fe_3Se_2(CO)_9$.

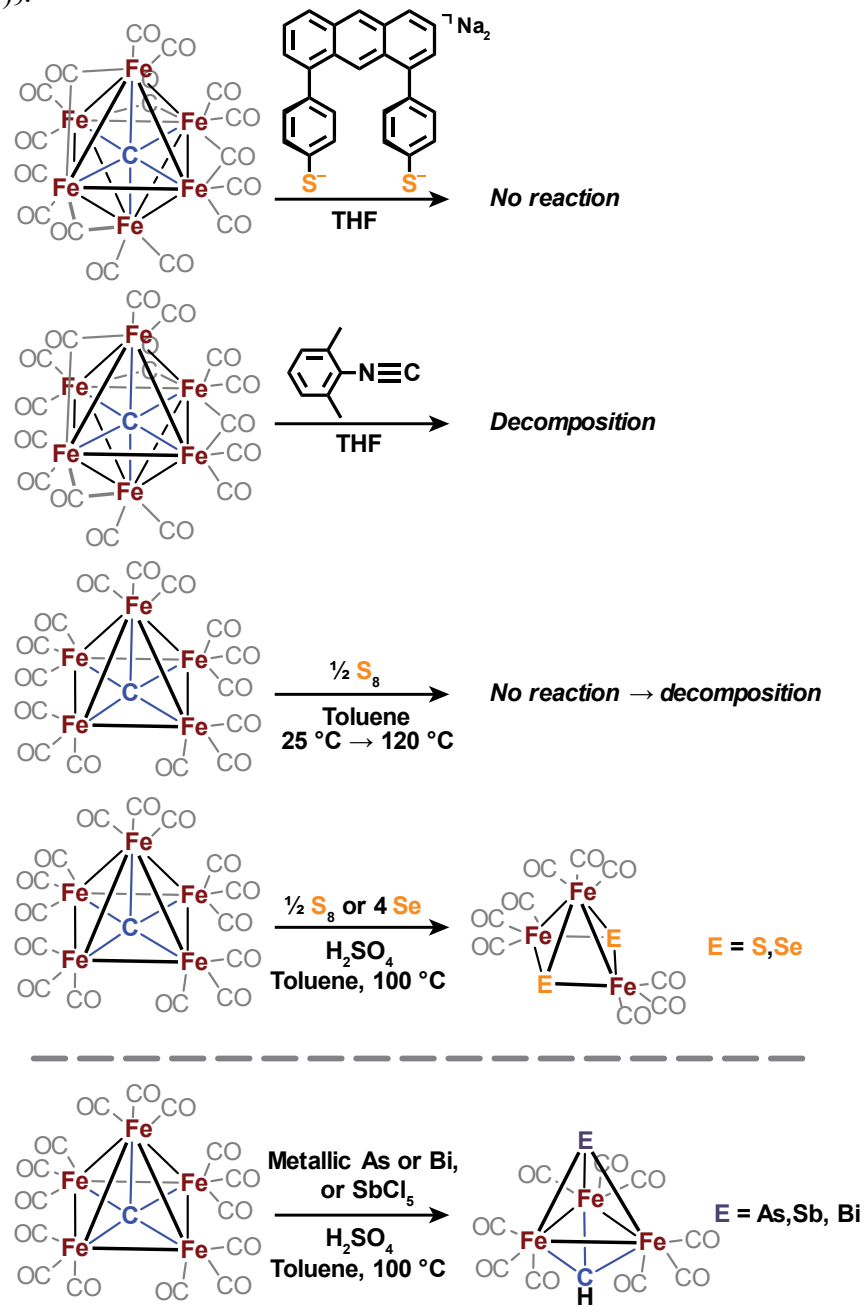

Scheme 4.4 Various reaction conditions attempted to pursue controlled ligand substitution onto iron carbide clusters (*top*) and schematic representation of reaction conditions reported in ref. [165] (*bottom*).

Finally, the utilization of triphenyl antimony sulfide ($Ph_3Sb{=}S$) as a thermoneutral sulfur atom donor was considered, due to its behavior as a weak sulfur-donating ability and the absence of S–S bonds such as those seen in elemental sulfur.[166] Preparation of the reagent for *in situ* use was achieved following literature procedures whereby triphenylanitmony ($SbPh_3$) was brominated with Br_2 to synthesize and isolate Ph_3SbBr_2. Subsequent heating of this compound at 80 °C in the presence of $S(SiMe_3)_2$ in toluene for 2 days provided a yellow solution nominally containing $Ph_3Sb{=}S$ (and Me_3SiBr). The solution was cooled to room temperature and transferred *via* cannula into a stirring toluene suspension of $[Fe_6]^{2-}$ cooled over a water-ice bath and allowed to warm up to room temperature overnight (**Scheme 4.5**). After removing the solvent *in vacuo*, the resulting tar-like semi-solid was extracted into pentane. The initial pentane extractions provided a dark-red solution. After these initial washes, a slight but persistent amber color was continually obtained and separated from the initial dark-colored extractions. Despite not achieving colorless washes, Et_2O extractions were performed and behaved similarly to the extractions in pentane (initially a few dark red extractions followed by persistently light-red extractions). Finally, extraction into fluorobenzene again provided a dark red color in its extractions.

This series of extractions from nonpolar to progressively polar (in order: pentane, Et_2O, FPh, THF, DCE, MeCN) solvents — sometimes colloquially referred to in the Rose group as an "inorganic column" — is generally a successful separation strategy for purification of both neutral and charged products from iron cluster reactions. However, the tar-like composition of the crude solid and the persistently colored washes are indicative of residual reaction solvent (in this case toluene) convoluting the solubility behavior of compounds in the mixture. A viable purification strategy to rectify this would be to suspend the crude mixture in Et_2O (prior to any extraction procedure), mechanically remove and

solid adhered to the flask, and stir for several hours. After stirring, hexanes (or an alternative higher-boiling, nonpolar solvent) may be added into the suspension, and all solvents removed *in vacuo*. If a powdered solid is obtained, the "inorganic column" can be conducted and the solubilities of each layer will assuredly be representative of the genuine solubility of the compounds in that layer. However, the utilization of this trituration technique prior to extraction was unfortunately not utililed in this reaction. This led to a mixture of products in each layer, which obstructed the growth of crystals suitable for X-ray diffraction. (A successful example of the purification and isolation of compounds from these complicated mixtures of iron clusters is outlined in Section 4.3.)

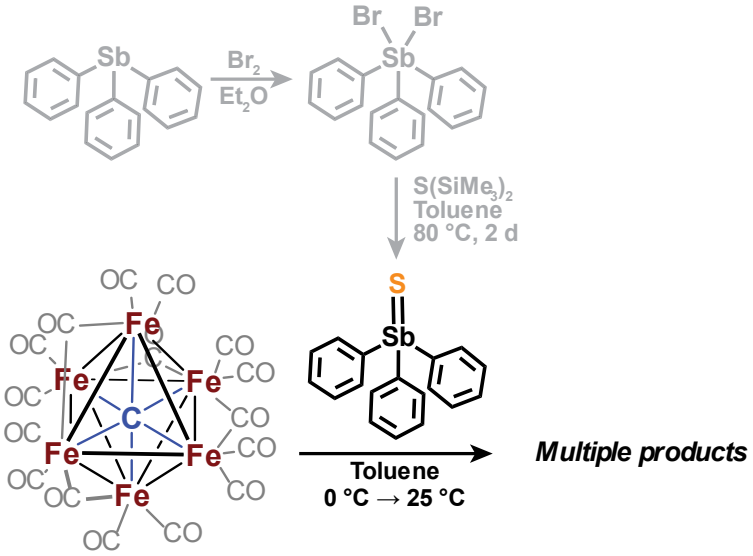

Scheme 4.5 *In situ* synthesis of triphenyl antimony sulfide and reaction conditions for sulfur donation into $[Fe_6]^{2-}$ cluster.

Nonetheless, the individual extractions described above were dried *in vacuo* and the solids characterized by IR spectroscopy (**Figure 4.1**). Both pentane layers as well as the concentrated Et_2O layer exhibited features at approximately 2021, 1993, and 1976 cm^{-1}.

However, the observed variation in relative peak intensities was indicative of the presence of multiple neutral compounds. These compounds may likely be separated by column chromatography and isolated as pure products. Additionally, the 1993 cm^{-1} and 1976 cm^{-1} bands do not correspond to any of the three neutral compounds described in Section 4.3 (all of which are *supra* 2002 cm^{-1}). The dilute Et_2O and concentrated FPh layers each exhibit a broad peak in the carbonyl stretching region, though the feature obtained from the Et_2O layer is considerably blue-shifted by 12 cm^{-1}, likely an artifact of averaging features from compounds that are genuinely Et_2O-soluble with those that display "faux" solubility in the absence of prior trituration. Similar to several peaks in the nonpolar layers, the 1949 cm^{-1} is red-shifted relative to the IR features of the compounds reported below.

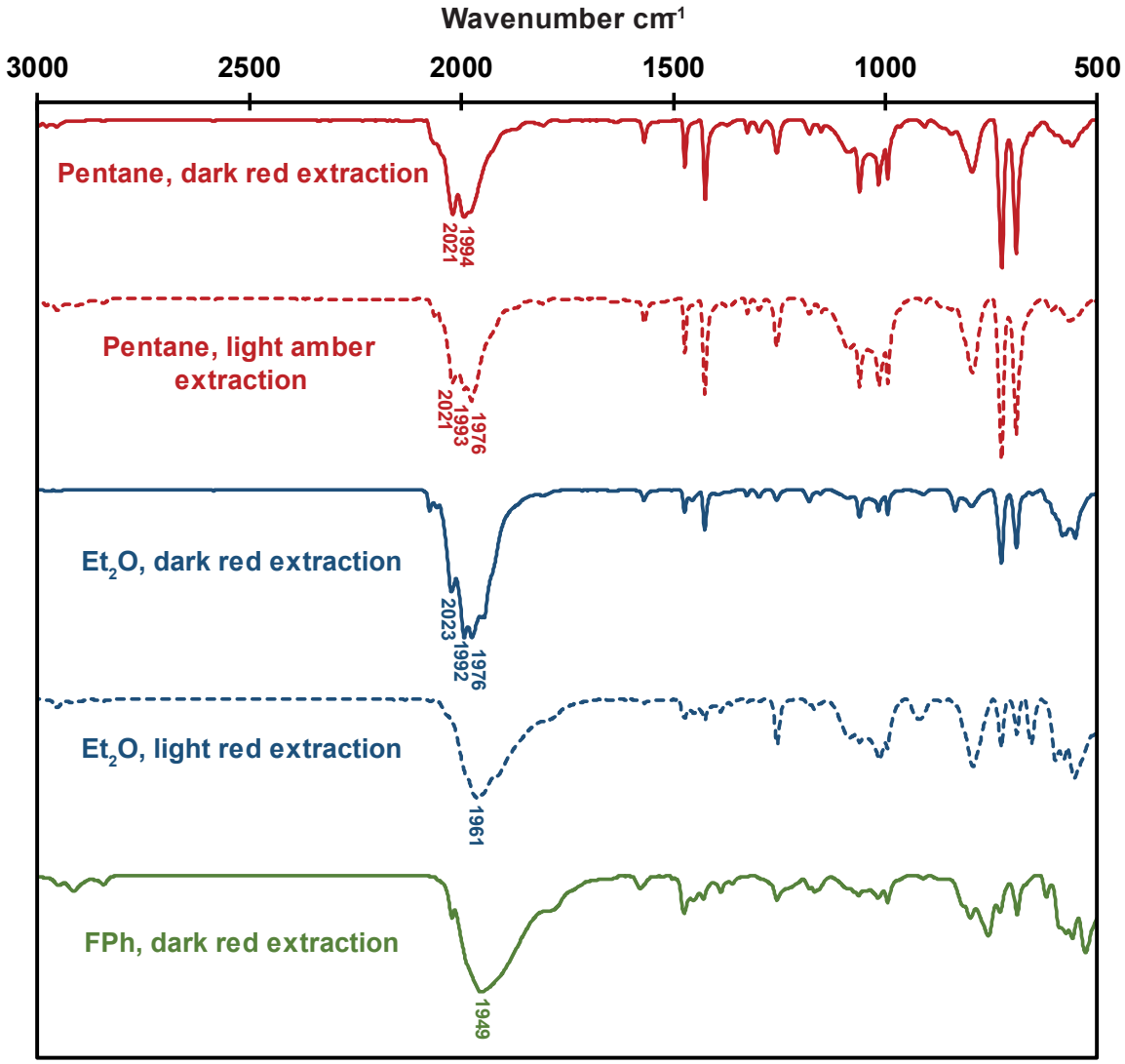

Figure 4.1 IR spectra for product mixtures obtained from various extractions collected from the reaction mixture of $[Fe_6]^{2-}$ and $Ph_3Sb{=}S$. Each extraction was dried *in vacuo* and the spectrum collected on the resultant solid.

4.3 Electrophillic Sulfur Sources: Isolation of Sulfide-Containing Carbidocabonyl Iron Clusters

Because of the undesirable results obtained from using conventional Lewis basic ligands with the anionic and neutral iron clusters, we sought an alternative strategy for achieving sulfide incorporation. At the time, the only report of successful ligation by a sulfur-based donation set upon carbidocarbonyl iron clusters was a 1988 publication by Shriver *et al.* describing the synthesis and isolation of SO_2-ligated Fe_6 and Fe_5 clusters.[162] However, the use of these SO_2 clusters as isolable intermediates in pursuit of ultimately a sulfide-ligated iron-carbide clusters was a suspected "dead-end" in the absence of a strategy for successful reduction and oxide removal from SO_2 (see **Scheme 4.2** for reported achievement of S-ligated cluster *via* an SO_2 intermediate reported by Rauchfuss *et al.* 2019). However, the observation that, upon ligation, SO_2 behaves electrophilically (therefore oxidizing the anionic cluster) — and the additional observation that the gallery of reported heteroleptic carbidocarbonyl iron clusters in the Cambridge Structural Database (CSD) feature initial oxidation prior to ligand incorporation (NO, $H^+ \rightarrow H^-$, Lewis acidic Cu- and Au-bearing reagents)[30] — prompted to us seek out similarly electrophilic sulfur-based ligand sets.

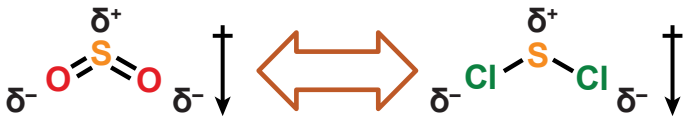

Scheme 4.6 Schematic indication of dipole in electropositive sulfur reagents.

As such, a synthetic strategy centered around S_2Cl_2 was deemed appropriate for sulfide incorporation. While SCl_2 is more structurally analogous to SO_2 (**Scheme 4.6**), the reported instability of the reagent and its spontaneous conversion to S_2Cl_2 marked it as less preferable. Treatment of the hexa-nuclear cluster $(NEt_4)_2[Fe_6(\mu_6\text{-}C)(CO)_{16}]$ with S_2Cl_2

afforded the asymmetric, sulfide-bridged 'dimer of clusters' $(NEt_4)_2\{[(CO)_{15}(\mu_6\text{-}C)Fe_6](\mu_4\text{-}S)[Fe_5(\mu_5\text{-}C)(CO)_{13}]\}$ (**5**), which features a four-coordinate bridging sulfide tethered between a six-iron and a five-iron cluster — each one with an interstitial carbide. Additionally, an attempt to replicate this reaction stoichiometrically using equimolar amounts of $(NEt_4)_2[Fe_6(\mu_6\text{-}C)(CO)_{16}]$, $[Fe_5(\mu_5\text{-}C)(CO)_{15}]$, and elemental sulfur produced the symmetric sulfide-bridged dimer $(NEt_4)_2\{[Fe_5(\mu_5\text{-}C)(CO)_{13}]_2(\mu_4\text{-}S)\}$ (**6**). Furthermore, efforts to characterize the full reaction product profile of both reactions afforded two sulfo(carbide)-containing clusters bearing biologically relevant sulfide (S^{2-}) ligands: First, the persulfide-containing cluster $[\{Fe_4(\kappa_2S\text{–}\kappa_4C)(CO)_{10}\}(\mu_3\text{-}S)(\mu_3\text{-}S_2)Fe(CO)_3]$ (**7**) was isolated in the reaction for **5**. Second and more notably, the multi-sulfide-containing cluster $[\{Fe_4(\kappa_2S\text{–}\kappa_4C)(CO)_{10}\}(\mu_3\text{-}S)_2Fe(CO)_3]$ (**8**) was isolated from the reaction for **6**. Clusters **7** and **8** each feature a remarkable inorganic (sulfo)carbide $\{C\text{–}S\}^{4-}$ motif, higher-valent Fe ions, multiple sulfur sites, and an ostensibly 'dangler' iron site.

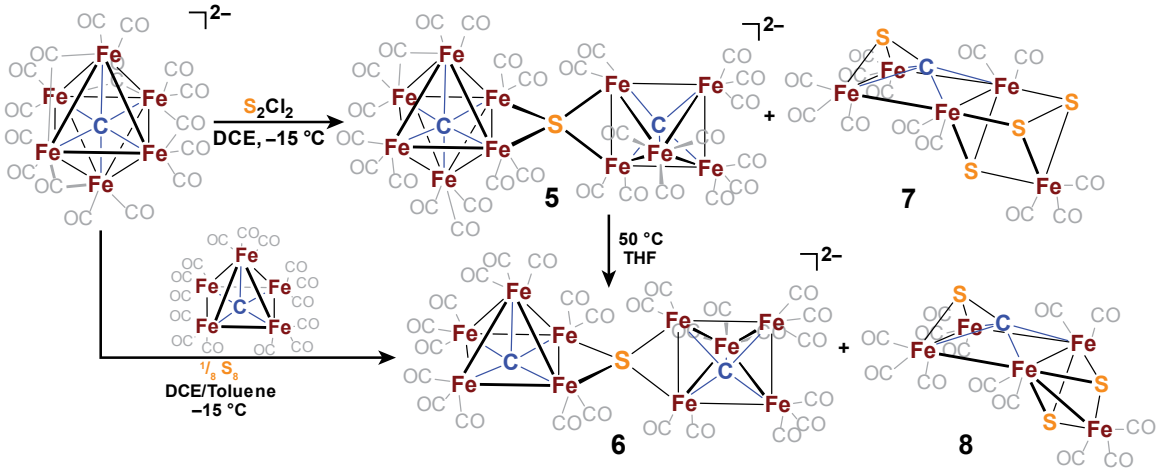

Scheme 4.7 Synthetic scheme depicting the electrophilic sulfurization of $[Fe_6]^{2-}$ to afford the charged μ_4-S clusters **5** and **6**, as well as the neutral $\{CS\}^{4-}$ clusters **7** and **8**. The non-carbide cluster $Fe_3S_2(CO)_9$ is generated as a side product in both reactions but has been omitted here. Cluster **5** can spontaneously be converted to **6** by heating at 50 °C.

4.3.1 Synthesis and Isolation of Charged, Sulfide-Bridged Dimers

To accomplish successful sulfurization of $(NEt_4)_2[Fe_6(\mu_6\text{-}C)(CO)_{16}]$, a violet solution of $[Fe_6]^{2-}$ was treated with 0.5 equiv S_2Cl_2 in 1,2-dichloroethane (DCE) at –15 °C and allowed to warm to room temperature. The resulting dark-red solution was dried *in vacuo* and the residue was triturated thoroughly with Et_2O/hexanes to afford a dry powder, which was subsequently washed with pentane then Et_2O. The remaining solid was extracted into fluorobenzene (FPh), and vapor diffusion of Et_2O provided dark red, single crystals suitable for X-ray diffraction. Initial diffraction data using Cu Kα radiation (λ = 1.54184 Å) exhibited adverse fluorescence from the Fe atoms that obscured high-angle data. Alternatively, data collected using a Mo Kα radiation (λ = 0.71073 Å) proved superior, identifying a $P\bar{1}$ unit cell and structure solution revealing a 'dimer of clusters' structure bridged by a 4-coordinate sulfide (**Figure 4.3**). The asymmetric cluster includes one 6-iron unit and one 5-iron unit, resulting in the formula $(NEt_4)_2\{[(CO)_{15}(\mu_6\text{-}C)Fe_6](\mu_4\text{-}S)[Fe_5(\mu_5\text{-}C)(CO)_{13}]\}$ (**5**). The IR spectrum of crystalline **5** (**Figure 4.2**) exhibits a single, broad peak in the CO region at 1973 cm^{-1}. However, the fluorobenzene-soluble mother liquor contained a significant amount of unconverted Fe_6 starting material, as evidenced by the presence of the bridging CO stretch at 1959 cm^{-1}. While mild heating (50 °C) did not provide full conversion, subsequent reactions with one full equiv of S_2Cl_2 (two S atoms per Fe_6 cluster) at –15 °C followed by IR analysis revealed full conversion of the Fe_6 starting material (no 1959 cm^{-1} feature). Crystallization of this material from FPh/Et_2O vapor diffusion and subsequent XRD data collection confirmed the isolation of **5** in higher yields.

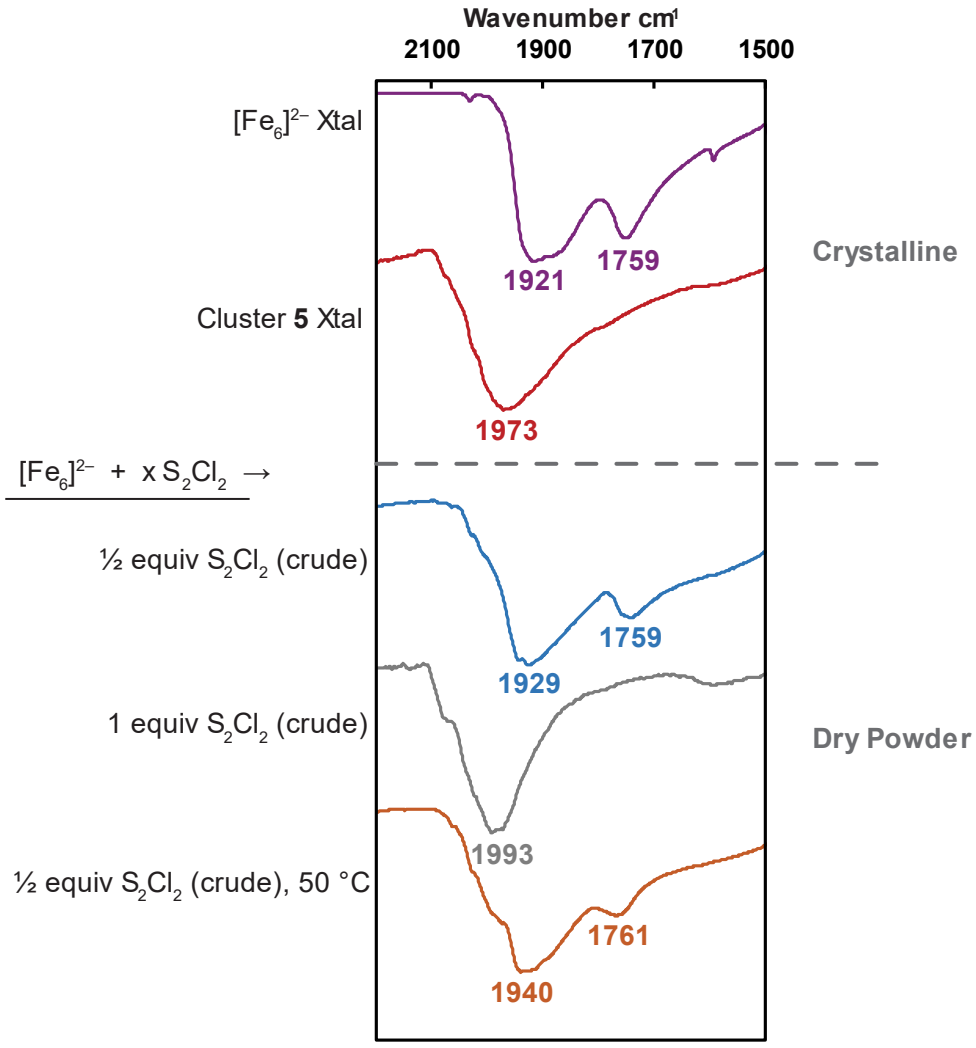

Figure 4.2 IR spectra of crystalline $(Et_4N)_2[Fe_6(\mu_6\text{-}C)(CO)_{16}]$ and cluster **5** (*top*); IR spectra resulting from various conditions for reaction of $(Et_4N)_2[Fe_6(\mu_6\text{-}C)(CO)_{16}]$ with S_2Cl_2 (*bottom*). In each case, the reaction mixture was dried down and washed with Et_2O. Reaction of starting cluster with half equiv of S_2Cl_2 at –15 °C (blue) or 50 °C (orange) yields spectra suggestive of unconverted $(Et_4N)_2[Fe_6(\mu_6\text{-}C)(CO)_{16}]$, as indicated by the presence of the bridging CO peak at 1759 cm^{-1}. Reaction with a full equiv of S_2Cl_2 at –15 °C (grey) yields a spectrum in which the bridging peak is no longer apparent.

The crystal structure of **5** (**Figure 4.3**) reveals Fe–S distances [2.203(3), 2.189(3), 2.188(3), 2.169(2) Å] that are noticeably short for a CO supported {$Fe_2(\mu_4$-S)Fe_2} motif. Exploration of this motif in the CSD[30] produces an average of 2.25 ± 0.01 Å (see **Table C.1** in Appendices); the average Fe–S bond distance of 2.19 ± 0.01 Å in **5** is thus remarkably short. Indeed, the longest bond length in **5** at 2.203(3) Å is shorter than the shortest recorded CSD Fe–S bond (2.215 Å) in an {$Fe_2(\mu_4$-S)Fe_2} motif. On the other hand, the acute ∠FeSFe angles (69.84° and 71.87°) fall within the expected range (66.10° to 72.35°), with the larger angle oriented towards the Fe_6 unit. In comparison to the bond metrics found in FeMoco,[14] the Fe–S bond falls short of the average Fe–S bond found in the active site (2.25 ± 0.03 Å). The average Fe–Fe bond distance of 2.65 ± 0.06 Å in **5** is unremarkable. Thus, the presence of the sulfide does not induce any notable elongation or compression of Fe–Fe bond lengths in Fe5–Fe8. Similarly, the Fe–C bond distances in the six- and five-iron units resemble those of the Fe_6 and Fe_5 carbidocarbonyl iron clusters discussed in previous chapters. The average Fe–C bond distance in the six-iron unit of cluster **5** is 1.89 ± 0.01 Å (see Appendix B for individual bond distances), compared to 1.881 ± 0.005 Å in the published Fe_6 cluster.[106] In the 5-iron unit of cluster **5**, the equatorial iron sites average an Fe–C bond distance of 1.86 ± 0.01 Å, while the axial iron resides at an elongated bond distance of 1.95(1) Å. This is strikingly similar to the published Fe_5 neutral cluster [(Fe_{eq}–C_{avg} = 1.88 ± 0.02 Å; Fe_{ax}–C = 1.949(7) Å]. The Fe–C bonds found in **5**, however, are shorter than the FeMoco average of 2.00 ± 0.02 Å. Lastly, the ^{13}C NMR spectrum of **5** (**Figure 4.16**) in THF reveals resonances consistent with the solid-state structure: two distinct carbide resonances are observed at 483.8 and 478.0 ppm. Each peak is easily assigned to the appropriate carbide based on spectra for the dianionic Fe_6 (484.7 ppm) and dianionic Fe_5 (478.8 ppm) clusters. Thus, each carbide in **5** is slightly deshielded with respect to their counterpart in the non-sulfide dianionic clusters.

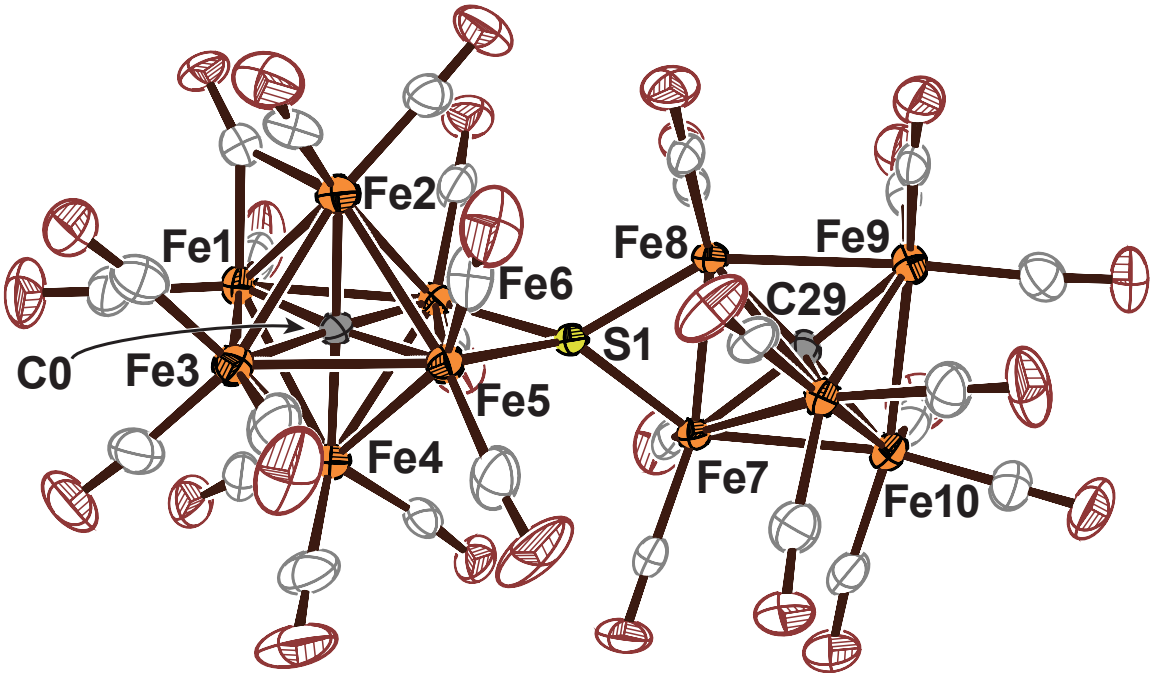

Figure 4.3 Thermal ellipsoid plots (50% probability) of $(NEt_4)_2\{[(CO)_{15}(\mu_6\text{-}C)Fe_6](\mu_4\text{-}S)[Fe_5(\mu_5\text{-}C)(CO)_{13}]\}$ (**5**). Orange = Fe; Gray = C; Yellow = S; Maroon = O. Two NEt_4^+ cations have been removed for clarity (see Appendix A for unabridged structure).

The generation of side products and the presence of chloride in the synthesis of **5** led us to seek more straightforward reaction conditions. As this cluster can be thematically formulated as an Fe_6 cluster, an Fe_5 cluster, a sulfur bridge and an overall 2^- charge, we attempted to stoichiometrically construct **5** via the introduction of elemental sulfur into a solution of $(Et_4N)_2[Fe_6(\mu_6\text{-}C)(CO)_{16}]$ and $[Fe_5(\mu_5\text{-}C)(CO)_{15}]$ (**Scheme 4.6**, *bottom*). This combination of iron clusters was prepared in DCE at –15 °C, and a toluene solution of elemental sulfur was added dropwise. After removal of solvent *in vacuo*, trituration, washing, and extraction of the Et_2O-insoluble compound into FPh, slow vapor diffusion of Et_2O again gave X-ray quality crystals. To our surprise, crystal structure solution in *Pbca* revealed a symmetric dimer of Fe_5 clusters bridged by the same 4-coordinate sulfide motif (**Figure 4.4**), resulting in the simplified formula $(NEt_4)_2\{[Fe_5(\mu_5\text{-}C)(CO)_{13}]_2(\mu_4\text{-}S)\}$ (**6**).

The Fe–C bond distances of this cluster are similar to the Fe_5 component of **5**, exhibiting an average Fe_{eq}–C bond distance of 1.87 ± 0.01 Å and an average Fe_{ax}–C bond distance of 1.961 ± 0.005 Å. The dianionic unit of **6** exhibits slightly distorted C_2 symmetry with a dihedral angle of 88.92° between the Fe1–C0–S1 and Fe10–C27–S1 planes. The average Fe–S distance of 2.175 ± 0.005 Å, however, is notably *shorter* than the already short distance found in **5**. The acute ∠Fe–S–Fe angles (70.44° and 70.77°) again fall within the expected range for the Fe_2SFe_2 motif. IR analysis of **6** suggests relatively oxidized iron sites with respect to **5**, providing a further blue shifted ν_{CO} peak at 1991 cm^{-1} (**Figure 4.17**). The ^{13}C NMR spectrum of **6** (**Figure 4.18**) in THF exhibits a single carbide resonance observable at 477.6 ppm, consistent with chemically equivalent Fe_5 clusters in solution.

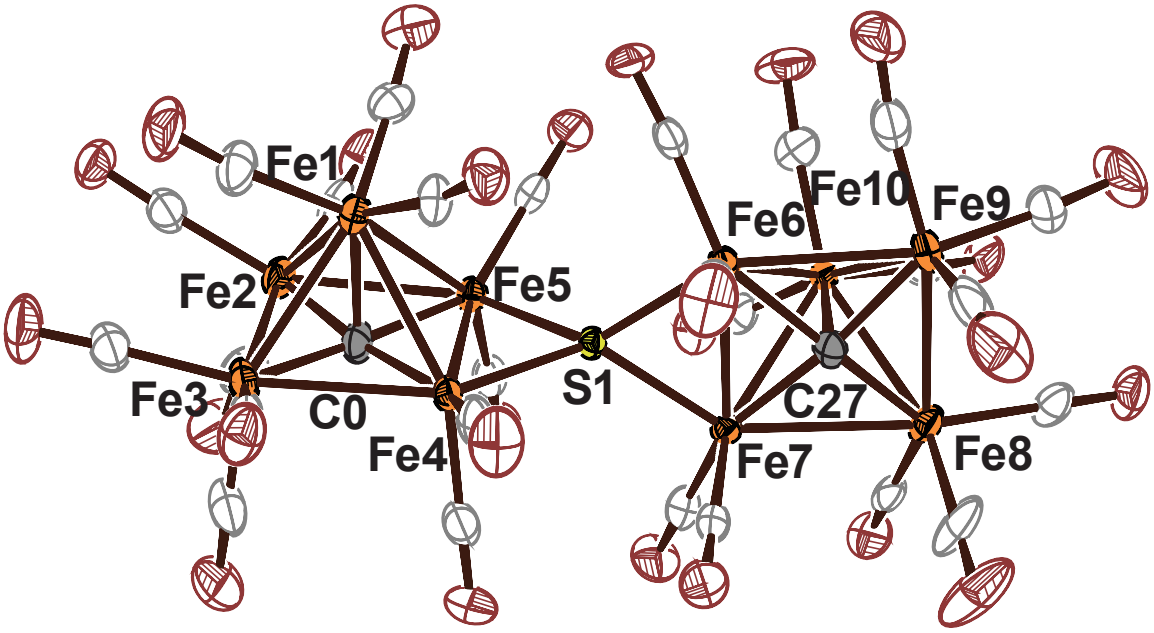

Figure 4.4 Thermal ellipsoid plots (50% probability) of $(NEt_4)_2\{[Fe_5(\mu_5\text{-}C)(CO)_{13}]_2(\mu_4\text{-}S)\}$ (**6**). Orange = Fe; Gray = C; Yellow = S; Maroon = O. Two NEt_4^+ cations have been removed for clarity (see Appendix A for unabridged structure).

4.3.2 Purification and Isolation of Neutral, Sulfo-Carbide Clusters

Our efforts to fully characterize the product profiles for the reactions described above prompted us to separate and purify the neutral compounds dissolved in the nonpolar layers. The pentane and Et_2O layers collected during the synthesis of **5** were both demonstrated to contain two compounds which can be separated by column chromatography through silica gel with pentane or hexanes as the eluent. The major component of the pentane extraction is a deep, bright red compound, while the majority component of the Et_2O layer was a red-orange compound. Isolation and crystallization (by cooling to –20 °C) of the highly pentane-soluble bright red compound generated the well-known cluster $Fe_3S_2(CO)_9$.[167,168] More remarkably, XRD of crystals from the red-orange Et_2O-soluble layer identified a $P\bar{1}$ unit cell, and subsequent structure solution revealed a remarkable CO-supported iron-sulfur cluster featuring a "carbide-like" site, multiple sulfur atoms, and a 'dangler' iron (**Figure 4.5**), resulting in the formula [{$Fe_4(\kappa_2S–\kappa_4C)(CO)_{10}$}($\mu_3$-S)($\mu_3$-$S_2$)$Fe(CO)_3$] (**7**). Additionally, it was later found that column chromatography of the Et_2O layer is unnecessary; crystals of the same compound can be easily achieved by removal of solvent *in vacuo*, dissolution in pentane, and crystallization by slow cooling to –20 °C.

A thorough search through the CSD for {$Fe_4(\mu_4$-C)} motifs exclusively returns clusters in which the irons sites adopt a 'butterfly' geometry about the carbide, marking the planar geometry displayed in **7** as unique. While the average Fe–Fe bond distance (2.66 ± 0.09 Å) is typical of iron-carbonyl-carbide clusters, the average Fe–C distance of 1.97 ± 0.04 Å is remarkably longer than average for this type of cluster and instead is quite close to the average Fe–C distance found in FeMoco (2.00 ± 0.02 Å). This elongation is — in part — an artifact of the displaced position of the carbide from the Fe_4 plane, such that the carbide actually resides 0.59 Å above the least-squares plane derived from the positions of

the four Fe atoms. While the presence of a true C–S bond [1.714(5) Å] does preclude the C from being an authentic C^{4-} carbide, this bonding motif is reminiscent of the proposed biogenesis mode of carbide insertion into the M-cluster as postulated by Wiig, Hu, and Ribbe.[24,25] In this biogenesis scheme, a S-bound methyl group undergoes H• atom abstraction by radical S-adenosyl-L-methionine (SAM) before proceeding to subsequent dehydrogenation/deprotonation. The presence of the $\{C–S\}^{4-}$ motif (i.e. tetra-deprotonated methylthiol) in **7** thus serves as the first rudimentary structural model for intermediates in M-cluster biosynthesis. Lastly, the Fe–S distances found in **7** are notable as the average distance of 2.27 ± 0.03 Å is considerably elongated compared to **5** and **6**, placing it closer to that of FeMoco (2.25 ± 0.03 Å). Of particular note, if 'belt sulfides' are excluded from the FeMoco average, the similarity is even more pronounced as the average Fe–S of 2.27 ± 0.03 Å in FeMoco is *exactly on par* with that of **7**. Two of the S sites (S3, S4) are bonded (2.048(2) Å) resulting in the presence of a persulfide S–S bond. Finally, the ^{13}C NMR spectrum of **7** (**Figure 4.20**) in C_6D_6 exhibits a dramatic upfield shift of the carbide peak to 312.8 ppm, consistent with the conversion of the carbide from a C^{4-} to a $\{CS\}^{4-}$ motif. Because of the inorganic carbide, multiple sulfide sites, and multiple iron sites present in cluster **7**, this represents the first report of such a cluster in the context of a suitable, synthetic starting-point for building FeMoco analogues. Still, the engagement of S1 with the carbide and proximity of S3 to S4 designating these sites as persulfide leaves only a single sulfur site (S2) to be considered as an authentic S^{2-} site.

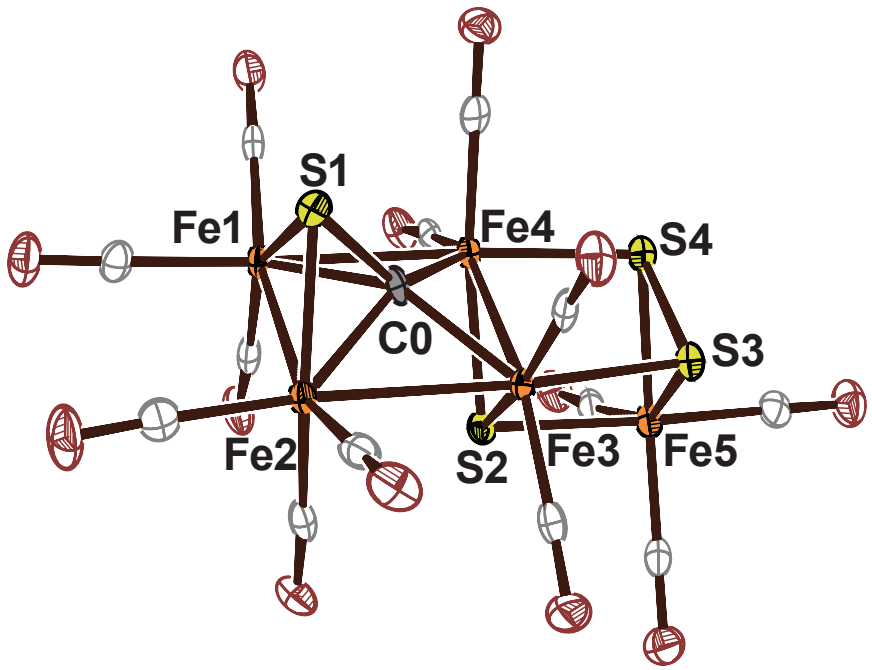

Figure 4.5 Thermal ellipsoid plots (50% probability) of [{$Fe_4(\kappa_2S–\kappa_4C)(CO)_{10}$}($\mu_3$-S)($\mu_3$-$S_2$)$Fe(CO)_3$] (**7**). Orange = Fe; Gray = C; Yellow = S; Maroon = O.

Purification of the nonpolar layers collected during the synthesis of **6** provides similar results to that of **5** with the addition of $[Fe_5]^0$, which necessitated the use of column chromatography for complete seperation of clusters. Passing the pentane extraction layer through a silica gel column with hexanes as the eluent first produces a deep, bright red band of $Fe_3S_2(CO)_9$, followed by a red-brown band of $[Fe_5]^0$. Once these two bands have eluted, the final red-orange band was eluted with 10% DCM in hexanes. Removal of solvent, dissolution in pentane, and cooling to –20 °C afforded crystals which were identified as a different *Pbcn* unit cell. Structure solution revealed a cluster phylochemically similar to **7** and having the formula [{$Fe_4(\kappa_2S–\kappa_4C)(CO)_{10}$}($\mu_3$-$S)_2Fe(CO)_3$] (**8**) (**Figure 4.6**). Average bond distances are quite similar to those in **7** with the marked difference being the average Fe–S of 2.25 ± 0.03 Å in **8**, which is *exactly on par* with that of FeMoco (see **Table 4.1**). The key difference, however, displayed in **8** is

the absence of a sulfur site (S4 in **7**), therefore designating S3 as a second face-bridging sulfide (S^{2-}) site (in addition to S2). The absence of the S4 site, however, does induce a break in the C_s chemical symmetry displayed in cluster **7**, such that the Fe5–Fe3 distance has shortened to 2.616(1) Å. While we found that synthesis of cluster **8** has in fact been previously reported from the reaction of $Fe_3(CO)_{12}$ with CS_2 at 80 °C,[169] the absence of this structure from the CSD coupled with the fact that the original report has seemingly remained in obscurity from the bioinorganic synthetic modelling community has hindered its utilization as an obvious candidate for nitrogenase structural modeling.

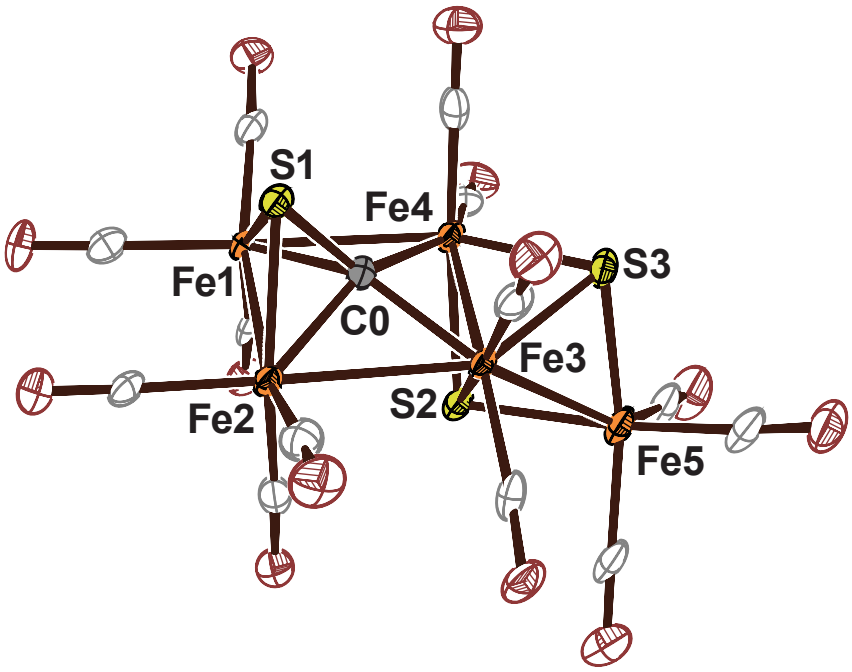

Figure 4.6 Thermal ellipsoid plots (50% probability) of [{$Fe_4(\kappa_2S–\kappa_4C)(CO)_{10}$}($\mu_3$-$S)_2Fe(CO)_3$] (**8**). Orange = Fe; Gray = C; Yellow = S; Maroon = O.

	5	6	7	8	FeMoco
Fe–Fe	**2.65** ± 0.06	**2.64** ± 0.05	**2.66** ± 0.09	**2.7** ± 0.1	**2.63** ± 0.04
Fe–C	**1.88** ± 0.03	**1.88** ± 0.04	**1.97** ± 0.04	**1.96** ± 0.02	**2.00** ± 0.02
Fe–S	**2.19** ± 0.01	**2.175** ± 0.005	**2.27** ± 0.03	**2.25** ± 0.03	**2.25** ± 0.03

Table 4.1 Selected bond distance averages of the clusters described in this work compared with the corresponding averages found in the nitrogenase cofactor (FeMoco).

4.4 Spectroscopic and Computational Evaluation of Clusters

While the electronic structures of carbidocarbonyl iron cluster typically comprises of low-valent, diamagentic Fe sites, we became interested in the effect upon the spectroscopic oxidation states of the clusters are single or multiple sulfur sites became incorporated into the ligation sphere. The FeMoco cluster consists entirely of ferrous and ferric iron sites. Therefore, efforts towards probing for higher oxidation-state iron sites in synthetic clusters were forthcoming: A combination of IR, X-ray photoelectron spectroscopy (XPS), and density functional theory (DFT) calculations — in conjunction with rudimentary rationalizations based on observed bond metrics from crystal structures — were employed to glean insight into the electronic structures at the Fe centers of these Fe-C-S clusters.

4.4.1 Spectroscopic Oxidation State of Cluster 5

Initially, due to the elemental proximity of sulfur (Z=16) and chlorine (Z=17), the presence of the sulfide was additionally confirmed via air-free X-ray photoelectron spectroscopy (XPS) of **5**. XPS analysis of the S 2*p* region provides a feature at 162.8 eV (**Figure 4.7**, *top*) in the high-resolution spectrum. This feature is notably absent in the XP

spectra of the dianionic Fe_6 or the neutral Fe_5 clusters. Additionally, the fact that the S 2*p* feature for **5** is ~1 eV lower in binding energy than elemental sulfur (163.9 eV)[170] is indicative of a negative partial charge upon the sulfur site, suggesting a formal assignment of cluster **5** as two neutral clusters bridged by a dianionic sulfide. Additional support for this assignment is found in the high-resolution spectra of the Fe 2*p* region (**Figure 4.7**, *bottom*). The prominent Fe 2*p*3/2 features in the spectra for **5**, dianionic Fe_6, and neutral Fe_5 appear at 708.1 eV, 707.9 eV, and 708.7 eV, respectively and the spectra for Fe_6 and Fe_5 are in good agreement with previously reported spectra of the compoounds.[106,171] The higher Fe 2*p* binding energy of cluster **5** relative to the Fe_6 dianion demonstrates an overall increase in Fe oxidation state from the precursor. On the other hand, cluster **5** maintains a lower binding energy relative to neutral Fe_5, reflecting the overall decrease in average formal Fe oxidation state. This trend of increasing formal oxidation state upon removal of an iron site between two clusters of similar overall charge has been demonstrated previously in both XPS and X-ray absorption spectroscopy.[49,106,171]

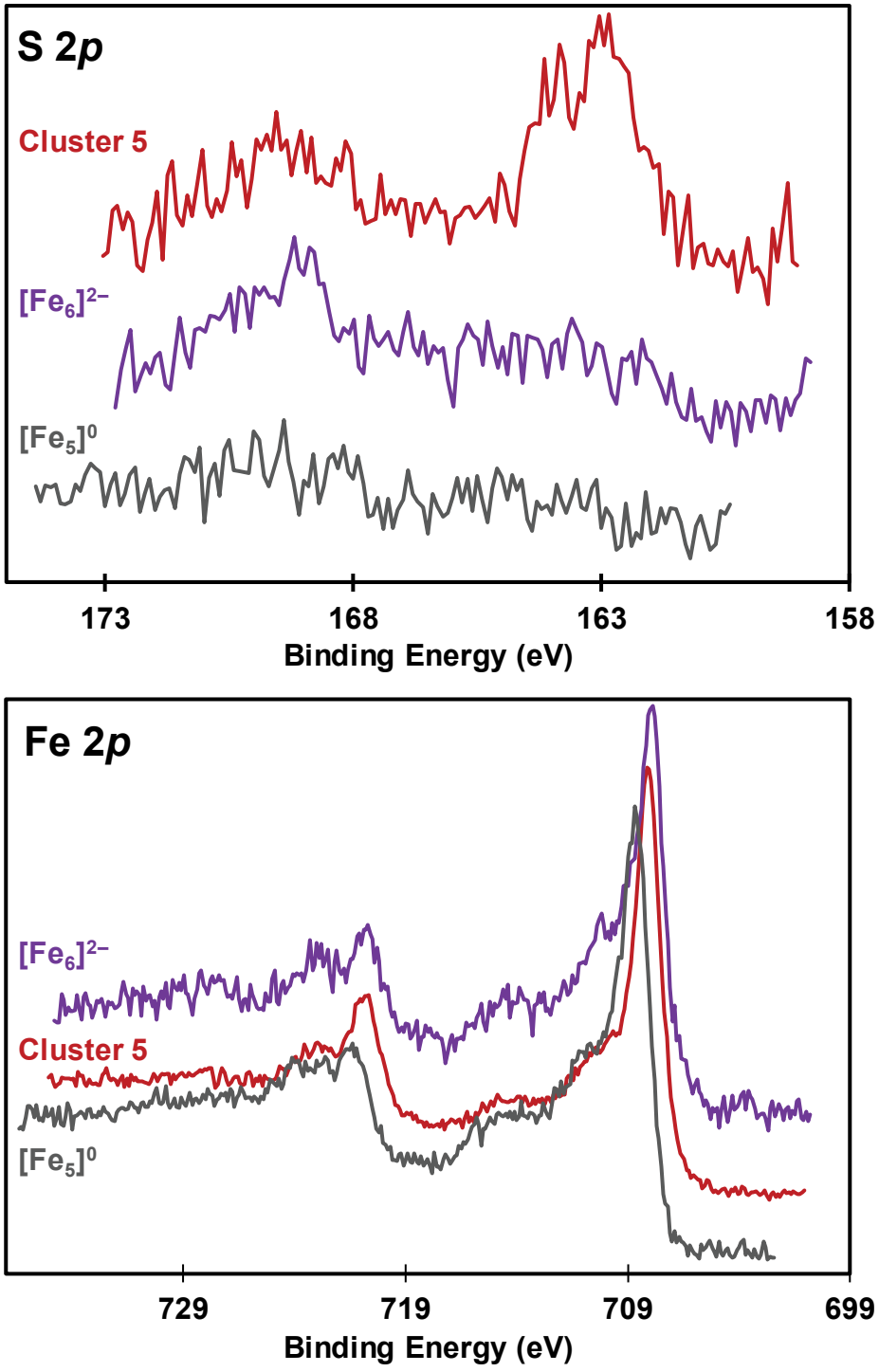

Figure 4.7 High-resolution X-ray photoelectron spectrum (XPS) of the sulfur 2*p* region (*top*) and iron 2*p* region (*bottom*). Red: Cluster **5**; purple: $(Et_4N)_2[Fe_6(\mu_6\text{-}C)(CO)_{16}]$; dark grey: $[Fe_5(\mu_5\text{-}C)(CO)_{15}]$.

The model of separate, neutral Fe_6 and Fe_5 units and a bridging S^{2-} is further supported by Wade's electron counting rules for transition metal clusters per Polyhedral Skeletal Electron Pair Theory (PSEPT).[115] If each unit is considered separately — and the sulfide and overall 2– charge are excluded — the electron count for the Fe_6 and Fe_5 cluster are 82 e^- and 70 e^-, respectively. Each of these falls 4 e^- short of the prescribed PSEPT total of 8 missing electrons. Inclusion of the sulfide (6 e^-) and the 2^- charge (2 e^-) then satisfies PSEPT prediction (**Figure 4.8**) for each monomeric unit of the cluster. Additional evidence for the model depicted in **Figure 4.8** (neutral Fe clusters and a bridging S^{2-}) can be found in the IR analysis of these clusters (**Figure 4.9**). The IR spectrum of **5** displays a very blue-shifted (with respect to the starting cluster) and broad carbonyl peak at $\nu = 1973$ cm^{-1}. For comparison, oxidation of the dianionic Fe_6 cluster to the neutral Fe_6 species induces a blue ν_{CO} shift from 1921 cm^{-1} to 1958 cm^{-1}.[106] Similarly, the value for the dianionic Fe_5 cluster (1919 cm^{-1}) is blue-shifted upon conversion to the corresponding neutral cluster (1978 cm^{-1}). These data further support the postulation that **5** (1973 cm^{-1}) is comprised of essentially neutral Fe_6 and Fe_5 units.

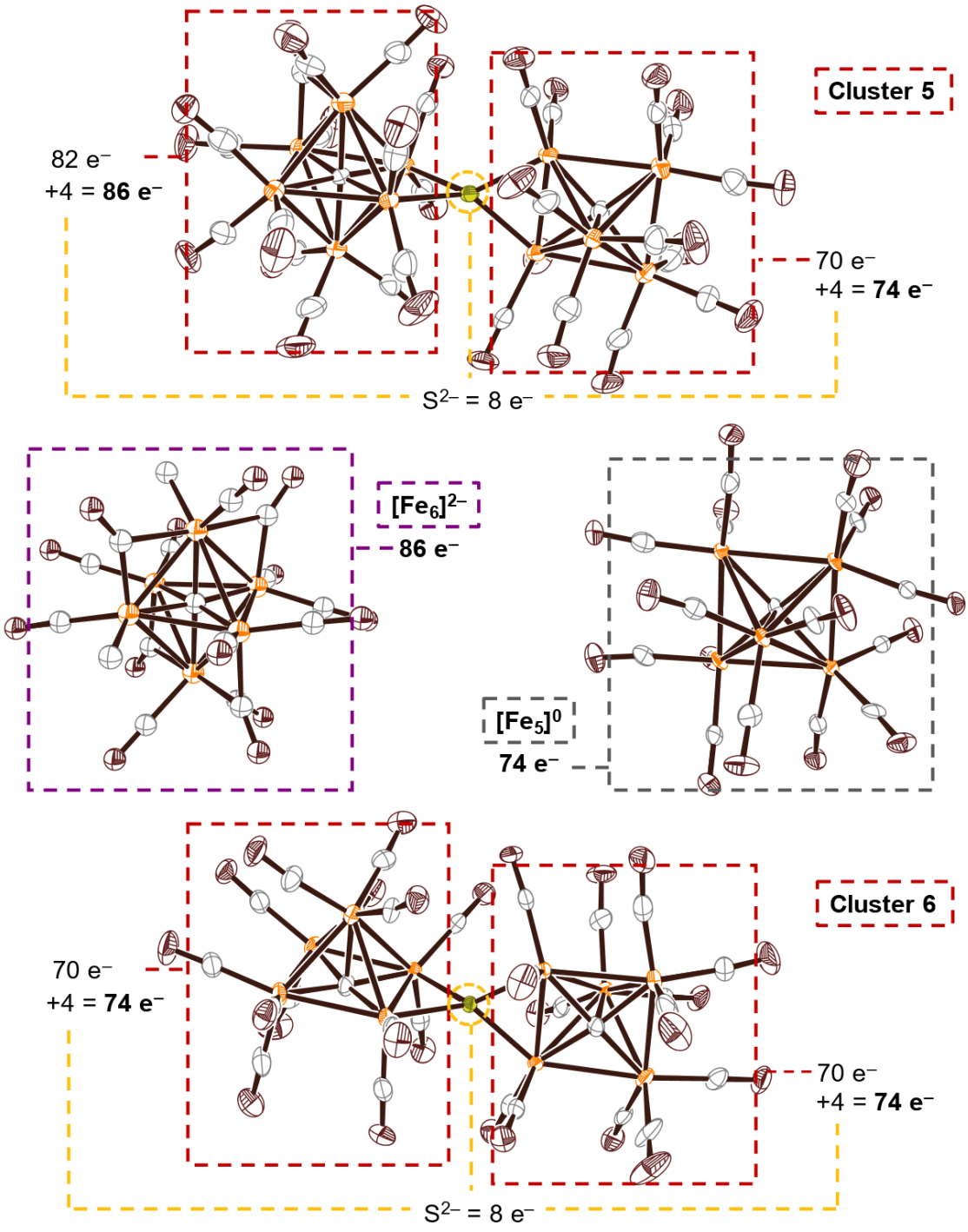

Figure 4.8 Theoretical electron count of clusters **5**, $[Fe_6]^{2-}$, $[Fe_5]^0$, and **6** as prescribed by PSEPT.

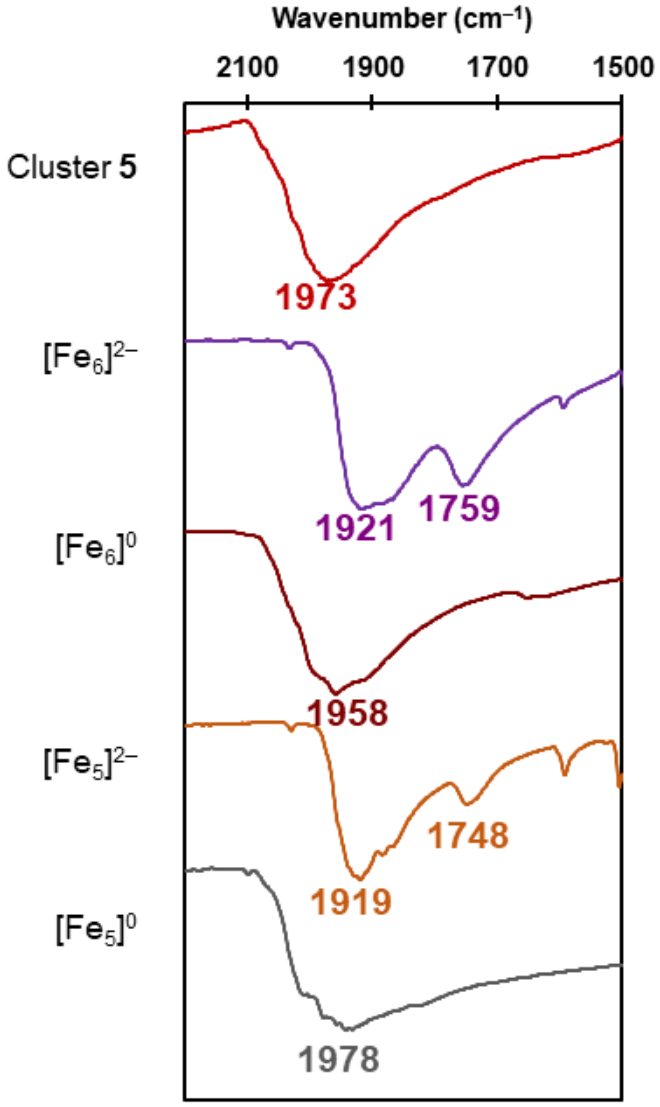

Figure 4.9 IR spectra of crystalline samples of the following (from top to bottom): (red) $(NEt_4)_2\{[(CO)_{15}(\mu_6\text{-}C)Fe_6](\mu_4\text{-}S)[Fe_5(\mu_5\text{-}C)(CO)_{13}]\}$ (**5**); (purple) $(Et_4N)_2[Fe_6(\mu_6\text{-}C)(CO)_{16}]$; (dark red) $[Fe_6(\mu_6\text{-}C)(CO)_{18}]$; (orange) $(Et_4N)_2[Fe_5(\mu_5\text{-}C)(CO)_{14}]$; (dark grey) $[Fe_5(\mu_5\text{-}C)(CO)_{15}]$.

4.4.2 DFT Orbital Analysis of Clusters 5 and 6

To probe the electronic structures of **5** and **6**, DFT calculations were performed (B3PW91/G6-31). The geometry optimized structures provided satisfactory agreement with X-ray structure, affording a root mean square (RMS) deviation from bond distances of 0.063 Å among all Fe–Fe, Fe–$C_{carbide}$, and Fe–S bonds for **5** (**Table 4.2**) and an RMS deviation of 0.043 Å for **6 (Table 4.3)**. MO analysis of **5** (**Figure 4.10**) revealed that the HOMO–1 and HOMO orbitals are defined primarily by Fe–Fe bonding interactions on the Fe_6 or Fe_5 units, respectively. The valence electrons on the Fe_6 unit (HOMO–1), in particular, localize on sites closest to the sulfide. In contrast, the HOMO is evenly distributed among all Fe sites in the Fe_5 unit. This may suggest that while valence electrons in the more charge-diffuse Fe_6 unit are drawn towards the electronegative sulfide, the valence electrons located on the Fe_5 unit remain more tightly bound, as expected based on the higher average Fe oxidation state (vs Fe_6 unit). Indeed, the crystal structure also supports this assessment as the sulfide sits slightly (0.01 Å) closer to the Fe_6 unit than the Fe_5, implying an asymmetry in the interactions between the sulfide and each respective cluster.

The HOMO–1 and HOMO orbitals lie relatively close in energy (1097 cm^{-1} apart) compared with a HOMO/LUMO gap of 10096 cm^{-1}. Similar to the HOMO–1 and HOMO, the LUMO and LUMO+2 localize on either the Fe_6 and Fe_5 units, with the Fe_6-localized LUMO lying 2853 cm^{-1} below the LUMO+2. The LUMO, which resides primarily on the Fe_6 unit, involves an atomic *p* orbital from the bridging sulfide that is in-phase with orbitals of the Fe6 site and out-of-phase with those of Fe5. The contribution to the out-of-phase interaction is larger and so has been designated as an overall 'anti-bonding' interaction. The LUMO+2, which clearly depicts an S–Fe_5 anti-bonding interaction, suggests that bond cleavage with the Fe_6 unit will be more accessible than with the Fe_5 unit. As a crude

comparison, low-level energy calculations (B3PW91/G3-21) were performed on the Shriver *et. al.* SO_2-bound clusters[162] without geometry optimization. In both the 6-iron and 5-iron cluster, the O_2S–Fe_n anti-bonding orbital appears at LUMO+2 in each compound. Here, the LUMO+2 of the six-iron cluster is energetically 4609 cm^{-1} lower than that of the five-iron, a trend which correlates with the pattern seen for **5**. Finally, the LUMO+1 depicts anti-bonding interaction with CO ligands on the Fe_6. This is to be expected as 2 e^- reduction of the carbonyl-only monomeric clusters typically results in loss of a CO ligand.

Similar to the valence orbitals of **5**, the HOMO of **6** (**Figure 4.11**) is primarily characterized as bonding orbitals between the Fe atoms of the clusters and is nonbonding with respect to the sulfide. In contrast to the asymmetric cluster **5**, the orbitals generated for **6** exhibit symmetry about the C_2 axis — the HOMO, in particular, being antisymmetric about the C_2 axis. Similar to the LUMO and LUMO+2 of **5**, the LUMO and LUMO+1 of **6** depict antibonding interactions between the sulfide and the clusters that are symmetric about the C_2 axis. Similar to the conclusions for **5**, it might be surmised that a 2 e^- reduction of **6** would result in heterolytic cleavage of the bridged cluster. On the basis of rules prescribed by PSEPT, it would be reasonable to expect the reduction to yield a neutral sulfide cluster and highly reduced tetra-anionic CO-only Fe_5 cluster (74 e^- per cluster).[136]

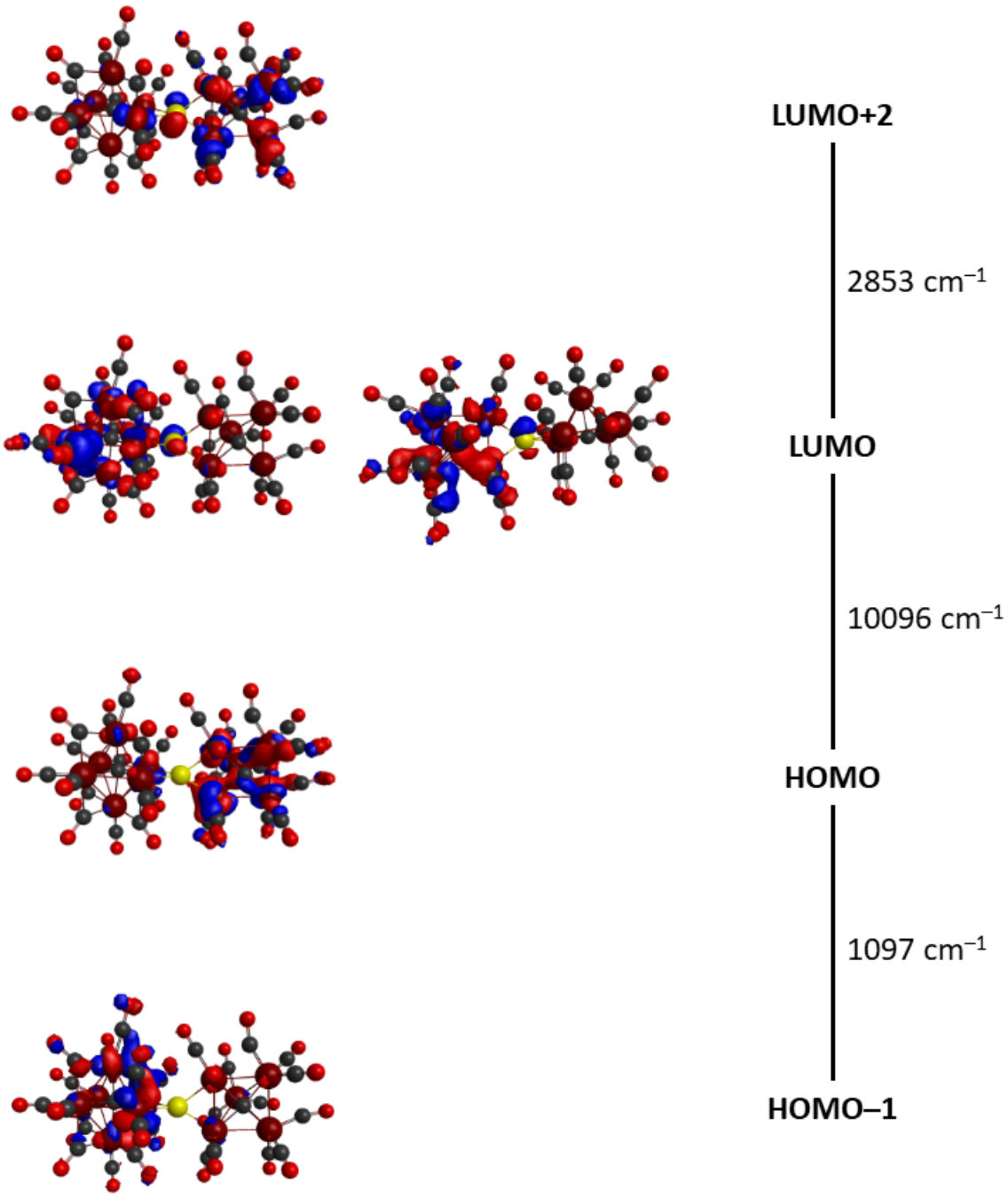

Figure 4.10 Calculated HOMO–1, HOMO, LUMO, and LUMO+2 orbitals of **5**.

Bond	Xtal, 5	DFT, 5	Deviation
C0–Fe1	1.87(1)	1.909	-0.038
C0–Fe2	1.880(8)	1.852	0.029
C0–Fe3	1.88(1)	1.849	0.032
C0–Fe4	1.904(8)	1.851	0.053
C0–Fe5	1.88(1)	1.882	-0.001
C0–Fe6	1.90(1)	1.836	0.065
C29–Fe7	1.864(9)	1.885	-0.020
C29–Fe8	1.865(9)	1.836	0.030
C29–Fe9	1.870(9)	1.846	0.025
C29–Fe10	1.854(9)	1.86	-0.005
C29–Fe11	1.95(1)	1.941	0.010
S1–Fe5	2.189(3)	2.212	-0.023
S1–Fe6	2.203(3)	2.191	0.012
S1–Fe7	2.188(3)	2.231	-0.043
S1–Fe8	2.169(2)	2.146	0.023
Fe1–Fe2	2.571(2)	2.55	0.021
Fe1–Fe3	2.663(2)	2.686	-0.023
Fe1–Fe4	2.750(2)	2.553	0.197
Fe1–Fe6	2.680(2)	2.72	-0.040
Fe2–Fe3	2.670(2)	2.611	0.059
Fe2–Fe5	2.655(2)	2.679	-0.024
Fe2–Fe6	2.718(2)	2.607	0.111
Fe3–Fe4	2.622(2)	2.624	-0.002
Fe3–Fe5	2.733(2)	2.605	0.128
Fe4–Fe5	2.685(2)	2.806	-0.121
Fe4–Fe6	2.686(2)	2.622	0.064
Fe5–Fe6	2.578(2)	2.56	0.018
Fe7–Fe8	2.494(2)	2.507	-0.013
Fe7–Fe10	2.681(2)	2.606	0.075
Fe7–Fe11	2.669(2)	2.587	0.082
Fe8–Fe9	2.678(2)	2.698	-0.020
Fe8–Fe11	2.657(2)	2.579	0.078
Fe9–Fe10	2.671(2)	2.639	0.032
Fe9–Fe11	2.600(2)	2.533	0.067
Fe10–Fe11	2.593(2)	2.525	0.068
		RMS =	**0.063**

Table 4.2 Bond distance comparisons between XRD data and DFT-optimized structure (B3PW91/G6-31) of **5**. The deviation of each bond from the XRD data is shown, along with a calculated RMS value for all deviations related here. Bonds involving the carbonyl ligands were not considered.

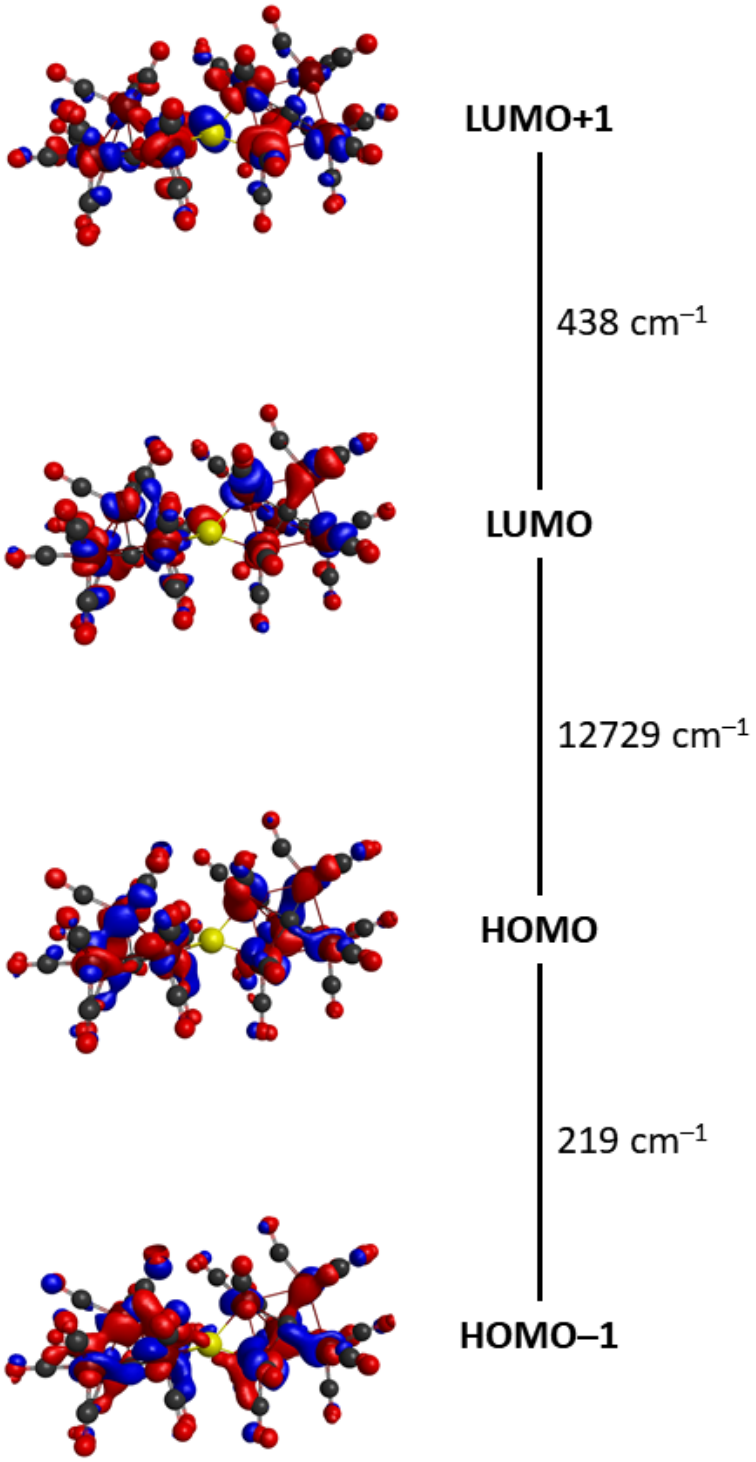

Figure 4.11 Calculated HOMO–1, HOMO, LUMO, and LUMO+1 orbitals of **6**.

Bond	Xtal, 6	DFT, 6	Deviation
C0–Fe1	1.957(7)	1.933	0.024
C0–Fe2	1.861(6)	1.851	0.01
C0–Fe3	1.866(6)	1.852	0.014
C0–Fe4	1.875(6)	1.847	0.028
C0–Fe5	1.872(6)	1.878	-0.006
C27–Fe6	1.878(6)	1.878	0
C27–Fe7	1.857(6)	1.846	0.011
C27–Fe8	1.877(7)	1.852	0.025
C27–Fe9	1.867(6)	1.851	0.016
C27–Fe10	1.964(6)	1.934	0.03
S1–Fe4	2.175(2)	2.168	0.007
S1–Fe5	2.176(2)	2.217	-0.041
S1–Fe6	2.168(2)	2.218	-0.05
S1–Fe7	2.180(2)	2.167	0.013
Fe1–Fe2	2.614(1)	2.533	0.081
Fe1–Fe3	2.614(1)	2.526	0.088
Fe1–Fe4	2.650(1)	2.572	0.078
Fe1–Fe5	2.650(1)	2.604	0.046
Fe2–Fe3	2.681(2)	2.648	0.033
Fe2–Fe5	2.672(1)	2.626	0.046
Fe3–Fe4	2.677(1)	2.675	0.002
Fe4–Fe5	2.520(1)	2.509	0.011
Fe6–Fe7	2.508(1)	2.509	-0.001
Fe4–Fe9	2.654(1)	2.626	0.028
Fe6–Fe10	2.646(1)	2.604	0.042
Fe7–Fe8	2.692(1)	2.675	0.017
Fe7–Fe10	2.668(1)	2.572	0.096
Fe8–Fe9	2.700(2)	2.648	0.052
Fe8–Fe10	2.568(1)	2.526	0.042
Fe9–Fe10	2.620(1)	2.533	0.087
		RMS=	**0.044**

Table 4.3 Bond distance comparisons between XRD data and DFT-optimized structure (B3PW91/G6-31) of **6**. The deviation of each bond from the XRD data is shown, along with a calculated RMS value for all deviations related here. Bonds involving the carbonyl ligands were not considered.

4.4.3 Probe for Ferrous 'Dangler' Iron in Clusters 7 and 8

The presence of a putatively ferrous 'dangler' Fe site in **7** and **8** with a more σ-donating coordination sphere ({**Fe**$S_3(CO)_3$} in **7**; {**Fe**$S_2(CO)_3$} in **8**) suggests that a progressive approach towards biologically relevant Fe^{II}/Fe^{III} sites is possible. Indeed, preliminary insight into this possibility gained by comparison of Fe–C(O) bond distances among Fe sites as a proxy for the extent of π-backbonding to CO at that site. Notably, the 'dangler' Fe5 site in cluster **7** demonstrates elongated Fe–C(O) bond distances (1.81 ± 0.02 Å) versus sites Fe1–Fe4 (1.799 ± 0.007 Å). Cluster **8** exhibits a similar trend, but to a lesser extent (Fe5: 1.82 ± 0.02 Å; Fe1–Fe4: 1.81 ± 0.01 Å.) DFT Mulliken charges analysis (B3PW91/6-31G) on the carbonyl C sites was evaluated as a proxy for π-backbonding. In cluster **7**, The C(O) sites on Fe5 exhibit the highest Mulliken charges (**Figure 4.12**, *left*), consistent with a decreased extent of π-backbonding due to the nominally higher oxidation state of Fe5. The Fe1 and Fe2 carbonyl C sites exhibited the greatest extent of CO π-backbonding, indicating that the high Mulliken charge on these Fe sites cannot be entirely attributed to oxidation state. Similar analysis of **8** (**Figure 4.12**, *right*) reveals an Fe5 site that is of median oxidation state relative to the cluster. This is likely an artifact of the close Fe5–Fe3 contact that facilitates direct electron exchange to this site and greater oxidation state delocalization.

We note that Mössbauer spectroscopy is notoriously difficult to interpret in iron carbonyl clusters due to the intermingling and competing effects of formal oxidation state versus π-backbonding to CO ligands (thus affecting charge at nucleus). That is, lower oxidation states in iron-carbonyls typically exhibit *higher isomer shifts* than higher oxidation states[49] — in contrast to the trend observed in standard coordination chemistry. This counter-intuitive trend is somewhat realized in the analysis of Mulliken charges on the Fe sites in cluster **7**. As conventionally expected, the *six*-coordinate 'dangler' site Fe5

in $\{S_3\mathbf{Fe}(CO)_3\}$ ligation exhibits a relatively higher Mulliken charge (+0.24) compared to the adjacent *seven*-coordinate Fe3 and Fe4 sites (+0.15) in $\{S_2(C)(Fe)_2\mathbf{Fe}(CO)_2\}$ ligation. Meanwhile, the distal *seven*-coordinate Fe1 and Fe2 sites in $\{S(C)(Fe)_2\mathbf{Fe}(CO)_3\}$ ligation — which exhibit the highest extent of π-backbonding based on carbonyl metrics and DFT — exhibit the highest Mulliken charges (+0.25), nominally due to presence of extremely strong π-backbonding from these lowest-valent sites. Such effects lead to the counter-intuitive (and often unpredictable) trends in Mössbauer spectroscopy.

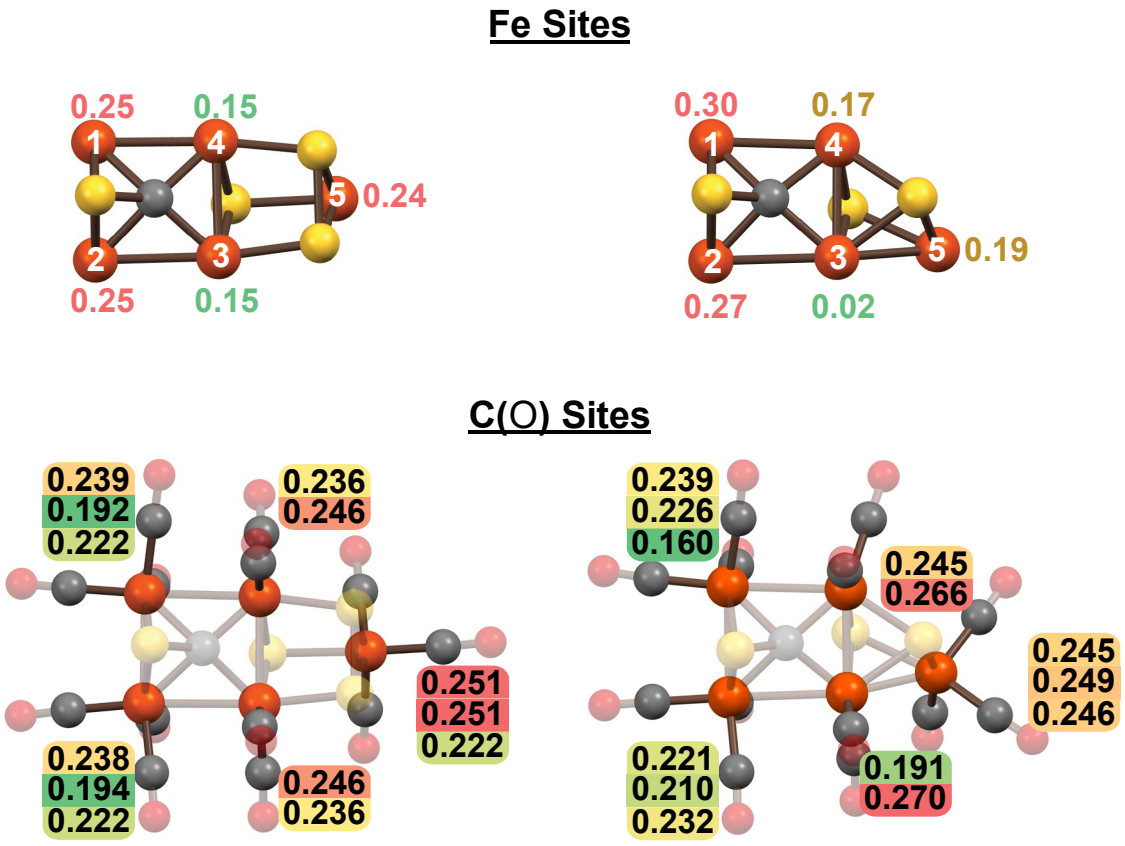

Figure 4.12 Calculated Mulliken charges on Fe sites (*top*) and carbonyl C sites (*bottom*) of clusters **7** (*left*) and **8** (*right*). A color gradient of red to green is used to indicate the most charge-positive Fe sites (red) to the least-positive (green) or C sites with the least extent of backbonding (red) to the greatest extent (green). Mulliken charge analysis of the Fe5 site in cluster **7** by these metrics consistently indicates this site to be the most oxidized Fe site in **7**.

Thus, we deemed an electron spectroscopy method to be the preferred path of investigation. To spectroscopically probe for a ferrous site in **7**, high-resolution XPS data in the Fe 2*p* region was collected (**Figure 4.13**). Component peak fitting of this region reveals three distinct peaks at binding energies (BE) of 711.6, 709.4, and 707.5 eV in the 2*p*(3/2) region and 724.6, 722.2, and 720.5 eV in the 2*p*(1/2) region with approximately 1:2:2 peak area ratios. The lower BE 2*p*(3/2) peaks at 709.4, and 707.5 eV are attributed to the four Fe sites with direct Fe–Fe and Fe–C bonding that encircle the carbide. Furthermore, DFT reveals that the HOMO in **7** (**Figure 4.14**) is strongly localized in the Fe1–Fe2 bond, which further indicates that the lowest BE components (720.5 and 707.5 eV; ~2 Fe sites by integration) are attributable to Fe1 and Fe2. These values are slightly higher binding energies relative to **5**, $[Fe_6]^{2-}$, and even $[Fe_5]^0$ (**Figure 4.7**, *bottom*); this is consistent with an overall increased 'average' Fe oxidation state in **7**. Finally, the highest binding energy feature at 711.6 eV (by integration, ~1 Fe site) is attributed to the dangler Fe5 site by both integration and BE, which falls within expected range for a ferrous and CO-supported iron site.[172,173] Consistent with all the above data and interpretation, the overall increase in average and localized oxidation states in **7** is spectroscopically obvious in the higher CO stretching frequencies observed in the IR spectrum (**Figure 4.19**) where all ν_{CO} values range upwards from 2002 cm^{-1}. These are significantly blue-shifted relative to **5** ($\nu_{CO} \geq 1973$ cm^{-1}) and **6** ($\nu_{CO} \geq 1991$ cm^{-1}) and is additionally consistent with the presence of a ferrous site.

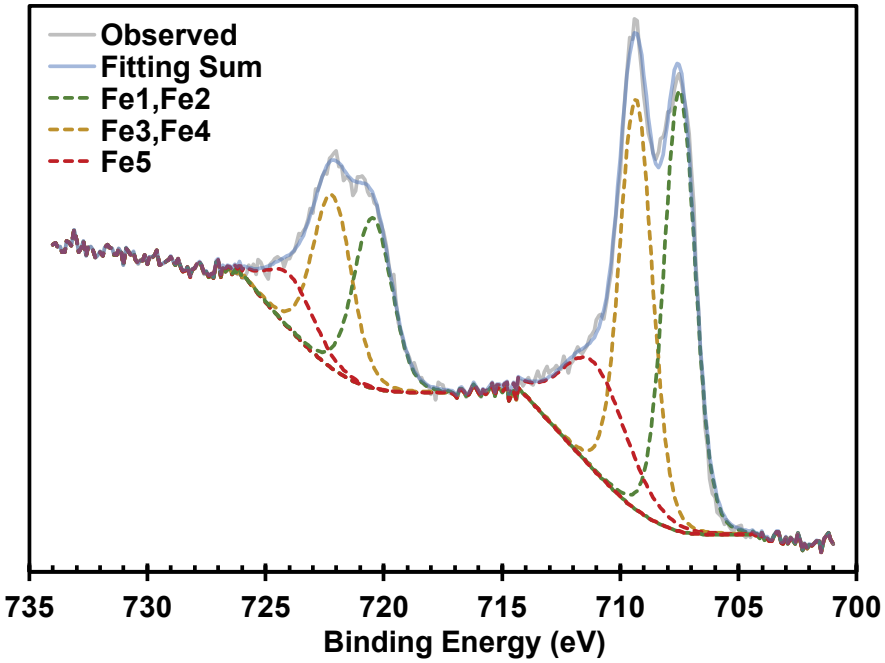

Figure 4.13 Observed high-resolution X-ray photoelectron spectrum (XPS) and component fitting of the iron 2*p* region of cluster **7**.

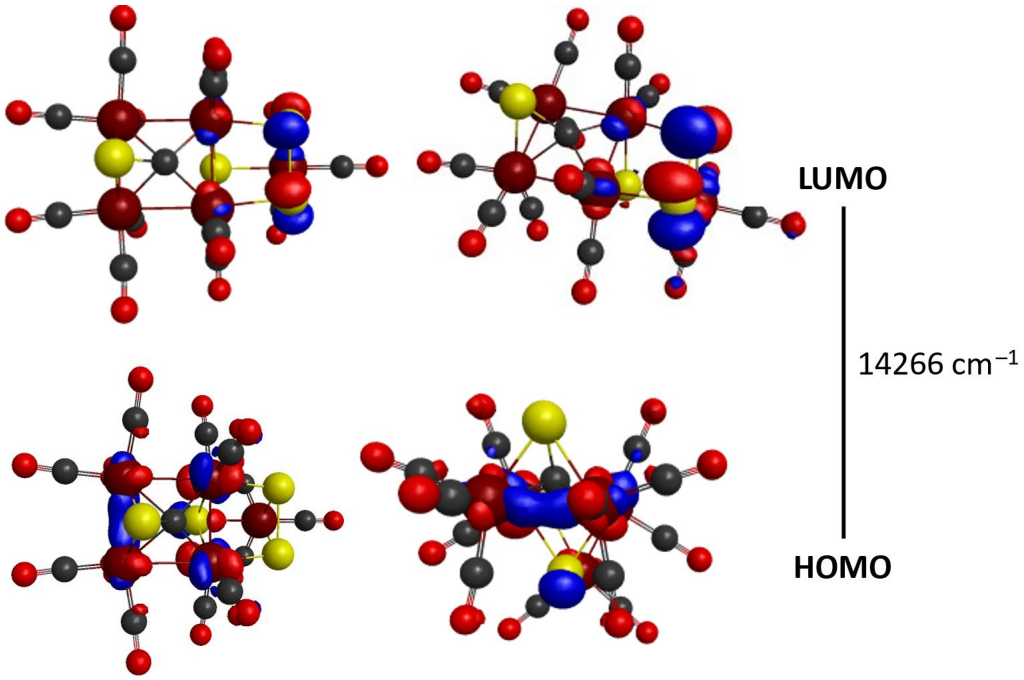

Figure 4.14 Calculated HOMO and LUMO orbitals of **7**.

Bond	Xtal, 7	DFT	Deviation
C0–Fe1	2.011(4)	1.974	0.0374
C0–Fe2	1.995(4)	1.974	0.0214
C0–Fe3	1.957(5)	1.931	0.0265
C0–Fe4	1.932(4)	1.931	0.0014
C0–S1	1.714(5)	1.751	-0.0365
Fe1–S1	2.252(1)	2.286	-0.0339
Fe2–S1	2.248(1)	2.286	-0.0379
Fe3–S2	2.265(1)	2.306	-0.0409
Fe3–S3	2.269(1)	2.293	-0.0239
Fe4–S2	2.264(1)	2.306	-0.0419
Fe4–S4	2.270(1)	2.293	-0.0229
Fe5–S2	2.334(1)	2.368	-0.0339
Fe5–S3	2.282(1)	2.313	-0.0309
Fe5–S4	2.271(1)	2.313	-0.0419
S3–S4	2.048(2)	2.097	-0.0488
Fe1–Fe2	2.6145(9)	2.565	0.04959
Fe1–Fe4	2.7271(9)	2.694	0.03319
Fe2–Fe3	2.7484(9)	2.568	0.18049
Fe3–Fe4	2.5602(9)	2.695	-0.13471
		RMS=	**0.061**

Table 4.4 Bond distance comparisons between XRD data and DFT-optimized structure (B3PW91/G6-31) of **7**. The deviation of each bond from the XRD data is shown, along with a calculated RMS value for all deviations related here. Bonds involving the carbonyl ligands were not considered.

4.5 CONCLUSIONS

In summary, using two straight-forward, one-step reaction methods, we have synthesized and structurally characterized a pair (**5** and **6**) of all-iron metalloclusters bearing an interstitial carbide and inorganic μ_4-sulfide. The Fe···S bond distances in **5** and **6** are quite short compared to similar {$Fe_4(\mu_4$-S)} compounds at 2.19 ± 0.01 Å and 2.175 ± 0.005 Å, respectively, providing two of the shortest reported average Fe···S distances to date. While the sulfurizing reagents utilized in these reactions involved electropositive or neutral sulfur donors, XPS of **5** and DFT analyses of both are indicative of a negative partial charge at the sulfur site. Additionally, DFT analyses of the antibonding orbitals with sulfide in **5** and **6** provide avenues for future work in pursuing monomeric sulfide ligated

derivatives. Additionally, isolation and characterization of **7** and **8** has provided the first synthetic example of an iron cluster containing multiple sulfur sites and a 'carbide-like' site where both Fe···C and Fe···S distances are highly comparable to those in FeMoco. The presence of a C–S contact is markedly reminiscent of a proposed biosynthetic pathway towards carbide insertion into the M-cluster and may pro-vide valuable characterization information in proposing intermediates that occur throughout biogenesis. Finally, the presence of multiple sulfur sites, higher valent iron, and a ferrous 'dangler' Fe site in **7** may finally 'unlock the synthetic door' towards structurally modeling the M-cluster.

4.6 Experimental Procedures

4.6.1 Solvents and Reagents

Fluorobenzene (Oakwood Chemical) and 1,2-dichloroethane (Fisher Scientific) were dried by distillation over molecular sieves and underwent three freeze-pump-thaw cycles prior to use. All other solvents were purchased as HPLC grade from EMD, Fisher, Macron or J.T. Baker, and dried through an alumina column system (Pure Process Technology). Deuterated solvents (THF-d_8, and C_6D_6) were purchased from Cambridge Isotopes and used as received. 1,8-bis(4-(methylthio)phenyl)anthracene was prepared following previous reports.[174] $(Et_4N)_2[Fe_6(\mu_6\text{-}C)(CO)_{16}]$ and $[Fe_5(\mu_5\text{-}C)(CO)_{15}]$ were prepared as described in Chapter 2. Triphenyl antimony ($SbPh_3$, Sigma Aldrich), bromine (Br_2, Alfa Aesar), bis(trimethylsilyl)sulfide ($S(SiMe_3)_2$, Acros Organics), *tert*-nonyl mercaptan (Sigma Aldrich), sodium hydride (NaH, Sigma Aldrich), disulfur dichloride (S_2Cl_2, Chem Service Inc.) and poly(ethylene oxide) (PEO, Sigma Aldrich) were used as received.

4.6.2 Synthetic Procedures

1,8-bis(4-mercaptophenyl)anthracene An aliquot of *tert*-nonyl mercaptan (6.1774 g, 38.53 mmol) was added into a DMF suspension of NaH (0.9097 g, 37.91 mmol in 100 mL) and stirred for 5 minutes under air-free conditions. A measure of solid 1,8-bis(4-(methylthio)phenyl)anthracene (2.00 g, 4.73 mmol) was added, and the suspension was refluxed at 160°C overnight. The reaction was quenched with addition of aqueous HCl (0.15 M, 100 mL) and the resulting yellow precipitate was isolated via vacuum filtration and washed with degassed water. The wet slurry was triturated repeatedly with Et_2O and dried *in vacuo* to afford a yellow solid. Yield: 1.55 g (80%). ^{1}H NMR (400 MHz, $CDCl_3$): δ 8.52 (1H, s), 8.45 (1H, s), 8.02 (2H, d), 7.51 (2H, t), 7.38 (3H, m), 7.34 (8H, m), 3.58 (2H, s). HRMS (CI+) m/z: $[M+H]^+$ Calcd for $C_{26}H_{19}S_2$ 395.0929. Found 395.0877. [M] Calcd for $C_{26}H_{18}S_2$ 394.0850. Found 394.0843.

***In situ* Generation of Disodium 1,8-bis(phenylthiolato) Anthracene and Reaction with $[Fe_6]^{2-}$** Under an argon box atmosphere, a vial charged with a suspension of 1,8-bis(4-mercaptophenyl)anthracene (74.6 mg, 0.189 mmol) in 10 mL THF. Solid NaH (8.4 mg, 0.35 mmol) was added to the suspension, resulting in the effervescence of H_2 gas. The resulting solution was added dropwise into a vial charged with $(Et_4N)_2[Fe_6(\mu_6\text{-}C)(CO)_{16}]$ (201.0 mg, 0.1904 mmol) in 3 mL THF, and the solution stirred overnight. The resulting violet solution was analyzed by rigorous ocular spectroscopy; however, no significant changes were detected.

Ph_3SbBr_2 On a Schlenk line under N_2 atmosphere, a 100-mL Schlenk flask charged with $SbPh_3$ (2.50 g, 7.08 mmol) in 20 mL Et_2O was cooled over a water-ice bath. A solution of liquid bromine (0.4 mL, 7.8 mmol) dissolved in 2 mL Et_2O was added dropwise and the suspension stirred for 1 h, resulting in a white precipitate. The supernatant was decanted and the solid washed with 20-mL portions of Et_2O until the washes appeared colorless. The

contents of the flask were dried *in vacuo*, affording a quantitative yield of white powder. ^{1}H NMR (400 MHz, $CDCl_3$): δ 8.18 (2H, m), δ 7.50 (3H, m).

Caution: The Et_2O washes collected during workup contain bromine which should be neutralized with sodium thiosulfate prior to disposal.

***In situ* Generation of $Ph_3Sb{=}S$ and Reaction with $[Fe_6]^{2-}$** On a Schlenk line under N_2 atmosphere, a 100-mL Schlenk flask charged with Ph_3SbBr_2 (204.4 mg, 0.399 mmol) and $S(SiMe_3)_2$ (69.6 mg, 0.390 mmol) in 40 mL toluene was heated and stirred at 80 °C for 2 d, providing a light-yellow solution. A separate 100-mL Schlenk flask was charged with $(Et_4N)_2[Fe_6(\mu_6\text{-}C)(CO)_{16}]$ (399.9 mg, 0.3788 mmol) suspended in 10 mL toluene and cooled over a water-ice bath. The $Ph_3Sb{=}S$ toluyl solution was cooled to room temperature and transferred *via* cannula into the stirring $[Fe_6]^{2-}$ solution, and the reaction mixture stirred overnight. Toluene was removed from the reaction *in vacuo*, and the flask was transferred into an argon-atmosphere glovebox. The semi-solid residue was extracted into pentane and passed through Celite until the pentane extraction obtained became only slightly colored. The pentane was removed *in vacuo* to afford a dark red solid. Selected IR peaks (**Figure 4.1**), solid, ν(CO): 2021(s), 1994(s) cm^{-1}. Continued extraction into pentane provided a lightly colored solution, which was subsequently dried. Selected IR peaks, solid, ν(CO): 2021(s), 1993(s), 1976(s) cm^{-1}. Similarly, extraction into Et_2O provided a concentrated (selected IR peaks, solid, ν(CO): 2023(m), 1992(s), 1976(s) cm^{-1}) and a dilute (selected IR peaks, solid, ν(CO): 1961(s,br) cm^{-1}) layer. Finally, the Et_2O-insoluble solids were extracted into FPh and dried. Selected IR peaks, solid, ν(CO): 1949(s,br) cm^{-1}. The remaining FPh-insoluble solid was not extracted.

$(NEt_4)_2\{[(CO)_{15}(\mu_6\text{-}C)Fe_6](\mu_4\text{-}S)[Fe_5(\mu_5\text{-}C)(CO)_{13}]\}$ (5) On a Schlenk line under N_2 atmosphere, a 50-mL flask was charged with a violet 10 mL solution of $(Et_4N)_2[Fe_6(\mu_6\text{-}C)(CO)_{16}]$ (399.9 mg, 0.3788 mmol) in 1,2-dichloroethane (DCE), and the

flask was cooled to –15 °C. Liquid S_2Cl_2 (51.2 mg, 0.3791 mmol) was diluted into 0.5 mL of DCE and added dropwise into the flask via syringe needle. The solution was allowed to warm to room temperature and stir overnight, resulting in a dark red-orange solution. The DCE was removed under reduced pressure and the flask transferred into a glovebox under argon atmosphere. The semi-solid material was extracted into Et_2O and any insoluble material adhered to the sides of the flask was mechanically loosened with a stainless-steel spatula. After several hours of stirring, *n*-hexane was added into the flask, and all volatiles were removed *in vacuo*. The resulting solid was washed with 10 mL portions of pentane until colorless. The remaining solid was treated similarly with Et_2O and fluorobenzene. The fluorobenzene extractions were collected, and Et_2O was introduced via vapor diffusion, affording dark red crystals suitable for X-ray diffraction. Yield: 101.3 mg (15%). Selected IR peaks (**Figure 4.15**), solid, ν(CO): 1973(s) cm^{-1}. $^{13}C\{^1H\}$ NMR (150.8 MHz, THF-H_8, **Figure 4.16**): interstitial carbide peaks at δ 483.8 and 478.0 ppm. Anal. calcd. for $C_{46}H_{40}O_{28}Fe_{11}SN_2$: C, 32.21; H, 2.35; N, 1.63. Found: C, 27.40; H, 1.68; N, 1.86.

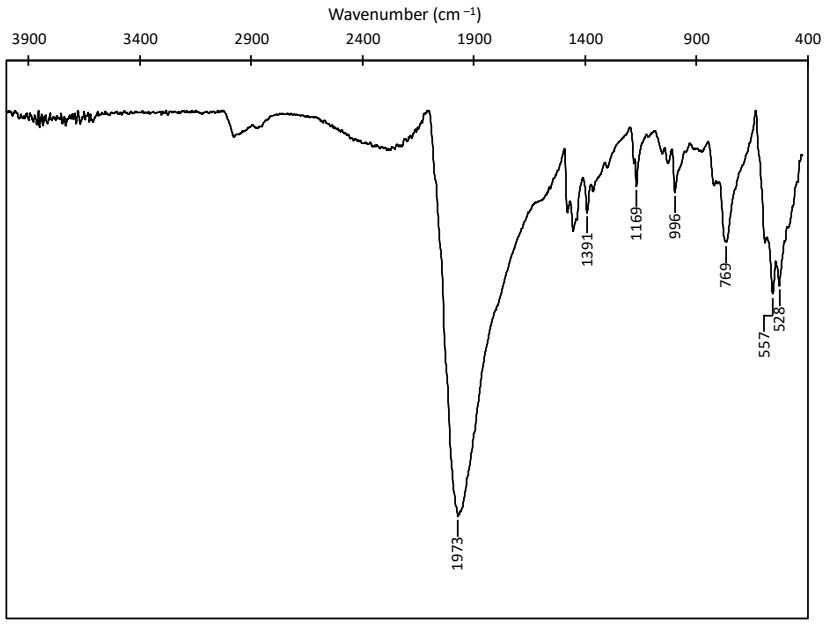

Figure 4.15 IR spectrum of $(NEt_4)_2\{[(CO)_{15}(\mu_6\text{-}C)Fe_6](\mu_4\text{-}S)[Fe_5(\mu_5\text{-}C)(CO)_{13}]\}$ (**5**) in the solid state.

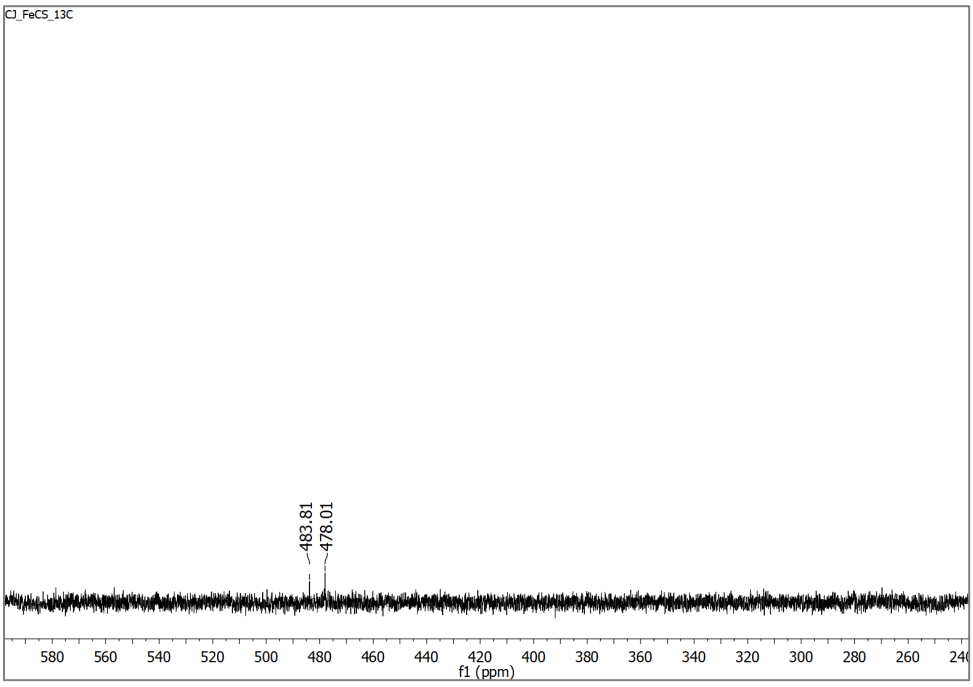

Figure 4.16 Carbide region of the ^{13}C NMR spectrum of $(NEt_4)_2\{[(CO)_{15}(\mu_6\text{-}C)Fe_6](\mu_4\text{-}S)[Fe_5(\mu_5\text{-}C)(CO)_{13}]\}$ (**5**) in THF-H_8 at 25 °C.

$(NEt_4)_2\{[Fe_5(\mu_5\text{-}C)(CO)_{13}]_2(\mu_4\text{-}S)\}$ (6) On a Schlenk line under N_2 atmosphere, a 50-mL flask was charged with a black 10 mL solution of $(Et_4N)_2[Fe_6(\mu_6\text{-}C)(CO)_{16}]$ (153.3 mg, 0.1452 mmol) and $[Fe_5(\mu_5\text{-}C)(CO)_{15}]$ (101.1 mg, 0.1421 mmol) in DCE, and the flask was cooled to –15 °C. A separate solution of elemental sulfur (5.6 mg, 0.17 mmol S atoms) was prepared in 10 mL of toluene and added dropwise into the flask via syringe needle. The solution was allowed to warm to room temperature and stir overnight, resulting in a dark red-orange solution. The solvent was reduced to half its volume *in vacuo*, and the solution was again stirred overnight. The remaining solution was dried *in vacuo* and the flask brought into a glovebox under argon atmosphere. The semi-solid material was extracted into Et_2O and any insoluble material adhered to the sides of the flask was mechanically loosened with a stainless-steel spatula. After several hours of stirring, *n*-hexane was added into the flask, and all volatiles were removed *in vacuo*. The black solid was washed with pentane then Et_2O until colorless washes of each were obtained. The Et_2O-insoluble solid was extracted into fluorobenzene, passed through a Celite filter, and vapor diffusion of Et_2O afforded dark red crystals suitable for X-ray diffraction. Selected IR peaks (**Figure 4.17**), solid, ν(CO): 2001(s), 1991(s), 1979(s), 1965(s) cm^{-1}. $^{13}C\{^1H\}$ NMR (150.8 MHz, THF-H_8, **Figure 4.18**): interstitial carbide peaks at δ 477.6 ppm. Anal. calcd. for $C_{44}H_{40}Fe_{10}N_2O_{26}S$: C, 32.96; H, 2.51; N, 1.75. Found: C, 32.78; H, 2.63; N, 1.53.

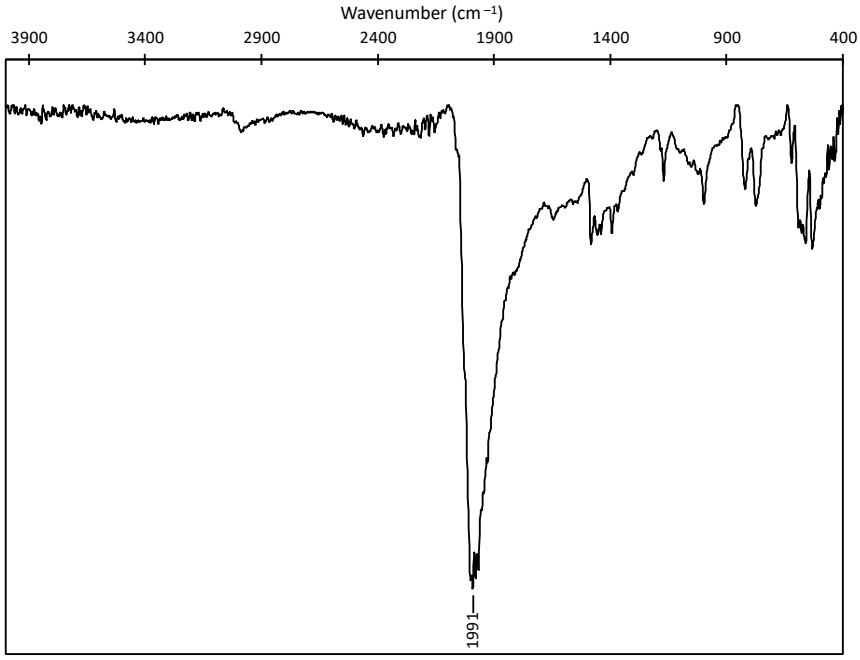

Figure 4.17 IR spectrum of $(NEt_4)_2\{[Fe_5(\mu_5\text{-}C)(CO)_{13}]_2(\mu_4\text{-}S)\}$ (**6**) in the solid state.

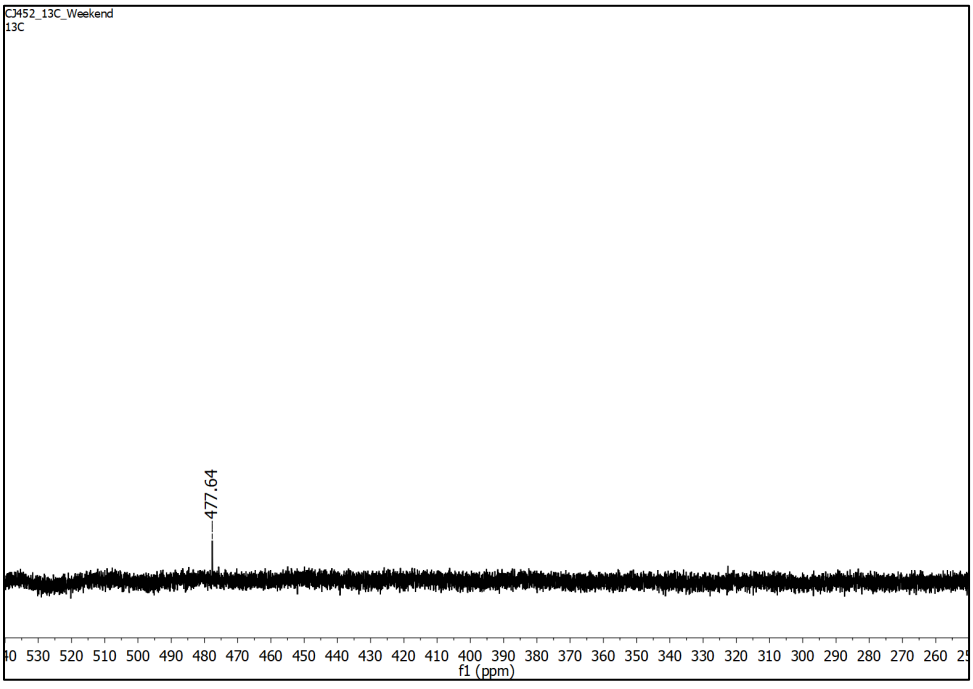

Figure 4.18 Carbide region of ^{13}C NMR spectrum of $(NEt_4)_2\{[Fe_5(\mu_5\text{-}C)(CO)_{13}]_2(\mu_4\text{-}S)\}$ (**6**) in THF-H_8 at 25 °C.

[{Fe$_4$(κ^2S–κ^4C)(CO)$_{10}$}(μ_3-S)(μ_3-S$_2$)Fe(CO)$_3$] (7) During the workup described in the synthesis of **5**, the Et_2O extraction was collected, passed through a Celite filter, and dried *in vacuo*. The solid was dissolved into pentane and incubated at –20 °C, affording dark-red crystals suitable for X-ray diffraction. Yield: 14.5 mg. Selected IR peaks (**Figure 4.19**), solid, ν(CO): 2095(w), 2070(m), 2035(s), 2002(s) cm^{-1}. $^{13}C\{^1H\}$ NMR (150.8 MHz, C_6D_6, **Figure 4.20**): interstitial carbide peaks at δ 312.8 ppm.

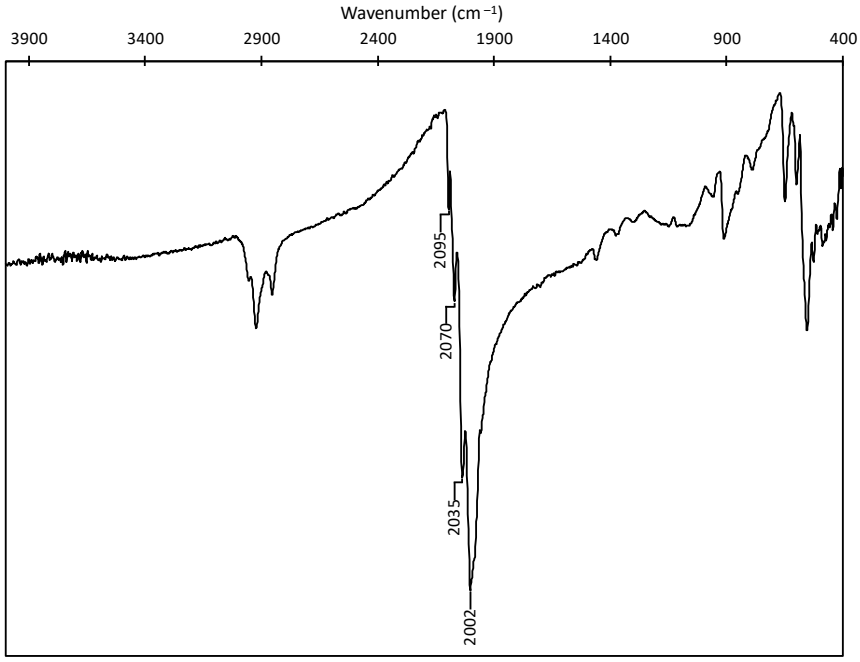

Figure 4.19 IR spectrum of [{Fe$_4$(κ^2S–κ^4C)(CO)$_{10}$}(μ_3-S)(μ_3-S$_2$)Fe(CO)$_3$] (**7**) in the solid state.

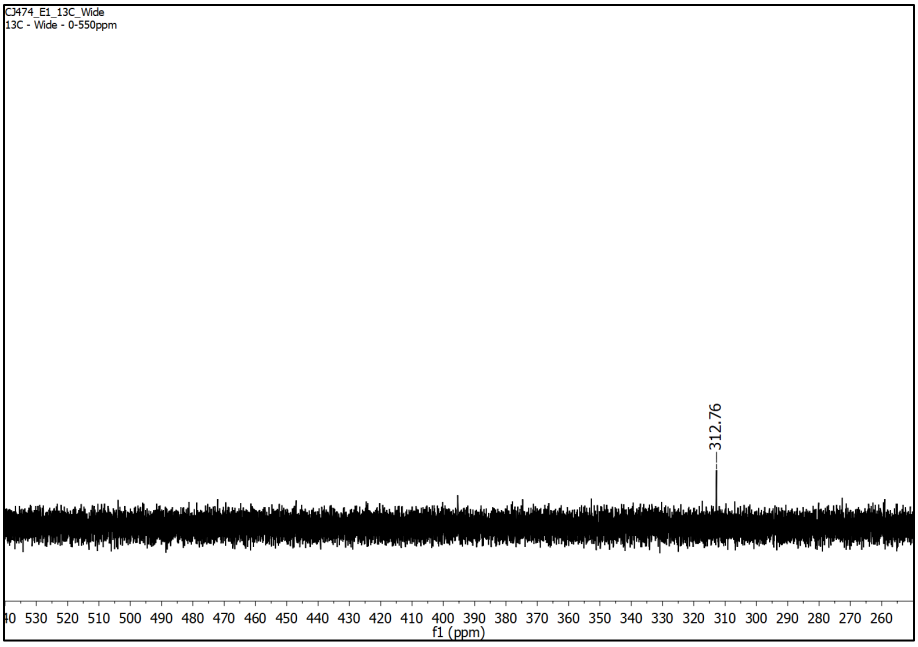

Figure 4.20 Carbide region of the ^{13}C NMR spectrum of [{$Fe_4(\kappa^2S–\kappa^4C)(CO)_{10}$}$(\mu_3\text{-}S)(\mu_3\text{-}S_2)Fe(CO)_3$] (**7**) in C_6D_6 at 25 °C.

[{$Fe_4(\kappa^2S–\kappa^4C)(CO)_{10}$}$(\mu_3\text{-}S)_2Fe(CO)_3$] (8) During the workup described in the synthesis of **6**, the pentane extraction was collected and passed through a silica gel column (2.5 cm × 8 cm) with hexanes as the eluent. The crude mixture separates into three distinct bands: (1) a deep red compound identified as $Fe_3S_2(CO)_9$, (2) a red-brown band as [$Fe_5(\mu_5\text{-}C)(CO)_{15}$] starting material, and (3) the target compound, which presents as a red-orange band. The red-orange band was collected and incubated at –20 °C, affording black crystals suitable for X-ray diffraction.

4.6.3 Additional Experimental Information

Physical Measurements NMR spectra were recorded at ambient temperature on a Varian VNMRS 600 instrument equipped with a 5 mm AutoXDB PFG probe. For **5** and **6**, a blank sample of THF-d_8 was used to lock and shim. Sample spectra were collected on

solutions with non-deuterated solvent (denoted below as THF-H_8) contained within an air-free sample tube. NMR of **7** was collected in C_6D_6. IR spectra were recorded on a Bruker Alpha spectrometer equipped with a diamond ATR crystal.

X-ray Photoelectron Spectroscopy XPS samples of $[Fe_6]^{2-}$, $[Fe_5]^0$, and **5** were prepared by dissolving 10 mg of the analyte into separate poly(ethylene oxide) (PEO)/MeCN (30.1 mg/mL) solutions. XPS sample of **3** was prepared as a solid powder packed onto copper tape. Spectra were recorded using a Kratos Axis Ultra XPS equipped with an Al−Kα X-ray source monochromated to 1486.6 eV. The photoelectron takeoff angle was 0°, and the pressure in the acquisition chamber was on the order of 10^{-9} Torr for all samples analyzed. Survey scans were obtained under the following conditions: pass energy of 80, 1.000 eV step size, and 300 ms dwell time. Region scans were obtained under the following conditions: pass energy of 20, 0.100 eV step size, and 1400 ms dwell time. All peaks in the spectra for $[Fe_6]^{2-}$, $[Fe_5]^0$, and **5** were referenced against the PEO C 1*s* peak (286.3 eV) for each dataset. Peaks in the spectra of **7** were referenced to adventitious carbon (284.8 eV).

Computational Methods Calculations were performed using the Firefly version 8 software package.[175] The electronic structures of the clusters were optimized from the X-ray crystal structure coordinates using the B3PW91 DFT functional. Energy and orbital calculations were initially performed using the 3-21G basis set, followed by geometry optimization in the same basis set. The optimized structures then underwent energy and orbital calculations, followed again by geometry optimizations using the 6-31G basis set. Final geometry optimizations and energy calculations were performed with applied heavy atom polarization functions (NDFUNC = 1). All calculations were performed using restricted Hartree-Fock and spin multiplicity of 1. The resulting structures and orbitals were visualized with MacMolPlt.[176]

Closing Remarks

The pursuit for model compounds of structural relevance to FeMoco has inspired many creative research avenues for synthetic chemists. Still, the "Holy Grail" for synthetic FeMoco modeling — a paramagnetic iron cluster with inorganic sulfides, an interstitial carbide, and heterometal Mo — remains unaccomplished. In our own venture to progress ever closer towards achieving this goal, we utilize carbidocarbonyl iron clusters as a synthetic starting point for structural modeling of the nitrogenase cofactor. These clusters have been studied for decades as catalytic candidates for hydrogenation, Fischer-Tropsch chemistry, H_2 evolution, and CO_2 reduction catalysis. In the context of nitrogenase chemistry, $[Fe_6(\mu_6\text{-}C)(CO)_{16}]^{2-}$ served a crucial role in the assignment of the interstitial carbide in FeMoco (and later FeVco). However, further utilization of the cluster for nitrogenase modelling is sparse, and it has been generally dismissed as difficult to synthetically control for the purposes of constructing a viable structural model.

Built upon the syntheses first described by Tachikawa, Muetterties, and Bradley, detailed synthetic procedures for the optimized generation of the various carbidocarbonyl iron clusters — including the novel $[Fe_6]^0$ cluster — have been related in Chapter 2. The cluster adhere well to the electron counting rules developed by Wade and Mingos for rationalizing the core structure and ligand count of polyhedral clusters. Thus in Chapter 3, electron-counting rules were used to determine appropriate molybdenum-bearing reagents for incorporation into the cluster core. Finally, the work discussed in Chapter 4 demonstrates a strategy to achieve successful CO→S ligand substitution *via* the utilization of electrophilic sulfur sources, leading to progressively higher oxidation state Fe sites. These synthetic approaches to heterometal incorporation and oxidative sulfur insertion will serve as fundamental stepping-stones towards future endeavors in utilizing and

functionalizing carbidocarbonyl iron clusters as synthetic precursors to ultimately biomimetically modeling the nitrogenase active site cluster. And so: Although members of the synthetic modelling community have previously dismissed carbidocarbonyl iron clusters as difficult to work with for nitrogenase-relevant modelling, it is our hope that the work relayed in this dissertation has demonstrated that you can — in fact — teach this old dog new tricks.

Appendix A: X-ray Crystal Structures and Relevant Experimental Details

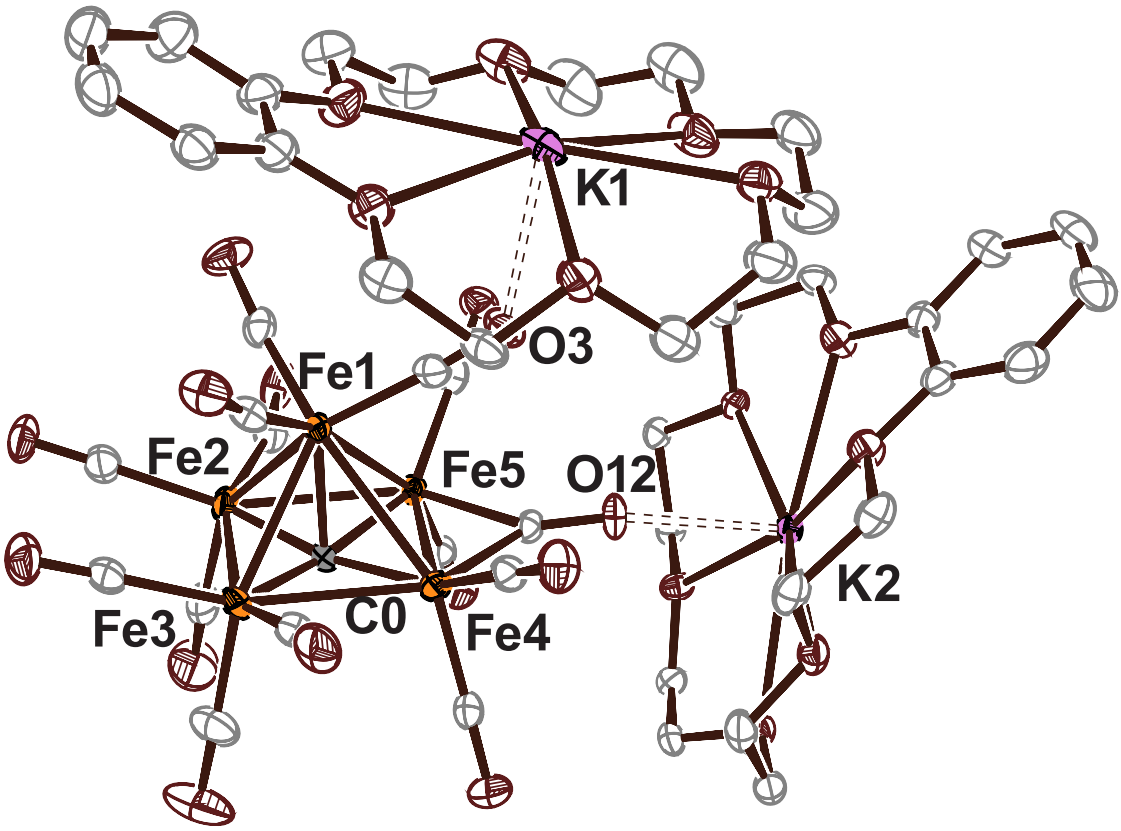

Figure A.1 Thermal ellipsoid plot (50% probability) of $[K(benzo\text{-}18\text{-}crown\text{-}6)]_2[Fe_5(\mu_5\text{-}C)(CO)_{14}]$ (**1**). Orange = Fe; Gray = C; Maroon = O; Pink = K. Hydrogen atoms and one DCE solvent molecule have been removed for clarity.

X-ray Diffraction and Crystal Structure Solution of [K(benzo-18-crown-6)]$_2$[Fe$_5$(μ_6-C)(CO)$_{13}$(μ_2-CO)] (1) Experimental Details

Crystals were grown as black needles by vapor diffusion of Et_2O into a solution of **1** in DCE at –20 °C. The data crystal had approximate dimensions: 0.31 × 0.11 × 0.11 mm. The data were collected on a Nonius Kappa CCD diffractometer using a Bruker AXS Apex II detector using a Mo Kα radiation source (λ = 0.71073 Å) with graphite monochromator. A total of 15685 frames of data were collected. Data reduction were performed using the SAINT V8.27B.[177] The structure was solved by direct methods using SHELXT[178] and refined by full-matrix least-squares on F^2 with anisotropic displacement parameters for the non-H atoms using SHELXL-2014/7.[179] A solvent molecule assigned as diethyl ether was badly disordered; and attempts to model the disorder were unsatisfactory. The contributions to the scattering factors due to these solvent molecules were removed by solvent mask in Olex2.[180] The function, $\Sigma w(|F_o|^2 - |F_c|^2)^2$, was minimized, where $w = 1/[(\sigma(F_o))^2 + (0.0326*P)^2 + (4.3345*P)]$ and $P = (|F_o|^2 + 2|F_c|^2)/3$. $R_w(F^2)$ refined to 0.1278, with R(F) equal to 0.0471 and a goodness of fit S = 1.035. The data were checked for secondary extinction effects but no correction was necessary. Neutral atom scattering factors and values used to calculate the linear absorption coefficient are from the International Tables for X-ray Crystallography.[181] All figures were generated using Ortep3 for Windows.[182]

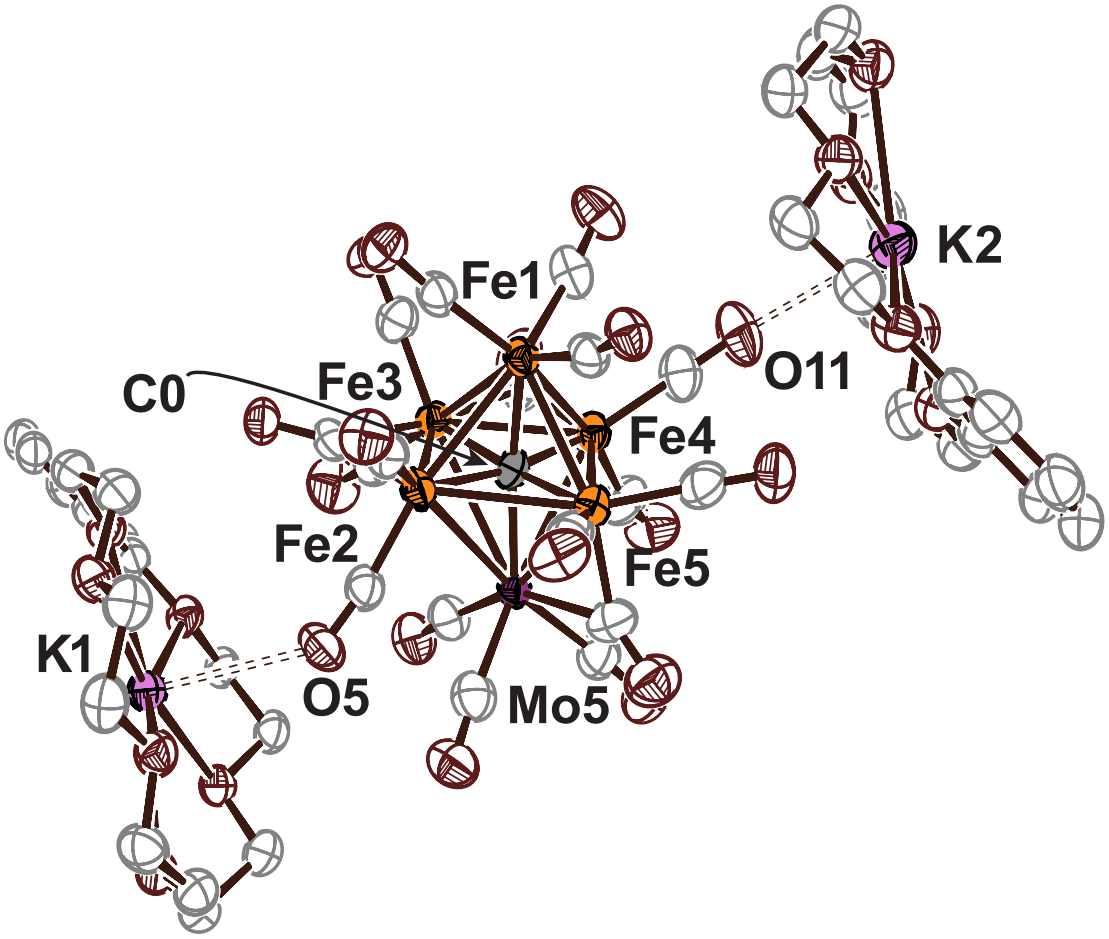

Figure A.2 Thermal ellipsoid plot (50% probability) of [K(benzo-18-crown-6)]$_2$[Fe$_5$Mo(μ_6-C)(μ_2-CO)$_3$(CO)$_{14}$] (**2**). Orange = Fe; Purple = Mo; Gray = C; Maroon = O; Pink = K. Hydrogen atoms and two FPh solvent molecules have been removed for clarity.

X-ray Diffraction and Crystal Structure Solution of [K(benzo-18-crown-6)]$_2$[Fe$_5$Mo(μ_6-C)(CO)$_{14}$(μ_2-CO)$_3$] (2) Experimental Details

Crystals were grown as black plates by diffusion of Et_2O into an FPh solution of **2**. The data crystal had approximate dimensions; 0.208 × 0.093 × 0.051 mm. The data were collected on an Agilent Technologies SuperNova Dual Source diffractometer using a μ-focus Cu Kα radiation source (λ = 1.5418 Å) with collimating mirror monochromators. Data collection, unit cell refinement and data reduction were performed using Agilent Technologies CrysAlisPro V 1.171.37.31.[183] The structure was solved by direct methods using SIR2004[184] and refined by full-matrix least-squares on F^2 with anisotropic displacement parameters for the non-H atoms using SHELXL-2014/7.[179] Structure analysis was aided by use of the programs PLATON98[185] and WinGX.[186] The hydrogen atoms were calculated in ideal positions with isotropic displacement parameters set to 1.2 × *U*eq of the attached atom.

Initially, the Mo atom was refined with a site occupancy factor of 1. However, the displacement parameters on the Mo were expected to be comparable to those of the Fe atoms, which were in an equivalent bonding environment. Upon refinement of the Mo atom, it was clear that its displacement parameters were higher than those of the Fe atoms. This fact was interpreted to mean that the Mo atom position was partially occupied. In subsequent refinements, the site occupancy for the Mo atom was refined while its displacement parameters were set to be equivalent to the Fe atoms. In this way, the Mo atom site occupancy refined to 78%. The site occupancy was fixed at this value in the final refinement model.

Additionally, two molecules of fluorobenzene appeared to be badly disordered. In one, there were two components of the disorder group. In the second molecule, it appeared that there were at least three orientations based on what appeared to be the F atom. The

disorder was modeled in the same way for each molecule. For example, the site occupancy for one component of the disorder was assigned to the variable x. The site occupancy for the second component was assigned to (1-x). A common isotropic displacement parameter was refined for all non-H atoms of the two components while refining x. The geometry of all the different molecules of fluorobenzene was restrained to be equivalent throughout the refinement procedure. Upon convergence of x, the site occupancy factors were fixed, and the displacement parameters were refined with restraints to keep them approximately equivalent. Essentially, the same procedure was applied to the three-component disordered fluorobenzene except that the site occupancy factors were restrained to sum to unity using the SUMP instruction in SHELXTL-2016/6. The data were checked for secondary extinction effects, but no correction was necessary. Neutral atom scattering factors and values used to calculate the linear absorption coefficient are from the International Tables for X-ray Crystallography (1992).[181] Figures were generated using Ortep3 for Windows.[182]

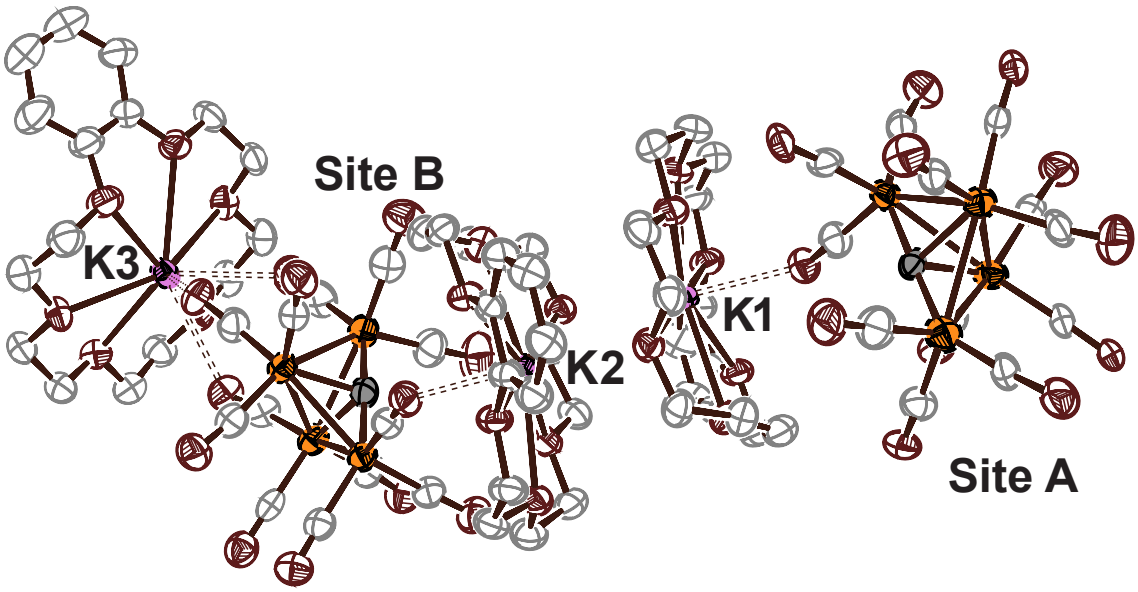

Figure A.3 Thermal ellipsoid plot (50% probability) of $[K(benzo\text{-}18\text{-}crown\text{-}6)]_2[Fe_4(\mu_4\text{-}C)(CO)_{12}]$ (**3**). Orange = Fe; Gray = C; Maroon = O; Pink = K. Hydrogen atoms and two FPh solvent molecules have been removed for clarity.

X-ray Diffraction and Crystal Structure Solution of [K(benzo-18-crown-6)]$_2$[Fe$_4$(μ_4-C)(CO)$_{12}$] (3) Experimental Details

Crystals were grown as black plates by diffusion of Et_2O into a fluorobenzene solution of [K(benzo-18-crown-6)]$_2$[Fe$_4$(μ_4-C)(CO)$_{12}$]. The data crystal had approximate dimensions: 0.120 × 0.089 × 0.038 mm. The data was collected on an Agilent Technologies SuperNova Dual Source diffractometer using a μ-focus Cu Kα radiation source (λ = 1.5418 Å) with collimating mirror monochromators. Data collection, unit cell refinement, and data reduction were performed using Agilent Technologies CrysAlisPro V 1.171.37.31.[183] The structure was solved by direct methods using SHELXT[178] and refined by full-matrix least-squares on F^2 with anisotropic displacement parameters for the non-H atoms using SHELXL-2014/7.[179] Structure analysis was aided by use of the programs PLATON98[185] and WinGX.[186] The hydrogen atoms were calculated in ideal positions with isotropic displacement parameters set to 1.2 × *U*eq of the attached atom. The function, $\Sigma w(|F_o|^2 - |F_c|^2)^2$, was minimized, where $w = 1/[(\sigma(F_o))^2 + (0.0326*P)^2 + (4.3345*P)]$ and $P = (|F_o|^2 + 2|F_c|^2)/3$. $R_w(F^2)$ refined to 0**.** 1968, with R(F) equal to 0.0748 and a goodness of fit S = 0.874. The data were checked for secondary extinction effects, but no correction was necessary. Neutral atom scattering factors and values used to calculate the linear absorption coefficient are from the International Tables for X-ray Crystallography (1992).[181] All figures were generated using Ortep3 for Windows.[182]

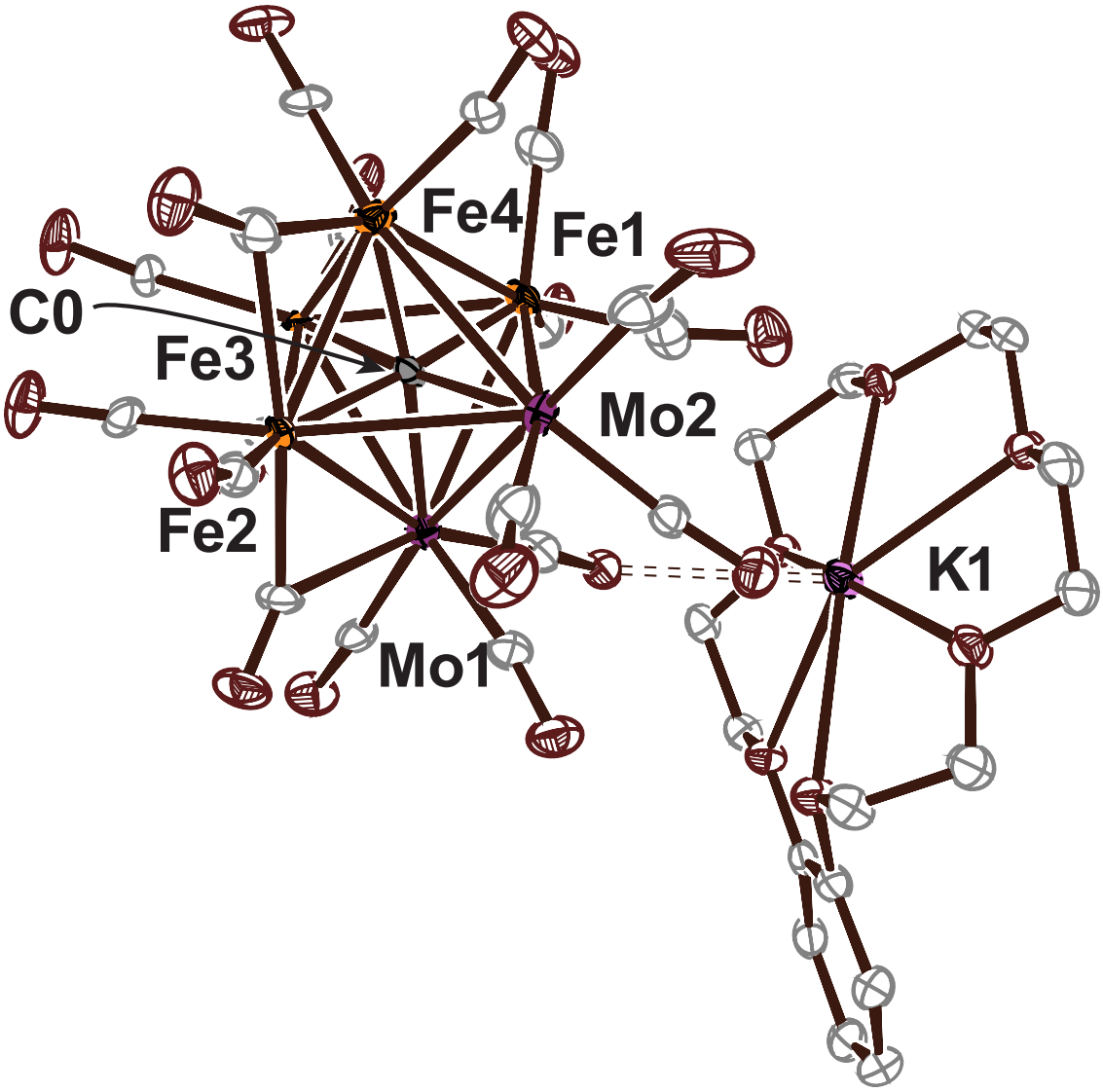

Figure A.4 Thermal ellipsoid plot (50% probability) of $[K(benzo\text{-}18c6)]_2[Fe_4Mo_2(\mu_6\text{-}C)(CO)_{16}(\mu_2\text{-}CO)_2]$ (**4**). Orange = Fe; Purple = Mo; Gray = C; Maroon = O; Pink = K. Hydrogen atoms have been removed for clarity.

X-ray Diffraction and Crystal Structure Solution of [K(benzo-18-crown-6)]$_2$[Fe$_4$Mo$_2$(μ_6-C)(CO)$_{16}$(μ_2-CO)$_2$] (4) Experimental Details

Crystals were grown as black plates by diffusion of Et_2O into a solution of [K(benzo-18-crown-6)]$_2$[Fe$_4$Mo$_2$(μ_6-C)(CO)$_{16}$(μ_2-CO)$_2$] dissolved in 1:1 1,2-dichloroethane/fluorobenzene. The data crystal had approximate dimensions: 0.29 × 0.22 × 0.18 mm. The data were collected on a Rigaku AFC12 diffractometer with a Saturn 724+ CCD using a graphite monochromator with MoKα radiation (λ = 0.71073Å). A total of 6698 frames of data were collected using ω-scans with a scan range of 0.5° and a counting time of 45 seconds per frame. The data were collected at 100 K using a Rigaku XStream low temperature device.

Data reduction were performed using the Rigaku Americas Corporation's Crystal Clear version 1.40.[187] The structure was solved by direct methods using SHELXT[178] and refined by full-matrix least-squares on F^2 with anisotropic displacement parameters for the non-H atoms using SHELXL-2014/7.[179] The hydrogen atoms on carbon were calculated in ideal positions with isotropic displacement parameters set to 1.2 × U_{eq} of the attached atom. The function, $\Sigma w(|F_o|^2 - |F_c|^2)^2$, was minimized, where $w = 1/[(\sigma(F_o))^2 + (0.0326*P)^2 + (4.3345*P)]$ and $P = (|F_o|^2 + 2|F_c|^2)/3$. $R_w(F^2)$ refined to 0.1631, with R(F) equal to 0.0707 and a goodness of fit S = 1.503. The data were checked for secondary extinction effects, but no correction was necessary. Neutral atom scattering factors and values used to calculate the linear absorption coefficient are from the International Tables for X-ray Crystallography (1992).[181] All figures were generated using Ortep3 for Windows.[182]

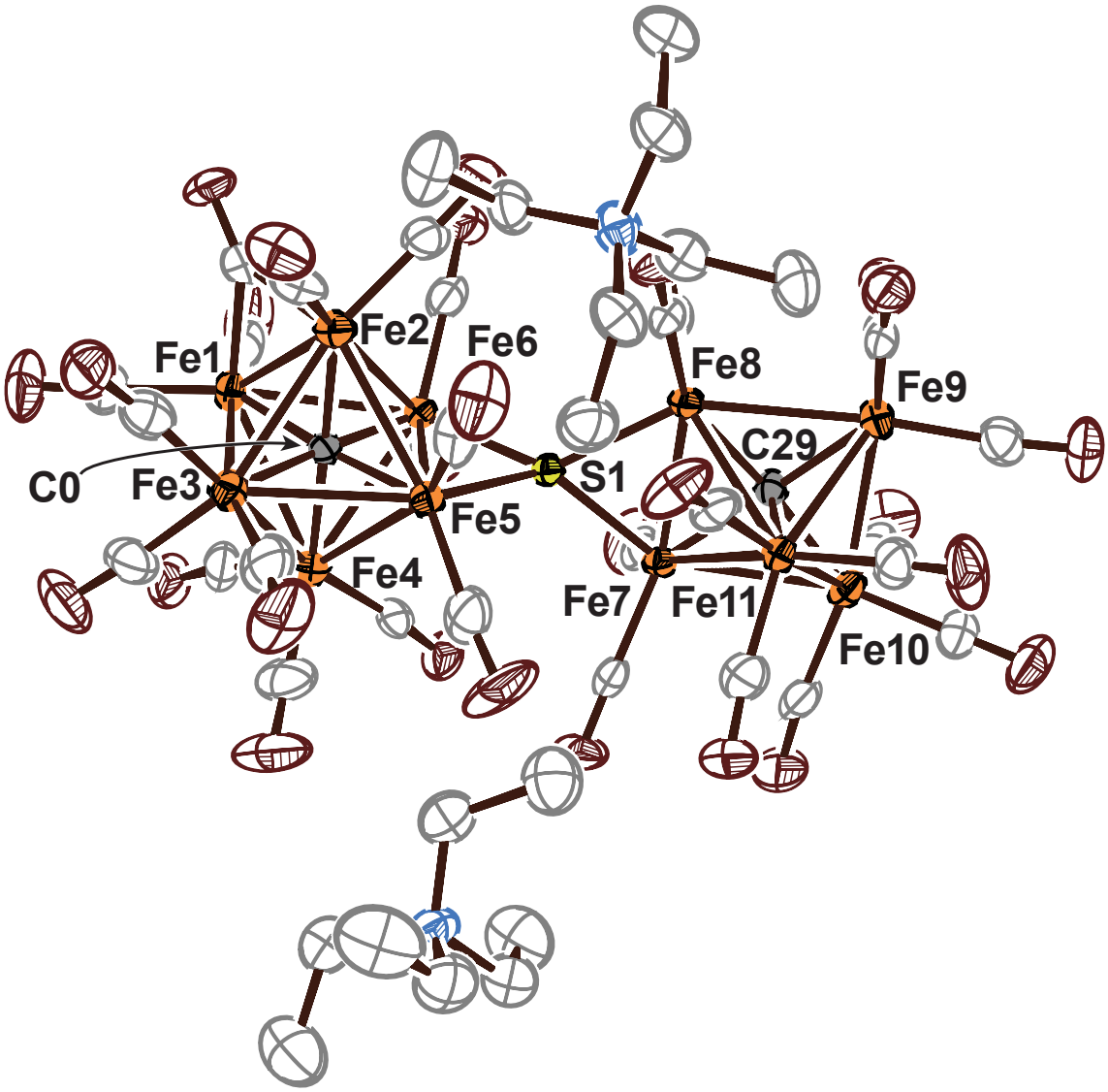

Figure A.5 Full thermal ellipsoid plot (50% probability) of $(NEt_4)_2\{[(CO)_{15}(\mu_6\text{-}C)Fe_6](\mu_4\text{-}S)[Fe_5(\mu_5\text{-}C)(CO)_{13}]\}$ (**5**). Orange = Fe; Gray = C; Yellow = S; Maroon = O; Blue = N. Hydrogen atoms omitted for clarity.

X-ray Diffraction and Crystal Structure Solution of $(NEt_4)_2\{[(CO)_{15}(\mu_6\text{-}C)Fe_6](\mu_4\text{-}S)[Fe_5(\mu_5\text{-}C)(CO)_{13}]\}$ (5) Experimental Details

Crystals were grown as dark red prisms by vapor diffusion of Et_2O into a fluorobenzene solution of **5**. The data crystal had approximate dimensions: 0.12 × 0.10 × 0.04 mm. The data was collected on a Rigaku AFC12 diffractometer with a Saturn 724+ CCD using a graphite monochromator with Mo Kα radiation (λ = 0.71073 Å). A total of 69325 frames of data were collected using ω-scans with a scan range of 0.5° and a counting time of 45 seconds per frame. The data were collected at 100 K using a Rigaku XStream low temperature device.

Data reduction were performed using the Rigaku Americas Corporation's Crystal Clear version 1.40.[187] The structure was solved by direct methods using SHELXT[178] and refined by full-matrix least-squares on F^2 with anisotropic displacement parameters for the non-H atoms using SHELXL-2014/7.[179] The hydrogen atoms on carbon were calculated in ideal positions with isotropic displacement parameters set to 1.2 × U_{eq} of the attached atom. The refinement exhibited signs of twinning, and so the utility TwinRotMat in Platon98[185] was used to the twin law. The function, $\Sigma w(|F_o|^2 - |F_c|^2)^2$, was minimized, where $w = 1/[(\sigma(F_o))^2 + (0.0326*P)^2 + (4.3345*P)]$ and $P = (|F_o|^2 + 2|F_c|^2)/3$. $R_w(F^2)$ refined to 0.2119, with R(F) equal to 0.0823 and a goodness of fit S = 1.037. The data were checked for secondary extinction effects but no correction was necessary. Neutral atom scattering factors and values used to calculate the linear absorption coefficient are from the International Tables for X-ray Crystallography.[181] All figures were generated using Ortep3 for Windows.[182]

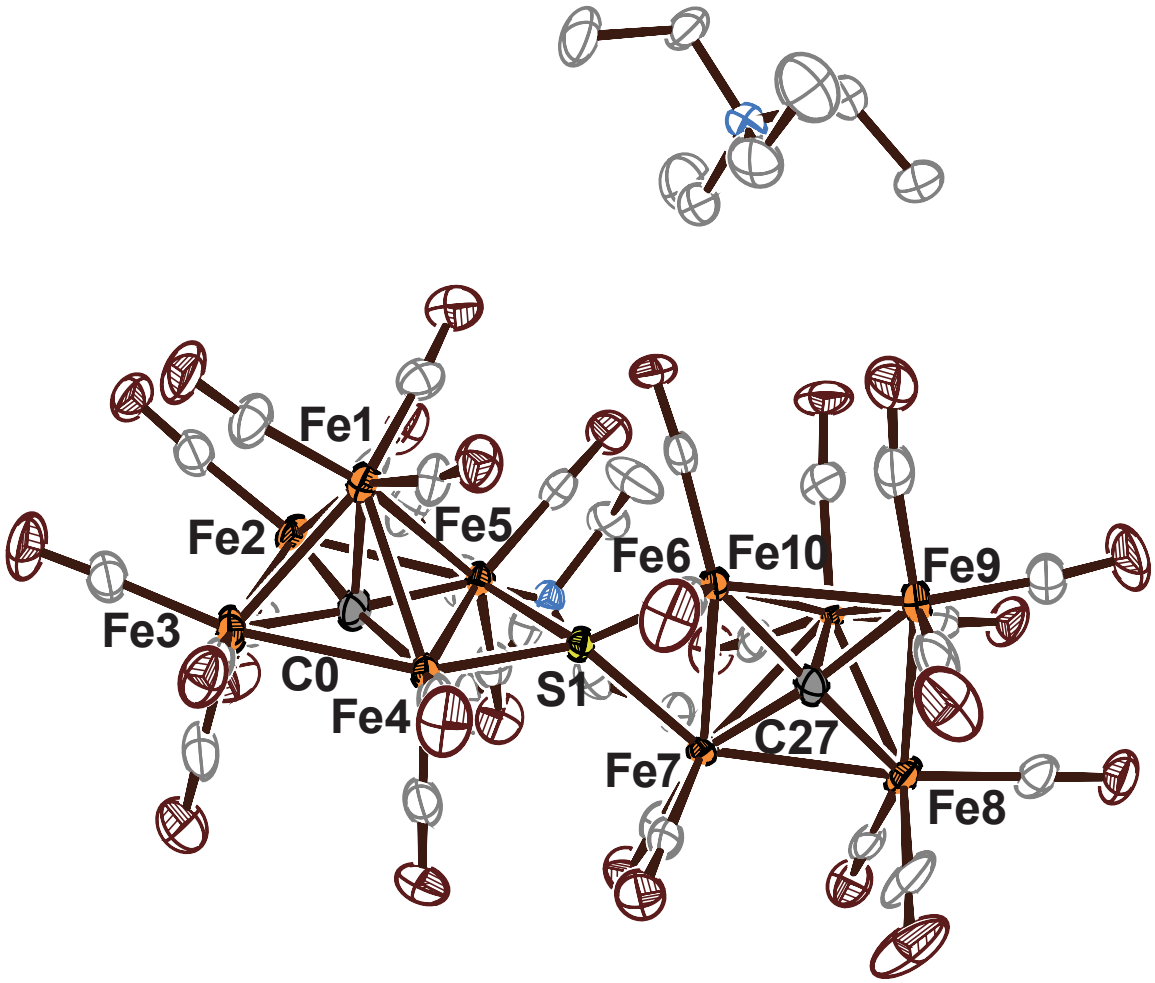

Figure A.6 Full thermal ellipsoid plot (50% probability) of $(NEt_4)_2\{[Fe_5(\mu_5\text{-}C)(CO)_{13}]_2(\mu_4\text{-}S)\}$ (**6**). Orange = Fe; Gray = C; Yellow = S; Maroon = O; Blue = N. Hydrogen atoms omitted for clarity.

X-ray Diffraction and Crystal Structure Solution of $(NEt_4)_2\{[Fe_5(\mu_5\text{-}C)(CO)_{13}]_2(\mu_4\text{-}S)\}$ (6) Experimental Details

Crystals were grown as dark red prisms by vapor diffusion of Et_2O into a fluorobenzene solution of **6**. The data crystal had approximate dimensions: 0.30 × 0.19 × 0.13 mm. The data were collected on an Agilent Technologies SuperNova Dual Source diffractometer using a μ-focus Mo Kα radiation source (λ = 0.71073 Å) with collimating mirror monochromators. A total of 15527 frames of data were collected using ω-scans with a scan range of 0.5° and a counting time of 45 seconds per frame. The data were collected at 99.9 K using a Rigaku XStream low temperature device. Details of crystal data, data collection and structure refinement are listed in **Table S1**.

Data reduction were performed using the Agilent Technologies CrysAlisPro V 1.171.37.31.[183] The structure was solved by direct methods using SHELXT[178] and refined by full-matrix least-squares on F^2 with anisotropic displacement parameters for the non-H atoms using SHELXL-2014/7.[179] The hydrogen atoms on carbon were calculated in ideal positions with isotropic displacement parameters set to 1.2 × U_{eq} of the attached atom. The function, $\Sigma w(|F_o|^2 - |F_c|^2)^2$, was minimized, where $w = 1/[(\sigma(F_o))^2 + (0.0326*P)^2 + (4.3345*P)]$ and $P = (|F_o|^2 + 2|F_c|^2)/3$. $R_w(F^2)$ refined to 0.1631, with R(F) equal to 0.0747 and a goodness of fit S = 0.868. The data were checked for secondary extinction effects but no correction was necessary. Neutral atom scattering factors and values used to calculate the linear absorption coefficient are from the International Tables for X-ray Crystallography.[181] All figures were generated using Ortep3 for Windows.[182]

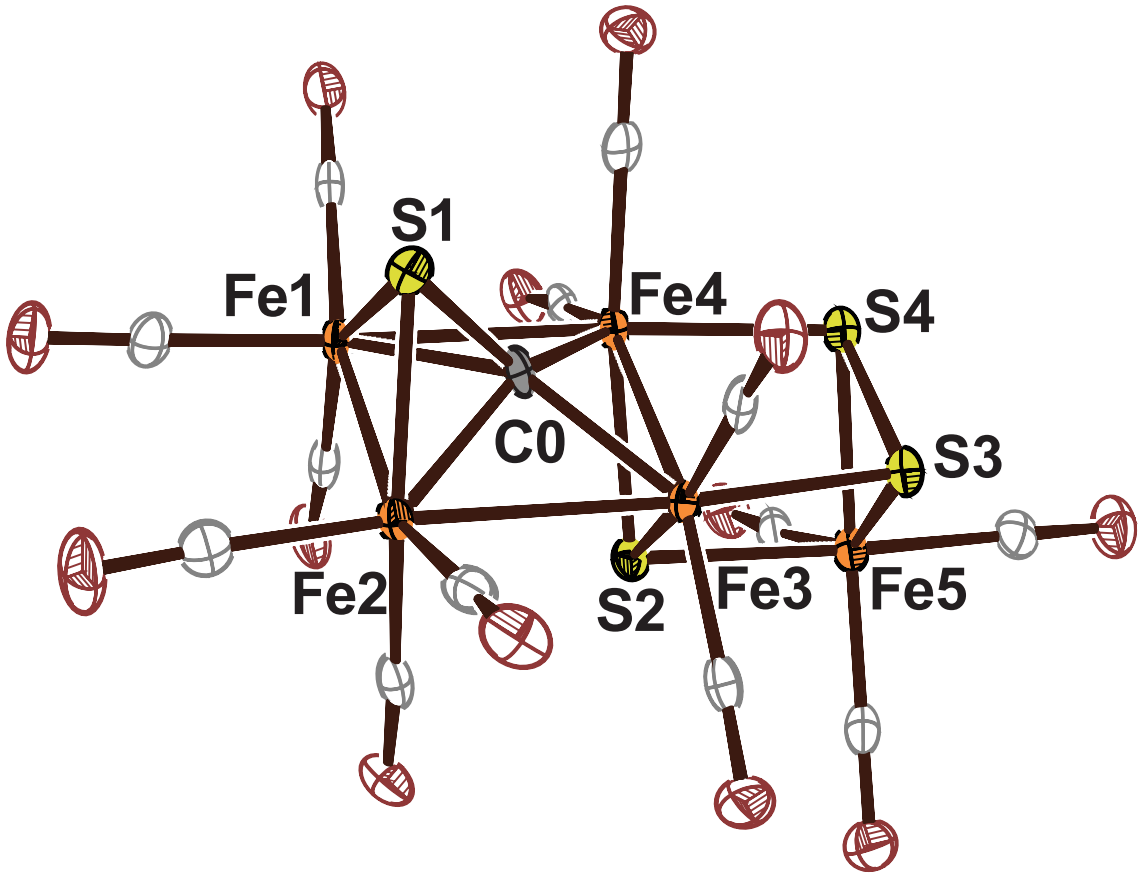

Figure A.7 Thermal ellipsoid plots (50% probability) of [{$Fe_4(\kappa_2S–\kappa_4C)(CO)_{10}$}($\mu_3$-S)($\mu_3$-$S_2$)$Fe(CO)_3$] (**7**). Orange = Fe; Gray = C; Yellow = S; Maroon = O.

X-ray Diffraction and Crystal Structure Solution of [{$Fe_4(\kappa^2S–\kappa^4C)(CO)_{10}$}($\mu_3$-S)($\mu_3$-$S_2$)$Fe(CO)_3$] (7) Experimental Details

Crystals were grown as red prisms by cooling of a saturated Et_2O solution of **7** to –20 °C. The data crystal had approximate dimensions: 0.23 × 0.07 × 0.07 mm. The data were collected on a Nonius Kappa CCD diffractometer using a Bruker AXS Apex II detector using a Mo Kα radiation source (λ = 0.71073 Å) with graphite monochromator. A total of 5779 frames of data were collected using ω-scans with a scan range of 0.7° and a counting time of 42 seconds per frame. The data were collected at 100.1 K using a Rigaku XStream low temperature device.

Data reduction were performed using the SAINT V8.27B.[177] The structure was solved by direct methods using SHELXT[178] and refined by full-matrix least-squares on F^2 with anisotropic displacement parameters for the non-H atoms using SHELXL-2014/7.[179] The function, $\Sigma w(|F_o|^2 - |F_c|^2)^2$, was minimized, where $w = 1/[(\sigma(F_o))^2 + (0.0326*P)^2 + (4.3345*P)]$ and $P = (|F_o|^2 + 2|F_c|^2)/3$. $R_w(F^2)$ refined to 0.0927, with R(F) equal to 0.0480 and a goodness of fit S = 0.9545. The data were checked for secondary extinction effects but no correction was necessary. Neutral atom scattering factors and values used to calculate the linear absorption coefficient are from the International Tables for X-ray Crystallography.[181] All figures were generated using Ortep3 for Windows.[182]

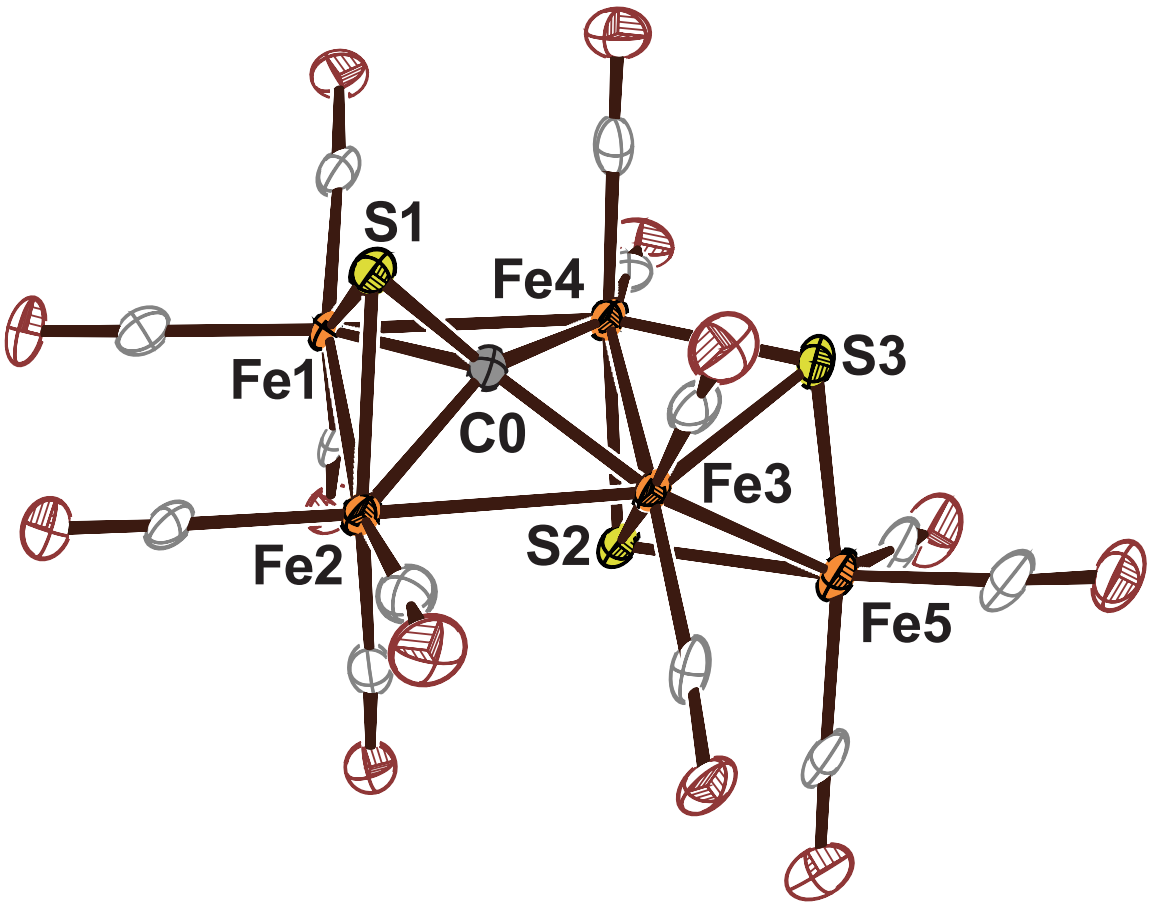

Figure A.8 Thermal ellipsoid plots (50% probability) of [{$Fe_4(\kappa_2S–\kappa_4C)(CO)_{10}$}($\mu_3$-$S)_2Fe(CO)_3$] (**8**). Orange = Fe; Gray = C; Yellow = S; Maroon = O.

X-ray Diffraction and Crystal Structure Solution of [{$Fe_4(\kappa^2S–\kappa^4C)(CO)_{10}$}($\mu_3$-$S)_2Fe(CO)_3$] (8) Experimental Details

Crystals were grown as dark plates by cooling of a saturated pentane solution of **8** to –20 °C. The data crystal had approximate dimensions: 0.12 × 0.06 × 0.03 mm. The data were collected on an Agilent Technologies SuperNova Dual Source diffractometer using a μ-focus Cu Kα radiation source (λ = 1.54184 Å) with collimating mirror monochromators. A total of 4387 frames of data were collected using ω-scans with a scan range of 0.5° and a counting time of 45 seconds per frame. The data were collected at 99.9 K using a Rigaku XStream low temperature device.

Data reduction were performed using the Agilent Technologies CrysAlisPro V 1.171.37.31.[183] The structure was solved by direct methods using SHELXT[178] and refined by full-matrix least-squares on F^2 with anisotropic displacement parameters for the non-H atoms using SHELXL-2014/7.[179] The function, $\Sigma w(|F_o|^2 – |F_c|^2)^2$, was minimized, where $w = 1/[(\sigma(F_o))^2 + (0.0326*P)^2 + (4.3345*P)]$ and $P = (|F_o|^2 + 2|F_c|^2)/3$. $R_w(F^2)$ refined to 0.1404, with R(F) equal to 0.0522 and a goodness of fit S = 1.0382. The data were checked for secondary extinction effects but no correction was necessary. Neutral atom scattering factors and values used to calculate the linear absorption coefficient are from the International Tables for X-ray Crystallography.[181] All figures were generated using Ortep3 for Windows.[182]

Appendix B: Crystallographic Bond Metrics

Table B.1 Selected bond distances for **1** and **2**.

	Bond (1)	**Length (Å)**	**Bond (2)**	**Length (Å)**
Fe_{ax}–$C_{carbide}$	Fe1–C0	1.994(3)	Fe1–C0	1.937(6)
Fe_{eq}–$C_{Carbide}$	Fe2–C0	1.859(3)	Fe2–C0	1.896(5)
	Fe3–C0	1.857(3)	Fe3–C0	1.902(4)
	Fe4–C0	1.860(3)	Fe4–C0	1.887(5)
	Fe5–C0	1.887(3)	Fe5–C0	1.881(4)
Fe_{ax}–Fe_{eq}	Fe1–Fe2	2.5990(6)	Fe1–Fe2	2.639(1)
	Fe1–Fe3	2.5757(7)	Fe1–Fe3	2.632(1)
	Fe1–Fe4	2.6300(7)	Fe1–Fe4	2.640(1)
	Fe1–Fe5	2.5969(6)	Fe1–Fe5	2.629(1)
Fe_{eq}–Fe_{eq}	Fe2–Fe3	2.6961(7)	Fe2–Fe3	2.586(1)
	Fe3–Fe4	2.6552(6)	Fe3–Fe4	2.573(1)
	Fe4–Fe5	2.5289(7)	Fe4–Fe5	2.800(1)
	Fe5–Fe2	2.6250(6)	Fe5–Fe2	2.718(1)
Mo–C			Mo1–C0	2.113(6)
Mo–Fe_{eq}			Mo1–Fe2	2.9666(9)
			Mo1–Fe3	3.054(1)
			Mo1–Fe4	2.861(1)
			Mo1–Fe5	2.769(1)

Table B.2 Selected bond distances for **3** and **4**.

	Bond (3)	**Length (Å)**	**Bond (4)**	**Length (Å)**
Fe–$C_{carbide}$	Fe1A–C0A	1.75(1)	Fe3–C0	1.91(1)
	Fe1B–C0B	1.783(7)	Fe4–C0	1.95(2)
	Fe2A–C0A	1.77(1)	Fe5–C0	1.90(1)
	Fe2B–C0B	1.797(7)	Fe6–C0	1.90(1)
	Fe3A–C0A	1.99(1)		
	Fe3B–C0B	1.95(1)		
	Fe4A–C0A	1.96(2)		
	Fe4B–C0B	1.973(8)		
Mo–$C_{carbide}$			Mo1–C0	2.12(1)
			Mo2–C0	2.11(2)
Fe-Fe	Fe1A–Fe3A	2.621(4)	Fe3–Fe4	2.556(4)
	Fe1B–Fe3B	2.619(2)	Fe3–Fe5	2.628(5)
	Fe1A–Fe4A	2.661(4)	Fe3–Fe6	2.664(4)
	Fe1B–Fe4B	2.633(2)	Fe4–Fe5	2.736(3)
	Fe2A–Fe3A	2.659(3)	Fe4–Fe6	2.644(3)
	Fe2B–Fe3B	2.643(2)		
	Fe2A–Fe4A	2.610(3)		
	Fe2B–Fe4B	2.644(2)		
	Fe3A–Fe4A	2.566(4)		
	Fe3B–Fe4B	2.534(2)		
Mo–Fe			Mo1–Fe4	2.872(3)
			Mo1–Fe5	2.858(3)
			Mo1–Fe6	2.926(3)
			Mo2–Fe4	2.944(4)
			Mo2–Fe5	2.917(2)
			Mo2–Fe6	2.816(2)
Mo–Mo			Mo1–Mo2	3.077(3)

Table B.3 Selected bond distances for **5** and **6**.

	Bond (5)	**Length (Å)**	**Bond (6)**	**Length (Å)**
Fe–$C_{carbide}$	Fe1–C0	1.87(1)	Fe1–C0	1.957(7)
	Fe2–C0	1.880(8)	Fe2–C0	1.861(6)
	Fe3–C0	1.88(1)	Fe3–C0	1.866(6)
	Fe4–C0	1.904(8)	Fe4–C0	1.875(6)
	Fe5–C0	1.88(1)	Fe5–C0	1.872(6)
	Fe6–C0	1.90(1)	Fe6–C27	1.878(6)
	Fe7–C29	1.864(9)	Fe7–C27	1.857(6)
	Fe8–C29	1.865(9)	Fe8–C27	1.877(7)
	Fe9–C29	1.870(9)	Fe9–C27	1.867(6)
	Fe10–C29	1.854(9)	Fe10–C27	1.964(6)
	Fe11–C29	1.95(1)		
Fe–S	S1–Fe5	2.189(3)	S1–Fe4	2.175(2)
	S1–Fe6	2.203(3)	S1–Fe5	2.176(2)
	S1–Fe7	2.188(3)	S1–Fe6	2.168(2)
	S1–Fe8	2.169(2)	S1–Fe7	2.180(2)
Fe–Fe	Fe1–Fe2	2.571(2)	Fe1–Fe2	2.614(1)
	Fe1–Fe3	2.663(2)	Fe1–Fe3	2.614(1)
	Fe1–Fe4	2.750(2)	Fe1–Fe4	2.650(1)
	Fe1–Fe6	2.680(2)	Fe1–Fe5	2.650(1)
	Fe2–Fe3	2.670(2)	Fe2–Fe3	2.681(2)
	Fe2–Fe5	2.655(2)	Fe2–Fe5	2.672(1)
	Fe2–Fe6	2.718(2)	Fe3–Fe4	2.677(1)
	Fe3–Fe4	2.622(2)	Fe4–Fe5	2.520(1)
	Fe3–Fe5	2.733(2)	Fe6–Fe7	2.508(1)
	Fe4–Fe5	2.685(2)	Fe6–Fe9	2.654(1)
	Fe4–Fe6	2.686(2)	Fe6–Fe10	2.646(1)
	Fe5–Fe6	2.578(2)	Fe7–Fe8	2.692(1)
	Fe7–Fe8	2.494(2)	Fe7–Fe10	2.668(1)
	Fe5–Fe6	2.678(2)	Fe8–Fe9	2.700(2)
	Fe5–Fe6	2.671(2)	Fe8–Fe10	2.568(1)
	Fe5–Fe6	2.681(2)	Fe9–Fe10	2.620(1)
	Fe5–Fe6	2.669(2)		
	Fe5–Fe6	2.657(2)		
	Fe5–Fe6	2.600(2)		
	Fe5–Fe6	2.593(2)		

Table B.4 Selected bond distances for **7** and **8**.

	Bond (7)	**Length (Å)**	**Bond (8)**	**Length (Å)**
Fe–$C_{carbide}$	Fe1–C0	2.011(4)	Fe1–C0	1.959(5)
	Fe2–C0	1.995(4)	Fe2–C0	1.975(5)
	Fe3–C0	1.957(5)	Fe3–C0	1.975(5)
	Fe4–C0	1.932(4)	Fe4–C0	1.932(6)
C–$Plane_{Fe_4}$		0.59		0.54
C–S	C0–S1	1.714(5)	C0–S1	1.727(5)
Fe–S	S1–Fe1	2.252(1)	S1–Fe1	2.263(1)
	S1–Fe2	2.248(1)	S1–Fe2	2.257(2)
	S2–Fe3	2.265(1)	S2–Fe3	2.256(1)
	S2–Fe4	2.264(1)	S2–Fe4	2.297(2)
	S2–Fe5	2.334(1)	S2–Fe5	2.243(2)
	S3–Fe3	2.269(1)	S3–Fe3	2.251(2)
	S3–Fe5	2.282(1)	S3–Fe4	2.194(2)
	S4–Fe4	2.270(1)	S3–Fe5	2.205(2)
	S4–Fe5	2.271(1)		
S–S	S3–Fe4	2.048(2)		
Fe–Fe	Fe1–Fe2	2.6145(9)	Fe1–Fe2	2.629(1)
	Fe1–Fe4	2.7271(9)	Fe1–Fe4	2.782(1)
	Fe2–Fe3	2.7484(9)	Fe2–Fe3	2.775(1)
	Fe3–Fe4	2.5602(9)	Fe3–Fe4	2.464(1)
			Fe3–Fe5	2.616(1)

Appendix C: Miscellaneous Data

Table C.1 Bond metrics of CO-supported [$Fe_2(\mu_4$-S)Fe_2] motifs as found in the Cambridge Structural Database. In total, 54 structures with available 3D coordinates were found, containing 66 [$Fe_2(\mu_4$-S)Fe_2] motifs. **∠FeSFe** refers only to the acute angles at the S atom where the two Fe are bonded to each other.

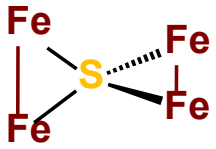

REFCODE	∠FeSFe (°)		Fe–S (Å)			
AXEVOO	69.72	69.02	2.247	2.245	2.236	2.235
	69.49	68.07	2.261	2.254	2.253	2.238
AXEVUU	68.88	68.12	2.244	2.239	2.239	2.238
	69.00	68.95	2.239	2.238	2.236	2.229
BAFHUM	72.35	68.31	2.262	2.258	2.246	2.243
FEHBIE	69.09	68.72	2.251	2.249	2.243	2.231
FIRDAL	68.66	66.35	2.275	2.256	2.255	2.255
	68.66	66.25	2.274	2.262	2.259	2.253
FONXAH10	69.29	66.88	2.273	2.271	2.259	2.247
	68.90	67.27	2.275	2.275	2.271	2.257
FUPBAT	69.04	68.71	2.255	2.245	2.243	2.239
GAFGUP	68.84	68.70	2.245	2.244	2.238	2.236
GIHGAF	68.66	68.47	2.257	2.246	2.246	2.243
GIHGAF01	68.74	68.56	2.255	2.246	2.246	2.243
GIHGAF02	68.86	68.86	2.250	2.250	2.236	2.236
GOGKEU	70.04	67.38	2.264	2.256	2.251	2.239
	69.57	67.24	2.267	2.263	2.261	2.255
HIZCAU	69.24	69.04	2.241	2.240	2.231	2.226
HOMCIW	69.21	68.81	2.242	2.240	2.238	2.231
ICTCFE	69.94	66.10	2.319	2.311	2.288	2.278
IRIBIU	71.57	69.07	2.249	2.227	2.221	2.215
JOJHEW	70.38	67.27	2.275	2.263	2.260	2.229
KOLJUQ	69.34	68.51	2.259	2.258	2.242	2.236
KOLKEB	69.78	68.42	2.260	2.259	2.249	2.227
MAZMIJ	69.31	67.56	2.262	2.253	2.252	2.241
MCPFEC	70.83	68.30	2.263	2.248	2.247	2.236
MOYCEI	70.17	69.93	2.248	2.243	2.241	2.240
MOYCIM	71.71	68.63	2.251	2.247	2.242	2.237
MOYCOS	69.16	66.58	2.284	2.280	2.264	2.263
	69.39	67.24	2.267	2.265	2.263	2.249
MTFESL	68.83	68.77	2.254	2.252	2.246	2.238
MUVSUR	68.81	68.43	2.249	2.244	2.243	2.235
MUVSUR01	68.67	68.19	2.257	2.245	2.244	2.237
OBITIE	69.28	69.10	2.252	2.249	2.243	2.215
PUYPEF	70.93	70.80	2.251	2.251	2.233	2.231
QASFUN	68.89	68.51	2.244	2.238	2.234	2.232
QEBVUO	68.86	68.04	2.263	2.253	2.252	2.248

QEBWAV	68.48	68.31	2.259	2.258	2.248	2.240
	68.48	68.31	2.259	2.258	2.248	2.240
QOFZUH	69.21	69.02	2.241	2.238	2.232	2.231
QUGSUG	68.88	68.30	2.251	2.246	2.244	2.241
	68.88	68.30	2.251	2.246	2.244	2.241
QUXSAE	69.00	68.62	2.245	2.241	2.240	2.235
UTAPAH	69.11	69.04	2.244	2.242	2.240	2.238
UTAPEL	69.05	68.67	2.245	2.245	2.242	2.242
VAHXUY	69.10	67.04	2.284	2.273	2.267	2.264
	69.33	67.29	2.278	2.266	2.262	2.256
WIMGOQ	70.93	68.10	2.247	2.246	2.238	2.234
WIMGUW	68.52	68.22	2.250	2.250	2.249	2.245
WIWFIR	68.79	68.77	2.262	2.253	2.245	2.238
WOFRAK	68.58	68.47	2.257	2.245	2.244	2.242
XAMGIE	71.04	68.09	2.257	2.254	2.253	2.249
XAXDEF	69.59	68.11	2.246	2.245	2.231	2.226
XAXDEF01	69.59	68.11	2.246	2.245	2.231	2.226
XAXDIJ	69.26	66.79	2.277	2.272	2.256	2.251
	69.26	66.79	2.277	2.272	2.256	2.251
XAXDIJ01	69.26	66.79	2.277	2.272	2.256	2.251
	69.26	66.79	2.277	2.272	2.256	2.251
XIVDOV	69.28	68.98	2.243	2.243	2.238	2.230
	69.16	69.14	2.251	2.240	2.236	2.234
XOPPEX	70.91	68.42	2.253	2.250	2.249	2.220
XOPPIB	70.92	68.43	2.250	2.240	2.236	2.218
XOPPOH	69.81	68.29	2.263	2.261	2.255	2.232
YATJEK	68.79	68.29	2.253	2.248	2.241	2.238
ZABKES	68.46	68.46	2.256	2.256	2.244	2.244
MICWED	70.45	68.41	2.246	2.245	2.243	2.235
Average	**69 ± 1**		**2.25 ± 0.01**			
Max	**72.35**		**2.319**			
Min	**66.10**		**2.215**			

References

(1) Canfield, D. E.; Glazer, A. N.; Falkowski, P. G. The Evolution and Future of Earth's Nitrogen Cycle. *Science* **2010**, *330* (6001), 192–196. https://doi.org/10.1126/science.1186120.

(2) Shilov, A. E. Catalytic reduction of molecular nitrogen in solutions. *Russ. Chem. Bull.* **2003**, *52* (12), 2555–2562. https://doi.org/10.1023/B:RUCB.0000019873.81002.60.

(3) Jia, H.-P.; Quadrelli, E. A. Mechanistic aspects of dinitrogen cleavage and hydrogenation to produce ammonia in catalysis and organometallic chemistry: relevance of metal hydride bonds and dihydrogen. *Chem. Soc. Rev.* **2014**, *43* (2), 547–564. https://doi.org/10.1039/C3CS60206K.

(4) Zhan, C.-G.; Nichols, J. A.; Dixon, D. A. *J. Phys. Chem. A* **2003**, *107* (20), 4184–4195. https://doi.org/10.1021/jp0225774.

(5) Kramer, D. A. Mineral Commodity Profiles: Nitrogen. U.S Department of the Interior: U. S. Geological Survey **2004**. Open-file Report 2004-1290. https://pubs.usgs.gov/of/2004/1290.

(6) Kelly, T. D.; Matos, G. R. Nitrogen statistics. In *Historical statistics for mineral and material commodities in the United States*. U.S. Geological Survey **2005** Data Series *140*.

(7) *Catalysts for Nitrogen Fixation*; Smith, B. E., Richards, R. L., Newton, W. E., Eds.; Springer Netherlands: Dordrecht, **2004**. https://doi.org/10.1007/978-1-4020-3611-8.

(8) Foster, S. L.; Bakovic, S. I. P.; Duda, R. D.; Maheshwari, S.; Milton, R. D.; Minteer, S. D.; Janik, M. J.; Renner, J. N.; Greenlee, L. F. Catalysts for nitrogen

reduction to ammonia. *Nat. Catal.* **2018**, *1* (7), 490–500. https://doi.org/10.1038/s41929-018-0092-7.

(9) Shamelessly adapted from Dr. Rose's bio-inorganic class: Rose, M. J. Class notes. From *Bio-inorganic Chemistry: Structure, Catalysis and Spectroscopy*. **Fall 2014**.

(10) Hoffman, B. M.; Lukoyanov, D.; Yang, Z.-Y.; Dean, D. R.; Seefeldt, L. C. Mechanism of Nitrogen Fixation by Nitrogenase: The Next Stage. *Chem. Rev.* **2014**, *114* (8), 4041–4062. https://doi.org/10.1021/cr400641x.

(11) Eady, R. R. Structure−Function Relationships of Alternative Nitrogenases. *Chem. Rev.* **1996**, *96* (7), 3013–3030. https://doi.org/10.1021/cr950057h.

(12) Georgiadis, M.; Komiya, H.; Chakrabarti, P.; Woo, D.; Kornuc, J.; Rees, D. Crystallographic Structure of the Nitrogenase Iron Protein from *Azotobacter vinelandii*. *Science* **1992**, *257* (5077), 1653–1659. https://doi.org/10.1126/science.1529353.

(13) Kim, J.; Rees, D. Structural Models for the Metal Centers in the Nitrogenase Molybdenum-Iron Protein. *Science* **1992**, *257* (5077), 1677–1682. https://doi.org/10.1126/science.1529354.

(14) Zhang, L.-M.; Morrison, C. N.; Kaiser, J. T.; Rees, D. C. Nitrogenase MoFe protein from *Clostridium pasteurianum* at 1.08 Å resolution: comparison with the *Azotobacter vinelandii* MoFe protein. *Acta Crystallogr. Sect. D Biol. Crystallogr.* **2015**, *71* (2), 274–282. https://doi.org/10.1107/S1399004714025243.

(15) Goddard, T. D.; Huang, C. C.; Meng, E. C.; Pettersen, E. F.; Couch, G. S.; Morris, J. H.; Ferrin, T. E. UCSF ChimeraX: Meeting modern challenges in visualization and analysis. *Protein Sci.* **2018**, *27* (1), 14–25. https://doi.org/10.1002/pro.3235.

(16) Shah, V. K.; Brill, W. J. Isolation of an iron-molybdenum cofactor from nitrogenase. *Proc. Natl. Acad. Sci.* **1977**, *74* (8), 3249–3253. https://doi.org/10.1073/pnas.74.8.3249.

(17) Van De Bogart, M.; Beinert, H. Micro Methods for the Quantitative Determination of Iron and Copper in Biological Material. *Anal. Biochem.* **1967**, *20* (2), 325–334. https://doi.org/10.1016/0003-2697(67)90038-3.

(18) Einsle, O.; Tezcan, F. A.; Andrade, S. L. A.; Schmid, B.; Yoshida, M.; Howard, J. B.; Rees, D. C. Nitrogenase MoFe-Protein at 1.16 Å Resolution: A Central Ligand in the FeMo-Cofactor. *Science* **2002**, *297* (5587), 1696–1700. https://doi.org/10.1126/science.1073877.

(19) Smith, B. E. Nitrogenase Reveals Its Inner Secrets. *Science* **2002**, *297* (5587), 1654–1655. https://doi.org/10.1126/science.1076659.

(20) Macrae, C. F.; Sovago, I.; Cottrell, S. J.; Galek, P. T. A.; McCabe, P.; Pidcock, E.; Platings, M.; Shields, G. P.; Stevens, J. S.; Towler, M.; Wood, P. A. *Mercury 4.0*: from visualization to analysis, design and prediction. *J. Appl. Crystallogr.* **2020**, *53* (1), 226–235. https://doi.org/10.1107/S1600576719014092.

(21) Spatzal, T.; Aksoyoglu, M.; Zhang, L.; Andrade, S. L. A.; Schleicher, E.; Weber, S.; Rees, D. C.; Einsle, O. Evidence for Interstitial Carbon in Nitrogenase FeMo Cofactor. *Science* **2011**, *334* (6058), 940–940. https://doi.org/10.1126/science.1214025.

(22) Lancaster, K. M.; Roemelt, M.; Ettenhuber, P.; Hu, Y.; Ribbe, M. W.; Neese, F.; Bergmann, U.; DeBeer, S. X-ray Emission Spectroscopy Evidences a Central Carbon in the Nitrogenase Iron-Molybdenum Cofactor. *Science* **2011**, *334* (6058), 974–977. https://doi.org/10.1126/science.1206445.

(23) Delgado-Jaime, M. U.; Dible, B. R.; Chiang, K. P.; Brennessel, W. W.; Bergmann, U.; Holland, P. L.; DeBeer, S. Identification of a Single Light Atom within a Multinuclear Metal Cluster Using Valence-to-Core X-ray Emission Spectroscopy. *Inorg. Chem.* **2011**, *50* (21), 10709–10717. https://doi.org/10.1021/ic201173j.

(24) Wiig, J. A.; Hu, Y.; Lee, C. C.; Ribbe, M. W. *Science* **2012**, *337* (6102), 1672–1675. https://doi.org/10.1021/ic201173j.

(25) Wiig, J. A.; Hu, Y.; Ribbe, M. W. Refining the pathway of carbide insertion into the nitrogenase M-cluster. *Nat. Commun.* **2015**, *6* (1), 8034. https://doi.org/10.1038/ncomms9034.

(26) Rettberg, L. A.; Wilcoxen, J.; Lee, C. C.; Stiebritz, M. T.; Tanifuji, K.; Britt, R. D.; Hu, Y. Probing the coordination and function of Fe_4S_4 modules in nitrogenase assembly protein NifB. *Nat. Commun.* **2018**, *9* (1), 2824. https://doi.org/10.1038/s41467-018-05272-8.

(27) Sickerman, N. S.; Ribbe, M. W.; Hu, Y. Nitrogenase Cofactor Assembly: An Elemental Inventory. *Acc. Chem. Res.* **2017**, *50* (11), 2834–2841. https://doi.org/10.1021/acs.accounts.7b00417.

(28) Jasniewski, A. J.; Wilcoxen, J.; Tanifuji, K.; Hedman, B.; Hodgson, K. O.; Britt, R. D.; Hu, Y.; Ribbe, M. W. Spectroscopic Characterization of an Eight-Iron Nitrogenase Cofactor Precursor that Lacks the "9th Sulfur." *Angew. Chemie Int. Ed.* **2019**, *58* (41), 14703–14707. https://doi.org/10.1002/anie.201907593.

(29) Tanifuji, K.; Lee, C. C.; Sickerman, N. S.; Tatsumi, K.; Ohki, Y.; Hu, Y.; Ribbe, M. W. Tracing the 'ninth sulfur' of the nitrogenase cofactor via a semi-synthetic approach. *Nat. Chem.* **2018**, *10* (5), 568–572. https://doi.org/10.1038/s41557-018-0029-4.

(30) Groom, C. R.; Bruno, I. J.; Lightfoot, M. P.; Ward, S. C. The Cambridge Structural Database. *Acta Crystallogr.* **2016**, *B72*, 171–179. https://doi.org/10.1107/S2052520616003954.

(31) Rees, J. A.; Bjornsson, R.; Schlesier, J.; Sippel, D.; Einsle, O.; DeBeer, S. The Fe–V Cofactor of Vanadium Nitrogenase Contains an Interstitial Carbon Atom. *Angew. Chemie Int. Ed.* **2015**, *54* (45), 13249–13252. https://doi.org/10.1002/anie.201505930.

(32) Hu, Y.; Lee, C. C.; Ribbe, M. W. Extending the Carbon Chain: Hydrocarbon Formation Catalyzed by Vanadium/Molybdenum Nitrogenases. *Science* **2011**, *333* (6043), 753–755. https://doi.org/10.1126/science.1206883.

(33) Sippel, D.; Einsle, O. The structure of vanadium nitrogenase reveals an unusual bridging ligand. *Nat. Chem. Biol.* **2017**, *13* (9), 956–960. https://doi.org/10.1038/nchembio.2428.

(34) Sippel, D.; Rohde, M.; Netzer, J.; Trncik, C.; Gies, J.; Grunau, K.; Djurdjevic, I.; Decamps, L.; Andrade, S. L. A.; Einsle, O. A bound reaction intermediate sheds light on the mechanism of nitrogenase. *Science* **2018**, *359* (6383), 1484–1489. https://doi.org/10.1126/science.aar2765.

(35) Hu, Y.; Ribbe, M. W. Nitrogenase assembly. *Biochim. Biophys. Acta – Bioenerg.* **2013**, *1827* (8–9), 1112–1122. https://doi.org/10.1016/j.bbabio.2012.12.001.

(36) Lee, C. C.; Hu, Y.; Ribbe, M. W. Insights into Hydrocarbon Formation by Nitrogenase Cofactor Homologs. *mBio* **2015**, *6* (2), 1–6. https://doi.org/10.1128/mBio.00307-15.

(37) Rawlings, J.; Shah, V. K.; Chisnell, J. R.; Brill, W. J.; Zimmermann, R.; Münck, E.; Orme-Johnson, W. H. Novel Metal Cluster in the Iron-Molybdenum Cofactor

of Nitrogenase. *J. Biol. Chem.* **1978**, *253* (4), 1001–1004. https://www.jbc.org/content/253/4/1001.

(38) Liu, H. I.; Burgess, B. K.; Natoli, C. R.; Filipponi, A.; Gavini, N.; Hedman, B.; Di Cicco, A.; Hodgson, K. O. EXAFS Studies of FeMo-Cofactor and MoFe Protein: Direct Evidence for the Long-Range Mo-Fe-Fe Interaction and Cyanide Binding to the Mo in FeMo-Cofactor. *J. Am. Chem. Soc.* **1994**, *116* (6), 2418–2423. https://doi.org/10.1021/ja00085a022.

(39) Johnson, M. K.; Thomson, A. J.; Robinson, A. E.; Smith, B. E. Characterization of the paramagnetic centres of the molybdenum-iron protein of nitrogenase from *Klebsiella pneumoniae* using low temperature magnetic circular dichroism spectroscopy. *Biochim. Biophys. Acta – Protein Struct.* **1981**, *671* (1), 61–70. https://doi.org/10.1016/0005-2795(81)90094-5.

(40) Spatzal, T.; Einsle, O.; Andrade, S. L. A. Analysis of the Magnetic Properties of Nitrogenase FeMo Cofactor by Single-Crystal EPR Spectroscopy. *Angew. Chemie Int. Ed.* **2013**, *52* (38), 10116–10119. https://doi.org/10.1002/anie.201303000.

(41) Spatzal, T.; Schlesier, J.; Burger, E.-M.; Sippel, D.; Zhang, L.; Andrade, S. L. A.; Rees, D. C.; Einsle, O. Nitrogenase FeMoco investigated by spatially resolved anomalous dispersion refinement. *Nat. Commun.* **2016**, *7*, 10902. https://doi.org/10.1038/ncomms10902.

(42) Hoffman, B. M.; Roberts, J. E.; Orme-Johnson, W. H. ^{95}Mo and ^{1}H ENDOR Spectroscopy of the Nitrogenase MoFe Protein. *J. Am. Chem. Soc.* **1982**, *104* (3), 860–862. https://doi.org/10.1021/ja00367a042.

(43) Cramer, S. P.; Hodgson, K. O.; Gillum, W. O.; Mortenson, L. E. The Molybdenum Site of Nitrogenase. Preliminary Structural Evidence from X-Ray

Absorption Spectroscopy. *J. Am. Chem. Soc.* **1978**, *100* (11), 3398–3407. https://doi.org/10.1021/ja00479a023.

(44) Bjornsson, R.; Lima, F. A.; Spatzal, T.; Weyhermüller, T.; Glatzel, P.; Bill, E.; Einsle, O.; Neese, F.; DeBeer, S. Identification of a spin-coupled Mo(III)in the nitrogenase iron–molybdenum cofactor. *Chem. Sci.* **2014**, *5* (8), 3096–3103. https://doi.org/10.1039/C4SC00337C.

(45) Rees, J. A.; Bjornsson, R.; Kowalska, J. K.; Lima, F. A.; Schlesier, J.; Sippel, D.; Weyhermüller, T.; Einsle, O.; Kovacs, J. A.; DeBeer, S. *Dalt. Trans.* **2017**, *46* (8), 2445–2455. https://doi.org/10.1039/C7DT00128B.

(46) Siegbahn, P. E. M. Model Calculations Suggest that the Central Carbon in the FeMo-Cofactor of Nitrogenase Becomes Protonated in the Process of Nitrogen Fixation. *J. Am. Chem. Soc.* **2016**, *138* (33), 10485–10495. https://doi.org/10.1021/jacs.6b03846.

(47) Siegbahn, P. E. M. The mechanism for nitrogenase including all steps. *Phys. Chem. Chem. Phys.* **2019**, *21* (28), 15747–15759. https://doi.org/10.1039/C9CP02073J.

(48) Anderson, J. S.; Rittle, J.; Peters, J. C. Catalytic conversion of nitrogen to ammonia by an iron model complex. *Nature* **2013**, *501* (7465), 84–87. https://doi.org/10.1038/nature12435.

(49) McGale, J.; Cutsail, G. E.; Joseph, C.; Rose, M. J.; DeBeer, S. Spectroscopic X-ray and Mössbauer Characterization of M_6 and M_5 Iron(Molybdenum)-Carbonyl Carbide Clusters: High Carbide-Iron Covalency Enhances Local Iron Site Electron Density Despite Cluster Oxidation. *Inorg. Chem.* **2019**, *58* (19), 12918–12932. https://doi.org/10.1021/acs.inorgchem.9b01870.

(50) Wiig, J. A.; Lee, C. C.; Hu, Y.; Ribbe, M. W. Tracing the Interstitial Carbide of the Nitrogenase Cofactor during Substrate Turnover. *J. Am. Chem. Soc.* **2013**, *135* (13), 4982–4983. https://doi.org/10.1021/ja401698d.

(51) Van Stappen, C.; Thorhallsson, A. T.; Decamps, L.; Bjornsson, R.; DeBeer, S. Resolving the structure of the E_1 state of Mo nitrogenase through Mo and Fe K-edge EXAFS and QM/MM calculations. *Chem. Sci.* **2019**, *10* (42), 9807–9821. https://doi.org/10.1039/C9SC02187F.

(52) Van Stappen, C.; Davydov, R.; Yang, Z.-Y.; Fan, R.; Guo, Y.; Bill, E.; Seefeldt, L. C.; Hoffman, B. M.; DeBeer, S. Spectroscopic Description of the E_1 State of Mo Nitrogenase Based on Mo and Fe X-ray Absorption and Mössbauer Studies. *Inorg. Chem.* **2019**, *58* (18), 12365–12376. https://doi.org/10.1021/acs.inorgchem.9b01951.

(53) Yandulov, D. V.; Schrock, R. R. Catalytic Reduction of Dinitrogen to Ammonia at a Single Molybdenum Center. *Science* **2003**, *301* (5629), 76–78. https://doi.org/10.1126/science.1085326.

(54) Spatzal, T.; Perez, K. A.; Einsle, O.; Howard, J. B.; Rees, D. C. Ligand binding to the FeMo-cofactor: Structures of CO-bound and reactivated nitrogenase. *Science* **2014**, *345* (6204), 1620–1623. https://doi.org/10.1126/science.1256679.

(55) Spatzal, T.; Perez, K. A.; Howard, J. B.; Rees, D. C. Catalysis-dependent selenium incorporation and migration in the nitrogenase active site iron-molybdenum cofactor. *Elife* **2015**, *4*. https://doi.org/10.7554/eLife.11620.

(56) Siegbahn, P. E. M. A Major Structural Change of the Homocitrate Ligand of Probable Importance for the Nitrogenase Mechanism. *Inorg. Chem.* **2018**, *57* (3), 1090–1095. https://doi.org/10.1021/acs.inorgchem.7b02493.

(57) Chatt, J.; Dilworth, J. R.; Richards, R. L. Recent Advances in the Chemistry of Nitrogen Fixation. *Chem. Rev.* **1978**, *78* (6), 589–625. https://doi.org/10.1021/cr60316a001.

(58) Barney, B. M.; McClead, J.; Lukoyanov, D.; Laryukhin, M.; Yang, T.-C.; Dean, D. R.; Hoffman, B. M.; Seefeldt, L. C. Diazene (HN=NH) Is a Substrate for Nitrogenase: Insights into the Pathway of N_2 Reduction. *Biochemistry* **2007**, *46* (23), 6784–6794. https://doi.org/10.1021/bi062294s.

(59) Seefeldt, L. C.; Yang, Z.; Lukoyanov, D. A.; Harris, D. F.; Dean, D. R.; Raugei, S.; Hoffman, B. M. Reduction of Substrates by Nitrogenases. *Chem. Rev.* **2020**, in press. https://doi.org/10.1021/acs.chemrev.9b00556.

(60) Rittle, J.; Peters, J. C. An Fe-N_2 Complex That Generates Hydrazine and Ammonia via Fe=NNH_2: Demonstrating a Hybrid Distal-to-Alternating Pathway for N_2 Reduction. *J. Am. Chem. Soc.* **2016**, *138* (12), 4243–4248. https://doi.org/10.1021/jacs.6b01230.

(61) Arashiba, K.; Miyake, Y.; Nishibayashi, Y. A molybdenum complex bearing PNP-type pincer ligands leads to the catalytic reduction of dinitrogen into ammonia. *Nat. Chem.* **2011**, *3* (2), 120–125. https://doi.org/10.1038/nchem.906.

(62) Nishibayashi, Y. Recent Progress in Transition-Metal-Catalyzed Reduction of Molecular Dinitrogen under Ambient Reaction Conditions. *Inorg. Chem.* **2015**, *54* (19), 9234–9247. https://doi.org/10.1021/acs.inorgchem.5b00881.

(63) Kuriyama, S.; Arashiba, K.; Nakajima, K.; Matsuo, Y.; Tanaka, H.; Ishii, K.; Yoshizawa, K.; Nishibayashi, Y. Catalytic transformation of dinitrogen into ammonia and hydrazine by iron-dinitrogen complexes bearing pincer ligand. *Nat. Commun.* **2016**, *7*, 12181. https://doi.org/10.1038/ncomms12181.

(64) Lee, Y.; Mankad, N. P.; Peters, J. C. Triggering N_2 uptake via redox-induced expulsion of coordinated NH_3 and N_2 silylation at trigonal bipyramidal iron. *Nat. Chem.* **2010**, *2* (7), 558–565. https://doi.org/10.1038/nchem.660.

(65) Creutz, S. E.; Peters, J. C. Catalytic Reduction of N_2 to NH_3 by an Fe–N_2 Complex Featuring a C-Atom Anchor. *J. Am. Chem. Soc.* **2014**, *136* (3), 1105–1115. https://doi.org/10.1021/ja4114962.

(66) Creutz, S. E.; Peters, J. C. Diiron Bridged-Thiolate Complexes That Bind N_2 at the $Fe^{II}Fe^{II}$, $Fe^{II}Fe^{I}$, and $Fe^{I}Fe^{I}$ Redox States. *J. Am. Chem. Soc.* **2015**, *137* (23), 7310–7313. https://doi.org/10.1021/jacs.5b04738.

(67) Chiang, K. P.; Bellows, S. M.; Brennessel, W. W.; Holland, P. L. Multimetallic cooperativity in activation of dinitrogen at iron–potassium sites. *Chem. Sci.* **2014**, *5* (1), 267–274. https://doi.org/10.1039/C3SC52487F.

(68) MacLeod, K. C.; Vinyard, D. J.; Holland, P. L. A Multi-iron System Capable of Rapid N_2 Formation and N_2 Cleavage. *J. Am. Chem. Soc.* **2014**, *136* (29), 10226–10229. https://doi.org/10.1021/ja505193z.

(69) Čorić, I.; Mercado, B. Q.; Bill, E.; Vinyard, D. J.; Holland, P. L. Binding of dinitrogen to an iron–sulfur–carbon site. *Nature* **2015**, *526* (7571), 96–99. https://doi.org/10.1038/nature15246.

(70) Kovacs, J. A.; Holm, R. H. Assembly of Vanadium-Iron-Sulfur Cubane Clusters from Mononuclear and Linear Trinuclear Reactants. *J. Am. Chem. Soc.* **1986**, *108* (2), 340–341. https://doi.org/10.1021/ja00262a050.

(71) Fomitchev, D. V.; McLauchlan, C. C.; Holm, R. H. Heterometal Cubane-Type MFe_3S_4 Clusters (M = Mo, V) Trigonally Symmetrized with Hydrotris(pyrazolyl)borate(1−) and Tris(pyrazolyl)methanesulfonate(1−) Capping Ligands. *Inorg. Chem.* **2002**, *41* (4), 958–966. https://doi.org/10.1021/ic011106d.

(72) Reed, C. J.; Agapie, T. Tetranuclear Fe Clusters with a Varied Interstitial Ligand: Effects on the Structure, Redox Properties, and Nitric Oxide Activation. *Inorg. Chem.* **2017**, *56* (21), 13360–13367. https://doi.org/10.1021/acs.inorgchem.7b02114.

(73) Arnett, C. H.; Kaiser, J. T.; Agapie, T. Remote Ligand Modifications Tune Electronic Distribution and Reactivity in Site-Differentiated, High-Spin Iron Clusters: Flipping Scaling Relationships. *Inorg. Chem.* **2019**, *58* (23), 15971–15982. https://doi.org/10.1021/acs.inorgchem.9b02470.

(74) Taniyama, N.; Ohki, Y.; Tatsumi, K. Synthesis of V/Fe/S Clusters Using Vanadium(III) Thiolate Complexes Bearing a Phenoxide-Based Tridentate Ligand. *Inorg. Chem.* **2014**, *53* (11), 5438–5446. https://doi.org/10.1021/ic4030603.

(75) Ohta, S.; Ohki, Y.; Hashimoto, T.; Cramer, R. E.; Tatsumi, K. A Nitrogenase Cluster Model [Fe_8S_6O] with an Oxygen Unsymmetrically Bridging Two Proto-Fe_4S_3 Cubes: Relevancy to the Substrate Binding Mode of the FeMo Cofactor. *Inorg. Chem.* **2012**, *51* (21), 11217–11219. https://doi.org/10.1021/ic301348f.

(76) Liu, L.; Rauchfuss, T. B.; Woods, T. J. Iron Carbide–Sulfide Carbonyl Clusters. Inorg. Chem. 2019, 58 (13), 8271–8274. https://doi.org/10.1021/acs.inorgchem.9b01231.

(77) Braye, E. H.; Dahl, L. F.; Hubel, W.; Wampler, D. L. The Preparation, Properties and Structure of the Iron Carbonyl Carbide $Fe_5(CO)_{15}C$. *J. Am. Chem. Soc.* **1962**, *84* (24), 4633–4639. https://doi.org/10.1021/ja00883a004.

(78) Churchill, M. R.; Wormald, J.; Knight, J.; Mays, M. J. Synthesis and Crystallographic Characterization of [Me_4N^+][$Fe_6(CO)_{16}C^{2-}$], a Hexanuclear

Carbidocarbonyl Derivative of Iron. *J. Am. Chem. Soc.* **1971**, *93* (12), 3073–3074. https://doi.org/10.1021/ja00741a058.

(79) Churchill, M. R.; Wormald, J. Crystal and Molecular Structure of Tetramethylammonium Carbidohexadecacarbonylhexaferrate(2–), $[Me_4N]_2[Fe_6(CO)_{16}C]$, a Hexanuclear Iron Cluster Complex with an Encapsulated Six-co-ordinate Carbon Atom. *J. Chem. Soc., Dalt. Trans.* **1974**, 2410–2415. https://doi.org/10.1039/DT9740002410.

(80) Kulkarni, A.; Lobo-Lapidus, R. J.; Gates, B. C. Metal clusters on supports: synthesis, structure, reactivity, and catalytic properties. *Chem. Commun.* **2010**, **46** (33), 5997. https://doi.org/10.1039/c002707n.

(81) Lobo-Lapidus, R. J.; Gates, B. C. J. Catal. 2009, 268 (1), 89–99. https://doi.org/

(82) Argo, A. M.; Gates, B. C. Rhenium complexes and clusters supported on γ-Al_2O_3: Effects of rhenium oxidation state and rhenium cluster size on catalytic activity for *n*-butane hydrogenolysis. *J. Phys. Chem. B* **2003**, *107* (23), 5519–5528. https://doi.org/10.1016/j.jcat.2009.09.006.

(83) Holt, E. M.; Whitmire, K.; Shriver, D. F. O-Alkylation and Structural Rearrangement of CO Ligands in $[Fe_4(CO)_9(\mu\text{-}CO)_3(\mu_3\text{-}CO)]^{2-}$; X-ray Crystal Structure of $[N(PPh_3)_2][Fe_4(CO)_{11}(\mu\text{-}CO)(\mu_3\text{-}COMe)]$. *J. Chem. Soc., Chem. Commun.* **1980**, *4* (16), 778–779. https://doi.org/10.1039/C39800000778.

(84) Kolis, J. W.; Basolo, F.; Shriver, D. F. Reactivity of Metal Carbide Clusters: Alkylation and Protonation of $[Fe_5(CO)_{14}C]^{2-}$. *J. Am. Chem. Soc.* **1982**, *104* (21), 5626–5630. https://doi.org/10.1021/ja00385a011.

(85) Shriver, D. F.; Sailor, M. J. Transformations of Carbon Monoxide and Related Ligands on Metal Ensembles. *Acc. Chem. Res.* **1988**, *21* (10), 374–379. https://doi.org/10.1021/ar00154a004.

(86) Beno, M. A.; Williams, J. M.; Tachikawa, M.; Muetterties, E. L. Fischer–Tropsch Chemistry: Structure of a Seminal η^2-CH Cluster Derivative, $HFe_4(\eta^2\text{-}CH)(CO)_{12}$. *J. Am. Chem. Soc.* **1980**, *102* (13), 4542–4544. https://doi.org/10.1021/ja00533a052.

(87) Tachikawa, M.; Muetterties, E. L. Metal Clusters. 25. A Uniquely Bonded C–H Group and Reactivity of a Low-Coordinate Carbidic Carbon Atom. *J. Am. Chem. Soc.* **1980**, *102* (13), 4541–4542. https://doi.org/10.1021/ja00533a051.

(88) Beno, M. A.; Williams, J. M.; Tachikawa, M.; Muetterties, E. L. A Closed Three-Center Carbon–Hydrogen–Metal Interaction. A Neutron Diffraction Study of $HFe_4(\eta^2\text{-}CH)(CO)_{12}$. *J. Am. Chem. Soc.* **1981**, *103* (6), 1485–1492. https://doi.org/10.1021/ja00396a032.

(89) Whitmire, K.; Shriver, D. F.; Holt, E. M. Structural and Isotope Tracer Study of the Proton Induced Reduction of CO in $[Fe_4(CO)_{11}(\mu\text{-}CO)(\mu_3\text{-}COMe)]^-$; X-ray Crystal Structure of $[Fe_4H(CO)_{12}COMe]$. *J. Chem. Soc., Chem. Commun.* **1980**, *4* (16), 780–781. https://doi.org/10.1039/C39800000780.

(90) Andrews, M. A.; Kaesz, H. D. Reversible Hydrogenation and Dehydrogenation of Cluster Bound Acimidoyl and Alkylidenimido Groups. Synthesis of Complexes Containing Triply Bridging Nitrene and Nitrile Ligands. *J. Am. Chem. Soc.* **1979**, *101* (24), 7255–7259. https://doi.org/10.1021/ja00518a020.

(91) Nguyen, A. D.; Rail, M. D.; Shanmugam, M.; Fettinger, J. C.; Berben, L. A. Electrocatalytic Hydrogen Evolution from Water by a Series of Iron Carbonyl Clusters. *Inorg. Chem.* **2013**, *52* (21), 12847–12854. https://doi.org/10.1021/ic4023882.

(92) Rail, M. D.; Berben, L. A. Directing the Reactivity of $[HFe_4N(CO)_{12}]^-$ toward H^+ or CO_2 Reduction by Understanding the Electrocatalytic Mechanism. *J. Am. Chem. Soc.* **2011**, *133* (46), 18577–18579. https://doi.org/10.1021/ja208312t.

(93) Taheri, A.; Berben, L. A. Making C–H bonds with CO_2: production of formate by molecular electrocatalysts. *Chem. Commun.* **2016**, *52* (9), 1768–1777. https://doi.org/10.1039/C5CC09041E.

(94) Ghosh, S.; Hogarth, G.; Kabir, S. E.; Miah, A. L.; Salassa, L.; Sultana, S.; Garino, C. Synthesis and Molecular Structure of $[Fe_4(CO)_{10}(\mu_4\text{-O})(\kappa^2\text{-dppn})]$ (dppn = 1,8-bis(diphenylphosphino)naphthalene): A Missing Piece in the $[M_4(CO)_{12}(\mu_4\text{-E})]^{n-}$ (M = Fe, Ru; E = C, N, O; *n* = 2, 1, 0) Puzzle. *Organometallics* **2009**, *28* (24), 7047–7052. https://doi.org/10.1021/om900855v.

(95) Ghosh, S.; Holt, K. B.; Kabir, S. E.; Richmond, M. G.; Hogarth, G. Electrocatalytic proton reduction catalysed by the low-valent tetrairon-oxo cluster $[Fe_4(CO)_{10}(\kappa^2\text{-dppn})(\mu_4\text{-O})]^{2-}$ [dppn = 1,1′-bis(diphenylphosphino)naphthalene]. *Dalt. Trans.* **2015**, *44* (11), 5160–5169. https://doi.org/10.1039/C4DT03323J.

(96) Mond, L.; Langer, C. XCIII.—On Iron Carbonyls. *J. Chem. Soc., Trans.* **1891**, *59*, 1090–1093. https://doi.org/10.1039/CT8915901090.

(97) Speyer, E.; Wolf, H. Über die Bildungsweise von Eisen-nonacarbonyl aus Eisen-pentacarbonyl. *Berichte der Dtsch. Chem. Gesellschaft (A and B Series)* **1927**, *60* (6), 1424–1425. https://doi.org/10.1002/cber.19270600626.

(98) Hieber, W.; Leutert, F. Über Metallcarbonyle. XII. Die Basenreaktion des Eisenpentacarbonyls und die Bildung des Eisencarbonylwasserstoffs. *Zeitschrift für Anorg. und Allg. Chemie* **1932**, *204* (1–2), 145–164. https://doi.org/10.1002/zaac.19322040115.

(99) Paolieri, M.; Ciabatti, I.; Fontani, M. Paolo Chini: The Chemical Architect of Metal Carbonyl Clusters. *J. Clust. Sci.* **2019**, *30* (6), 1623–1631. https://doi.org/10.1007/s10876-019-01607-7.

(100) Tachikawa, M.; Geerts, R. L.; Muetterties, E. L. Metal carbide clusters synthesis systematics for heteronuclear species. *J. Organomet. Chem.* **1981**, *213* (1), 11–24. https://doi.org/10.1016/S0022-328X(00)93947-0.

(101) Tachikawa, M.; Sievert, A. C.; Muetterties, E. L.; Thompson, M. R.; Day, C. S.; Day, V. W. Metal Clusters. 24. Synthesis and Structure of Heteronuclear Metal Carbide Clusters. *J. Am. Chem. Soc.* **1980**, *102* (5), 1725–1727. https://doi.org/10.1021/ja00525a047.

(102) Hill, E. W.; Bradley, J. S.; Cassidy, J.; Whitmire, K. H. Tetrairon Carbido Carbonyl Clusters. *Inorg. Synth.* **2007**, *27*, 182–188. https://doi.org/10.1002/9780470132586.ch36.

(103) Bradley, J. S. In *Metal Clusters*; Moskovits, M., Ed.; John Wiley & Sons, Inc., **1986**; pp 105–130.

(104) Bradley, J. S.; Harris, S.; Newsam, J. M.; Hill, E. W.; Leta, S.; Modrick, M. A. Syntheses and Molecular and Electronic Structures of the μ_4-Methylidyne Clusters $[Fe_4(CO)_{12}C{\bullet}C(O)OCH_3]^-$ and $[Fe_4(CO)_{12}C{\bullet}C(O)CH_3]^-$: An Analysis of Steric and Bonding Effects. *Organometallics* **1987**, *6* (10), 2060–2069. https://doi.org/10.1021/om00153a005.

(105) Bradley, J. S.; Ansell, G. B.; Hill, E. W. Homogeneous Carbon Monoxide Hydrogenation on Multiple Sites: A Dissociative Pathway to Oxygenates. *J. Am. Chem. Soc.* **1979**, *101* (24), 7417–7419. https://doi.org/10.1021/ja00518a055.

(106) Kuppuswamy, S.; Wofford, J. D.; Joseph, C.; Xie, Z.; Ali, A. K.; Lynch, V. M.; Lindahl, P. A.; Rose, M. J. Structures, Interconversions, and Spectroscopy of Iron

Carbonyl Clusters with an Interstitial Carbide: Localized Metal Center Reduction by Overall Cluster Oxidation. *Inorg. Chem.* **2017**, *56* (10), 5998–6012. https://doi.org/10.1021/acs.inorgchem.7b00741.

(107) Strong, H.; Krusic, P. J.; Filippo, J. S.; Keenan, S.; Finke, R. G. *Inorg. Synth.* **2007**, *28*, 203–207. https://doi.org/10.1002/9780470132593.ch52.

(108) Shupp, J. P.; Rose, A. R.; Rose, M. J. Synthesis and interconversions of reduced, alkali–metal supported iron–sulfur–carbonyl complexes. *Dalt. Trans.* **2017**, 46 (28), 3–10. https://doi.org/10.1039/C7DT01506B.

(109) Shupp, J. P.; Rose, M. J. Facile hydrogen atom abstraction and sulfide formation in a methyl-thiolate capped iron-sulfur-carbonyl cluster. *Dalt. Trans.* **2019**, *49* (1), 23–26. https://doi.org/10.1039/c9dt04098f.

(110) van Buskirk, G.; Knobler, C. B.; Kaesz, H. D. Crystal and Molecular Structure of the $[\{(C_6H_5)_3P\}_2N]^+$ Salt of $[Fe_4(CO)_{13}]^{2-}$. A Structural Isomer of the Anion along a Valence Tautomeric Coordinate. *Organometallics* **1985**, *4* (1), 149–153. https://doi.org/10.1021/om00120a024.

(111) Holt, E. M.; Whitmire, K. H.; Shriver, D. F. The role of metal cluster interactions in the proton-induced reduction of CO. The crystal structures of $[PPN]\{HFe_4(CO)_{12}\}$ and $HFe_4(CO)_{12}(\eta^2\text{-}COCH_3)$. *J. Organomet. Chem.* **1981**, *213* (1), 125–137. https://doi.org/10.1016/S0022-328X(00)93954-8.

(112) Kolis, J. W.; Drezdzon, M. A.; Shriver, D. F.; Furuya, F. R.; Gladfelter, W. L. Bis[μ-Nitrido-Bis(Triphenylphosphorus)(1+)] μ_4-Carbido-Dodecacarbonyl-Tetraferrate(2–), $[PPN]_2[Fe_4C(CO)_{12}]$. *Inorg. Synth.* **2007**, *26*, 246–249. https://doi.org/10.1002/9780470132579.ch43.

(113) Bradley, J. S.; Hill, E. W.; Ansell, G. B.; Modrick, M. Mechanism of the Reaction of $[Fe_6C(CO)_{16}]^{2-}$ with Tropylium Bromide To Give $[Fe_4(CO)_{12}CCO_2Me]^-$ and

the Molecular Structure of $(Et_4N)_2[Fe_5C(CO)_{12}Br_2]$, a Proposed Intermediate in This Reaction. *Organometallics* **1982**, *1* (12), 1634–1639. https://doi.org/10.1021/om00072a016.

(114) Bradley, J. S.; Ansell, G. B.; Leonowicz, M. E.; Hill, E. W. Synthesis and Molecular Structure of μ^4-Carbido-μ^2-carbonyl-dodecacarbonyltetrairon, a Neutral Iron Butterfly Cluster Bearing an Exposed Carbon Atom. *J. Am. Chem. Soc.* **1981**, *103* (16), 4968–4970. https://doi.org/10.1021/ja00406a062.

(115) Wade, K. The Structural Significance of the Number of Skeletal Bonding Electron-pairs in Carboranes, the Higher Boranes and Borane Anions, and Various Transition-metal Carbonyl Cluster Compounds. *J. Chem. Soc. D Chem. Commun.* **1971**, (15), 792. https://doi.org/10.1039/c29710000792.

(116) Mingos, D. M. P. A General Theory for Cluster and Ring Compounds of the Main Group and Transition Elements. *Nat. Phys. Sci.* **1972**, *236* (68), 99–102. https://doi.org/10.1038/physci236099a0.

(117) Mingos, D. M. P. Polyhedral Skeletal Electron Pair Approach. A Generalised Principle for Condensed Polyhedra. *J. Chem. Soc. Chem. Commun.* **1983**, *4* (12), 706–708. https://doi.org/10.1039/c39830000706.

(118) Mingos, D. M. P.; Wales, D. J. *Introduction to Cluster Chemistry*, 1st ed.; Prentice-Hall Inc: Englewood Cliffs, New Jersey, **1990**.

(119) Coucouvanis, D.; Al-Ahmad, S.; Salifoglou, A.; Dunham, W. R.; Sands, R. H. A New Cubane Cluster with the $[MoFe_3S_4]^0$ Core and Possible Relevance to the Fe_3-Centers in Ferredoxins. The Synthesis, Structure and Properties of the $[Fe_3S_4(SEt)_3Mo(CO)_3]^{3\ominus}$ Anion. *Angew. Chemie Int. Ed.* **1988**, *27* (10), 1353–1355. https://doi.org/10.1002/anie.198813531.

(120) Coucouvanis, D.; Mosier, P. E.; Demadis, K. D.; Patton, S.; Malinak, S. M.; Kim, C. G.; Tyson, M. A. The Catalytic Reduction of Hydrazine to Ammonia by the $MoFe_3S_4$ Cubanes and Implications Regarding the Function of Nitrogenase. Evidence for Direct Involvement of the Molybdenum Atom in Substrate Reduction. *J. Am. Chem. Soc.* **1993**, *115* (25), 12193–12194. https://doi.org/10.1021/ja00078a079.

(121) Han, J.; Koutmos, M.; Ahmad, S. Al; Coucouvanis, D. Rational Synthesis of High Nuclearity Mo/Fe/S Clusters: The Reductive Coupling Approach in the Convenient Synthesis of $(Cl_4\text{-cat})_2Mo_2Fe_6S_8(PR_3)_6$ [R = Et, ^{n}Pr, ^{n}Bu] and the New $[(Cl_4\text{-cat})_2Mo_2Fe_2S_3O(PEt_3)_3Cl]\cdot 1/2(Fe(PEt_3)_2(MeCN)_4)$ and $(Cl_4\text{-cat})_2Mo_2Fe_3S_5(PEt_3)_5$ Clusters. *Inorg. Chem.* **2001**, *40* (23), 5985–5999. https://doi.org/10.1021/ic0104914.

(122) Koutmos, M.; Coucouvanis, D. Borohydride Anions as Terminal Ligands on a Fe/Mo/S Cluster. Synthesis, Structure, and Characterization of the [(Cl 4 -cat)(PPr 3)MoFe 3 S 4 (BH 4) 2] 2 (Bu 4 N) 4 Double-Fused Cubane. Inorg. Chem. 2004, 43 (21), 6508–6510. https://doi.org/ 10.1021/ic049275w

(123) Koutmos, M.; Georgakaki, I. P.; Coucouvanis, D. Borohydride, Azide, and Chloride Anions As Terminal Ligands on Fe/Mo/S Clusters. Synthesis, Structure and Characterization of $[(Cl_4\text{-cat})(PPr_3)MoFe_3S_4(X)_2]_2(Bu_4N)_4$ and $[(Cl_4\text{-cat})(PPr_3)MoFe_3S_4(PPr_3)(X)]_2(Bu_4N)_2$ ($X = N^{3-}$, BH^{4-}, Cl^-) Double-Fused Cubanes. NMR Reactivity Studies of $[(Cl_4\text{-cat})(PPr_3)MoFe_3S_4(BH_4)_2]_2(Bu_4N)_4$. *Inorg. Chem.* **2006**, *45* (9), 3648–3656. https://doi.org/10.1021/ic052156b.

(124) Coucouvanis, D.; Challen, P. R.; Koo, S. M.; Davis, W. M.; Butler, W.; Dunham, W. R. Stepwise Synthesis and Structural Characterization of the $\{[MoFe_3S_4Cl_2(Cl_4cat)]_2(\mu_2\text{-}S)_2\}^{6-}$ and $\{[MoFe_3S_4Cl_2(Cl_4cat)]_2(\mu_2\text{-}S)(\mu_2\text{-}OH\}^{5-}$

Doubly Bridged Double Cubanes Obtained by the Coupling of [$MoFe_3S_4$] Clusters. *Inorg. Chem.* **1989**, *28* (23), 4181–4183. https://doi.org/10.1021/ic00322a001.

(125) Kanatzidis, M. G.; Coucouvanis, D. New $[Fe_6S_6Cl_6(Mo(CO)_3)_2]^{n-}$ Clusters (n = 3, 4). Derivatives of either $[Fe_6S_6Cl_6]^{3-}$ or $[Fe_4S_4Cl_4]^{2-}$ with Possible Relevance to the Fe/Mo/S Center in Nitrogenase. *J. Am. Chem. Soc.* **1986**, *108* (2), 337–338. https://doi.org/10.1021/ja00262a048.

(126) Coucouvanis, D.; Salifoglou, A.; Kanatzidis, M. G.; Simopoulos, A.; Kostikas, A. Synthesis, Structural Characterization, and Electronic Structures of the $[Fe_6S_6(X)_6(Mo(CO)_3)_2]^{3-}$ Clusters (X = Cl, Br). *J. Am. Chem. Soc.* **1987**, *109* (12), 3807–3808. https://doi.org/10.1021/ja00246a063.

(127) Coucouvanis, D.; Salifoglou, A.; Kanatzidis, M. G.; Dunham, W. R.; Simopoulos, A.; Kostikas, A. Synthesis, Structural Characterization, and Electronic Properties of the $[(Fe_6S_6X_6)(M(CO)_3)_2]^{n-}$ Anions (M = Mo, W; n = 3, 4; X = Cl, Br, I). Heteronuclear Clusters of Possible Structural Relevance to the Fe/Mo/S Center in Nitrogenase. *Inorg. Chem.* **1988**, *27* (22), 4066–4077. https://doi.org/10.1021/ic00295a034.

(128) Malinak, S. M.; Demadis, K. D.; Coucouvanis, D. Catalytic Reduction of Hydrazine to Ammonia by the VFe_3S_4 Cubanes. Further Evidence for the Direct Involvement of the Heterometal in the Reduction of Nitrogenase Substrates and Possible Relevance to the Vanadium Nitrogenases. *J. Am. Chem. Soc.* **1995**, *117* (11), 3126–3133. https://doi.org/10.1021/ja00116a017.

(129) Zuo, J.-L.; Zhou, H.-C.; Holm, R. H. Vanadium−Iron−Sulfur Clusters Containing the Cubane-type [VFe_3S_4] Core Unit: Synthesis of a Cluster with the Topology of

the P^N Cluster of Nitrogenase. *Inorg. Chem.* **2003**, *42* (15), 4624–4631. https://doi.org/10.1021/ic0301369.

(130) Zhang, Y.; Zuo, J.-L.; Zhou, H.-C.; Holm, R. H. Rearrangement of Symmetrical Dicubane Clusters into Topological Analogues of the P Cluster of Nitrogenase: Nature's Choice? *J. Am. Chem. Soc.* **2002**, *124* (48), 14292–14293. https://doi.org/10.1021/ja0279702.

(131) Komuro, T.; Kawaguchi, H.; Lang, J.; Nagasawa, T.; Tatsumi, K. $[MoFe_3S_4]^{3+}$ and $[MoFe_3S_4]^{2+}$ cubane clusters containing a pentamethylcyclopentadienyl molybdenum moiety. *J. Organomet. Chem.* **2007**, *692* (1–3), 1–9. https://doi.org/10.1016/j.jorganchem.2006.07.047.

(132) Della Pergola, R.; Sironi, A.; Manassero, C.; Manassero, M. Hydridocopper Complexes Embedded in Iron Carbidocarbonyl Clusters: Synthesis, Reactivity, and Structure of $[Fe_4C(CO)_{12}CuCl]^{2-}$, $[Fe_4C(CO)_{12}Cu(\eta^2\text{-}BH_4)]^{2-}$, $[\{Fe_4C(CO)_{12}Cu_2(\mu\text{-}H)\}_2]^{2-}$, and $[\{Fe_4C(CO)_{12}Cu_2(\mu\text{-}O\mathit{i}Pr)\}_2]^{2-}$. *Organometallics* **2010**, *29* (22), 5885–5889. https://doi.org/10.1021/om1006775.

(133) Della Pergola, R.; Sironi, A.; Moret, M.; Bergantin, S.; Mussini, P. R.; Panigati, M. Cyclic dimers of variable size, formed from FeCu carbide clusters: Synthesis, structure and electrochemical behaviour of $[\{Fe_4C(CO)_{12}Cu_2(\mu\text{-}X)\}_2]^{n-}$, (X = phenylthiolate, pyrazolate, (n = 2) or diphenolate (n = 4)). *J. Organomet. Chem.* **2013**, *728*, 23–29. https://doi.org/10.1016/j.jorganchem.2013.01.006.

(134) Johnson, B. F. G.; Kaner, D. A.; Lewis, J.; Raithby, P. R.; Rosales, M. J. Syntheses and structural characterisations of some novel mixed-metal iron-gold carbido clusters; X-ray crystal structures of $Fe_4AuC(\mu\text{-}H)(CO)_{12}(PPh_3)$ and $Fe_4Au_2C(CO)_{12}(PEt_3)_2$. *J. Organomet. Chem.* **1982**, *231* (3), C59–C64. https://doi.org/10.1016/S0022-328X(00)92900-0.

(135) Rossell, O.; Seco, M.; Segalés, G.; Alvarez, S.; Pellinghelli, M. A.; Tiripicchio, A.; de Montauzon, D. Iron−Gold (or −Mercury) Carbide Clusters Derived from $[Fe_6C(CO)_{16}]^{2-}$. X-ray Crystal Structures of $(NEt_4)[Fe_6C\{AuPPh_3\}(CO)_{16}]$ and $[Fe_4C\{AuPPh_3\}(CO)_{11}(NO)]$. *Organometallics* **1997**, *16* (2), 236–245. https://doi.org/10.1021/om9605802.

(136) Bortoluzzi, M.; Ciabatti, I.; Cesari, C.; Femoni, C.; Iapalucci, M. C.; Zacchini, S. Synthesis of the Highly Reduced $[Fe_6C(CO)_{15}]^{4-}$ Carbonyl Carbide Cluster and Its Reactions with H^+ and $[Au(PPh_3)]^+$. *Eur. J. Inorg. Chem.* **2017**, *2017* (25), 3135–3143. https://doi.org/10.1002/ejic.201700169.

(137) Rossell, O.; Seco, M.; Segalés, G.; Pellinghelli, M. A.; Tiripicchio, A. Iron/gold carbide clusters containing Fe_5Au or Fe_5Au_2 skeletons: X-ray crystal structure of $[Fe_5CAu_2(CO)_{14}(dppm)]$. *J. Organomet. Chem.* **1998**, *571* (1), 123–128. https://doi.org/10.1016/S0022-328X(98)00854-7.

(138) Hriljac, J. A.; Swepston, P. N.; Shriver, D. F. Syntheses of Reactive Mixed-Metal Carbide Clusters and Their Interaction with Proton Sources. *Organometallics* **1985**, *4* (1), 158–166. https://doi.org/10.1021/om00120a026.

(139) Slovokhotov, Y. L.; Struchkov, Y. T.; Lopatin, V. E.; Gubin, S. P. "Nut-in-the-nutshell" type of metal cluster coordination by the ligands. X-ray investigation of two carbonyl clusters $[RhFe_5C(CO)_{16}]^-$ and $[Rh_5Fe(CO)_{16}]^-$ with a specific disorder of the metal polyhedron. *J. Organomet. Chem.* **1984**, *266* (2), 139–146. https://doi.org/10.1016/0022-328X(84)80124-2.

(140) Lopatin, V. E.; Gubin, S. P.; Mikova, N. M.; Tsybenov, M. T.; Slovokhotov, Y. L.; Struchkov, Y. T. Mossbauer Spectroscopy Study of the Composition of Carbido Carbonyl Clusters. *J. Organomet. Chem.* **1985**, *292* (1–2), 275–286. https://doi.org/10.1023/A:1022044403089.

(141) Saha, S.; Zhu, L.; Captain, B. Synthesis and Structural Characterization of Bimetallic Iron−Nickel Carbido Cluster Complexes. *Inorg. Chem.* **2010**, *49* (7), 3465–3472. https://doi.org/10.1021/ic100057x.

(142) Adams, R. D.; Captain, B.; Fu, W. New Mixed Metal Cluster Complexes Containing Platinum. The Synthesis and Structural Characterizations of $PtFe_4(CO)_{12}(COD)(\mu_5\text{-}C)$ and $PtFe_4(CO)_{12}(PMe_2Ph)_2(\mu_5\text{-}C)$. *J. Clust. Sci.* **2001**, *12*, 303–312. https://doi.org/10.1023/A:1016647718163.

(143) Viculis, L. M.; Mack, J. J.; Mayer, O. M.; Hahn, H. T.; Kaner, R. B. Intercalation and exfoliation routes to graphite nanoplatelets. *J. Mater. Chem.* **2005**, *15* (9), 974–978. https://doi.org/10.1039/b413029d.

(144) Cotton, F. A.; Mccleverty, J. A.; White, J. E.; King, R. B.; Fronzaglia, A. F.; Bisnette, M. B. Tricarbonyl(Cycloheptatriene)-Molybdenum(0). *Inorg. Synth.* **1990**, *28*, 45–47. https://doi.org/10.1002/9780470132593.ch9.

(145) Reina, R.; Rodríguez, L.; Rossell, O.; Seco, M.; Font-Bardia, M.; Solans, X. Electrophilic Additions of Metal Fragments Containing 11- and 12-Group Elements to the Anion Carbide Cluster $[Fe_5MoC(CO)_{17}]^{2-}$. X-ray Crystal Structures of $(NEt_4)[Fe_5MoAuC(CO)_{17}(PMe_3)]$ and $[Fe_5MoAu_2C(CO)_{17}(dppm)]$. *Organometallics* **2001**, *20* (8), 1575–1579. https://doi.org/10.1021/om000976k.

(146) Yuki, M.; Tanaka, H.; Sasaki, K.; Miyake, Y.; Yoshizawa, K.; Nishibayashi, Y. Iron-catalysed transformation of molecular dinitrogen into silylamine under ambient conditions. *Nat. Commun.* **2012**, *3*, 1254. https://doi.org/10.1038/ncomms2264.

(147) Filippou, A. C.; Rosenauer, T. A Reaction Pathway of $[Fe(CO)_5]$ with Alkynes via Ferrabicyclobutenones. *Angew. Chemie Int. Ed.* **2002**, *41* (13), 2393–2396.

https://doi.org/10.1002/1521-3773(20020703)41:13<2393::AID-ANIE2393>3.0.CO;2-3.

(148) Sioda, R. E.; Cowan, D. O.; Koski, W. S. Study of the Radical Anion Formation of Some Diphenylacetylenes in Dimethylformamide. *J. Am. Chem. Soc.* **1967**, *89* (2), 230–234. https://doi.org/10.1021/ja00978a008.

(149) Wawzonek, S.; Wearring, D. Polarographic Studies in Acetonitrile and Dimethylformamide. IV. Stability of Anion-free Radicals. *J. Am. Chem. Soc.* **1959**, *81* (9), 2067–2069. https://doi.org/10.1021/ja01518a009.

(150) Cortese, N. A.; Heck, R. F. Palladium-Catalyzed Reductions of α,β-Unsaturated Carbonyl Compounds, Conjugated Dienes, and Acetylenes with Trialkylammonium Formates. *J. Org. Chem.* **1978**, *43* (20), 3985–3987. https://doi.org/10.1021/jo00414a048.

(151) Itoh, T.; Nagano, T.; Hirobe, M. The $[Fe_4S_4(SR)_4]^{2-}$ catalytic reduction of diphenylacetylene to *cis*-stilbene in the presence of $NaBH_4$. *Tetrahedron Lett.* **1980**, *21* (14), 1343–1346. https://doi.org/10.1016/S0040-4039(00)74571-0

(152) Speelman, A. L.; Čorić, I.; Van Stappen, C.; DeBeer, S.; Mercado, B. Q.; Holland, P. L. Nitrogenase-Relevant Reactivity of a Synthetic Iron–Sulfur–Carbon Site. *J. Am. Chem. Soc.* **2019**, *141* (33), 13148–13157. https://doi.org/10.1021/jacs.9b05353.

(153) Vela, J.; Stoian, S.; Flaschenriem, C. J.; Münck, E.; Holland, P. L. A Sulfido-Bridged Diiron(II) Compound and Its Reactions with Nitrogenase-Relevant Substrates. *J. Am. Chem. Soc.* **2004**, *126* (14), 4522–4523. https://doi.org/10.1021/ja049417l.

(154) Arnet, N. A.; Dugan, T. R.; Menges, F. S.; Mercado, B. Q.; Brennessel, W. W.; Bill, E.; Johnson, M. A.; Holland, P. L. Synthesis, Characterization, and

Nitrogenase-Relevant Reactions of an Iron Sulfide Complex with a Bridging Hydride. *J. Am. Chem. Soc.* **2015**, *137* (41), 13220–13223. https://doi.org/10.1021/jacs.5b06841.

(155) Moula, G.; Matsumoto, T.; Miehlich, M. E.; Meyer, K.; Tatsumi, K. Synthesis of an All-Ferric Cuboidal Iron-Sulfur Cluster $[Fe^{III}_4S_4(SAr)_4]$. *Angew. Chemie Int. Ed.* **2018**, *57* (36), 11594–11597. https://doi.org/10.1002/anie.201803679.

(156) Tanifuji, K.; Tajima, S.; Ohki, Y.; Tatsumi, K. Interconversion between $[Fe_4S_4]$ and $[Fe_2S_2]$ Clusters Bearing Amide Ligands. *Inorg. Chem.* **2016**, *55* (9), 4512–4518. https://doi.org/10.1021/acs.inorgchem.6b00352.

(157) Tanifuji, K.; Lee, C. C.; Ohki, Y.; Tatsumi, K.; Hu, Y.; Ribbe, M. W. Combining a Nitrogenase Scaffold and a Synthetic Compound into an Artificial Enzyme. *Angew. Chemie Int. Ed.* **2015**, *54* (47), 14022–14025. https://doi.org/10.1002/anie.201507646.

(158) Sickerman, N. S.; Tanifuji, K.; Lee, C. C.; Ohki, Y.; Tatsumi, K.; Ribbe, M. W.; Hu, Y. Reduction of C_1 Substrates to Hydrocarbons by the Homometallic Precursor and Synthetic Mimic of the Nitrogenase Cofactor. *J. Am. Chem. Soc.* **2017**, *139* (2), 603–606. https://doi.org/10.1021/jacs.6b11633.

(159) Xu, G.; Wang, Z.; Ling, R.; Zhou, J.; Chen, X.-D.; Holm, R. H. Ligand metathesis as rational strategy for the synthesis of cubane-type heteroleptic iron–sulfur clusters relevant to the FeMo cofactor. *Proc. Natl. Acad. Sci.* **2018**, *115* (20), 5089–5092. https://doi.org/10.1073/pnas.1801025115.

(160) Shupp, J. P.; Rose, A. R.; Rose, M. J. Synthesis and interconversions of reduced, alkali–metal supported iron–sulfur–carbonyl complexes. *Dalt. Trans.* **2017**, *46* (28), 9163–9171. https://doi.org/10.1039/C7DT01506B.

(161) Gourdon, A.; Jeannin, Y. Carbonyl Nitrosyl Clusters. Syntheses and Structures of $[Fe_5C(CO)_{13}(NO)]^-$, $[Fe_6C(CO)_{13}(NO)_2]^{2-}$, and $[Fe_3(CO)_8(NO)(NH)]^-$. *Organometallics* **1986**, *5* (12), 2406–2410. https://doi.org/10.1021/om00143a002.

(162) Bogdan, P. L.; Sabat, M.; Sunshine, S. A.; Woodcock, C.; Shriver, D. F. Anionic Iron Carbido Carbonyl Clusters with Sulfur Dioxide Ligands. *Inorg. Chem.* **1988**, *27* (11), 1904–1910. https://doi.org/10.1021/ic00284a018.

(163) Drance, M. J.; Mokhtarzadeh, C. C.; Melaimi, M.; Agnew, D. W.; Moore, C. E.; Rheingold, A. L.; Figueroa, J. S. Controlled Expansion of a Strong-Field Iron Nitride Cluster: Multi-Site Ligand Substitution as a Strategy for Activating Interstitial Nitride Nucleophilicity. *Angew. Chem. Int. Ed.* **2018**, *57* (40), 13057–13061. https://doi.org/10.1002/anie.201801206.

(164) Mokhtarzadeh, C. C.; Margulieux, G. W.; Carpenter, A. E.; Weidemann, N.; Moore, C. E.; Rheingold, A. L.; Figueroa, J. S. Synthesis and Protonation of an Encumbered Iron Tetraisocyanide Dianion. *Inorg. Chem.* **2015**, *54* (11), 5579–5587. https://doi.org/10.1021/acs.inorgchem.5b00730.

(165) Caballero, C.; Nuber, B.; Ziegler, M. L. Darstellung und Charakterisierung von trigonal bipyramidalen Methylidin-Clustern des Typs $EFe_3(CO)_9CH$ (E = As, Sb, Bi) durch Umsetzung des Carbidoclusters $Fe_5C(CO)_{15}$ mit metallischem Arsen und Wismut bzw. $SbCl_5$. *J. Organomet. Chem.* **1990**, *386* (2), 209–223. https://doi.org/10.1016/0022-328X(90)85246-U.

(166) Capps, K. B.; Wixmerten, B.; Bauer, A.; Hoff, C. D. Thermochemistry of Sulfur Atom Transfer. Enthalpies of Reaction of Phosphines with Sulfur, Selenium, and Tellurium, and of Desulfurization of Triphenylarsenic Sulfide, Triphenylantimony Sulfide, and Benzyl Trisulfide. *Inorg. Chem.* **1998**, *37* (12), 2861–2864. https://doi.org/10.1021/ic9715862.

(167) Wei, C. H.; Dahl, L. F. Crystal Structure of a 1:1 Mixture of Two Iron Carbonyl Sulfur Complexes, $S_2Fe_3(CO)_9$ and $S_2Fe_2(CO)_6$. *Inorg. Chem.* **1965**, *4* (4), 493–499. https://doi.org/10.1021/ic50026a012.

(168) Bard, A. J.; Cowley, A. H.; Leland, J. K.; Thomas, G. J. N.; Norman, N. C.; Jutzi, P.; Morley, C. P.; Schlüter, E. Synthesis, Structures, and Reactivities of Some Pentamethylcyclopentadienyl–Sulphur Compounds. *J. Chem. Soc., Dalt. Trans.* **1985**, 1303–1307. https://doi.org/10.1039/DT9850001303.

(169) Broadhurst, P. V.; Johnson, B. F. G.; Lewis, J.; Raithby, P. R. Reaction of CS_2 with Metal Cluster Carbonyls of the Iron Triad: Synthesis and X-ray Structure of $[Fe_5(CO)_{13}S_2(CS)]$ Containing a Six-Electron Donor Thiocarbonyl Group. *J. Am. Chem. Soc.* **1981**, *103* (11), 3198–3200. https://doi.org/10.1021/ja00401a043.

(170) Smart, R. S. C.; Skinner, W. M.; Gerson, A. R. XPS of Sulphide Mineral Surfaces: Metal-Deficient, Polysulphides, Defects and Elemental Sulphur. *Surf. Interface Anal.* **1999**, *28* (1), 101–105. https://doi.org/10.1002/(SICI)1096-9918(199908)28:1<101::AID-SIA627>3.0.CO;2-0.

(171) Sosinsky, B. A.; Norem, N.; Shelly, J. Spectroscopic Study of a Series of Iron Carbido Clusters. *Inorg. Chem.* **1982**, *21* (1), 348–356. https://doi.org/10.1021/ic00131a063.

(172) Grosvenor, A. P.; Kobe, B. A.; Biesinger, M. C.; McIntyre, N. S. Investigation of multiplet splitting of Fe 2p XPS spectra and bonding in iron compounds. *Surf. Interface Anal.* **2004**, *36* (12), 1564–1574. https://doi.org/10.1002/sia.1984.

(173) Barber, M.; Connor, J. A.; Guest, M. F.; Hall, M. B.; Hillier, I. H.; Meredith, W. N. E. High Energy Photoelectron Spectroscopy of Transition Metal Complexes. Part 1. – Bonding in Substituted and Unsubstituted First Row Carbonyls. *Faraday Discuss. Chem. Soc.* **1972**, *54*, 219–226. https://doi.org/10.1039/DC9725400219.

(174) Manes, T. A. Molecular scaffolding : setting foundations for metal complexation and bioinorganic modeling, The University of Texas at Austin, **2018**. http://hdl.handle.net/2152/68087.

(175) Granovsky, A. A. *Firefly version 8* http://classic.chem.msu.su/gran/firefly/index.html.

(176) Bode, B. M.; Gordon, M. S. Macmolplt: A graphical user interface for GAMESS. *J. Mol. Graph. Model.* **1998**, *16* (3), 133–138. https://doi.org/10.1016/S1093-3263(99)00002-9.

(177) *SAINT*. Bruker AXS Inc.: Madison, WI 2012.

(178) Sheldrick, G. M. *SHELXT* - Integrated space-group and crystal-structure determination. *Acta Crystallogr. Sect. A* **2015**, *A71* (1), 3–8. https://doi.org/10.1107/S2053273314026370.

(179) Sheldrick, G. M. Crystal structure refinement with SHELXL. *Acta Crystallogr. Sect. C* **2015**, *C71* (1), 3–8. https://doi.org/10.1107/S2053229614024218.

(180) *OlexSys*. OlexSys Ltd.:Durham University, UK **2019**.

(181) *International Tables for Crystallography*; Prince, E., Ed.; International Tables for Crystallography; International Union of Crystallography: Chester, England, **2006**; Vol. C. https://doi.org/10.1107/97809553602060000103.

(182) Farrugia, L. J. *WinGX* and *ORTEP* for *Windows*: an update. *J. Appl. Crystallogr.* **2012**, *45* (4), 849–854. https://doi.org/10.1107/S0021889812029111.

(183) *CrysAlisPro*. Agilent Technologies UK Ltd.: Oxford, UK **2013**.

(184) Altomare, A.; Burla, M. C.; Camalli, M.; Cascarano, G. L.; Giacovazzo, C.; Guagliardi, A.; Moliterni, A. G. G.; Polidori, G.; Spagna, R. SIR 97: a new tool for crystal structure determination and refinement. *J. Appl. Crystallogr.* **1999**, *32* (1), 115–119. https://doi.org/10.1107/S0021889898007717.

(185) *PLATON, A Multipurpose Crystallographic Tool*. Utrecht University: The Netherlands 1998.

(186) Farrugia, L. J. WinGX suite for small-molecule single-crystal crystallography. *J. Appl. Crystallogr.* **1999**, *32* (4), 837–838. https://doi.org/10.1107/S0021889899006020.

(187) *CrystalClear*. Rigaku Americas Corportion: The Woodlands, TX 2008.